

Body-Involved Fluid Dynamic Interactions and Performance Enhancement Mechanisms in Biological Propulsion

A
Dissertation
Presented to
the faculty of the School of Engineering and Applied Science
University of Virginia

in partial fulfillment
of the requirements for the degree

Doctor of Philosophy

by

Junshi Wang

August 2021

APPROVAL SHEET

This
Dissertation
is submitted in partial fulfillment of the requirements
for the degree of
Doctor of Philosophy

Author: Junshi Wang

This Dissertation has been read and approved by the examining committee:

Advisor: Haibo Dong

Advisor:

Committee Member: Daniel Quinn

Committee Member: Chloe Dedic

Committee Member: Matthew Reidenbach

Committee Member: Chengyu Li

Committee Member:

Committee Member:

Accepted for the School of Engineering and Applied Science:



Jennifer L. West, School of Engineering and Applied Science

August 2021

Abstract

After millions of years of evolution, aerial and aquatic animals in nature have developed specialized morphological features and superior locomotion strategies to interact with the surrounding fluids to achieve fast and efficient flying/swimming. Pronounced fluid dynamic interactions between the body and the fins/wings are commonly observed in insects/birds and fishes which can be beneficial for their propulsive performance.

This dissertation combines experimental and numerical approaches to examine the body-involved fluid dynamic interactions (BI-FDI) and the underlying flow physics in nature across major forms of body-propulsor configurations, morphological features, and locomotion modes. High-fidelity computational models with flying/swimming kinematics are built based on high-speed videos of live animal locomotion. Numerical simulations are then conducted using an immersed boundary based direct numerical flow solver to obtain the hydrodynamic performance and detailed flow field information for the analyses of performance enhancement and body-involved vortex dynamics.

It is found that aerodynamic/hydrodynamic performance enhancement owing to BI-FDI widely exists in the flying/swimming animals examined. Specifically, A 29% overall lift enhancement due to wing-body interaction is found in the “+”-type bilateral propulsion of hummingbird forward flight. Vortex dynamics results showed formations of unique body vortex pairs on the dorsal thorax of the hummingbird where low-pressure zones were created to generate more body lift. Significant interactions between body vortex and

leading-edge vortex (LEV) were observed, resulting in strengthened LEVs near the wing root and enhanced wing lift generation during the downstroke of the wings.

For in-line propulsion of thunniform swimming in tuna, it is found that the independently mobile finlets help increase caudal fin thrust by 8% and reduce trunk drag by 7%. The effect of swimming with finlets is equivalent to adding a propulsor with nominal propulsive efficiency of 23.6%. Detailed flow analysis reveals that the presence of finlets at the dorsal and ventral margins is responsible for the trunk drag reduction and the interactions between the finlet-induced vortex pair and the caudal fin is responsible for the caudal thrust enhancement. The pitching kinematics of finlets help reduce the finlet drag, lateral force amplitude, and power consumption, resulting in a higher nominal propulsive efficiency of 23.6% than the 16.6% of body-fixed finlets.

For in-line propulsion of carangiform swimming in trout, the dorsoventrally asymmetric dorsal fin and anal fin use different mechanisms to reduce trunk drag and enhance caudal fin thrust. The dorsal fin induces lateral flow and dorsal fin vortex that strengthen the leading edge vortex and creates a larger pressure difference between the two sides of the caudal fin, resulting in an 11% thrust increase. The presence of the anal fin prevents both the local lateral flow across the ventral edge of the trunk and the formation of peduncle vortex that is destructive for caudal fin thrust production, resulting in a 6.9% trunk drag reduction and a 4.3% caudal fin thrust increase, respectively. In addition, the pelvic fins help reduce all the anal fin drag owing to beneficial interactions.

For in-line propulsion of anguilliform swimming in the leech, both the trunk and the posterior sucker produce thrust from pressure forces and suction forces acting on the body surface to balance the viscous drag. The trunk induces a counter-rotating edge vortex pair that then interacts with the lateral edges of the trunk in the following stroke. A strong correlation between the more intense vortex-trunk interaction and larger suction thrust

production at the dorsal trunk surface is found when the aspect ratio of trunk cross section (AR) increases. The larger suction/pressure forces and the more dorsal-ventrally orientated normal vector of the trunk surface result in the larger thrust production at the trunk with higher AR. The vortex structure shows a less significant edge vortex at a lower Reynolds number. A similar pattern in thrust distribution along the body is found at different Reynolds numbers. The vortex structure shows severer edge vortex separations associated with more small-scaled vortex structures at higher Strouhal number and less strong edge vortex at lower Strouhal number. Thrust production of the anterior trunk is most sensitive to Strouhal number change.

Two major categories of the body-involved performance enhancement mechanisms—the deflection or prevention of transverse flow across body edges and wake capture or wake prevention at the propulsor—are found in the BI-FDIs examined in this dissertation work.

The overall findings of this dissertation advance the understanding of body-involved performance enhancement mechanisms in biological propulsion and provide novel physical insights into the design of aerial/underwater unmanned vehicles from a fluid dynamics perspective.

Acknowledgments

First of all, I would like to express my deepest gratitude and sincere thanks to my advisor Haibo Dong. It has been a wonderful journey doing research with Haibo's guidance along every step of the way. He taught me to be a careful researcher who discovers flow physics in nature, but also an effective communicator who promotes the implication of STEM to society. Haibo stood by me through every challenge and supported me in every venue, and for that, I consider him a friend as much as a mentor.

I would like to express my sincere gratitude to my committee members, Daniel Quinn, Chloe Dedic, Matthew Reidenbach, and Chengyu Li, for their inspiring guidance, warm encouragement, and constructive comments in my research.

I would like to give my heartfelt gratitude to my collaborators in the MURI team, George Lauder, Dylan Wainwright, and Valentina Di Santo, for their wonderful fish videos and valuable comments on the swimming projects, without which this dissertation would not be possible. My gratitude extends to Hilary Bart-Smith, Frank Fish, Keith Moored, and Joe Zhu for their help and insights throughout the MURI program.

Many thanks are given to my past and present teammates, Yan Ren, Geng Liu, Chengyu Li, Pan Han, Ayodeji Bode-Oke, Xiaolong Deng, Yu Pan, Yuchen Gong, and all other current and previous Flow Simulation Research Group (FSRG) members for their assistance, generosity, and advice throughout my Ph.D. study and life.

Finally, and foremost, I would like to express my profound gratitude to my family. To Wanyi, for her love, understanding, and support through the darkest and brightest days. It is her encouragement that gains me the strength to overcome difficulties in study and life. To my parents, I owe their unconditional love and support which always keeps me strong, which has led and will lead me to more than I can be.

Table of Contents

Abstract.....	2
Acknowledgments.....	5
Table of Contents.....	i
List of Figures.....	v
List of Tables.....	xix
1 Introduction.....	1
1.1 Motivation and Goals.....	1
1.2 Body-Involved Fluid Dynamic Interactions (BI-FDI).....	3
1.3 BI-FDI in Bilateral Propulsion.....	4
1.4 BI-FDI in In-Line Propulsion.....	6
1.5 Wing-Body Interaction in Hummingbird Forward Flight.....	9
1.6 Hydrodynamic Effect Finlets on Propulsive Performance in Thunniform Swimming	11
1.7 Hydrodynamic Roles of Dorsoventrally Asymmetric Dorsal fin and Anal Fin in Carangiform Swimming.....	13
1.8 Thrust Production Mechanism and BI-FDI in Anguilliform Swimming.....	14
1.9 Current Objectives.....	15
1.10 Outline of Thesis.....	19
2 Methodology.....	22
2.1 Numerical Method.....	22
2.2 High-Speed Videography and Kinematics Reconstruction.....	23
2.3 Level-Set Based Immersed Boundary Reconstruction for Complex Morphology.....	26
2.3.1 Numerical Algorithm.....	27
2.3.2 Validation Study.....	29

3	Bilateral Propulsion: Wing-Body Interaction and its Lift Enhancement Effect in Hummingbird Forward Flight.....	36
3.1	Kinematics and Geometry of Computational Model.....	37
3.2	Simulation Setup.....	41
3.3	Validation Study	43
3.4	Results and Discussions.....	46
3.4.1	Aerodynamic Performance	46
3.4.2	Vortex Topology.....	49
3.4.3	Surface Pressure.....	55
3.4.4	Effects of Body Angle on WBI.....	58
3.4.5	Effect of Advance Ratio on WBI.....	61
3.4.6	Effect of Tail Shape on WBI	65
3.5	Chapter Summaries.....	67
4	In-Line Propulsion: A Computational Hydrodynamic Analysis of Finlet Function.....	70
4.1	Tuna Kinematics and Finlet Morphology.....	71
4.2	Computational Setup.....	77
4.3	Results.....	81
4.3.1	Hydrodynamic Performance and Wake Topology of Finlets	81
4.3.2	Effects of Finlet-Finlet Interaction.....	87
4.3.3	Effect of Pitching Kinematics of Finlets.....	90
4.4	Discussion.....	97
4.5	Chapter Summaries.....	99
4.6	Supplementary Material.....	100
4.6.1	Analytical Representation of Finlet Model Kinematics Using Fourier Series	100
4.6.2	Validation Study on the Uniform Incoming Flow Assumption.....	101

4.6.3	Validation study on the reduced Reynolds number	103
4.6.4	Summary of finlet arrangement and kinematics used for computations.....	105
5	In-Line Propulsion: Hydrodynamic Interactions and Enhanced Propulsive Performance Owing to Finlets in Tuna Swimming.....	106
5.1	Tuna Morphology and Kinematics	107
5.2	Reconstruction of Computational Model with Swimming and Finlet Kinematics.....	109
5.3	Simulation Setup.....	113
5.4	Results.....	115
5.4.1	Hydrodynamic Performance and Vortex Dynamics of Tuna Swimming.....	116
5.4.2	Caudal Fin Thrust Enhancement and Trunk Drag Reduction Owing to Finlets...	121
5.4.3	Hydrodynamic Benefit of Pitching Kinematics of Finlets.....	128
5.5	Discussion.....	133
5.6	Chapter Summaries.....	134
6	In-Line Propulsion: Enhanced Hydrodynamic Performance by Dorsal Fin and Anal Fin in Trout Swimming	136
6.1	Trout Kinematics and Computational Modes	136
6.2	Computational Setup.....	139
6.3	Results.....	142
6.3.1	Hydrodynamic Performance and Vortex Structure of Trout Swimming.....	143
6.3.2	Caudal Fin Thrust Enhancement by Dorsal Fin.....	147
6.3.3	Trunk Drag Reduction and Caudal Fin Thrust Enhancement by Anal Fin.....	151
6.3.4	Constructive Interactions among Pelvic Fins, Anal Fin, and Caudal Fin.	157
6.4	Discussion.....	161
6.5	Chapter Summaries.....	162
7	In-Line Propulsion: Effect of Body Flattening on Thrust Production Mechanism and Vortex Dynamics in Leech Swimming.....	164

7.1	Leech Kinematics and Computational Modes	164
7.2	Simulation Setup.....	167
7.3	Results.....	170
7.3.1	Hydrodynamic Performance and Vortex Structure of Leech Swimming.....	172
7.3.2	Effect of Trunk Aspect Ratio.....	178
7.3.3	Effect of Reynolds Number	183
7.3.4	Effect of Strouhal Number.....	186
7.4	Discussion.....	189
7.5	Chapter Summaries.....	190
8	Concluding Remarks.....	193
8.1	Summary of Contributions.....	193
8.2	Summary of Body-Involved Performance Enhancement Mechanisms	197
8.3	Future Work.....	200
	Bibliography	201

List of Figures

Figure 1-1: Various unmanned vehicle designs using biomimetics or bioinspiration. (a) RoboBee, Harvard University [3], (b) Nano Hummingbird, AeroVironment, Inc. [4], (c) Tunabot, University of Virginia [5], (d) Mantabot, University of Virginia [6].	1
Figure 1-2: Body-involved fluid dynamic interaction (BI-FDI) of various forms in biological propulsion. (a) Wake schematic for wing-body interaction in cicada forward flight [7], (b) Leading edge vortex (LEV) on both the thorax and wings of a butterfly during flight [8], (c) Interaction of posterior body vortex with caudal fin in jackfish swimming [9], (d) Interaction of dorsal fin-induced body vortex with caudal fin in tuna-like swimming [10].	2
Figure 1-3: Categories of body-involved fluid dynamic interaction in nature. Major categories of body-propulsor configuration, morphological configuration, and locomotion mode are listed.	4
Figure 1-4: Various morphological configurations in nature. (a) “T”-type wing-body configuration in cicada (figure adapted from Wan et al. [22]), (b) “+”-type wing-body configuration in hummingbird, (c) Dorsal and ventral finlets in tuna (figure adapted from Wang et al. [23]), (d) Dorsoventrally asymmetric median fin configuration in trout, (e) lateral view of leech swimming.	6
Figure 1-5: Swimming modes associated with (a) body and caudal fin propulsion and (b) median/paired fin propulsion. Shaded areas contribute to thrust generation (figure adapted from Sfakiotakis et al. [27]).	8
Figure 2-1: Schematics of the virtual-scene kinematics reconstruction (VSKR) method.	24
Figure 2-2: Reconstruction of body and finlet kinematics of mackerel fish swimming.	25
Figure 2-3: Schematics of level set value calculation and propagation near the immersed boundary.	28
Figure 2-4: (a) Computational model of hummingbird used for the simulation, (b) schematics of the computational grids and boundary information. A dense mesh of 27 million is used for detecting the immersed boundary with $\Delta x = 0.02c$.	31

Figure 2-5: (a) Unstructured mesh of the hummingbird body and wings, (b) Calculated level set values of both the solid body and membrane wings on seven transverse plans cutting through the body and the wings, (c) Result of immersed boundary detected by level set values..... 32

Figure 2-6: Propagation of level set value during a flapping cycle of hummingbird forward flight. The level set values are plotted on seven transverse planes cutting through the body and the wings. The volume swept by the wings is shown at $t/T = 11/12$ with a grey iso-surface..... 32

Figure 2-7: (a) comparison of the instantaneous lift coefficient CL of the left wing between the previous work [8] and the present improved LS-IBRM, (b) Q-isosurface showing the vortex wake during hummingbird forward flight, (c) Z-vorticity contour on three slice-cuts on the body and the left wing. 33

Figure 2-8: (a) Unstructured mesh of the tuna-inspired underwater vehicle, (b) Calculated level set values of both the solid body and membrane caudal fin on ten transverse plans cutting through the body and the caudal fin, (c) Result of immersed boundary detected by level set values. (d) Level set value on slice cutting through the middle frontal plane of the model. The zero level set value boundary ($\phi = 0$) is used to reconstruct the immersed boundary shown in (c). 35

Figure 2-9: Wake structure of Tunabot forward swimming at slow (a), medium (b), and high (c) speed. The vortex wake is represented by Q-isosurface and flooded by z-vorticity. 35

Figure 3-1: (a) Hummingbird model with wing kinematics shown at four time-instants. The body frontal plane (in light orange), stroke plane (in light gray), and tip trajectory (in red) are shown in 3D. The stroke angle, ϕ , denotes the angular displacement of the wing in the stroke plane $o'y'z'$. The deviation angle, θ , is defined as the angle between the root-to-tip line of the wing and the stroke plane. The wing pitch angle, α , is the angle between the wing chord and the mid-frontal plane. (b) 2-D lateral view of the hummingbird model with wing chord (in blue on the wing) shown at three time instances during the downstroke. The mid-frontal plane (dashed line), stroke plane (dash-dot line) are shown together with the 2-D wing pitch angle, α_{2D} , body angle, β , and stroke plane angle, γ . The 2-D wing pitch angle, α_{2D} , is defined as the angle between the projection of the wing chord on the median plane and the orientation of the mid-frontal plane. 38

Figure 3-2: Comparisons of the wing tip trajectories between the present model and experimental data [49] in lateral (a) and top (b) views, respectively. Wing shape at six time-instants are shown in (a) during the upstroke and in (b) during the downstroke. (c) Comparison of the 2-D wing pitch angle α_{2D} between the present model and experimental data. The error bars indicate the range of the error in experimental measurements. (d) The time history of the modeled wing Euler angles, including the stroke angle, ϕ , the deviation angle, θ , and the wing pitch angle, α , during one flapping cycle..... 40

Figure 3-3: (a) Schematic of the computational domain, mesh, and boundary conditions used in the simulations of the present study. (b) Comparison of instantaneous lift coefficient of the left wing in the WO model between coarse mesh ($193 \times 87 \times 193 \approx 3.2$ million, $\Delta x = 0.081c$), medium mesh ($257 \times 129 \times 257 \approx 8.5$ million, $\Delta x = 0.046c$), fine mesh ($289 \times 161 \times 289 \approx 13.4$ million, $\Delta x = 0.034c$), and dense mesh ($305 \times 183 \times 305 \approx 17.0$ million, $\Delta x = 0.029c$). 43

Figure 3-4: (a) Comparison of instantaneous wing lift coefficient between present and literature data during hovering flight. (b) Comparisons of stroke-averaged lift coefficients during downstroke and upstroke, respectively. 45

Figure 3-5: Comparisons of instantaneous lift and thrust coefficients on the left wing (a) and the body (b), respectively, between the WB, WO, and BO models during one flapping cycle. Comparisons of the three-dimensional wake structure of the hummingbird between the WB (c)–(e) and WO (f)–(h) models at (i) $t/T = 0.1$ (c) and (f), (ii) $t/T = 0.27$ (d) and (g), and (iii) $t/T = 0.42$ (e) and (h), during the downstroke, respectively. The vortex structures of shear layer (SL), thorax vortex (TXV), leading-edge vortex (LEV), tip vortex (TV), root vortex (RV), and new thorax vortex (nTXV) are identified. The isosurface of the wake structures is visualized by $Q = 60$. The yellow dashed lines indicate the vortex core locations of the thorax vortex pair. 47

Figure 3-6: Comparison of the three-dimensional wake structure of the hummingbird between the WB (a)–(c) and WO (d)–(f) models at (i) $t/T = 0.52$ (a) and (d), (ii) $t/T = 0.63$ (b) and (e), and (iii) $t/T = 0.75$ (c) and (f), during the downstroke, respectively. The vortex structures of the shear layer (SL), root vortex (RV), and new thorax vortex (nTXV) are identified. The isosurface of the wake

structures is visualized by $Q = 60$. The yellow dashed lines indicate the vortex core locations of the thorax vortex pair. 50

Figure 3-7: Comparison of instantaneous spanwise vorticity contour (ω_z) between the WB (a), WO (b), and BO (c) models at $t/T = 0.27$ on three slice-cuts (Slice 1, 2, and 3) taken at $-0.1L$, $0.1L$ and $0.3L$ away from the wing root. Same slices are taken on the WO and BO models where applicable. ω_z is normalized by U_f/c . The wake structures are also shown in (a)–(c) with the shear layer (SL), thorax vortex (TXV), and root vortex (RV) identified. The 2-D vorticity and z-axial velocity contours on the slices are compared between the WB, WO, and BO models, respectively in (d) and (e). The z-axial velocity U_z is normalized by U_f . The z-axial velocity on slice cutting the body transverse plane is compared between the WB, WO, and BO models in (f). 52

Figure 3-8: Comparison of instantaneous spanwise vorticity contour (ω_z) between the WB (a) and WO (b) models at $t/T = 0.27$ on six slice-cuts taken at $-0.1L$, $0.1L$, $0.3L$, $0.5L$, $0.7L$, and $0.9L$ away from the wing root. The vorticity is normalized by U_f/c . (c) Circulations ($|\Gamma|$) of the LEVs at the six positions are calculated and compare between the WB and WO models. The circulation difference $|\Gamma_{WB}| - |\Gamma_{WO}|$ is also shown. $|\Gamma|$ is normalized by U_f/c 55

Figure 3-9: Comparisons of pressure isosurface (a)–(c) and model surface pressure distribution (d)–(f), respectively, between the WB, WO, and BO models at $t/T = 0.27$. In (a)–(c), the transparent outer shell is visualized by $C_p = -0.08$ and the inner core by $C_p = -0.25$. The pressure isosurfaces are flooded by C_p 56

Figure 3-10: Comparison of the pressure difference contour (ΔC_p) on the left wing between the WB (a) and the WO (b) model at $t/T = 0.27$. The lift enhancement distribution ($\Delta C_p|_{WB} - \Delta C_p|_{WO}$) on the left wing is shown in (c). The star shape in (c) denotes the location of maximum lift enhancement. The corresponding local chord averaged ΔC_p and $\Delta C_p|_{WB} - \Delta C_p|_{WO}$ are shown in (d)–(e), respectively. The cumulative $\Delta C_p|_{WB} - \Delta C_p|_{WO}$ from the wing tip to the wing root is shown in (e) with a red line. 58

Figure 3-11: (a) Comparison of cycle-averaged lift coefficients, \bar{C}_L , at various body angles, β , between the WB, WO, and BO models at $J = 0.464$. OLE ($\Delta \bar{C}_L$). The percentage of OLE attributed

to the body ($\Delta\bar{C}_L|_{\text{body}}/\Delta\bar{C}_L$) are shown in (b). (c) Comparison of cycle-averaged coefficient of power output, \bar{C}_{PW} , at various body angles. 59

Figure 3-12: Comparisons of three-dimensional wake structure (a)–(c) and pressure coefficient isosurface (d)–(f) of the WB model, respectively, at $t/T = 0.27$ between body angle, $\beta = 20^\circ$ (a) and (d), $\beta = 30^\circ$ (b) and (e), and $\beta = 50^\circ$ (c) and (f). The shear layer (SL) and the thorax vortex (TXV) are identified in (a)–(c). 60

Figure 3-13: (a) Comparison of cycle-averaged lift coefficients, \bar{C}_L , at various advance ratios, J , between the WB, WO, and BO models at $\beta = 30^\circ$. OLE ($\Delta\bar{C}_L$) and the percentage of OLE attributed to the wing pair ($\Delta\bar{C}_L|_{\text{wing pair}}/\Delta\bar{C}_L$) are shown in (b). 63

Figure 3-14: Comparisons of vortex structure (a) and (b), 2-D spanwise vorticity on slice-cut (c) and (d), and lift enhancement distribution contour on the left wing (e) and (f) of the WB model at $t/T = 0.27$ between $J = 0.317$ (a), (c), and (e) and $J = 0.619$ (b), (d), and (f), respectively. The Q -isosurface in (a,b) is visualized by $Q = 60$. The yellow dashed lines indicate the vortex core locations of the thorax vortex. ω_z is normalized by U_f/c . The star shapes in (e) and (f) denote the locations of maximum lift enhancement. 64

Figure 3-15: (a)–(c) Comparison of hummingbird body at three tail spans. The tail span ratios R_S in (a), (b), and (c) are 1.69, 1.00, and 0.64, respectively. (d) Comparison of cycle-averaged lift coefficients, \bar{C}_L , at various tail span ratios between the WB, WO, and BO models at $\beta = 30^\circ$ and $J = 0.464$ 66

Figure 3-16: Comparisons of pressure isosurface of WB model at $\beta = 30^\circ$, $J = 0.464$, and $t/T = 0.27$ between different tail span ratios at (a) $R_S = 0.64$, (b) $R_S = 1.00$, and (c) $R_S = 1.69$. the transparent outer shell is visualized by $C_p = -0.08$ and the inner core by $C_p = -0.25$. The pressure isosurfaces are flooded by C_p 67

Figure 4-1: (a) Live yellowfin tuna (*Thunnus albacares*) swimming (with nine finlets indicated by letters A to I). (b) Illustration of the dorsal and ventral finlets of a yellowfin tuna. (c) Dorsal and ventral finlets of a mackerel during free swimming. (d) Caudal peduncle region of a yellowfin tuna

with finlets. (e) A single tuna finlet to show the attached base and free posterior region. (f) Tuna finlet overlapped by the computational finlet model (red outline). 73

Figure 4-2: Top-view snapshots of a yellowfin tuna (*Thunnus albacares*) in forward swimming during one tail beat cycle. Nine finlets (A to I) are labeled in the upper left panel, but only the function of five (C to G) were analyzed in detail here. Body midline angle (δ) defines the angle between the body midline and the body sagittal plane. The geometric angle of attack (α) is the angle between the finlet and the body sagittal plane. Finlet angle (θ), effective angle of attack (α_{eff}), effective velocity (U_{eff}), swimming velocity (U_∞), and the instantaneous root velocity of the finlet (U_{root}) are also shown. 73

Figure 4-3: Reconstructed finlet motion during the left-to-right stroke and the right-to-left stroke, respectively, from a perspective view (a) and top view (b). In (a), A change in finlets color corresponds to a change in time of $T/24$. The instantaneous lateral root displacement (z/c), finlet angle (θ), and geometric angle of attack (α) of the five finlets during one tail beat cycle are plotted in (c–e), respectively. The maximum, minimum, and mean values of each finlet angle are shown in (f). 76

Figure 4-4: (a) Schematic of the computational mesh and boundary conditions used in the present simulation, where U_∞ denotes incoming flow speed. (b) Comparison of instantaneous drag coefficient of the isolated 1st finlet between coarse, medium, fine, and dense mesh. In (a), five finlets are shown at 24 different times throughout the tail beat cycle.. 79

Figure 4-5: Instantaneous drag coefficient (a), lateral force coefficient (b), and effective angle of attack (c) of finlets during one tail beat cycle of tuna forward swimming. (d) Three-dimensional wake structure of finlets at (i) $t/T=0.15$, (ii) $t/T=0.33$, (iii) $t/T=0.48$, (iv) $t/T=0.65$, (v) $t/T=0.81$, and (vi) $t/T=0.92$, respectively, from a perspective view. The isosurface of the wake structures is visualized by $Q=150$. The Q -isosurface is filled by the contour of vorticity ω_x which is normalized by U_∞/c . The tip vortex (TV), root vortex (RV), shear layer (SL), and leading edge vortex (LEV) are identified for each finlet. 83

Figure 4-6: Contour of ω_x on four vertical slices cutting the 2nd, 3rd, 4th, and 5th finlet, respectively, at (a) $t/T=0.33$, (b) $t/T=0.48$, (c) $t/T=0.81$, and (d) $t/T=0.92$, from a perspective view. ω_x is

normalized by U_∞/c . The centerlines of RV and TVs are illustrated with dotted red and blue lines, respectively, connecting vortex cores (white dots) on each slice. The tip vortex (TV) and root vortex (RV) are identified. 85

Figure 4-7: Contour of ω_y on a horizontal slice cutting through a horizontal slice 0.3s above the root of the 1st finlet at (a) $t/T=0.33$, (b) $t/T=0.48$, (c) $t/T=0.81$, and (d) $t/T=0.92$, respectively, from top view. ω_y is normalized by U_∞/c . The negative shear layer (nSL), positive shear layer (pSL), and leading edge vortex (LEV) are identified for each finlet. 87

Figure 4-8: (a) Comparison of instantaneous drag coefficient (C_D) between the isolated 2nd finlet and the 2nd finlet when located within the assembly of five. (b) Comparison of cycle-averaged drag coefficient (\bar{C}_D) between the isolated finlets and their within-assembly counterparts. 88

Figure 4-9: Comparisons of the vorticity ω_y (a,b) and pressure coefficient C_p (c,d) contours between the isolated 2nd finlet (a,c) and its in-assembly counterpart (b,d), respectively, at $t/T=0.48$ on a horizontal slice cutting through a chord of the 1st finlet. The negative shear layer (nSL), positive shear layer (pSL), and leading edge vortex (LEV) are identified. In (c), white arrows denote pressure force. 90

Figure 4-10: Comparisons of the instantaneous lateral force coefficient (a), power coefficient (b), effective angle of attack (c), wake structure (d,e), and x-vorticity contour (f,g), respectively, between finlets with and without pitching kinematics. The wake structures and x-vorticity contours are shown at $t/T=0.81$. The tip vortex (TV) and root vortex (RV) are identified for each finlet. 92

Figure 4-11: Comparisons of the cycle-averaged lateral force (a) and power coefficients (b), respectively, between the finlets with and without pitching kinematics. 93

Figure 4-12: Comparisons of instantaneous lateral force coefficients (a) and power coefficients (b), respectively, between the 5th finlet with and without pitching. In (a), the regions between constructive force and $C_z=0$ are marked with red plus sign (“+”) and those between the destructive force and $C_z=0$ are marked with blue minus sign (“-”). 95

Figure 4-13: Comparisons of the normalized pressure coefficient (C_p) contour of the finlets with (a) and without (b) pitching motions, respectively, at $t/T=0.81$ on a horizontal slice cutting

through a chord of the 1st finlet. α_{eff} denotes the effective angle of attack and U_{eff} denotes the effective velocity at finlet root. 96

Figure 4-14: Comparisons of the normalized lateral velocity (u_z/U_∞) isosurface (a,b) and contour (c,d) of the finlets with (a,c) and without (b,d) pitching kinematics, respectively, at $t/T=0.81$ on a horizontal slice cutting through a chord of the 1st finlet. 97

Figure 4-15: Comparison of vortex structure of flow past pitching finlets w/ (b,d) and w/o (a,c) body at mid-right-to-left (a,b) and mid-left-to-right (c,d) stroke, respectively. The blue vortex structure is identified by Q-isosurface with the same value of Q-criterion. 102

Figure 4-16: Instantaneous drag force coefficient ($C_{D,total}$) of the isolated 1st finlet and its pressure ($C_{D,pressure}$) and viscous ($C_{D,viscous}$) components at $Re=999.6$ 103

Figure 4-17: Cycle-averaged drag force coefficient ($\bar{C}_{D,total}$) of the isolated 1st finlet and its pressure ($\bar{C}_{D,pressure}$) and viscous ($\bar{C}_{D,viscous}$) components at various Re numbers. 104

Figure 4-18: Comparisons of the normalized lateral velocity (u_z/U_∞) contour between $Re=500$ (a), $Re=999.7$ (b), and $Re=2000$ (c) at $t/T=0.81$ on a horizontal slice cutting through a chord of the 1st finlet. 105

Figure 5-1: (a) Live yellowfin tuna (*Thunnus albacares*) swimming (with nine finlets indicated by letters A to I). (b) Illustration of body parts of a yellowfin tuna with dorsal and ventral finlets. (c) A single tuna finlet to show the attached base and free posterior region. (d) Posterior view of yellowfin tuna swimming showing pitching finlets. (e) Dorsal view of the caudal peduncle of a swimming tuna showing both the dorsal finlets and the lateral keel. 108

Figure 5-2: (a) A lateral view of the reconstructed computational model of a yellowfin tuna (*Thunnus albacares*) with trunk (in blue), dorsal and anal fins (in green), dorsal and anal finlets (in yellow), and caudal fin (in red). (b) A side-by-side comparison between the live tuna and the computational model from the top view at $t/T=0.2$. (c) Snapshots on the posterior body and dorsal finlets of a yellowfin tuna swimming steadily during a representative tail beat cycle. (d) Midlines of the reconstructed computational model during the left-to-right stroke (in blue) and right-to-left stroke (in red) of a tail beat cycle. (e) Reconstructed finlet kinematics and swimming kinematics

of the posterior trunk and caudal fin during the left-to-right stroke. (f) Reconstructed finlet kinematics and swimming kinematics of the posterior trunk and caudal fin during the right-to-left stroke. (g) A top view of dorsal finlet kinematics during a tail beat cycle. In (e), (f), and (g), a color change corresponds to a time change of $T/16$. (h) Instantaneous finlet angle (θ) of the dorsal finlets during a tail beat cycle. (i) Finlet angel ranges of the dorsal finlets during a tail beat cycle. 110

Figure 5-3: (a) Schematic of the computational mesh and boundary conditions used in the present simulation, where U_∞ denotes swimming speed. (b) Comparison of instantaneous thrust coefficient of the caudal fin between coarse, medium, and dense meshes. 113

Figure 5-4: (a) Instantaneous thrust coefficient and (b) power coefficient of the trunk, fins, and finlets during one tail beat cycle of tuna forward swimming. (c) Three-dimensional vortex wake structure of tuna swimming at (ii) $t/T=0.19$ from perspective view and top view, respectively. (d) x-vorticity contours at three transverse planes cutting through the posterior trunk and caudal fin. (e) Vortex structure of the posterior trunk, finlets, and caudal fin at (i) $t/T=0.02$, (ii) $t/T=0.19$, (iii) $t/T=0.35$, (iv) $t/T=0.56$, and (v) $t/T=0.69$, respectively, from both a perspective view and a top view. (f) Instantaneous surface pressure over the trunk, fins, and finlets at (ii) $t/T=0.19$. (g) Instantaneous thrust production over the trunk, fins, and finlets at (ii) $t/T=0.19$. The isosurface of the wake structures is visualized by $|\lambda_i|=5$. The λ_i -isosurface is filled by the contour of vorticity ω_x which is normalized by U_∞/L . The finlet induced vortex (FIV) and leading edge vortex (LEV) are identified. 117

Figure 5-5: (a) Comparison of instantaneous thrust coefficient (C_T) of trunk and caudal fin between the M1 and M2. (b) Instantaneous caudal fin thrust enhancement (ΔC_T) and trunk drag reduction (ΔC_D) of M1 with pitching finlets. 122

Figure 5-6: Comparison of (a) three-dimensional wake structure and (b) surface pressure C_p between M1 and M2 at $t/T=0.625$. (c) The surface pressure difference ΔC_p between M1 and M2. (d) Thrust enhancement ΔC_T regions in M1 owing to pitching finlets. (e) Comparison of vorticity contour and field pressure on slice A cutting through the posterior trunk between M1 and M2 (f) Comparison of vorticity contour, lateral velocity, and field pressure on slice B cutting through the caudal fin. PV denotes peduncle vortex, SL denotes shear layer. 124

Figure 5-7: (a) Comparison of three-dimensional wake structure between M1 and M2 at $t/T=0.313$. (b) The surface pressure difference ΔC_p between M1 and M2 at $t/T=0.313$. (c) Thrust enhancement ΔC_T regions in M1 owing to pitching finlets. (d) Comparison of vorticity contour and field pressure on slice C cutting through the caudal fin between M1 and M2. 127

Figure 5-8: (a) Comparison of instantaneous thrust coefficient (C_T) of trunk and caudal fin between the M1, M2, and M3. (b) Comparison of instantaneous caudal fin thrust enhancement (ΔC_T) between M1 and M3. (c) Comparison of lateral force of finlet 5, 6, and 7 between M1 and M3. Comparison of three-dimensional wake structure from (d) a lateral view and (e) a perspective view, (f) pitching kinematics of finlets, (g) and surface pressure C_p over trunk, finlets, and caudal fin between M1 and M3 at $t/T=0.604$. (h) The surface pressure difference ΔC_p between M1 and M3. (i) Thrust enhancement ΔC_T region on caudal fin in M3 owing to fixed finlets. (j) Comparison of vorticity contour and field pressure on slice E cutting through the posterior trunk and slice F cutting through the caudal fin between M1 and M3, respectively. 129

Figure 5-9: Comparison of cycle-averaged (a) drag coefficient (\bar{C}_D) and (b) power coefficient (\bar{C}_{PW}) of finlets between M1 and M3. 132

Figure 5-10: Schematics on mechanisms of (a) lateral flow deflection by finlets at the posterior trunk and (b) finlet-induced vortex (FIV) capture by caudal fin. 133

Figure 6-1: Morphological and kinematical modeling of juvenile rainbow trout (*Oncorhynchus mykiss*) during steady swimming. (a–b) High-speed camera images of live rainbow trout swimming overlapped with the reconstructed computational model from lateral and ventral views, respectively, at $t/T=1/6$. (c) Side-by-side comparison of live trout and computational mode from posterior view at $t/T=1/6$. (d) The reconstructed computational model of juvenile rainbow trout with fine surface mesh on body and fins. (e) Kinematics of rainbow trout swimming during a tail-beat cycle from a ventral view. (f) Reconstructed swimming kinematics of computational model during left-to-right (L-to-R) and right-to-left (R-to-L) strokes, respectively. (g) A single tuna finlet to show the attached base and free posterior region. (f) Midlines of the computational model during L-to-R (dashed) and R-to-L (solid) strokes, respectively. 138

Figure 6-2: (a) Schematic of the computational mesh and boundary conditions used in the present simulation, where U_∞ denotes incoming flow speed. (b) Comparison of instantaneous thrust coefficient C_T of the caudal fin between coarse, medium, fine, and dense mesh. 140

Figure 6-3: (a) Instantaneous thrust coefficient and (b) power coefficient of trunk and fins during one tail beat cycle of trout forward swimming. (c) Three-dimensional vortex wake structure of trout swimming at (iv) $t/T=0.71$ from perspective view and top view, respectively. (d) x-vorticity contours at four transverse planes cutting through the posterior trunk and caudal fin. (e) Vortex structure of the posterior trunk and fins at (i) $t/T=0.27$, (ii) $t/T=0.42$, (iii) $t/T=0.60$, and (iv) $t/T=0.71$, respectively, from perspective view, associated with trunk surface pressure contour from the top view. (f) Instantaneous surface pressure over the trunk and fins at (iv) $t/T=0.71$. (g) Instantaneous thrust production over the trunk and fins at (iv) $t/T=0.71$. The isosurface of the wake structures is visualized by $|\lambda_i|=3.7$. The λ_i -isosurface is filled by the contour of vorticity ω_x which is normalized by U_∞/L . The dorsal fin vortex (DFV), anal fin vortex (AFV), pelvic fin vortex (PFV), peduncle vortex (PV), and leading edge vortex (LEV) are identified. 145

Figure 6-4: (a) Comparisons of instantaneous thrust coefficient (C_T) of trunk and caudal fin between M1 and M2, respectively. (b) Instantaneous caudal fin thrust enhancement (ΔC_T) and trunk drag reduction (ΔC_D) of M1 owing to dorsal fin compared to M2. 148

Figure 6-5: Comparison of (a) three-dimensional wake structure, (b) vorticity contour and field pressure on slice A cutting through the caudal fin, and (c) surface pressure C_p between M1 and M2 at $t/T=0.71$. (d) The surface pressure difference ΔC_p on trunk and caudal fin between M1 and M2 at $t/T=0.71$. (e) Thrust enhancement ΔC_T region on caudal fin in M1 owing to the dorsal fin compared to M3. (f) Comparison of the isosurface of lateral flow (left) and lateral velocity contour on a coronal plane cutting through the dorsal fin and caudal fin (right). (g) The evolution of lateral velocity isosurface in M1 at (i) $t/T=0.27$, (ii) $t/T=0.42$, (iii) $t/T=0.60$, and (iv) $t/T=0.71$ 149

Figure 6-6: (a) Comparisons of instantaneous thrust coefficient (C_T) of trunk and caudal fin between M1 and M3, respectively. (b) Instantaneous caudal fin thrust enhancement (ΔC_T) and trunk drag reduction (ΔC_D) of M1 owing to anal fin compared to M3. 152

Figure 6-7: Comparison of (a) three-dimensional wake structure, (b) vorticity contour and field pressure on slice B cutting through the trunk and anal fin and slice C cutting through the caudal fin, and (c) surface pressure C_p between M1 and M3 at $t/T=0.42$. (d) The trunk surface pressure difference ΔC_p between M1 and M3 at $t/T=0.42$. (e) Thrust enhancement ΔC_T region on trunk in M1 owing to the anal fin compared to M3. 153

Figure 6-8: Comparison of (a) three-dimensional wake structure, (b) vorticity contour and field pressure on slice D cutting through the caudal fin, and (c) surface pressure C_p between M1 and M3 at $t/T=0.60$. (d) The surface pressure difference ΔC_p on trunk and caudal fin between M1 and M3 at $t/T=0.60$. (e) Thrust enhancement ΔC_T region on caudal fin in M1 owing to the anal fin compared to M3. 156

Figure 6-9: (a) Comparisons of instantaneous thrust coefficient (C_T) of dorsal fin and anal fin between M1 and M4, respectively. (b) Comparisons of instantaneous thrust coefficient (C_T) of trunk and caudal fin between M1 and M4, respectively. 158

Figure 6-10: Comparison of (a-b) three-dimensional wake structure and (c) surface pressure C_p between M1 and M4 at $t/T=0.42$. (d) The surface pressure difference ΔC_p on anal fin between M1 and M4 at $t/T=0.42$. (e) Thrust enhancement ΔC_T region on anal fin in M1 owing to the pelvic fin compared to M4. Comparison of (f) y-vorticity contour and (g) field pressure on a coronal plane (slice E) cutting through the pelvic fin, anal fin, and caudal fin. 160

Figure 6-11: Schematics on mechanisms of (a) dorsal fin vortex (DFV) and lateral flow capture by caudal fin, (b) peduncle vortex (PV) prevention by anal fin, and (c) lateral flow prevention by anal fin. 161

Figure 7-1: Morphological and kinematical modeling of the medicinal leech (*Hirudo medicinalis*) during steady swimming. (a-b) High-speed camera images of live medicinal leech swimming overlapped with the reconstructed computational model from lateral and ventral views, respectively, at $t/T=0.55$. (c) The reconstructed computational model of medicinal leech with fine surface mesh. (d) Kinematics of medicinal leech swimming during a tail-beat cycle from a lateral view. (e) Midlines of the reconstructed computational model with swimming kinematics during a tail beat cycle. Solid lines and dashed lines correspond to $0\sim 0.5T$ and $0.5T\sim 1.0T$, respectively. A

color change corresponds to a change in time of $T/12$. (f) Local velocity vectors along the body at $t/T=0.55$. (g) Spatial-temporal distribution of body midline curvature. (h) Spatial-temporal distribution of dorsal-ventral velocity (y-velocity) along body midline. (i) Spatial-temporal distribution of axial velocity (x-velocity) along body midline. 166

Figure 7-2: (a) Schematic of the computational mesh and boundary conditions used in the present simulation, where U_∞ denotes incoming flow speed. (b) Comparison of instantaneous thrust coefficient C_T of the leech model between coarse, medium, fine, and dense mesh. 168

Figure 7-3: (a) Instantaneous axial force coefficients, (b) lateral force coefficients, and (c) power coefficient of leech model during one tail beat cycle of forward swimming. (d) Three-dimensional vortex wake structure of leech swimming at $t/T=0.08$ (i), $t/T=0.23$ (ii), $t/T=0.42$ (iii), $t/T=0.60$ (iv), $t/T=0.77$ (v), and $t/T=0.92$ (vi) from perspective view. (e) Pressure isosurface surrounding the body at six corresponding time instances. (f) Surface pressure contour from dorsal, lateral, and ventral views associated with the distribution of thrust force on the surface from dorsal and ventral views. (g) Local velocity vectors and local hydrodynamic pressure force vectors along the body at $t/T=0.42$. (h) Instantaneous thrust distributions along the body at $t/T=0.417$. (i) Spatial-temporal thrust distributions along the body from the head to the tail tip during a tail beat cycle. (j) Cycle-averaged thrust distribution on dorsal and ventral body surfaces, respectively. (k) Cycle-averaged thrust distribution along the body. (l) Cumulative cycle-averaged thrust productions along the body. 174

Figure 7-4: Comparisons of (a) instantaneous axial force coefficients, (b) three-dimensional vortex wake structure, (c) pressure isosurface surrounding the body, (d) surface pressure contour from dorsal and ventral views, (e) local velocity and hydrodynamic pressure force vectors along the body, (f) Instantaneous thrust distributions along the body, (g) spatial-temporal thrust distribution along the body during a tail beat cycle, (j) cycle-averaged thrust distribution on dorsal and ventral surfaces, (h) cycle-averaged thrust distribution along the body, and (i) cumulative cycle-averaged thrust productions along the body at $t/T=0.417$ between M2 (left), M1 (middle), and M3 (right). 179

Figure 7-5: Comparison of vortex structure between (a) $AR=1.24$, (b) $AR=2.48$, and (c) $AR=4.96$ at $t/T=0.92$. Comparisons of dorsal surface thrust distribution and the vorticity and field pressure

contours at three transverse planes cutting through the high thrust-producing region between (d) $AR=1.24$, (e) $AR=2.48$, and (f) $AR=4.96$ at $t/T=0.92$ 182

Figure 7-6: Comparisons of (a) instantaneous axial force coefficients, (b) three-dimensional vortex wake structure, (c) pressure isosurface surrounding the body, (d) surface pressure contour from dorsal and ventral views, (e) local velocity and hydrodynamic pressure force vectors along the body, (f) Instantaneous thrust distributions along the body, (g) spatial-temporal thrust distribution along the body during a tail beat cycle, (j) cycle-averaged thrust distribution on dorsal and ventral surfaces, (h) cycle-averaged thrust distribution along the body, and (i) cumulative cycle-averaged thrust productions along the body at $t/T=0.417$ between $Re=15600$ (left), $Re=1560$ (middle), and $Re=156$ (right)..... 184

Figure 7-7: Comparisons of (a) instantaneous axial force coefficients, (b) three-dimensional vortex wake structure, (c) pressure isosurface surrounding the body, (d) surface pressure contour from dorsal and ventral views, (e) local velocity and hydrodynamic pressure force vectors along the body, (f) Instantaneous thrust distributions along the body, (g) spatial-temporal thrust distribution along the body during a tail beat cycle, (j) cycle-averaged thrust distribution on dorsal and ventral surfaces, (h) cycle-averaged thrust distribution along the body, and (i) cumulative cycle-averaged thrust productions along the body at $t/T=0.417$ between $St=0.355$ (left), $St=0.532$ (middle), and $St=0.798$ (right)..... 188

Figure 7-8: Schematics on mechanisms of edge vortex (EV) capture and early vertical flow separation. 190

List of Tables

Table 2-1: Parameters involved used for numerical computations.....	30
Table 3-1: Comparisons of key parameters between the present hummingbird model and the experimental data [49] at flight speed $U_f = 4 \text{ m s}^{-1}$	39
Table 3-2: Summary of the governing parameters used for numerical computations and their ranges	42
Table 3-3: Summary of key geometric and kinematical parameters of hummingbird hovering studies.	44
Table 3-4: Cycle-averaged lift and thrust coefficients and lift enhancements due to WBI.....	48
Table 3-5: Net lift enhancement ($\bar{C}_L _{WB} - \bar{C}_L _{WO/BO}$) change at various tail span ratios.....	67
Table 3-6: Summary of lift enhancement due to WBI on insects and birds.	68
Table 4-1: Summary of key parameters of tuna steady swimming and finlet kinematics.....	74
Table 4-2: Normalized geometric quantities of reconstructed finlet model.	77
Table 4-3: Cycle-averaged drag (\bar{C}_D) and lateral force (\bar{C}_Z) coefficients of finlet.	82
Table 4-4: Drag reduction due to finlet-finlet interaction.....	89
Table 4-5: Power reduction due to pitching kinematics of the finlets	94
Table 4-6: Coefficients of Fourier series representing the lateral displacement of finlet root ...	100
Table 4-7: Coefficients of Fourier series representing the surge displacement of finlet root.....	101
Table 4-8: Coefficients of Fourier series representing finlet angle θ	101
Table 4-9: Summary of finlet arrangement and kinematics used for computations.	105

Table 5-1: Normalized geometric quantities of trunk and fins	112
Table 5-2: Normalized geometric quantities of finlets (dorsal only).....	112
Table 5-3: Cycle-averaged thrust coefficient \bar{C}_T of different parts of the tuna models and the overall axial thrust force \bar{C}_X . Note that negative values denotes drag producing	120
Table 5-4: Cycle-averaged power coefficient \bar{C}_{PW} of different parts of the tuna models and the overall power consumption \bar{C}_{PW}	120
Table 5-5: Caudal fin thrust enhancement and trunk drag reduction by pitching finlets	122
Table 5-6: Cycle-averaged overall axial thrust force (\bar{C}_X) and overall power (\bar{C}_{PW}) coefficients, and nominal propulsive efficiency η_{nominal} of pitching finlets in M1.....	123
Table 5-7: Caudal fin thrust enhancement and trunk drag reduction by fixed finlets.	128
Table 5-8: Cycle-averaged overall thrust (\bar{C}_T) and power (\bar{C}_{PW}) coefficients of finlets and their changes.....	132
Table 5-9: Cycle-averaged overall axial force (\bar{C}_X) and power (\bar{C}_{PW}) coefficients, and nominal propulsive efficiency η_{nominal} of fixed finlets in M3.	133
Table 6-1: Normalized geometric quantities of the computational model of juvenile rainbow trout	139
Table 6-2: Cycle-averaged thrust (\bar{C}_T) coefficients of the trunk and fins in trout computational models.....	144
Table 6-3: Cycle-averaged power (\bar{C}_{PW}) coefficients of the trunk and fins in trout computational models.....	144
Table 6-4: Caudal fin thrust enhancement $\Delta\bar{C}_T$ and trunk drag reduction $\Delta\bar{C}_D$ owing to dorsal fin	148

Table 6-5: Caudal fin thrust enhancement $\Delta\bar{C}_T$ and trunk drag reduction $\Delta\bar{C}_D$ owing to anal fin	152
Table 6-6: Trunk and fin force changes owing to pelvic fin.....	158
Table 7-1: Normalized geometric quantities of the computational model	167
Table 7-2: Key morphological and flow parameters used and their ranges.	170
Table 7-3: Cycle-averaged thrust production (from each segment and overall), power consumption, and propulsive efficiency at $AR=1.24, 2.48, \text{ and } 4.96$	180
Table 7-4: Cycle-averaged thrust production (from each segment and overall), power consumption, and propulsive efficiency at $Re=15600, 1560, \text{ and } 156$	185
Table 7-5: Cycle-averaged thrust production (from each segment and overall), power consumption, and propulsive efficiency at $St=0.355, 0.532, \text{ and } 0.798$	187
Table 8-1: Performance enhancement mechanisms on the deflection or prevention of transverse flow across body edges	198
Table 8-2: Performance enhancement mechanisms on the wake capture or prevention	199

1 Introduction

1.1 Motivation and Goals

After millions of years of evolution, aerial and aquatic animals in nature have developed specialized morphological features and superior locomotion strategies to interact with the surrounding fluids and achieved fast, agile, and efficient flying/swimming [1, 2]. For example, the propulsive efficiency of a cetacean fluke can reach over 90% which is approximately 20% more than that of a standard marine propeller [1].

The favorable aerodynamic/hydrodynamic performance in nature is of particular interest to the design of unmanned vehicles. Over the past decades, new designs of aerial/underwater unmanned vehicles have been developed through the approaches of biomimetics and bioinspiration by either directly copying the morphology and kinematics from nature or using key relevant features to inspire the design, trying to match or even outperform biology (Figure 1-1). In either way, they have adopted the underlying mechanisms that give animals their outstanding performances, which is the key to any successful unmanned vehicle design. Therefore, learning the fluid dynamics of biological systems and finding the fundamental flow physics responsible for their great performances is critical for future designs and is the motivation of this work.

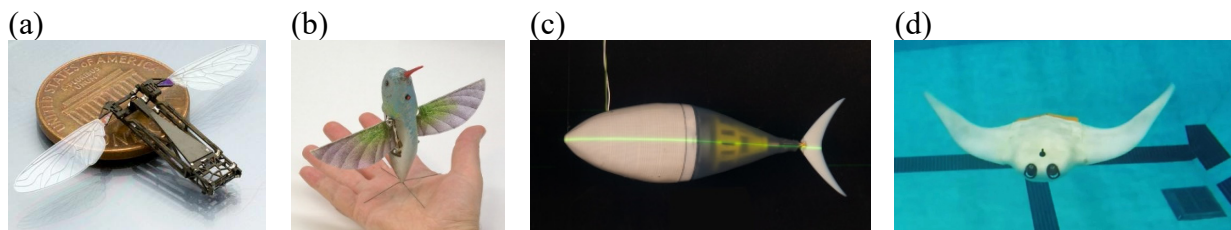


Figure 1-1: Various unmanned vehicle designs using biomimetics or bioinspiration. (a) RoboBee, Harvard University [3], (b) Nano Hummingbird, AeroVironment, Inc. [4], (c) Tunabot, University of Virginia [5], (d) Mantabot, University of Virginia [6].

The interactions between a biological system, such as a bird or a fish, and the surrounding fluid environment during locomotion contain rich flow physics. The nature of the fluid flow is highly unsteady owing to the oscillatory motion of the wings or fins and, for some fish species, the undulatory motion of the body. Since the body and the propulsors are working as an integrated system during flying or swimming, the fluid dynamic interactions between the body and the fins/wings are almost inevitable and sometimes can be pronounced and beneficial for propulsion (Figure 1-2). Besides, the wings of most birds and insects and the fins and the body of most fishes are usually flexible and sometimes deformable, and the morphological features of fishes are usually complex with multiple fins. These diverse properties add even more complexity to the body-involved fluid dynamic interactions (BI-FDI).

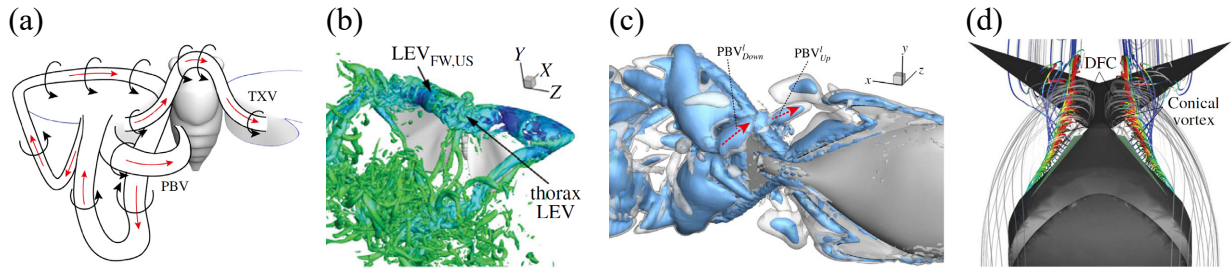


Figure 1-2: Body-involved fluid dynamic interaction (BI-FDI) of various forms in biological propulsion. (a) Wake schematic for wing-body interaction in cicada forward flight [7], (b) Leading edge vortex (LEV) on both the thorax and wings of a butterfly during flight [8], (c) Interaction of posterior body vortex with caudal fin in jackfish swimming [9], (d) Interaction of dorsal fin-induced body vortex with caudal fin in tuna-like swimming [10].

While BI-FDI is studied in a case-by-case manner in existing literature, this work aims to systematically explore BI-FDI in nature and the underlying flow physics. BI-FDI in major forms

of body-propulsor configurations and locomotion modes will be examined using an integrated experimental and numerical approach with high-fidelity morphology and kinematics reconstruction and high-accuracy direct numerical simulation. The propulsive performance and the interplay of vortical structures between the body and the propulsor will be analyzed in detail to reveal the fundamental mechanisms that cause potential performance enhancement. The general goals are to advance the understanding of body-involved performance enhancement mechanisms in biological propulsion and to provide novel physical insights into the design of aerial/underwater unmanned vehicles from a fluid dynamics perspective.

1.2 Body-Involved Fluid Dynamic Interactions (BI-FDI)

The most distinctive feature of biological propulsion is that animals use their unsteadily flapping wings, oscillating fins, or undulating body to produce lift or thrust forces in contrast to the fixed wings and constantly rotating propellers used in traditional aviation or marine propulsion. Such unsteady motions result in highly unsteady fluid fields where vortex dynamics are intense and are closely related to the propulsive performance. Major performance enhancement mechanisms associated with unsteady motions, such as added mass effect [11], and leading edge vortices [12-14], are widely found in flying [11-14] and swimming [15, 16] in nature.

Compared to these well-documented performance enhancement mechanisms that mainly involve the animal's propulsor, BI-FDI in flying and swimming was only found in recent years, and a limited number of bio-propulsion platforms in nature were studied. However, the diverse forms of body-propulsor configurations and locomotion modes in biological propulsion and the significant performance enhancements found in the existing literature [7, 9, 10, 17] suggest that

BI-FDI could be a robust and effective performance enhancement mechanism that widely exists in biological propulsion in nature, and could be a transferrable mechanism that benefits unmanned vehicle designs.

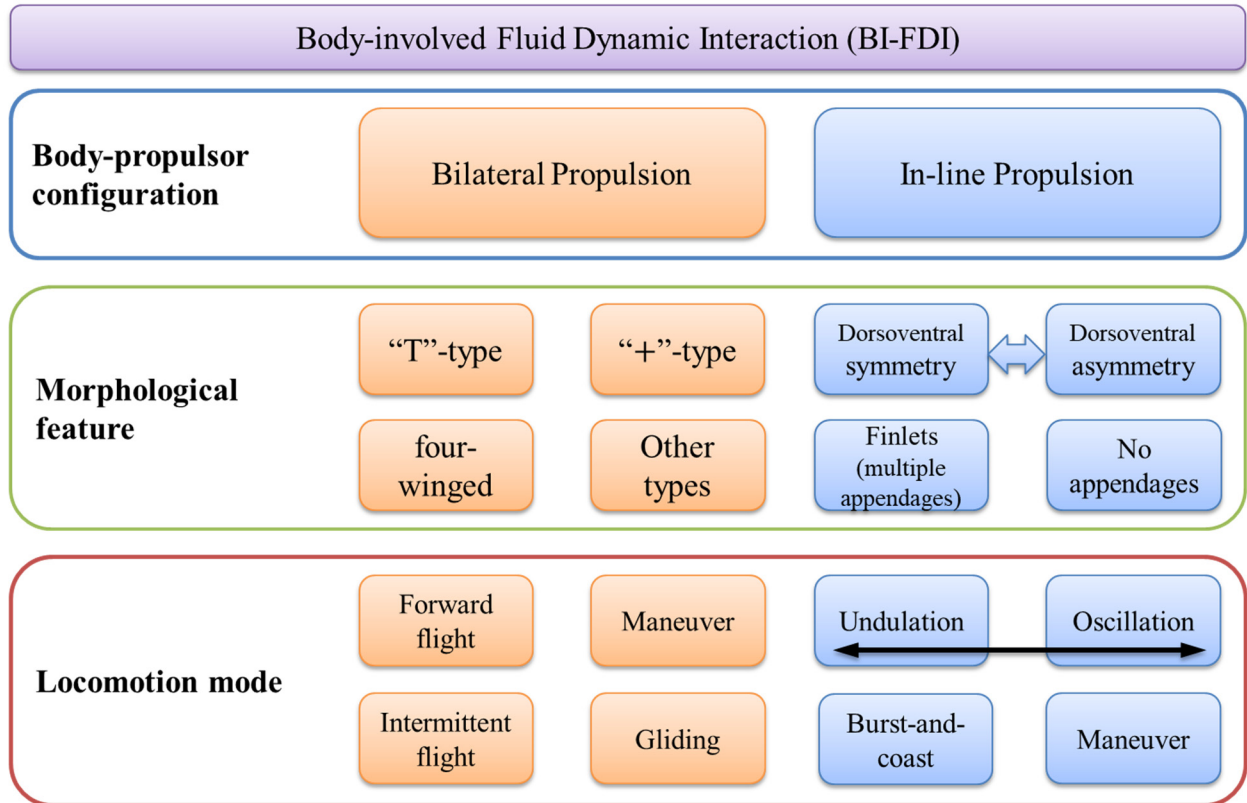


Figure 1-3: Categories of body-involved fluid dynamic interaction in nature. Major categories of body-propulsor configuration, morphological configuration, and locomotion mode are listed.

1.3 BI-FDI in Bilateral Propulsion

So far, there are two major body-propulsor configurations where significant BI-FDI is found (Figure 1-3): bilateral propulsion which is mainly adopted by flying animals, and in-line propulsion which is mainly found in swimming animals. In the bilateral propulsion configuration,

two propulsors are attached to the body with bilateral symmetry, while in the in-line configuration, a single propulsor is positioned posterior-most of the body.

Known examples of BI-FDI with bilateral configuration are cicada [7] and butterfly [8]. Specifically, significant lift enhancement was found in the cicada forward flight [7] due to vortex dynamics induced by the wing-body interaction (WBI), in which an 18.7% overall lift enhancement (OLE) was reported at a flight speed of 1.96 m s^{-1} and body angle of 28° . The cicada's body alone contributed 65% of the overall enhancement. Two unique vortex pairs were found at the thorax and the posterior part of the body, respectively. These body vortices helped generate low-pressure zones on the dorsal surface of the body and strengthened the wing LEVs, resulting in a significant lift increase on both the body and the wings. Wind tunnel test [18] and direct numerical simulation [8] of free-flying butterflies both showed an LEV-like vortex structure attached to the dorsal surface of the thorax, which connects the LEVs of the left and right wings to form a coherent LEV tube. A similar vortex structure was also found in tethered dragonflies [19] and hawk moths [20, 21] during forward flight. These observations suggested that WBI could be a common mechanism in the bilateral configuration of biological propulsion.

However, from a more specific morphological configuration standpoint of view (Figure 1-3), the bilateral propulsion with WBI found so far can be categorized as “T”-type, in which the leading edge of the wing is closed to the anterior-most of the head (Figure 1-4a). The reverse is true of “+”-type or “plus”-type flyers, where the leading edge of the wing is relatively away from the anterior-most of the head (Figure 1-4b). Insects, such as mosquitos and bees, and birds, such as hummingbirds and geese, fall within the “+”-type. It is still unknown how the body-propulsor configuration change within bilateral propulsion could affect WBI. One goal of this work is to

systematically study WBI and its lift enhancement effect in hummingbird forward flight to answer this question.

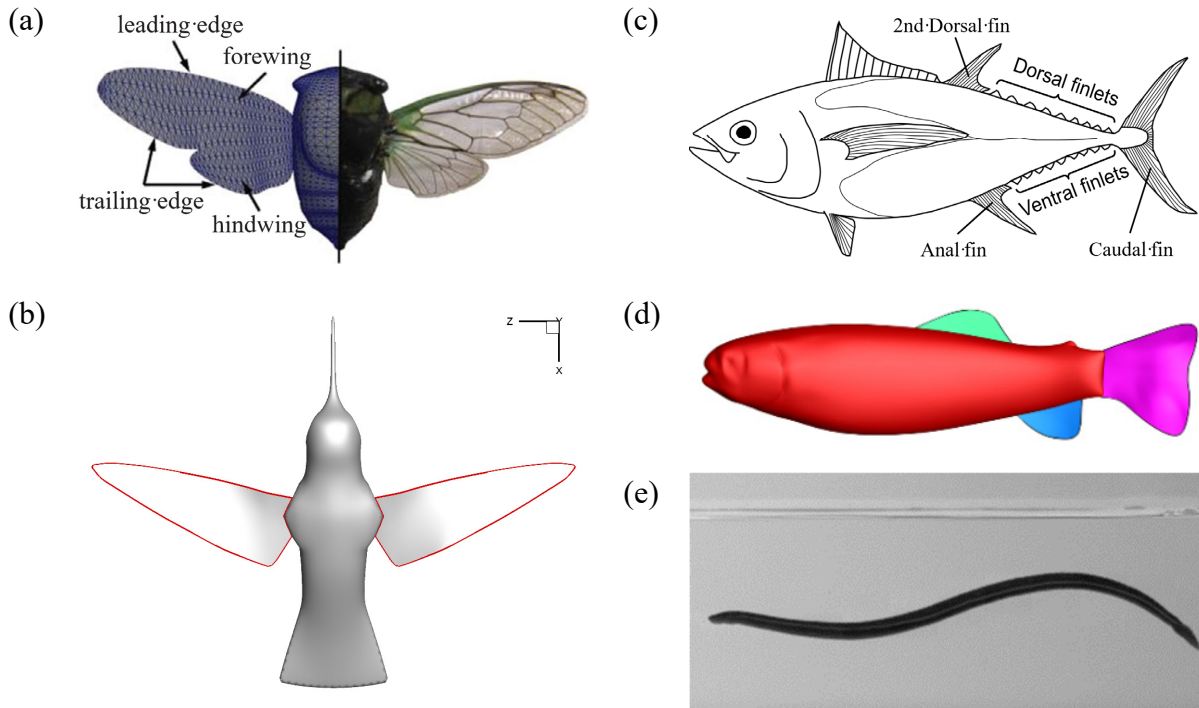


Figure 1-4: Various morphological configurations in nature. (a) “T”-type wing-body configuration in cicada (figure adapted from Wan et al. [22]), (b) “+”-type wing-body configuration in hummingbird, (c) Dorsal and ventral finlets in tuna (figure adapted from Wang et al. [23]), (d) Dorsoventrally asymmetric median fin configuration in trout, (e) lateral view of leech swimming.

1.4 BI-FDI in In-Line Propulsion

The in-line body-propulsor configuration mainly contains fishes that produce thrust with their undulating body and oscillating caudal fin, which are shown as the body and caudal fin

propulsions (Figure 1-5a). As fish species differ from one to another, the morphological configuration and locomotion mode also varies (Figure 1-5).

For fishes using in-line propulsion, their undulating body and oscillating fins can manipulate flows to leave a thrust producing reverse von Kármán vortex street in the wake. Despite the considerably higher Reynolds number in swimming as compared to flying, the oscillating caudal fin of fish also takes advantage of the lift enhancement mechanisms found in unsteady aerodynamics, such as added mass effect [15] and LEV [16]. Since the caudal fin is located posterior-most of a fish, the incoming flow will first interact with the body and other median fins before reaching the caudal fin. The vortex wake shed from the body and median fins could affect the hydrodynamic performance of the propulsor (Figure 1-2c&d). By using particle imaging velocimetry (PIV) measurements, significant body-fin and fin-fin interactions have been observed in the flow field of different species of fishes using in-line propulsion [24-26], and these results suggest constructive interactions for potential thrust enhancement at the caudal fin. Recently, the swimming speed enhancement due to the hydrodynamic interaction between dorsal/anal fins and the caudal fin was experimentally confirmed on a tuna-inspired fish model [10]. It was found that the LEV of the caudal fin is stabilized by the cross-flow induced by the dorsal fin, resulting in enhanced thrust production. Direct numerical simulation results of the steady swimming of two carangiform swimmers, jackfish [9] and sunfish [17], both showed significant trunk drag reduction and caudal fin thrust enhancement owing to the generation of dorsal fin-induced body vortex and its interplay with the caudal fin.

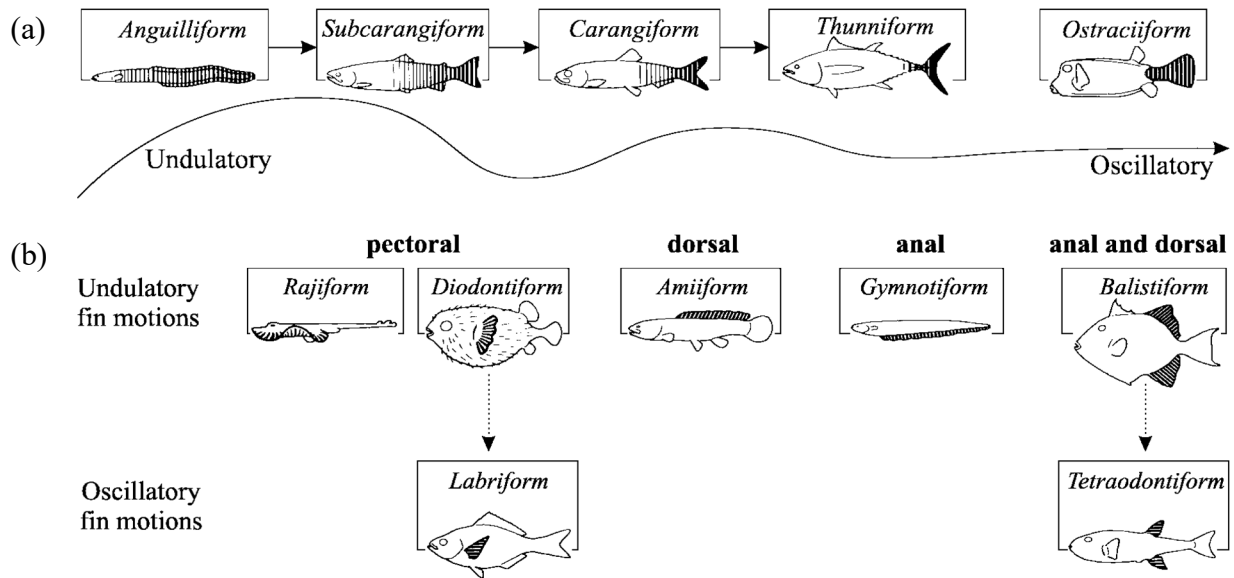


Figure 1-5: Swimming modes associated with (a) body and caudal fin propulsion and (b) median/paired fin propulsion. Shaded areas contribute to thrust generation (figure adapted from Sfakiotakis et al. [27]).

The existing literature suggests that the thrust enhancement mechanism owing to body-fin and fin-fin interactions could be robust in in-line propulsion. However, many open questions on BI-FDI of in-line propulsion remain unanswered because of the limited existing effort. From the morphological configuration point of view, because the independently mobile finlets found in Scombridae fishes (Figure 1-4d) are drastically different from the elongated dorsal/anal fins found in existing literature (Figure 1-2d&e), it is unknown what are the hydrodynamic functions of finlets, and how would the BI-FDI and potential performance enhancement mechanism be affected by the unique morphological feature of finlets and its kinematics. Questions on morphological configuration extend to the asymmetric dorsoventral configuration of median fins. The previously studied jackfish [9] and sunfish [17] both have a dorsoventrally symmetric dorsal fin and anal fin. It is unknown how the dorsoventrally asymmetric dorsal and anal fins in fishes like trout (Figure

1-4c) would affect the BI-FDI. In addition, it is unknown whether BI-FDI exists in swimming animals without appendages, like leeches. From the locomotion mode point of view, it is unknown how would BI-FDI and the potential performance enhancement mechanism be different between undulation and oscillation.

1.5 Wing-Body Interaction in Hummingbird Forward Flight

In unsteady aerodynamics, lift force generated by flapping wings is critical for flyers to overcome their body weight and stay afloat in the air [28]. Extensive experimental [29-31] and numerical [7, 32-35] studies have been performed to answer the question of how flapping wings augment and enhance lift during flight. Major mechanisms found include the added mass effect [11], delayed stall due to leading-edge vortices (LEV) [12-14], trailing-edge vortices effect [36], wake capturing [37], wing rotational circulation [37-39], and wing-wing interactions of various forms [40-44]. Besides the aforementioned lift augmentation mechanisms found on insect wings, the aerodynamic role of insect bodies has also been found to be considerable in the lift production of insect flyers such as cicada [7] and fruit fly [45] during forward flight by recent studies.

It is noteworthy that body vortices were also observed in the forward flight of various insects [18-21]. Wind tunnel test on free-flying butterflies [18] showed an LEV-like vortex structure attached to the dorsal surface of the thorax, which connects the LEVs of the left and right wings to form a coherent LEV tube. A similar vortex structure was also found in tethered dragonflies [19] and hawk moths [20, 21] during forward flight. These observations suggested that WBI could be a common mechanism adopted by flapping flyers in forward flight. However, there is a lack of research effort on experimentally visualizing body vortices in hummingbird flight which shares

similar flapping flight features with that of insects [46]. A recent numerical study on the fast forward flight of a hummingbird [47] showed the existence of vortex structures around the body at several time instants of a flapping cycle. However, no analysis of WBI or quantitative calculation of lift enhancement was reported.

One factor that may affect the intensity of WBI is the geometric configuration of the wing-body system, especially the shape difference near the wing root region where the WBI mainly happens. While high OLE was found in cicada [7], only 7.2% OLE due to WBI was found in a fruit fly model [45] during forward flight. It was further found the cicada wing had 35.3% of the wing area (A) within 30% range of the wing length (L) from the wing root ($A_{0.3L}/A = 35.3\%$) [7], whereas the $A_{0.3L}/A$ ratio for the fruit fly model [45] was only 21.2%. Thus, higher $A_{0.3L}/A$ ratio is likely to intensify the aerodynamic interactions between the body and the wings. Comparing to insect flyers, the $A_{0.3L}/A$ ratio of a typical hummingbird wing can reach up to 38% [48], which indicates a potentially higher lift enhancement due to WBI. In addition, the speed of a forward flying hummingbird (reported 12 m s^{-1} in the experimental study by Tobalske *et al.* [49]) usually surpasses the majority species of insects [50] but at a similar or lower flapping frequency [51]. This leads to a higher value of the advance ratio, J , defined as the ratio between the flight speed, U_f , and the mean wing tip speed, U_{tip} . An increasing advance ratio will result in more rapid growth of the LEV and enhance the vorticity production on the flapping wing [52], thus has the potential to further promote WBI.

1.6 Hydrodynamic Effect Finlets on Propulsive Performance in Thunniform Swimming

Finlets are commonly found on scombrid fishes (mackerels, bonitos, and tunas) which are known for their high swimming speed [53, 54] and long-distance swimming ability [55]. Finlets are a series of small, non-retractable fins located at the dorsal and ventral margins of the posterior body of scombrid fishes. Finlet placement is mirrored on the dorsal and ventral sides, and each finlet can move independently with its pitching kinematics [56, 57]. Although individual finlets are small, the summed area of the finlets of a mackerel can reach 15% of its caudal fin area [56-58]. In addition, finlets are located immediately upstream of the caudal fin (the main propulsor of the fish), which suggests that they may play an important role in the swimming dynamics of scombrid fishes.

A number of hypotheses regarding the hydrodynamic effects of finlets have been proposed, and these have mainly focused on possible flow control functions of finlets. One proposal suggested that finlets can redirect the transverse flow across the posterior body of fish to a longitudinal direction, thereby preventing the separation of the boundary layer and thus reducing drag [55, 59, 60]. Another hypothesis states that finlets can modulate crossflow over the posterior body like “flow fences” [61]. A similar hypothesis indicates that by interfering with vortices shed from the median dorsal and anal fins, finlets can control turbulence at the caudal peduncle [62] and provide a less turbulent flow environment for the caudal fin [63, 64]. However, experimental data that address these hypotheses have been challenging to acquire.

Nauen and Lauder [56] first quantified the morphology and kinematics of the chub mackerel (*Scomber japonicus*) finlets and proposed that they may help enhance the thrust generation at the caudal fin by directing flow longitudinally into the caudal fin vortex. Flow visualization data around the finlets and caudal peduncle of chub mackerel [58] were then obtained to confirm the

existence of redirected flow across the posterior body caused by the finlets. They also found the posterior-most finlet contributed to the local flow formation upstream of the caudal fin [58], which may provide favorable flow conditions for tail propulsion. However, detailed flow information such as 3-D wake structures for each finlet and potential hydrodynamic interactions among finlets was not possible to obtain due to technical limitations of the experiment. Moreover, previous research has not provided any hydrodynamic performance data such as drag/thrust, lateral forces, and power consumption for both individual finlets and the assembly of all finlets functioning together during locomotion. Hence it is still unknown if finlets are capable of producing thrust, or if they experience net drag.

Recently, Wainwright and Lauder [65] examined the effects of tuna finlets on swimming performance by water tunnel tests of a simplified tuna-like model with finlets that are capable of passive pitching or being completely fixed. Their performance results show that pitching finlets reduce the lateral forces, power consumption, and thrust production of the tuna-like model compared to models with fixed finlets or elongated fins of equal area, revealing a tradeoff between thrust and propulsive efficiency, but not supporting the hypothesis that finlets increase thrust.

A few previous numerical studies [66-68] on the hydrodynamics of simplified finlets have been conducted in fish-like propulsion, in which finlets were modeled as rigid strip-like elongated fins that were not independently mobile. Similar elongated dorsal/anal fins were studied in crevalle jack (*Caranx hippos*) swimming [9]. Among these results, finlets/fins were found to operate in local flow that is converging to the posterior body, mainly induced by the posteriorly narrowed body of the fishes [9, 67]. Enhanced mean thrust and propulsive efficiency attributed to the simplified finlets were found in a tuna-like model [66, 68]. Deflected flow across the caudal peduncle by the simplified finlets was also found [67], but the longitudinal flow was not affected

[67]. These findings using simplified finlets are in general agreement with the flow visualization data provided by Nauen and Lauder [58] and they partially support earlier hypotheses [55, 59, 60]. However, the simplified finlet models previously used were continuous fins rather than individually pitching finlets as in swimming scombrid fish. More complex and scombrid-like finlet models will be able to account for the potentially important hydrodynamic effects of finlet-finlet interactions and pitching kinematics.

1.7 Hydrodynamic Roles of Dorsoventrally Asymmetric Dorsal fin and Anal Fin in Carangiform Swimming

Many fishes of the Salmonidae family, such as trout and salmon, are high-performance carangiform swimmers known for their long-distance migrations and high-speed swimming against strong currents. Trout have been historically analyzed for fast and efficient swimming through experiments, and many have been focused on the kinematics and performance enabled by the undulation of the body and the main propulsor, the caudal fin. Recent studies have shown that the dorsal fin and anal fin play an important role in the hydrodynamics of trout swimming [25, 69, 70].

Drucker and Lauder [25] visualized the lateral flow jet produced by the dorsal fin of rainbow trout at various speeds and proposed that the tail can produce more thrust by intercepting the vortical wake shed from the dorsal fin and the shear layer shed from the adipose fin. Standen and Lauder [69] found that in brook trout steady swimming the anal fin produces lateral jet to the same side as the dorsal fin and that the flow field surrounding the caudal fin is greatly altered by the dorsal fin and the anal fin, indicating that the presence of dorsal and anal fins may substantially affect the hydrodynamic performance of the caudal fin.

However, detailed flow information—such as the 3-D vortical wake structure of the dorsal fin and anal fin and potential hydrodynamic interactions with the caudal fin—and hydrodynamic performance results—such as drag/thrust and power consumption—was not possible to obtain due to the technical limitations of the experiment. Hence, no direct evidence is available to support the caudal fin thrust enhancement hypothesis.

Previous numerical studies on the median fin interactions with dorsoventral symmetric dorsal and anal fins in jackfish [9] and sunfish [17] have shown significant thrust enhancement in the caudal fin. However, the anal fin and dorsal fin of trout are located at different longitudinal locations along the body. Moreover, the morphology of dorsal fin and anal fin in trout has a significantly higher aspect ratio than the elongated fins in jackfish and sunfish. It is unknown whether the dorsal fin and anal fin have varied hydrodynamic roles owing to the dorsoventrally asymmetric dorsal fin and anal fin, and how the BI-FDI be different from those previously found in fishes with dorsoventrally symmetric median fins.

1.8 Thrust Production Mechanism and BI-FDI in Anguilliform Swimming

Leeches are invertebrate anguilliform swimmers that perform dorsoventral undulations during swimming. One unique feature of the invertebrate leech that differs from the vertebrate fishes is that leeches are equipped with dorsoventral muscle along the body which contracts during swimming, resulting in a flattened body cross section profile and an elongated body length [71]. It is hypothesized that the flattening of body cross section in leech could enhance the thrust production of the body. However, owing to limited research efforts, the thrust production mechanism and associated fluid dynamics of leech swimming remain elusive.

Chen et al. [72] modeled the hydrodynamic force production along the leech body based on resistive and reactive force theories and found continuous thrust production along the body which increases posteriorly. However, the simplified force modeling could not provide surface pressure information or flow field data that help understand the thrust production mechanism. Because the leech body was modeled as 1D segments [72], the force model could not account for the change in body cross section shape, for example, the flattening of the body.

1.9 Current Objectives

A key general goal of this thesis is to examine the BI-FDI and relevant performance enhancement mechanisms in bilateral and in-line propulsions across wide ranges of morphological configuration and locomotion modes. Despite previous efforts made in BI-FDI, the current study will set out to answer the following questions:

1. How the “+”-type body-propulsor configuration in bilateral propulsion could affect the wing-body interaction.
2. What are the hydrodynamic functions of independently mobile finlets.
3. How would BI-FDI and the performance enhancement mechanism be affected by finlets and their kinematics in thunniform swimming?
4. How the dorsoventrally asymmetric dorsal and anal fins would affect the BI-FDI in carangiform swimming?
5. Does BI-FDI exist in anguilliform swimmer that is free from appendages? And how the body flattening would affect BI-FDI.

These questions will be explored using a combined experimental and computational approach with high-fidelity morphology and kinematics modeling approach and an in-house immersed-boundary-method-based direct numerical simulation (DNS) flow solver. The hydrodynamic performance and vortex dynamics of flying and swimming animals—including an “+”-type flyer, hummingbird, a thunniform swimmer, tuna, a carangiform swimmer, trout, and an anguilliform swimmer, leech—will be analyzed in detail.

Objective 1: Bilateral Propulsion: Wing-Body Interaction and its Lift Enhancement Effect in Hummingbird Forward Flight

Comprehensive numerical investigations are conducted on the aerodynamic performance and vortex dynamics of a hummingbird model during forward flight. The highlights in the methodologies of this work include a high-fidelity computational model, detailed analyses of vortex dynamics and aerodynamic performances, and parametric studies on key aerodynamic variables. The WBI is investigated in detail by comparing the computational results from the wing-body (WB) model to those from the wing-only (WO) and body-only (BO) models, including body vortex topology, lift generation, surface pressure, as well as axial velocity and circulation of LEVs. These analyses will be necessary to identify the fundamental flow phenomena associated with the WBI and to quantify the potential lift enhancement. Another effort made in this section is the parametric studies on body inclination angle, β , and advance ratio, J . Simulations are conducted over wide ranges of the two parameters, respectively, to exam whether the lift-enhancement mechanism is robust and general enough to exists at various flight conditions.

Objective 2: In-Line Propulsion: A Computational Hydrodynamic Analysis of Finlet Function

A combined experimental and numerical study is conducted on the hydrodynamics of tuna finlets during forward swimming. High-speed videos of the motion of finlets in freely-swimming yellowfin tuna (*Thunnus albacares*) were obtained to provide kinematic data on the *in vivo* motion of finlets. A biologically realistic model of finlets was reconstructed based on measurements of finlets in yellowfin tuna specimens and kinematics of live fish during free, forward swimming. Simulations of the flow past the model finlets were then conducted using a high-fidelity flow solver. By providing detailed flow field information and hydrodynamic performance data, we aim to extend previous experimental and computational research and fill the gap between numerical studies using simplified finlet models [66-68] and previous experimental work [56, 58]. Moreover, we are able to compute the effect of finlet-finlet interaction and the effect of pitching kinematics on the wake structure and hydrodynamic performance of finlets and compare the function of individual finlets with an assembled collective array of finlets present in tuna.

Objective 3: In-Line Propulsion: Hydrodynamic Interactions and Enhanced Propulsive Performance Owing to Finlets in Tuna Swimming

A combined experimental and numerical study is conducted to examine the hydrodynamic role of finlets in the propulsive performance of tuna locomotion with biologically realistic geometric and kinematic complexity. We aim to fill the gap between simplified finlet studies [10, 66, 73] and previous experimental work [56, 58, 65] by extending our previous work and providing quantitative data on the performance and flow field. By comparing hydrodynamic performance and vortex dynamics between computational models with and without finlets, we are able to quantify potential performance enhancement owing to finlets and reveal the change in flow physics,

thereby testing the thrust enhancing hypothesis of finlets. In addition, by comparing models with pitching finlets and fixed finlets, we are able to examine the potentially important effect of pitching kinematics on the performance and vortex dynamics of tuna swimming.

Objective 4: In-Line Propulsion: Enhanced Hydrodynamic Performance by Dorsal Fin and Anal Fin in Trout Swimming

A combined experimental and numerical study is conducted to examine the enhanced hydrodynamic performance by dorsal fin and anal fin in juvenile rainbow trout steady swimming. Four computational models, including the full fish model (M1: trunk (TK) + dorsal fin (DF) + anal fin (AF) + caudal fin (CF) + pelvic fins (PF)), the model with dorsal fin removed (M2: TK+AF+CF+PF), the model with anal fin removed (M3: TK+DF+CF+PF), and the model with pelvic fins removed (M4: TK+DF+AF+CF), were employed to examine the hydrodynamic effects of the dorsal fin, anal fin, and pelvic fins on the propulsive performance, respectively. For example, by comparing the hydrodynamic performance and vortex dynamics between the full fish model (M1) and the model with dorsal fin removed (M2), potential hydrodynamic interactions between dorsal fin, trunk, and caudal fin can be quantified.

Objective 5: In-Line Propulsion: Effect of Body Flattening on Thrust Production Mechanism and Vortex Dynamics in Leech Swimming

The thrust production mechanism and associated vortex dynamics in leech swimming are examined using a combined numerical and experimental approach. Effect of trunk cross section shape (AR), Reynolds number (Re), and Strouhal number (St) on the thrust production mechanism and vortex dynamics of leech during steady swimming are investigated over wide ranges of the parameters. High-fidelity flow simulations of leech swimming were conducted using both the original model (M1) at $AR=2.48$ and modified models (M2 at $AR=1.24$ and M3 at $AR=4.96$). The

effect of Reynolds number and Strouhal number on the hydrodynamic performance and vortex dynamics are examined by comparing the simulation results over wide ranges of Re (156~15600) and St (0.355~0.798).

1.10 Outline of Thesis

The remainder of the dissertation is organized as follows:

Chapter 2 describes details of the numerical method in section 2.1, the high-speed videography and the virtual-scene kinematics reconstruction (VSKR) method applied in the current study in section 2.2. In addition, the level set based immersed boundary reconstruction algorithm developed for the complex morphology encountered in the BI-FDI problems is introduced in section 2.3. The results of Chapter 2 form the basis of the following publications:

- Wang, J., Han, P., Deng, X., & Dong, H. (2020). A Versatile Level Set Based Immersed Boundary Reconstruction for Bio-Inspired Flow Applications. In *AIAA Scitech 2020 Forum* (p. 2235).
- Deng, X., Han, P., Wang, J., & Dong, H. (2018). A level set based boundary reconstruction method for 3-D bio-inspired flow simulations with sharp-interface immersed boundary method. In *2018 Fluid Dynamics Conference* (p. 4163).

Chapter 3 presents the computational results of wing-body interaction and its lift enhancement effect in hummingbird forward flight. Section 3.1, 3.2, and 3.3 describe the kinematics reconstruction, simulation setup, and validation study of the results, respectively. Section 3.4 compares the aerodynamic performance and vortex dynamics of various computational

models. Finally, a brief chapter summary is given in section 3.5. The results of Chapter 3 form the basis of the following publication:

- Wang, J., Ren, Y., Li, C., & Dong, H. (2019). Computational investigation of wing-body interaction and its lift enhancement effect in hummingbird forward flight. *Bioinspiration & biomimetics*, 14(4), 046010.

Chapter 4 presents the computational results of tuna finlets during forward swimming. Section 4.1 and 4.2 describe the kinematics reconstruction of finlets and simulation setup, respectively. Section 4.3 presents the hydrodynamic performance and vortex dynamics of finlets, the finlet-finlet interactions, and the effect of finlet pitching on hydrodynamics. A discussion of the results is given in section 4.4. A brief chapter summary is given in section 4.5. Supplementary material is given in section 4.6. Results of Chapter 4 form the basis of the following publication:

- Wang, J., Wainwright, D.K., Lindengren, R.E., Lauder, G.V., & Dong, H. (2020). Tuna locomotion: a computational hydrodynamic analysis of finlet function. *Journal of the Royal Society Interface*, 17(165), 20190590.

Chapter 5 presents the computational results of tuna swimming with independently mobile finlets. Section 5.1 and 5.2 describe the tuna kinematics and kinematics reconstruction of the computational model, respectively. Section 5.3 presents the simulation setup. Section 5.4 presents the hydrodynamic performance and vortex dynamics of swimming tuna, the hydrodynamic interactions and thrust enhancement owing to finlets, and the effect of finlet pitching on propulsive performance. A brief chapter summary is given in section 5.6. Results of Chapter 5 form the basis of the following publication:

- Wang, J., Wainwright, D.K., Lauder, G.V., & Dong, H. Tuna locomotion: a computational analysis of hydrodynamic interactions and enhanced propulsive performance owing to finlets. *Journal of the Royal Society Interface*, under preparation.

Chapter 6 presents the computational results of trout steady swimming. Section 6.1 and 6.2 describe the kinematics reconstruction of the computational model and simulation setup, respectively. Section 6.3 presents the hydrodynamic performance and vortex dynamics of swimming trout, and the hydrodynamic roles of the dorsal fin, anal fin, and pelvic fins. A brief chapter summary is given in section 6.5. Results of Chapter 6 form the basis of the following publication:

- Wang, J., Di Santo, V., Lauder, G.V., & Dong, H. Vortex dynamics and thrust enhancement mechanisms of fin-fin and fin-body interactions in fish swimming. *Journal of Fluid Mechanics*, under preparation.

Chapter 7 presents the computational results of leech steady swimming. Section 7.1 and 7.2 describe the kinematics reconstruction of the computational model and simulation setup, respectively. Section 7.3 presents the vortex dynamics and thrust production mechanism of leech swimming, and the effects of trunk cross section shape, Reynolds number, and Strouhal number on the hydrodynamic performance and thrust production. A brief chapter summary is given in section 7.5. Results of Chapter 7 form the basis of the following publication:

- Wang, J., & Dong, H. Effect of body flattening on thrust production mechanism and vortex dynamics of rhythmic undulatory swimming. *Journal of Fluid Mechanics*, under preparation.

Chapter 8 summarizes the conclusions of the current computational studies and points toward future work.

2 Methodology

2.1 Numerical Method

The governing equations of the biological flow problems solved in this work were the incompressible Navier-Stokes equations, as shown in the indicial form in equation (2-1):

$$\frac{\partial u_i}{\partial x_i} = 0; \quad \frac{\partial u_i}{\partial t} + \frac{\partial u_i u_j}{\partial x_j} = -\frac{\partial p}{\partial x_i} + \frac{1}{Re} \frac{\partial^2 u_i}{\partial x_i \partial x_j} \quad (2-1)$$

where u_i ($i = 1, 2, 3$) are the velocity components in x -, y -, and z -directions, respectively, p is the pressure, and Re is the Reynolds number.

The above equations were solved using a Cartesian-grid-based sharp-interface immersed-boundary method (IBM) [74]. The direct numerical simulation (DNS) solver employed a second-order central difference scheme for spatial discretization and a fractional step method for time stepping, which can provide a second-order accuracy in both space and time. The convective terms and diffusion terms were discretized using an Adams-Bashforth scheme and an implicit Crank-Nicolson scheme, respectively. Boundary conditions on immersed bodies were imposed through a “ghost-cell” procedure that can handle both solid bodies and membranes. This numerical approach has been successfully applied to simulate the flapping flight of hummingbird [23, 48], dragonfly [75, 76], and cicada [7] as well as the flapping propulsion of fish [9], manta ray [6], and fish-like swimming [10]. More details about this method can be found in Ref. [74, 77]. Related validations of the flow solver can be found in previous papers [22, 23, 78].

2.2 High-Speed Videography and Kinematics Reconstruction

In this study, high-speed videography is used to obtain the swimming kinematics of live animals, including yellowfin tuna, juvenile rainbow trout, and medicinal leech.

Specifically, both submerged GoPro cameras (GoPro Inc., USA) at 120 fps and 1920×1080 pixel resolution and submerged Photron high-speed cameras (Photron USA Inc., USA) at 250 to 500 fps and 1024×1024 to 2048×2048 pixel resolutions were used to film live yellowfin tunas freely swimming at the Greenfins Aquaculture Tuna Center (Narragansett, Rhode Island, USA). GoPro videos provided a lateral overview of tuna morphology (Figure 5-1a), and high-speed videos provided both a posterior view (Figure 5-1d) and a dorsal view (Figure 5-1e) of tuna morphology and swimming kinematics with detailed information on finlet morphology and pitching motions.

Three synchronized high-speed cameras (FASTCAM Mini AX50, Photron USA, Inc.) at 1000 fps and 1024×1024 pixel resolution were used to film the steady swimming kinematics of juvenile rainbow trout in a recirculating water tunnel (Figure 6-1) from lateral, ventral, and posterior views, respectively.

Two synchronized high-speed cameras (FASTCAM SA3, Photron USA, Inc.) at 500 fps and 1024×1024 pixel resolution were used to record live medicinal leech steady swimming in a transparent tank from lateral and ventral views, respectively (Figure 7-1a&b).

The swimming kinematics of the computational model is reconstructed using the virtual-scene kinematics reconstruction (VSKR) method in Autodesk Maya[®] (Autodesk, Inc.) which is developed from an image-guided reconstruction method [79] that has been successfully adopted

to reconstruct hummingbird [48], manta ray [80] and jackfish [9] swimming (see our previous work [9] for more details).

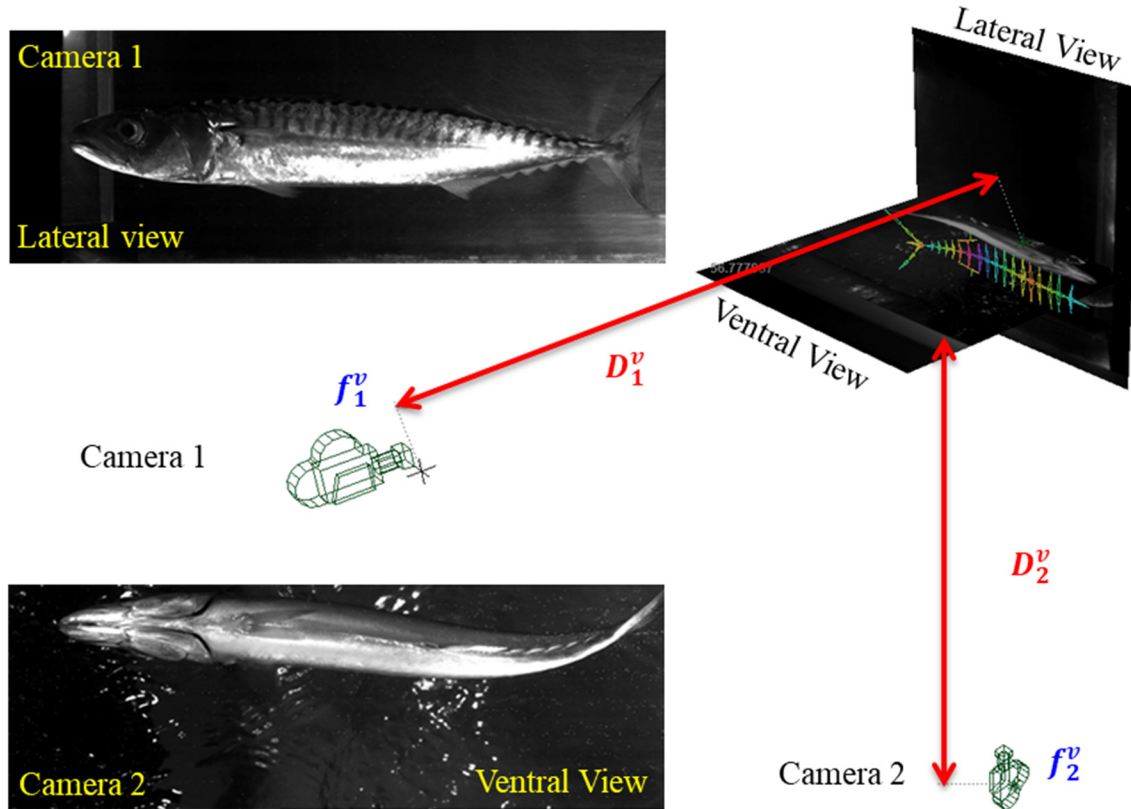


Figure 2-1: Schematics of the virtual-scene kinematics reconstruction (VSKR) method.

Figure 2-1: shows an example of the reconstruction of the body and finlet kinematics of a mackerel during steady swimming using VSKR. During reconstruction, virtual cameras are created with the same focal lengths and positions as those of the experimental cameras, as described in equations (2-2). Therefore, the perspective error of the reconstruction is significantly reduced.

$$f_i^v = f_i^e \quad D_i^v = D_i^e \quad (2-2)$$

where f_i^v is the focal length of the i -th camera in the virtual scene, f_i^e is the focal length of the i -th camera in the experimental scene, D_i^v is the distance from the object to the i -th camera in the virtual scene, and D_i^e is the distance from the object to the i -th camera in the experimental scene.

Figure 2-2 shows the simultaneous reconstruction of the undulating kinematics of the trunk, the deformation of the caudal fin, and the pitching and deviating kinematics of finlets in mackerel fish swimming, where virtual skeletons are bind with the geometry of the body parts and the joint angles are manipulated manually in Maya to match the high-speed images in the background.

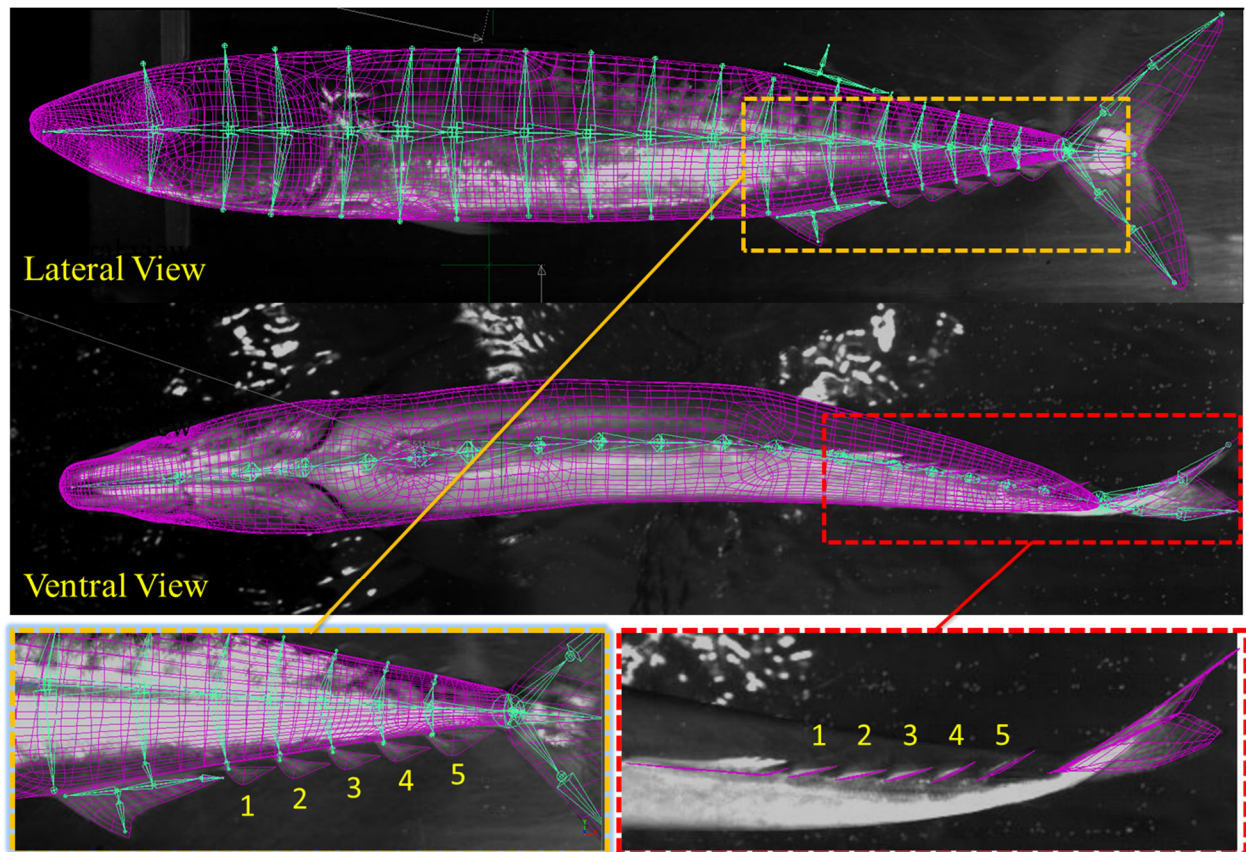


Figure 2-2: Reconstruction of body and finlet kinematics of mackerel fish swimming.

2.3 Level-Set Based Immersed Boundary Reconstruction for Complex Morphology

Bio-inspired flow applications, including insect flight, fish swimming, and biomedical problems, often involve complex body morphologies. For example, fish morphology can be complex with multiple appendages and sharp concave and convex parts. It is important to correctly detect the interface between the fluid and solid body during the simulations. The direct search method [74] and planned search method [81] are two of the existing methods for boundary reconstruction. However, when the geometry is too complex, erroneous detection on immersed boundary may happen and jeopardize the entire simulation. In addition, for high Reynolds number simulations, the body mesh and fluid mesh are dense, which will lead to expensive computational costs in determining the immersed boundary, reducing the efficiency of the conventional immersed boundary method.

To improve the efficiency and robustness of boundary searching in the immersed boundary method, Deng et al. [82] developed a level set based boundary reconstruction method for 3-D bio-inspired flow simulations with sharp-interface immersed boundary method. In their work, a level set based fast reconstruction method was developed to identify the immersed boundary of complex moving boundary by calculating signed distance in the vicinity of solid boundary and propagating the value to the surrounding domain efficiently. It successfully reduced the computation cost of boundary searching to between $O((L_D/\Delta x)^2)$ and $O((L_D/\Delta x)^3)$ and eliminated possibly errors due to the sharpness of the model surface.

In this section, we further develop the level set based immersed boundary reconstruction method (LS-IBRM) [82] to deal with bio-inspired models with both solid body and membrane. For flying and swimming animals in nature, the propulsors of the animals are relatively thin compared with the thickness of their bodies. It is reasonable to model the wings of insects/birds

and the caudal fins of fishes as membranes. Here we calculate the signed distance values of the membranes so that the level set value is extended to the membranes. Thus, the improved LS-IBRM can now deal with more complex bio-inspired geometries with both solid bodies and membranes while inheriting the efficiency and robustness of LS-IBRM that has been demonstrated in Ref. [82]. Next, we introduce the improved LS-IBRM and demonstrate two bio-inspired flow applications of hummingbird forward flight and tuna-inspired underwater vehicle swimming with computational models containing both solid body and membranes.

2.3.1 Numerical Algorithm

Figure 2-3 shows the schematics of level set value calculation and propagation near the immersed boundary in LS-IBRM. The major steps of LS-IBRM are listed below. More detailed descriptions of the algorithm of LS-IBRM can be found in our previous paper [82].

- Step 1: Find the neighbor grid points in the immediate vicinity of the solid boundary. After step 1, the neighbor grids points (solid black circle and square) are found.
- Step 2: For each neighbor grid point, find its neighbor elements on the immersed boundary and get the signed distance to the element. The signed distance value is recorded as the level set value ϕ . After step 2, the level set values of the neighbor grid points and searched grid points (hollowed black circle and square) are obtained.

Step 3: For other grid points in the computational domain, estimate the level set values based on the known neighbor points in a convenient way. After step 3, the level set values of the propagated grid points (hollowed green circle and square) are calculated.

Step 4: Use the level set values to decide the status of each grid point. After step 4, the solid (square) and fluid (circle) cells are decided.

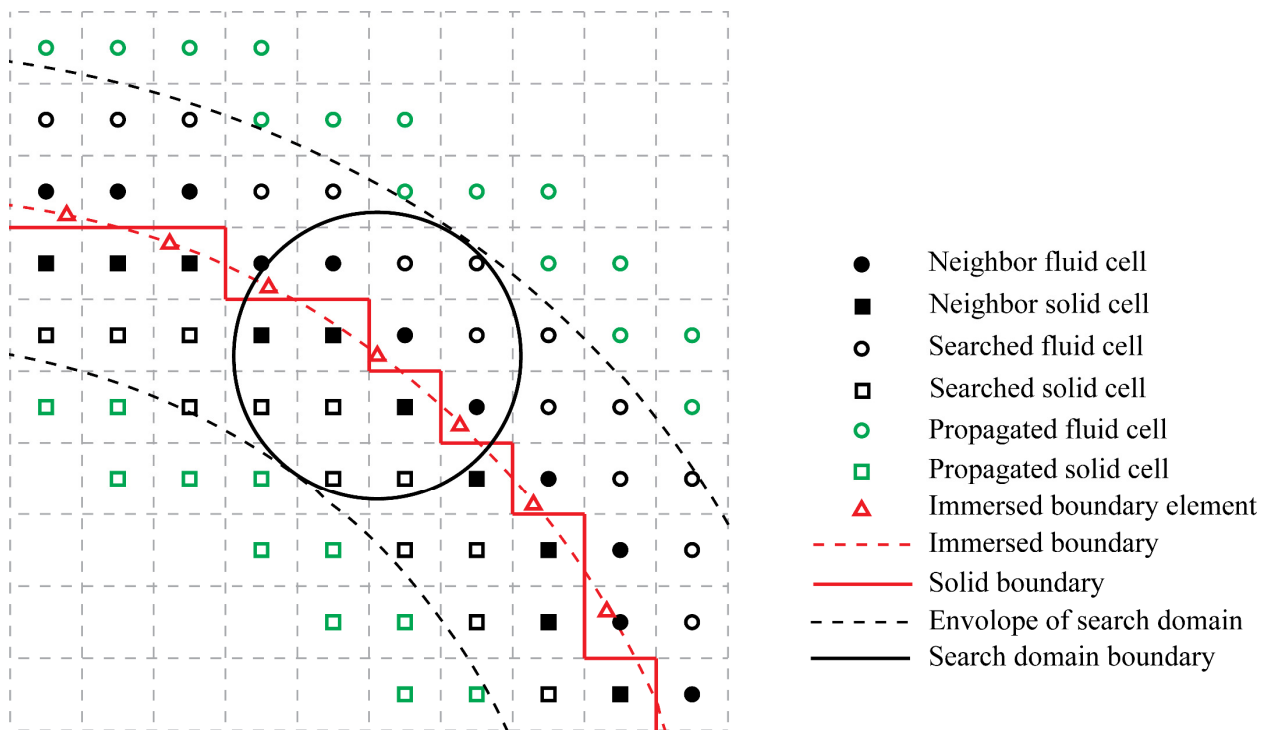


Figure 2-3: Schematics of level set value calculation and propagation near the immersed boundary.

The calculation of the level set value around the membrane is similar to that around the solid boundary. The major difference is that for membrane, the level set values are of the same sign

when located on the opposite side of the immersed boundary, while for the solid body, the level set values are of opposite signs. With the level set values on the membranes calculated, a new function to integrate the level set value is added in the present method. The integration of the level set value is achieved using the following equation (2-3).

$$\phi_{total} = \phi_i, \quad i = 1$$

$$\phi_{total} = \begin{cases} \phi_{total}, & \text{if } \phi_{total} > 0 \text{ and } \phi_i < 0 \\ \phi_i, & \text{if } \phi_{total} < 0 \text{ and } \phi_i > 0 \\ \max(\phi_{total}, \phi_i), & \text{if } \phi_{total}, \phi_i > 0 \\ -\min(|\phi_{total}|, |\phi_i|), & \text{if } \phi_{total}, \phi_i < 0 \end{cases} \quad i > 1 \quad (2-3)$$

where i is the i -th body, ϕ is the level set value. Thus, the level set values of both the solid body and the membranes are integrated and can be used to decide the immersed boundary of the entire system.

2.3.2 Validation Study

In this section, demonstrations of the improved LS-IBRM on hummingbird forward flight and tuna-inspired underwater vehicle steady swimming are presented with the integrated level set value, detected immersed boundary, and associated flow results.

A. Hummingbird Forward Flight

The validation study employs the forward flight of a hummingbird, as shown in Figure 2-4(a), which has been studied in our previous work [23]. The hummingbird body is treated as a solid body and the two wings are modeled as membranes that are directly attached to the body. The

hummingbird model shows complex geometric features including a very sharp beak and tail as well as the direct attachment of wings to the body at the wing root, which are challenging for immersed boundary detection. The purpose of simulating the same problem here is to validate the improved LS-IBRM to see if the level set based reconstruction of the membrane results in the same aerodynamic performance, and to show the advantage of improved LS-IBRM over the conventional boundary detection method for such complex geometry. Table 2-1 provides a summary of the parameters involved in the validation study. Here we use body angle β at 30° and advance ratio J at 0.464 with $J = U_f/U_{tip}$. U_f is the forward flight speed at 4 m s^{-1} and U_{tip} is the cycle-averaged wing tip velocity.

Table 2-1: Parameters involved used for numerical computations

$\beta(^{\circ})$	J
30	0.464

Figure 2-4(b) shows the schematics of the computational grids for the validation study. The computational domain has a dimension of $30c \times 30c \times 30c$, where c is the mid-chord length of the wing. The spacing of the cell is proven to be fine enough for the present simulation. The left boundary is set as velocity inlet with constant incoming flow velocity U . The zero-gradient boundary condition is applied to the right boundary to allow the convection of the vortices without significant reflection. The zero-stress boundary condition is provided at all vertical boundaries. A homogeneous Neumann boundary condition is used for the pressure at all boundaries. A no-slip boundary condition is applied at the hummingbird surface.

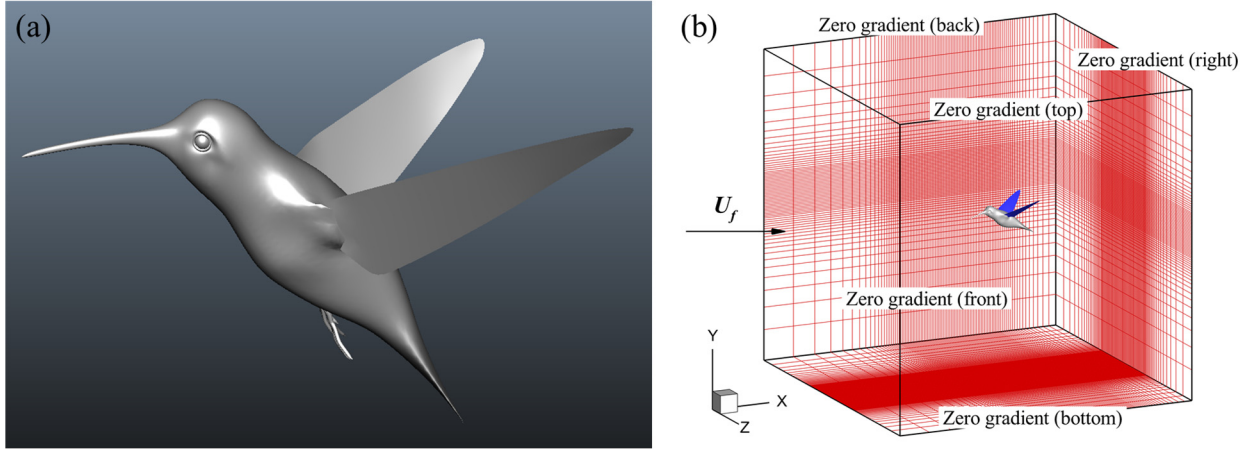


Figure 2-4: (a) Computational model of hummingbird used for the simulation, (b) schematics of the computational grids and boundary information. A dense mesh of 27 million is used for detecting the immersed boundary with $\Delta x = 0.02c$.

The unstructured mesh of the hummingbird body and wings is presented in Figure 2-5(a). There are 15568 triangular elements on the body and 996 on each wing, respectively. Figure 2-5(b) shows the calculated level set values of both the solid body and membrane wings on seven transverse plans cutting through the body and the wings. Zero level set value is found on the body surface. Positive level set values were found within the body and negative values in the fluid domain, which is as expected. On the wings, a zero level set value is found on the membrane surface. Figure 2-5(c) shows the immersed boundary reconstructed from the level set values. It is noticeable that fine steps exist on the body surface and edge of the wings due to the nature of the Cartesian grid based immersed boundary method, which can be improved by further increasing the mesh density of the membrane and the fluid grids.

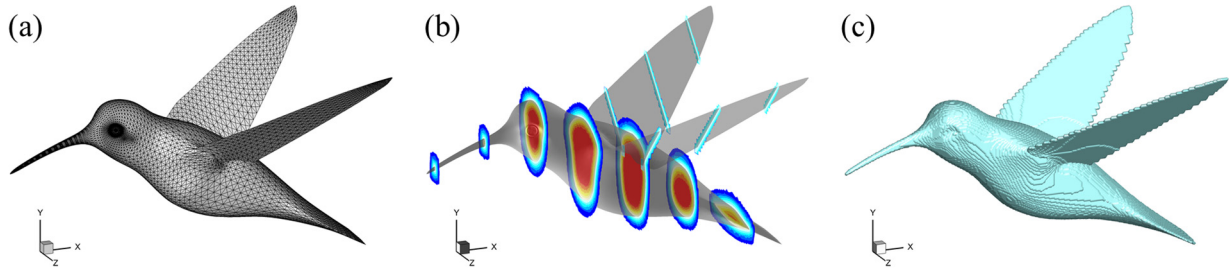


Figure 2-5: (a) Unstructured mesh of the hummingbird body and wings, (b) Calculated level set values of both the solid body and membrane wings on seven transverse planes cutting through the body and the wings, (c) Result of immersed boundary detected by level set values.

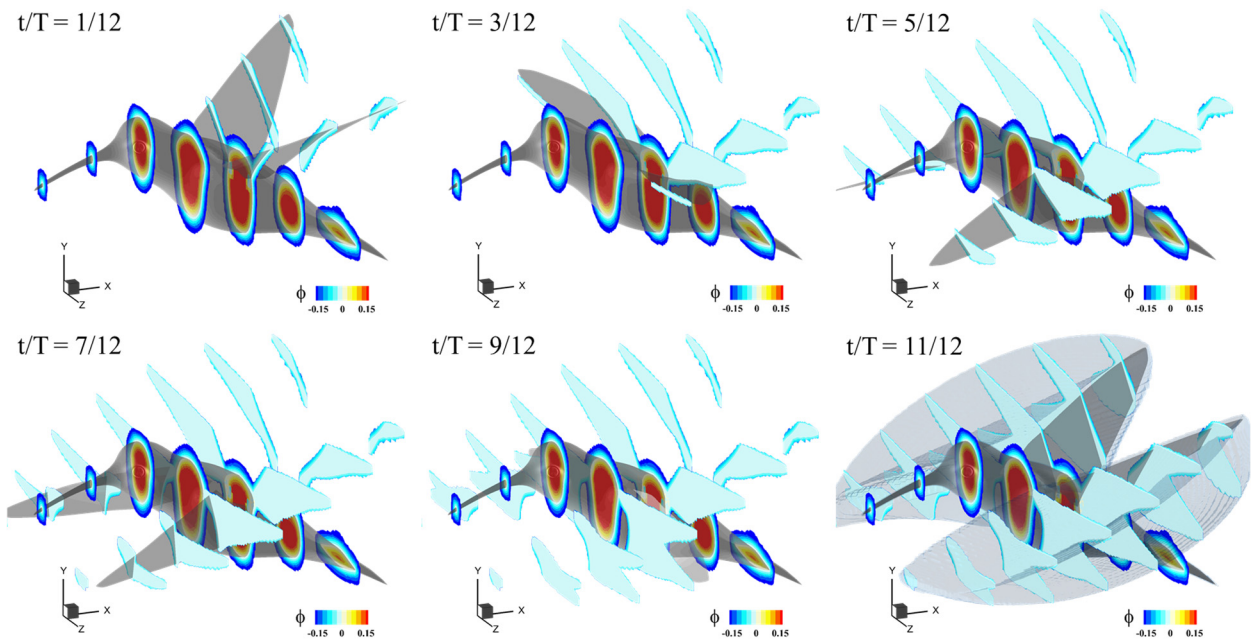


Figure 2-6: Propagation of level set value during a flapping cycle of hummingbird forward flight. The level set values are plotted on seven transverse planes cutting through the body and the wings. The volume swept by the wings is shown at $t/T = 11/12$ with a grey iso-surface.

Figure 2-6 shows the propagation of the level set value in the fluid domain during an entire flapping cycle. It is found level set values are only calculated within the volume that the wings have swept, which significantly reduced the computational cost. The grey iso-surface at $t/T = 11/12$ shows the envelope of the volume swept by the wings where the level set value has been calculated and updated.

Figure 2-7(a) shows the comparison of the instantaneous lift coefficient C_L ($C_L = F_L/0.5\rho U_{tip}^2 A$, where F_L is the lift force and A is the area of the wing) of the left wing between the previous work [23] using conventional immersed boundary reconstruction and the present improved LS-IBRM. It is found the present result converges with that from literature and the maximum difference in C_L amplitude is less than 0.8%. Thus, the improved LS-IBRM is validated. Figure 2-7(b) and Figure 2-7(c) shows the vortex wake structure represented by Q-isosurface and the z-vorticity (ω_z) contour on three slice cuts on the body and the left wing.

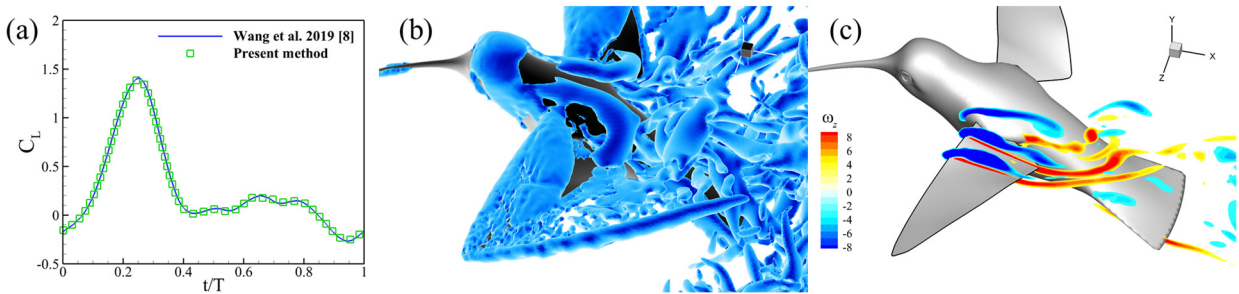


Figure 2-7: (a) comparison of the instantaneous lift coefficient C_L of the left wing between the previous work [8] and the present improved LS-IBRM, (b) Q-isosurface showing the vortex wake during hummingbird forward flight, (c) Z-vorticity contour on three slice-cuts on the body and the left wing.

B. Tuna-Inspired Underwater Vehicle Steady Swimming

The improved LS-IBRM is applied to the steady swimming of a tuna-inspired underwater vehicle known as Tunabot [5]. The hydrodynamics of Tunabot has been studied previously by Wang et al. [83]. The unstructured mesh of the Tunabot body and caudal fin is presented in Figure 2-8(a). There are 48320 triangular elements on the body and 1984 on the caudal fin, respectively. Figure 2-8(b) shows the calculated level set values of both the solid body and membrane caudal fin on ten transverse plans cutting through the body (eight slices) and the caudal fin (two slices). Level set value of zero is found on the body and caudal fin surface. Figure 2-8(c) shows the immersed boundary reconstructed from the level set values. Figure 2-8(d) shows the level set value on a slice cutting the middle frontal plane of the model. The black arrow indicates the immersed boundary identified by level set value $\phi = 0$. The improved LS-IBRM successfully calculated the level set value for both the body and the caudal fin. The resultant flow field is shown in Figure 2-9.

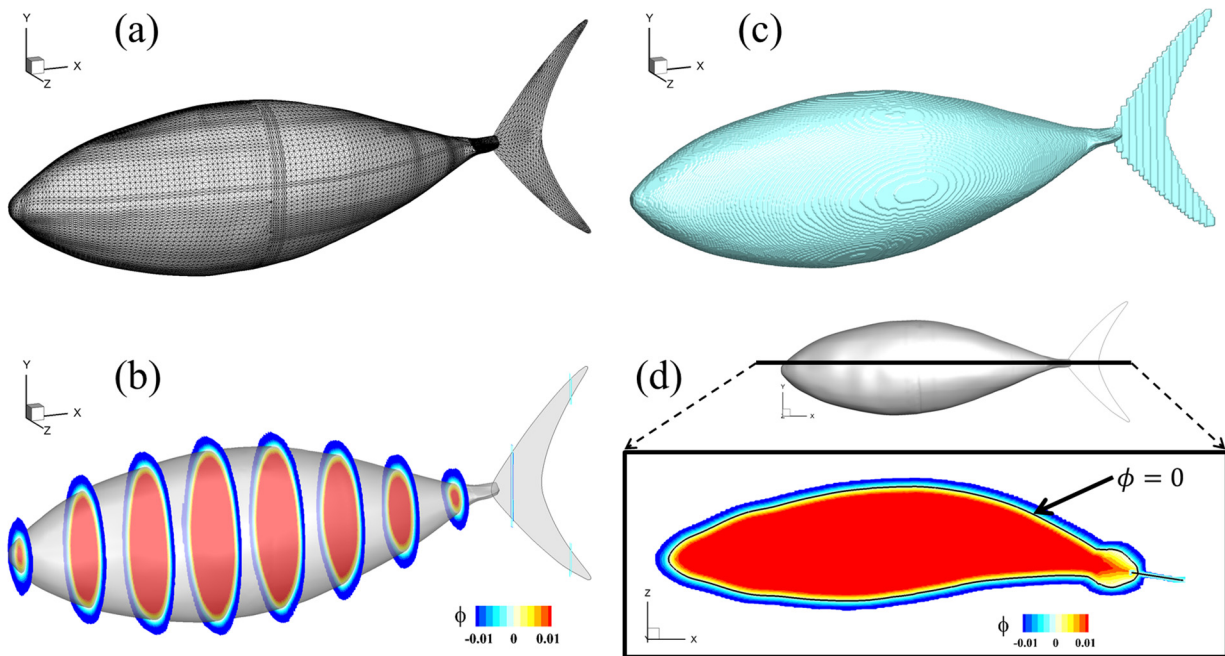


Figure 2-8: (a) Unstructured mesh of the tuna-inspired underwater vehicle, (b) Calculated level set values of both the solid body and membrane caudal fin on ten transverse plans cutting through the body and the caudal fin, (c) Result of immersed boundary detected by level set values. (d) Level set value on slice cutting through the middle frontal plane of the model. The zero level set value boundary ($\phi = 0$) is used to reconstruct the immersed boundary shown in (c).

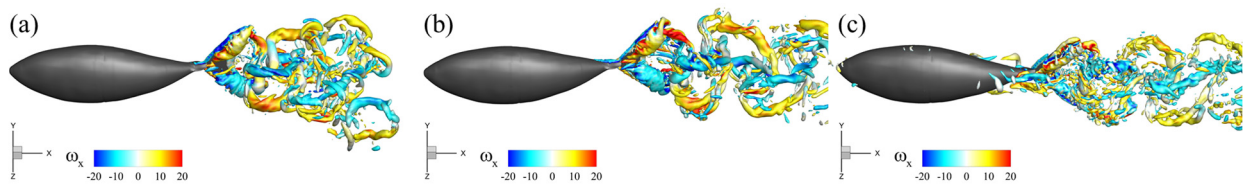


Figure 2-9: Wake structure of Tunabot forward swimming at slow (a), medium (b), and high (c) speed. The vortex wake is represented by Q-isosurface and flooded by z-vorticity.

3 Bilateral Propulsion: Wing-Body Interaction and its Lift

Enhancement Effect in Hummingbird Forward Flight

Lift enhancement mechanism due to wing-body interaction (WBI) was previously proved to be significant in the forward flight of insect flyers with wide-shape bodies, such as cicada. In order to further explore WBI and its lift enhancement effect in a flapping flight platform with different wing and body shapes, numerical investigations of WBI were performed on the forward flight of a hummingbird in this section.

Here we aim to systematically study WBI and its lift enhancement effect in hummingbird forward flight. In this section, comprehensive numerical investigations are conducted on the aerodynamic performance and vortex dynamics of a hummingbird model during forward flight. The highlights in the methodologies of this work include a high-fidelity computational model, detailed analyses of vortex dynamics and aerodynamic performances, and parametric studies on key aerodynamic variables. Firstly, the high-fidelity computational model adopted in this work can represent the geometric features of a hummingbird. The wing kinematics is modeled based on hummingbird forward flight data from literature [49]. Secondly, the WBI is investigated in detail by comparing the computational results from the wing-body (WB) model to those from the wing-only (WO) and body-only (BO) models, including body vortex topology, lift generation, surface pressure, as well as the axial velocity and circulation of LEVs. These analyses will be necessary to identify the fundamental flow phenomena associated with the WBI and to quantify the potential lift enhancement. Another effort made in this section is the parametric studies on body inclination angle, β , and advance ratio, J . Simulations are conducted over wide ranges of the two parameters,

Figure 3-1: (a) Hummingbird model with wing kinematics shown at four time-instants. The body frontal plane (in light orange), stroke plane (in light gray), and tip trajectory (in red) are shown in 3D. The stroke angle, ϕ , denotes the angular displacement of the wing in the stroke plane $o'y'z'$. The deviation angle, θ , is defined as the angle between the root-to-tip line of the wing and the stroke plane. The wing pitch angle, α , is the angle between the wing chord and the mid-frontal plane. (b) 2-D lateral view of the hummingbird model with wing chord (in blue on the wing) shown at three time instances during the downstroke. The mid-frontal plane (dashed line), stroke plane (dash-dot line) are shown together with the 2-D wing pitch angle, α_{2D} , body angle, β , and stroke plane angle, γ . The 2-D wing pitch angle, α_{2D} , is defined as the angle between the projection of the wing chord on the median plane and the orientation of the mid-frontal plane.

The wing flapping kinematics was modeled using a joint-based hierarchical subdivision surface method [79, 85] in Autodesk® Maya® (Autodesk Inc. Mill Valley, California, U.S.). This method has been successfully applied to the reconstructions of various flapping flight birds [48] and insects [7, 75]. The 4 m s^{-1} forward flight data used for the present kinematics modeling was collected from the experimental work by Tobalske *et al.* [49], in which, detailed body and wing kinematics information of rufous hummingbirds (*Selasphorus rufus*) were reported at various forward flight speeds. After kinematics modeling, the key geometric and kinematical parameters of the present hummingbird model, including the wing length, L , the wing span, s , the average wing chord length, c , the single-wing area, A , the body angle, β , the stroke plane angle, γ (shown in Figure 3-1(b)), and the flapping frequency, f , are listed and compared with experimental data in Table 3-1. The parameter definitions are the same as those in the literature. The parameter values of the present model all fell nicely within the value ranges of the experiment data [49]. Since the

corresponding positions of the wing and the body at the attachment were matched during modeling, there was no overlap or separation between wings and body at the wing root. For simplicity, the wing area was preserved from stroke to stroke in the present study.

Table 3-1: Comparisons of key parameters between the present hummingbird model and the experimental data [49] at flight speed $U_f = 4 \text{ m s}^{-1}$.

	Wing length, L (mm)	Wing span, s (mm)	Average wing chord length, c (mm)	Single-wing area, A (mm ²)	Body angle, β	Stroke plane angle, γ	Flapping frequency, f (Hz)
Present model	46	108	12.3	566	30°	28°	40
Experimental data	47±1	109±2	12±1	558±18	30°±8°	31°±5°	40±1

Validations on wing kinematics were conducted by comparing the wing tip trajectories, as shown in Figure 3-2(a) and (b), and the 2-D wing pitch angle, α_{2D} , as shown in Figure 3-2(c), between the present model and the experimental data [49]. The shape and range of the tip trajectories after kinematics modeling were in good agreement with the experimental results in both the lateral and the dorsal views. The 2-D wing pitch angle also fell well within the range of the experimental data. The modeled wing kinematics were described by three Euler angles, including the stroke angle, ϕ , the deviation angle, θ , and the wing pitch angle, α , defined in Figure 3-1(a). The time histories of the modeled wing Euler angles during one flapping cycle are shown in Figure 3-2(d).

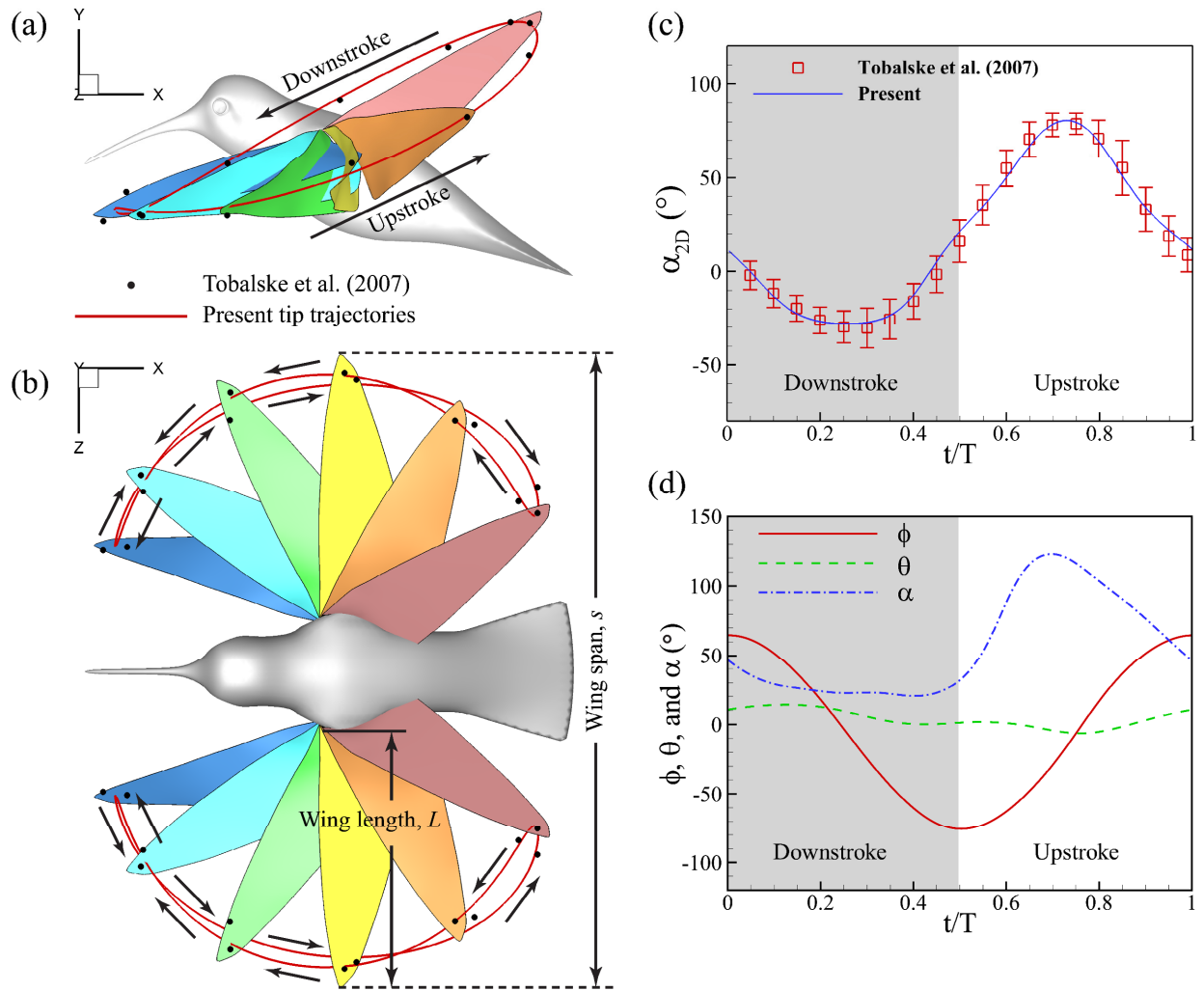


Figure 3-2: Comparisons of the wing tip trajectories between the present model and experimental data [49] in lateral (a) and top (b) views, respectively. Wing shape at six time-instants are shown in (a) during the upstroke and in (b) during the downstroke. (c) Comparison of the 2-D wing pitch angle α_{2D} between the present model and experimental data. The error bars indicate the range of the error in experimental measurements. (d) The time history of the modeled wing Euler angles, including the stroke angle, ϕ , the deviation angle, θ , and the wing pitch angle, α , during one flapping cycle.

In this study, the Reynolds number, Re_f , and the advance ratio, J , are defined as $Re_f = cU_f/\nu$ and $J = U_f/U_{tip}$, respectively, where ν is the kinematic viscosity of air ($\nu = 1.56 \times 10^{-5} \text{ m}^2 \text{ s}^{-1}$ at room temperature $25 \text{ }^\circ\text{C}$), U_{tip} is the cycle-averaged wing tip speed defined by $U_{tip} = (1/T) \int_0^T \sqrt{u_{tip}^2 + v_{tip}^2 + w_{tip}^2} dt$, in which T is the flapping period, u_{tip} , v_{tip} , and w_{tip} are the three velocity components in x , y , and z directions, respectively, at the wing tip. At forward speed $U_f = 4 \text{ m s}^{-1}$, Re_f is 3154 and J is 0.464. Here, the Re_f definition is consistent with that in the previous cicada [7] and hummingbird [47] forward flight studies. It is worth noting that the Reynolds number based on the cycle-averaged wing tip speed ($Re_{tip} = cU_{tip}/\nu$) can be obtained using the equation $Re_{tip} = \frac{1}{J}Re_f$.

3.2 Simulation Setup

The effect of WBI was studied by comparing simulation results across three computational models, including the wing-body (WB), the wing-only (WO), and the body-only (BO) models. The WB model included both the body and the wings of the hummingbird with wing kinematics, while the WO model only kept the wings with flapping kinematics and the BO model only kept the stationary body. With this approach, WBI in the WB model can be completely decoupled in WO and BO models, so that the effect of WBI can be examined by the comparisons of aerodynamic performance and vortex structure between the three models. In order to quantify the effect of governing parameters on the lift enhancement mechanism due to WBI, parametric studies were performed on body angle, β , and advance ratio, J , which were important for the aerodynamic performance and the resultant unsteady flow. The ranges of the governing parameters are listed in Table 3-2.

Table 3-2: Summary of the governing parameters used for numerical computations and their ranges

$\beta(^{\circ})$	J
10, 20, 30, 40, 50	0.309, 0.371, 0.464, 0.619, 0.982

A Cartesian computational grid with stretching grid configuration was employed in the simulations, as shown in Figure 3-3(a). The computational domain size was $30c \times 30c \times 30c$ with total grid points of about 13.4 million ($289 \times 161 \times 289$). High-resolution grids were generated in the vicinity of the computational model and in the wake to better resolve the vortical structures in the flow. The left-hand boundary was set as velocity inlet with constant incoming flow velocity U_f . The zero-gradient boundary condition was applied to the right-hand boundary to allow the convection of the vortices at the boundary without significant reflection. The zero-stress boundary condition was provided at all lateral boundaries. A homogeneous Neumann boundary condition was used for the pressure at all boundaries. A no-slip boundary condition was applied at the model surface.

The current size of the computational domain was proven to be large enough to obtain converged results based on extensive test simulations with different domain sizes. In addition, a convergence study on grid density was performed to guarantee grid-independent simulation results. Figure 3-3(b) illustrates the comparison of the instantaneous lift coefficient of the left wing in the WO model at three different grid densities. The grid spacings around the body for the coarse, medium, fine, and dense meshes were $0.081c$, $0.046c$, $0.034c$, and $0.029c$, respectively. The lift coefficient converged as the grid number increased. The difference in peak value between the fine

mesh case and the dense mesh case was less than 1.0%. Grid spacing $\Delta x = 0.034c$ was used for the computations in this study.

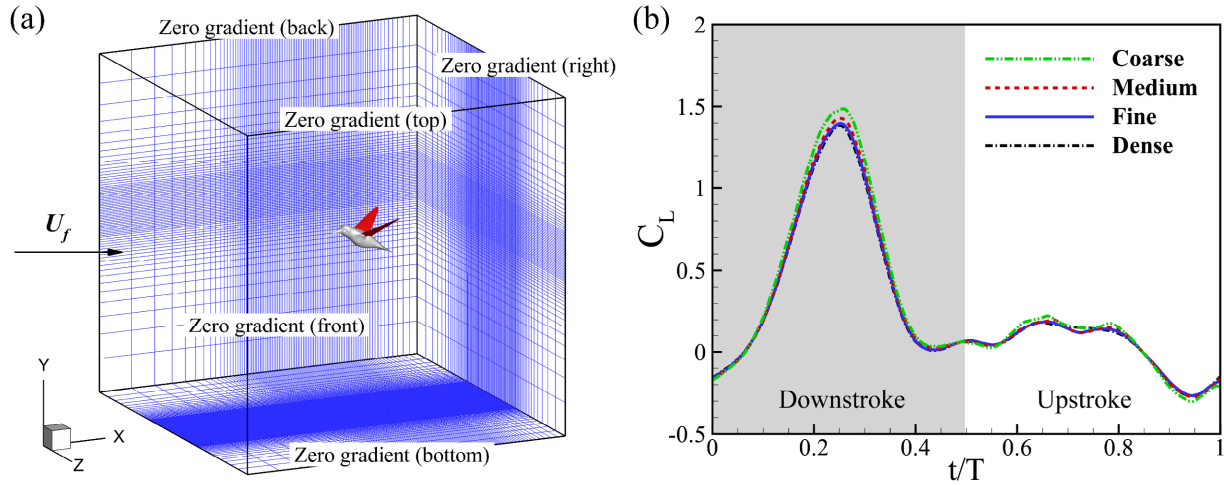


Figure 3-3: (a) Schematic of the computational domain, mesh, and boundary conditions used in the simulations of the present study. (b) Comparison of instantaneous lift coefficient of the left wing in the WO model between coarse mesh ($193 \times 87 \times 193 \approx 3.2$ million, $\Delta x = 0.081c$), medium mesh ($257 \times 129 \times 257 \approx 8.5$ million, $\Delta x = 0.046c$), fine mesh ($289 \times 161 \times 289 \approx 13.4$ million, $\Delta x = 0.034c$), and dense mesh ($305 \times 183 \times 305 \approx 17.0$ million, $\Delta x = 0.029c$).

3.3 Validation Study

To further validate the computational model and numerical solver used in this study, the aerodynamic performance of the present model at hovering flight condition was obtained and compared with numerical [84, 86] and experimental [87] data from previous literature. Note that the present hovering kinematics was modeled based on the hovering flight data [49] using the same

approach described in section 2.1. Key geometric and kinematical parameters of the present hovering model are listed and compared with previous hummingbird hovering studies in Table 3-3.

Table 3-3: Summary of key geometric and kinematical parameters of hummingbird hovering studies.

	Present hovering	Song et al., (2014)	Yang and Zhang, (2015)	Ingersoll et al., (2018)
Wing length, L , (mm)	46	44.7	45	51.4
Average wing chord length, c , (mm)	12.3	11.7	12.4	--
Single wing area, A (mm ²)	566	568	559	565
Flapping frequency, f (Hz)	41	42	43	41
Mean wing tip speed, U_{tip} (m s ⁻¹)	9.72	9.51	10.02	10.87

Aerodynamic forces acting on the body and wings of the hummingbird were computed by the direct integration of the surface pressure and shear forces. The lift (F_L) and thrust (F_T) forces were then nondimensionalized as lift (C_L) and thrust (C_T) coefficients to describe the aerodynamic performance of hummingbird in forward flight, as shown in equation (3-1),

$$C_L = \frac{F_L}{\frac{1}{2}\rho U_{tip}^2 A}, \quad C_T = \frac{F_T}{\frac{1}{2}\rho U_{tip}^2 A} \quad (3-1)$$

where, F_L points to y -positive, F_T points to x -positive, ρ is the density of the fluid, A denotes the area of a single wing, and U_{tip} is the mean wing tip speed.

Figure 3-4(a) compares the instantaneous wing lift coefficient during one flapping cycle between the present study and the literature data. Note that all C_L results were normalized using equation (3-1) so that they can be compared in the same nondimensional scale. The variation trend and magnitude of the present lift coefficient in hover were in reasonably good agreement with the previous results. Figure 3-4(b) shows the comparison of stroke-averaged lift coefficients of the downstroke and the upstroke, respectively. The present stroke-averaged lift coefficients were consistent with the previous results in both the downstroke and the upstroke.

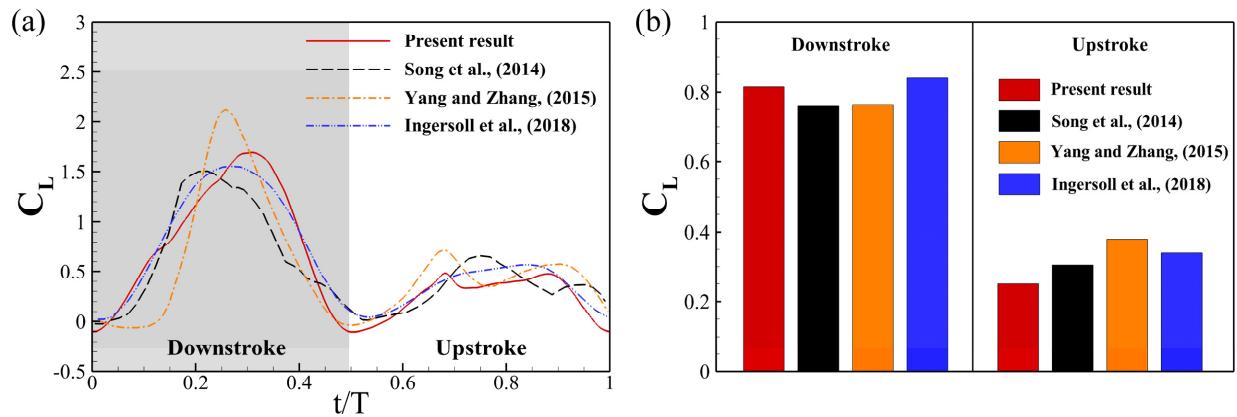


Figure 3-4: (a) Comparison of instantaneous wing lift coefficient between present and literature data during hovering flight. (b) Comparisons of stroke-averaged lift coefficients during downstroke and upstroke, respectively.

3.4 Results and Discussions

In this section, simulation results, including aerodynamic performance, wake topology, surface pressure, LEV axial velocity, and LEV circulation, of the WB, WO, and BO models are presented at $\beta = 30^\circ$ and $J = 0.464$. Parametric studies on β and J are also presented to study their effects on the WBI and lift enhancement.

3.4.1 Aerodynamic Performance

Figure 3-5(a) and (b) compare the instantaneous lift and thrust coefficient of the left wing and the body, respectively, between the three models. The force histories came from the fourth flapping cycle of the simulations when the flow fields reached periodic states. The solid lines in each figure indicate WB results, while the dashed lines indicate BO or WO results. Figure 3-5(a) shows that the wing lift force was mainly generated during the downstroke, which was consistent with the previous hummingbird forward flight study [47]. Comparing the WB and WO models, higher wing lift was found during the entire downstroke of the WB model, especially at mid-downstroke, indicating significant lift enhancement due to the existence of the hummingbird body. In Figure 3-5(b), substantial influences by WBI were also found on body forces. Both the body lift and drag showed significant fluctuations associated with the unsteady flapping motion of wings in the WB model, while no obvious fluctuation was observed in BO. The peak WB body lift happened at mid-downstroke with a peak amplitude about three times the WO value. The simultaneous lift enhancements observed in Figure 3-5(a) and (b) indicated strong aerodynamic interactions between the wings and the body.

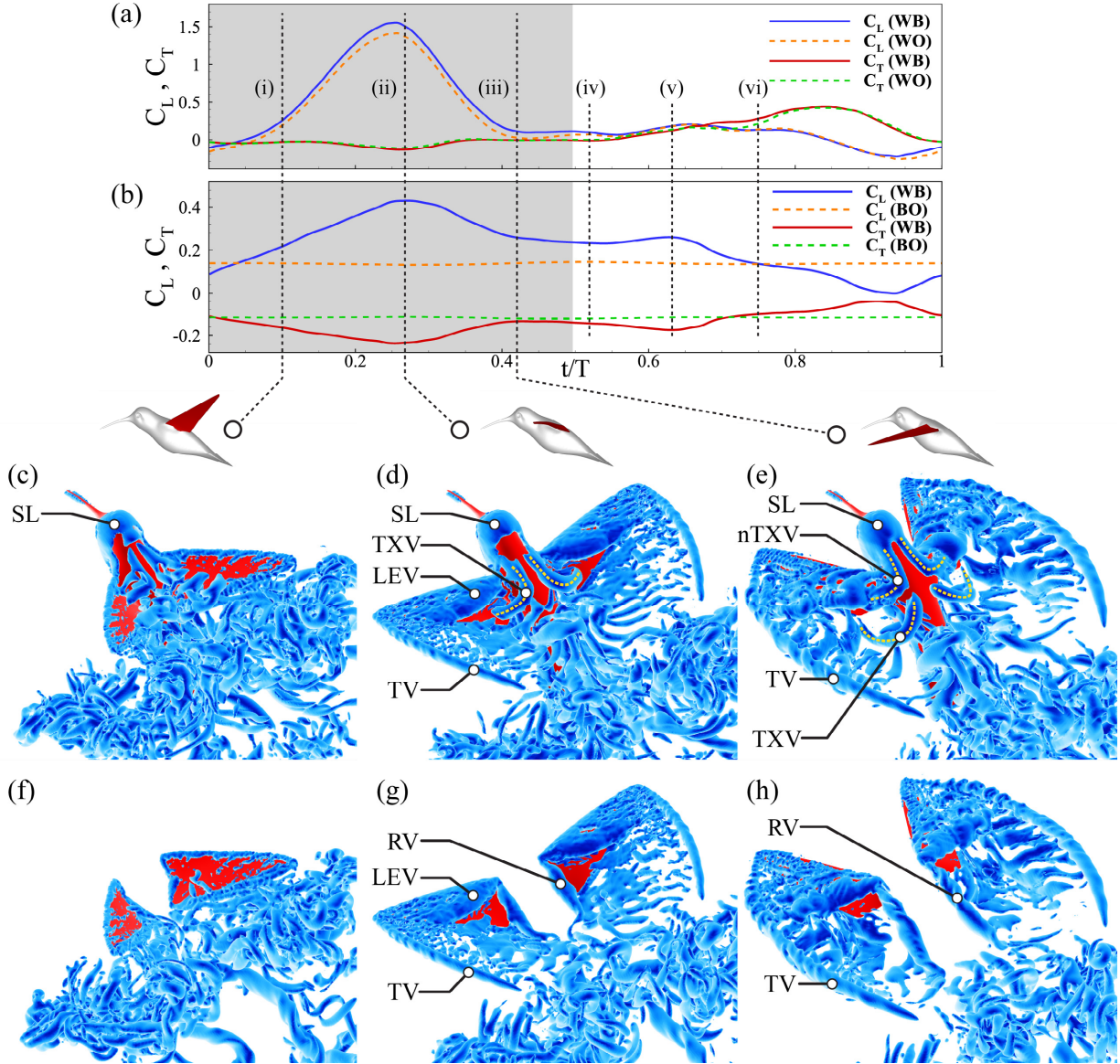


Figure 3-5: Comparisons of instantaneous lift and thrust coefficients on the left wing (a) and the body (b), respectively, between the WB, WO, and BO models during one flapping cycle. Comparisons of the three-dimensional wake structure of the hummingbird between the WB (c)–(e) and WO (f)–(h) models at (i) $t/T = 0.1$ (c) and (f), (ii) $t/T = 0.27$ (d) and (g), and (iii) $t/T = 0.42$ (e) and (h), during the downstroke, respectively. The vortex structures of shear layer (SL), thorax vortex (TXV), leading-edge vortex (LEV), tip vortex (TV), root vortex (RV), and new thorax

vortex (nTXV) are identified. The isosurface of the wake structures is visualized by $Q = 60$. The yellow dashed lines indicate the vortex core locations of the thorax vortex pair.

Table 3-4: Cycle-averaged lift and thrust coefficients and lift enhancements due to WBI

\bar{C}_L	Body	Wing-pair	Overall
WB	0.220	0.626	0.846
WO/BO	0.135	0.521	0.656
$\Delta\bar{C}_L$ (%)	63%	20%	29%

Table 3-4 quantifies the cycle-averaged lift (\bar{C}_L) and thrust (\bar{C}_T) productions of the WB, WO, and BO models, respectively. For the WB model, the overall thrust coefficient was 0.004, which was less than 0.5% of its overall lift, indicating a steady forward flight condition of the hummingbird. Lift enhancement due to WBI was defined as $\Delta\bar{C}_L = (\bar{C}_L|_{WB} - \bar{C}_L|_{WO/BO}) / \bar{C}_L|_{WO/BO}$. By comparing the cycle-averaged lift between WB and WO/BO, it was found the wing-pair lift increased by 20%, and the body lift increased by 63%, which all together contributed to an overall lift enhancement (OLE) of 29%. This enhancement was the strongest among OLEs that have been found in insects so far [7, 35, 45], demonstrating significant aerodynamic benefit due to WBI in hummingbird forward flight. It was also found the hummingbird wings played a major role in the lift enhancement ($0.626 - 0.521 = 0.105$) by contributing 55% of the overall lift increase ($0.846 - 0.656 = 0.190$), which was different from the body-dominated lift enhancement in the cicada forward flight study [7]. Over 96% of the OLE happened during the downstroke with the

largest enhancement emerged at the force peaks of the wing and body lift, being consistent with the cicada study.

3.4.2 Vortex Topology

Figure 3-5(c)–(h) compare the instantaneous wake structure of hummingbird forward flight between the WB and WO models during the downstroke. The 3-D vortex structures were visualized by the isosurface defined by Q -criterion [88] with $Q = \frac{1}{2}[|\mathbf{\Omega}|^2 - |\mathbf{\Lambda}|^2] > 0$. Here $\mathbf{\Lambda} = \frac{1}{2}[\Delta\mathbf{u} + (\Delta\mathbf{u})^T]$ and $\mathbf{\Omega} = \frac{1}{2}[\Delta\mathbf{u} - (\Delta\mathbf{u})^T]$ are the shear strain rate and vorticity tensors, respectively. The physical understanding of Q is the local balance between shear strain rate and vorticity magnitude. The Q -isosurfaces in Figure 3-5 are identified by $Q = 60$. Similar LEV and tip vortex (TV) were found between the two models, which was consistent with previous insect studies [7, 45, 89]. However, significant differences in vortex dynamics were found at the wing root and the body.

At early-downstroke ($t/T = 0.1$), a shear layer (SL) was found on the dorsal surface of the hummingbird head. Vortex structures without a coherent shape were found on the dorsal body thorax. No significant LEV was formed for both models. At mid-downstroke ($t/T = 0.27$), the SL was more developed. A strong thorax vortex (TXV) pair was formed as coherent L-shape vortex tubes connecting the dorsal thorax surface and the wing root. While in the WO model, the root vortex (RV) pair began to form. Similar RV formation was observed in the forward flight of an insect-like flapping wing [90]. The LEVs were in the maximum form for both the WB and the WO models, corresponding to the wing lift peak at this moment. Meanwhile, the tip vortices began to form. At late-downstroke ($t/T = 0.42$), the posterior parts of the TXV pair have shed from the

dorsal thorax and disconnected with the wing root. The remaining anterior parts developed into a new pair of L-shape thorax vortex (nTXV) that connected to the head SL and the wing root at its two ends. The strong head SL started to feed the nTXVs at this moment. While in the WO model, the RVs were more developed. The LEVs have detached from the leading edge for both models, corresponding to the significant wing lift drop at the moment.

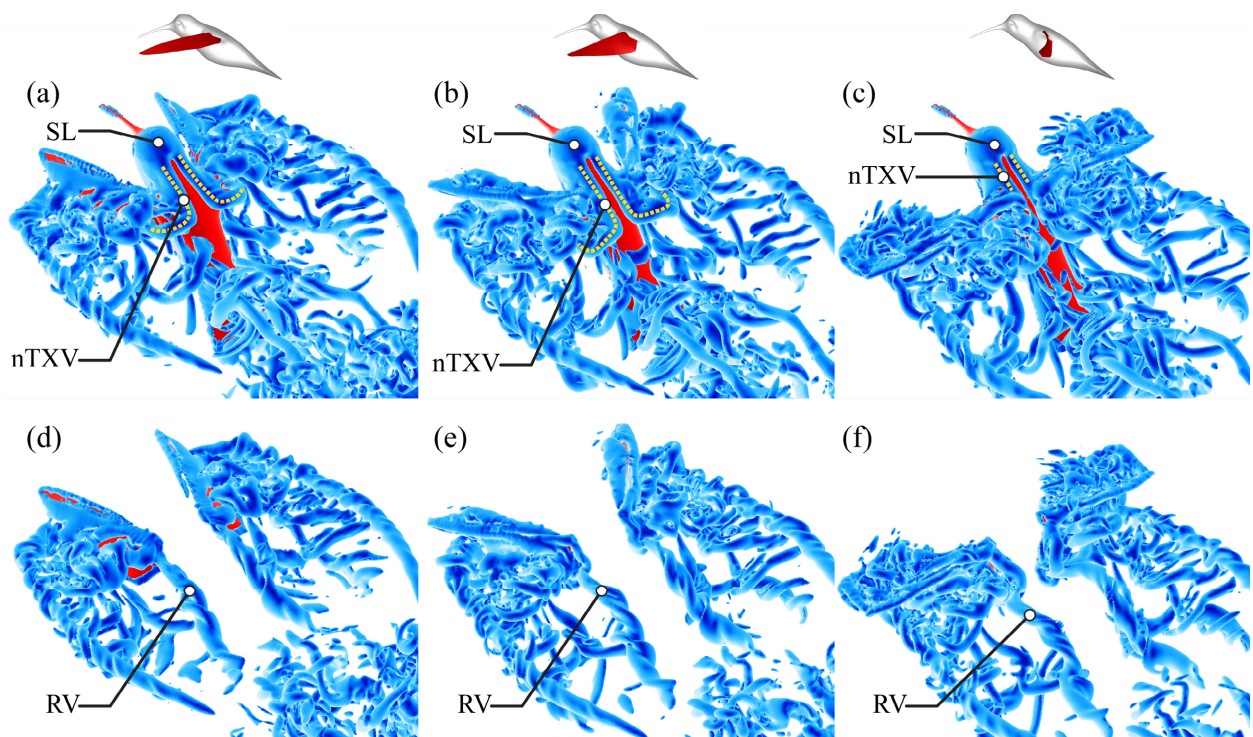


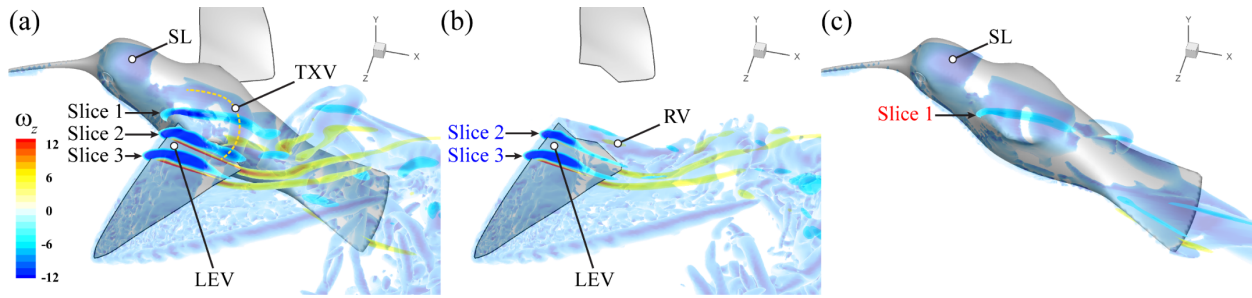
Figure 3-6: Comparison of the three-dimensional wake structure of the hummingbird between the WB (a)–(c) and WO (d)–(f) models at (i) $t/T = 0.52$ (a) and (d), (ii) $t/T = 0.63$ (b) and (e), and (iii) $t/T = 0.75$ (c) and (f), during the downstroke, respectively. The vortex structures of the shear layer (SL), root vortex (RV), and new thorax vortex (nTXV) are identified. The isosurface of the wake structure is visualized by $Q = 60$. The yellow dashed lines indicate the vortex core locations of the thorax vortex pair.

Figure 3-6 compares the wake structure between the WB and WO models during the upstroke. At early-upstroke ($t/T = 0.52$), the head SL continued to feed the nTXV pair to its maximum form. The posterior parts of the nTXV pair then detached from the wing root at $t/T = 0.52$ and further broke into small vortex structures at $t/T = 0.75$. While in the WO model, strong RV pair continued to grow from $t/T = 0.52$ to 0.75 .

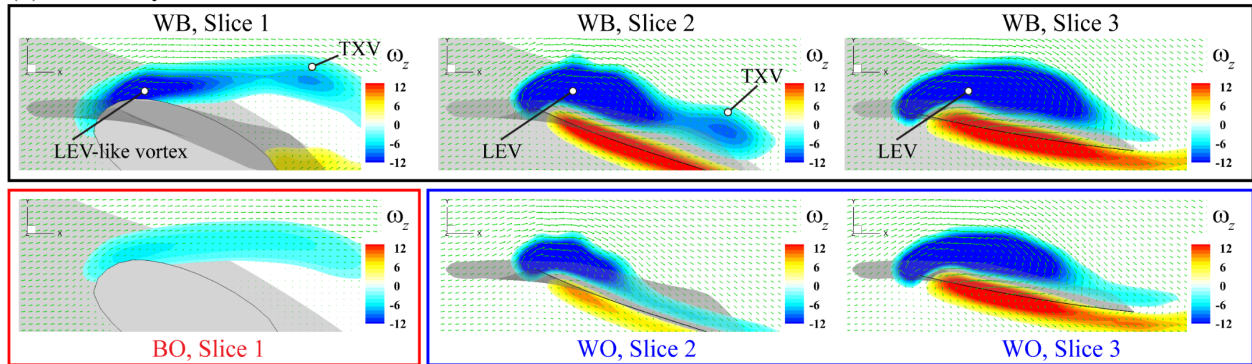
Although body vortex pairs, including TXV and posteriors body vortex pair, were also found in cicada forward flight [7], the shape and dynamics of the body vortices of the hummingbird were very different from those of the cicada. Specifically, the thorax vortex pair was formed twice (TXV and nTXV) during the downstroke flapping of the hummingbird, while it was found formed only once in cicada. In addition, the head SL played an important role in the formation of the TXV and nTXV in hummingbird forward flight by feeding them during most of the flapping cycle, which was not reported in cicada [7].

A strong correlation between the body vortex formation and the lift enhancement was found during the downstroke, especially during its second half ($t/T = 0.27$ to 0.42) when coherent TXVs and strong head SL were formed. In order to understand the cause of the lift enhancement on the wing and the body, detailed analyses on the vorticity and axial velocity of the LEV and TXV were conducted at $t/T = 0.27$, as shown in Figure 3-7.

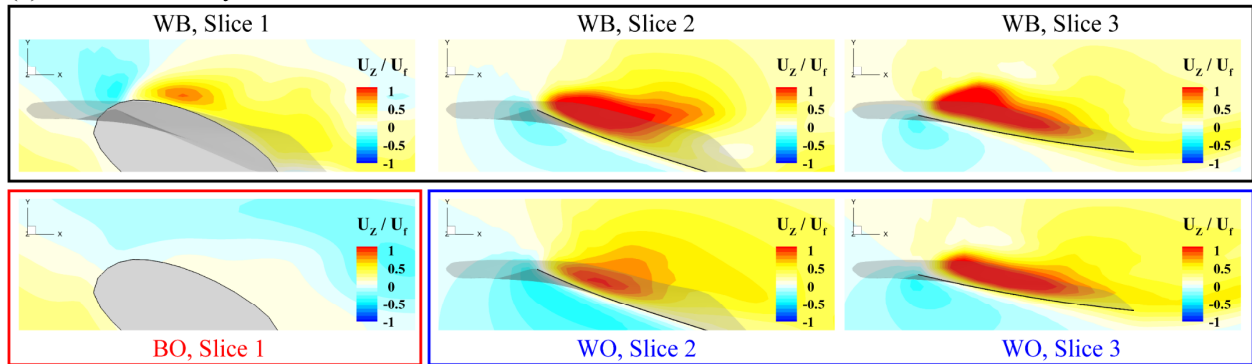
Figure 3-7(a)–(c) compare the spanwise vorticity (ω_z) contour on slices cutting through the body and the left wing between WB, WO, and BO models. Transparent Q -isosurfaces are also displayed associated with the vorticity contours. It was found the LEV and TXV cores identified by the ω_z contour overlapped with the vortex structures represented by the Q -isosurfaces, reaffirming the significance of the body vortex formed in the WB model.



(d) Z-Vorticity



(e) Z-Axial Velocity



(f) Z-Axial Velocity

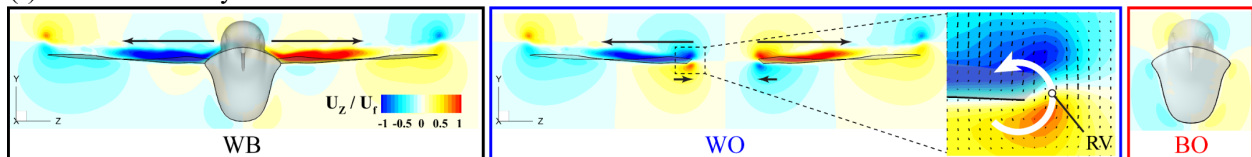


Figure 3-7: Comparison of instantaneous spanwise vorticity contour (ω_z) between the WB (a), WO (b), and BO (c) models at $t/T = 0.27$ on three slice-cuts (Slice 1, 2, and 3) taken at $-0.1L$, $0.1L$ and $0.3L$ away from the wing root. Same slices are taken on the WO and BO models where applicable. ω_z is normalized by U_f/c . The wake structures are also shown in (a)–(c) with the shear layer (SL), thorax vortex (TXV), and root vortex (RV) identified. The 2-D vorticity and z-axial velocity contours on the slices are compared between the WB, WO, and BO models, respectively

in (d) and (e). The z-axial velocity U_z is normalized by U_f . The z-axial velocity on slice cutting the body transverse plane is compared between the WB, WO, and BO models in (f).

Figure 3-7(d) compares the LEV and TXV contours in 2-D between the three models associated with velocity vectors. The body vortex was compared on Slice 1, where an LEV-like vortex was found on the WB body with a clear core structure identified by the circulating velocity vectors. However, only a slight shear layer was found on the BO model. On Slice 2, it was found the WB LEV core was much larger in size than that of the WO LEV. In addition, a significant TXV core was observed in WB, but not in WO. On Slice 3, the strength of WO LEV was still less than the WB, but more comparable. The comparisons of ω_z contour further explained the cause of lift enhancement on the wing and the body by linking the aerodynamic performance to the strengthened LEV and the LEV-like body vortex formed during WBI. In addition, the current ω_z contour of LEV-like body vortex shared a similar shape and vorticity distribution with those of the hawkmoth [21] and the butterfly [18], indicating that the LEV-like body vortex is a common flow phenomenon that exists in the forward flight of both the insects and birds.

The strengthened LEV in WB was further confirmed by comparing the z-axial velocity of the LEV core. Figure 3-7(e) shows the comparison of z-axial velocity (U_z) contour on slices between the three models. On Slice 1, substantial axial velocity emerged near the wing root of the WB model, while no U_z was observed in the BO model. On Slice 2 and 3, the axial flow of the WB LEV was found to be larger than that of the WO LEV, which was consistent with the stronger LEV core of the WB model shown in Figure 3-7(d).

Figure 3-7(f) shows the comparison of z-axial velocity on the YOZ-plane cutting through the wing root. Strong axial flow originated from the root part of the body was found on the dorsal side of the WB wings, but not on the ventral side. In contrast, for the WO wings, a substantial axial flow was found on the ventral side, especially near the wing roots. This velocity was thought to be induced by the RVs that formed at wing roots, as shown in Figure 3-5(g). To support this, the z-axial velocity field at the left wing root region of the WO model was highlighted and associated with velocity vectors, as shown in Figure 3-7(f). A strong counterclockwise circular flow around the wing root was observed. The circular flow from the ventral side of the wing bypassed the wing root to the dorsal side, which induced the positive z-axial velocity at the ventral side of the wing. A similar circular flow of root vortex was observed in the experimental study on the fapping flight of insect-like wings in hover [91]. For the BO model, no significant circular flow was found.

To further demonstrate the reinforcement of the LEV due to WBI, comparisons of ω_z contour and LEV circulation were made between WB and WO models on a series of slice-cuts taken along the wing length, as shown in Figure 3-8(a) and (b) and Figure 3-8(c), respectively. It was found the LEVs near the wing tip ($z/L > 0.5L$) of the two models were highly alike. However, the difference in the LEV strength between the two models became larger when the slice cut approached the wing root. This difference is reflected in the LEV circulation, $|\Gamma|$, calculated on each slice of the two models, as shown in Figure 3-8(c). The circulation difference, $|\Gamma_{WB}| - |\Gamma_{WO}|$, represents the enhancement in LEV strength. It was found the LEV enhancement increased monotonically as the slice-cut approached the wing root. The circulation value at $0.1L$ was greatly increased by 32% due to WBI.

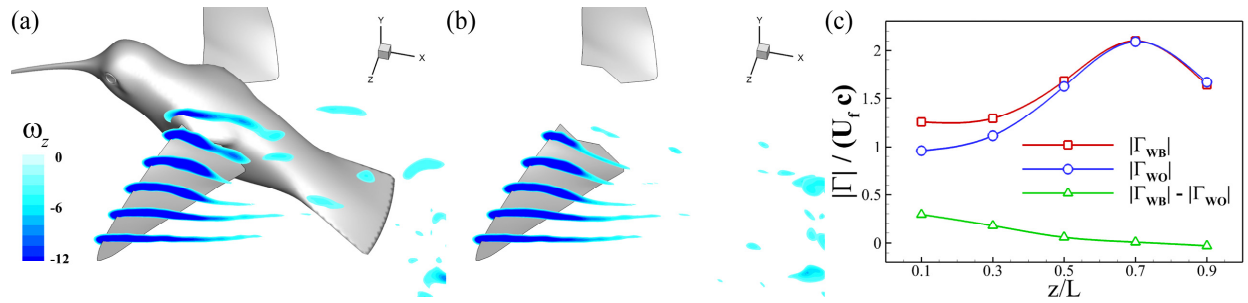


Figure 3-8: Comparison of instantaneous spanwise vorticity contour (ω_z) between the WB (a) and WO (b) models at $t/T = 0.27$ on six slice-cuts taken at $-0.1L$, $0.1L$, $0.3L$, $0.5L$, $0.7L$, and $0.9L$ away from the wing root. The vorticity is normalized by U_f/c . (c) Circulations ($|\Gamma|$) of the LEVs at the six positions are calculated and compared between the WB and WO models. The circulation difference $|\Gamma_{WB}| - |\Gamma_{WO}|$ is also shown. $|\Gamma|$ is normalized by $U_f c$.

3.4.3 Surface Pressure

The surface pressure of the hummingbird model was analyzed in order to understand the spatial distribution of the lift enhancement on the hummingbird body and wings. Figure 3-9 compares the pressure isosurface and the pressure distribution, respectively, between the WB, WO, and BO models at mid-downstroke ($t/T = 0.27$). The pressure coefficient was defined as $C_p = p/0.5\rho U_{tip}^2$, where p is the gauge pressure. In Figure 3-9(a)–(c), the transparent outer shell represents the pressure isosurface of $C_p = -0.08$ and the solid inner core of $C_p = -0.25$. It was found the outer shell in WB was a coherent surface covering the entire wing span and the dorsal surface of the head and thorax. However, the outer shells in WO were two smaller isosurfaces covering each wing and were separated by the gap between the wings. In the BO model, the outer shell was minimal, and no inner core was observed. The low-pressure region within the outer shell

of WB was much larger than its WO and BO counterparts combined, indicating a stronger low-pressure region above the hummingbird model created by WBI.

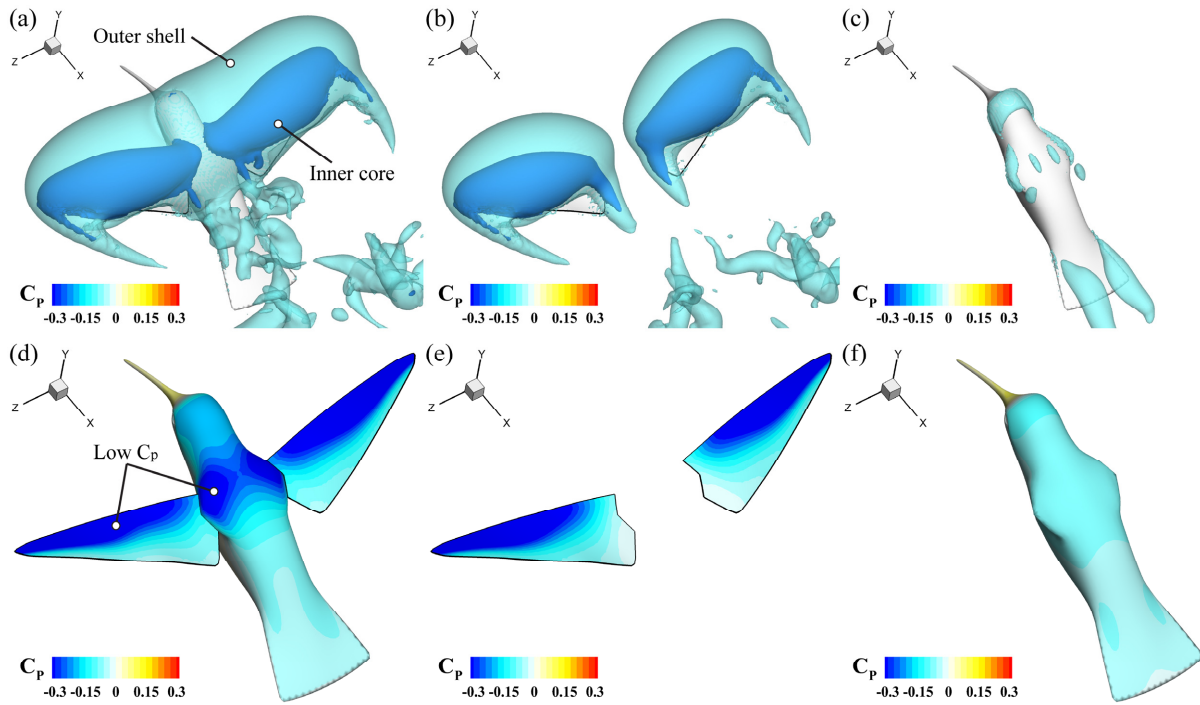


Figure 3-9: Comparisons of pressure isosurface (a)–(c) and model surface pressure distribution (d)–(f), respectively, between the WB, WO, and BO models at $t/T = 0.27$. In (a)–(c), the transparent outer shell is visualized by $C_p = -0.08$ and the inner core by $C_p = -0.25$. The pressure isosurfaces are flooded by C_p .

Figure 3-9(d)–(f) compare surface pressure distribution between the models. Significant low-pressure regions were found on the dorsal surfaces of the body thorax and wings of the WB model, which coincided with the locations of the inner cores of the pressure isosurfaces in Figure 3-9(a) and the LEV and TXV positions in Figure 3-5(d). Comparing WB and BO bodies, the lower

pressure on the dorsal thorax and head explained the significant lift enhancement on the body found in Figure 3-5(b) at $t/T = 0.27$. Comparing Figure 3-5(d) with Figure 3-9(d), it was found the locations of head SL and TXV overlapped with the low-pressure regions on the dorsal head and thorax of the body, indicating the body vortex formations due to WBI was the direct cause of the low surface pressure regions formed on the body and the fundamental reason for the body lift enhancement.

Figure 3-10 shows the analysis of the wing surface pressure at mid-downstroke ($t/T = 0.27$). The instantaneous local pressure coefficient difference (ΔC_p) between the ventral and dorsal surfaces of the left wing was calculated for the WB and WO models, as shown in Figure 3-10(a) and (b), respectively. Positive ΔC_p was found over the whole wing surface for both models, indicating lift production. High ΔC_p was concentrated at the leading edge, especially at the distal side, which was consistent with the larger LEV strength at the distal wing in Figure 3-8(c). Comparing the WB and WO models, lower ΔC_p was found at the root part of the WO wing. The chord-averaged ΔC_p was calculated for WB and WO models to illustrate the ΔC_p change along the wing length, as shown in Figure 3-10(d) and (e). The lower chord-averaged ΔC_p near the wing root region of WO ($z/L = 0\sim 0.4$) reaffirmed the lower ΔC_p observed at this region by the ΔC_p contour. The lift enhancement was represented by the difference in ΔC_p between the WB and WO models ($\Delta C_p|_{WB} - \Delta C_p|_{WO}$), as shown in Figure 3-10(c). It was found the lift enhancement concentrated in the region near the wing root. The local chord-averaged lift enhancement showed a dramatic increase towards the wing root in Figure 3-10(f). As a result, the cumulative data showed that over 80% of the lift enhancement laid within 40% of the wing length from the wing root ($z/L = 0\sim 0.4$), with the maximum lift enhancement located at $z/L = 0.15$.

The region of the wing lift enhancement found in Figure 3-10(c) coincided with the location of the strengthened LEV in Figure 3-8(a). In addition, the lift enhancement distribution along the wing length was consistent with the increased LEV circulation in Figure 3-8(c). The consistent results indicated that the strengthened LEV was the fundamental cause of the lift enhancement on the wings, which contributed to the majority 55% of the OLE due to WBI.

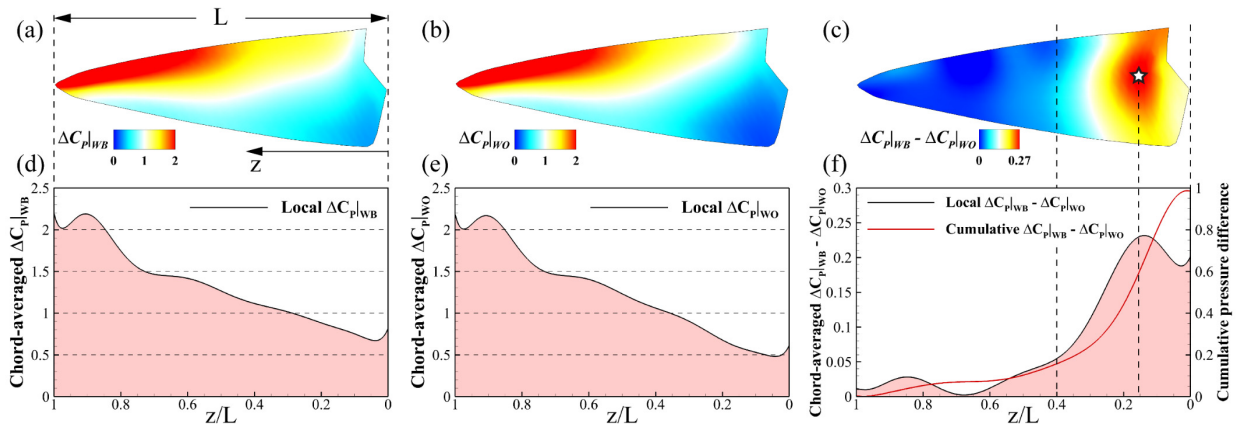


Figure 3-10: Comparison of the pressure difference contour (ΔC_P) on the left wing between the WB (a) and the WO (b) model at $t/T = 0.27$. The lift enhancement distribution ($\Delta C_P|_{WB} - \Delta C_P|_{WO}$) on the left wing is shown in (c). The star shape in (c) denotes the location of maximum lift enhancement. The corresponding local chord averaged ΔC_P and $\Delta C_P|_{WB} - \Delta C_P|_{WO}$ are shown in (d)–(e), respectively. The cumulative $\Delta C_P|_{WB} - \Delta C_P|_{WO}$ from the wing tip to the wing root is shown in (e) with a red line.

3.4.4 Effects of Body Angle on WBI

Figure 3-11(a) shows the changes in cycle-averaged lift coefficients with body angle. It was found all lift coefficients increased monotonically as the body angle increased. Significant

enhancement in the lift was found on both the wing pair and body at different body angles, resulting in enhanced overall lift coefficients. In Figure 3-11(b), OLE decreased from 40% to about 25% as the body angle increased from 20° to 50°, while the contributes of OLE from the body increased from about 38% to 50%.

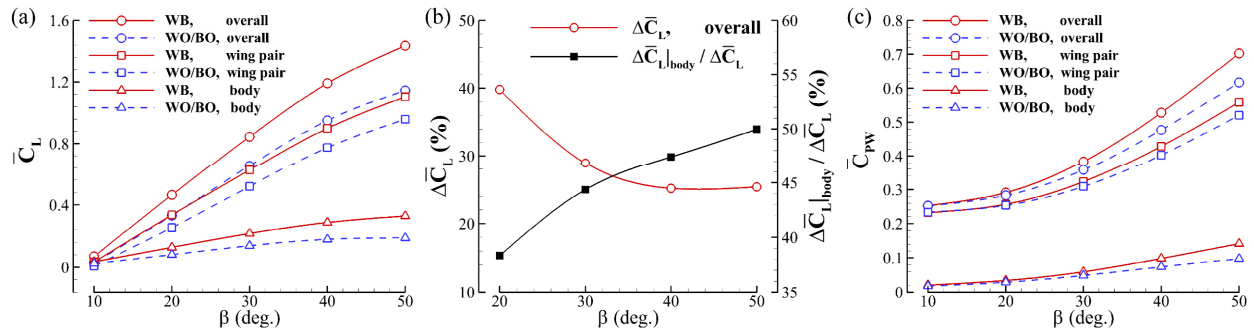


Figure 3-11: (a) Comparison of cycle-averaged lift coefficients, \bar{C}_L , at various body angles, β , between the WB, WO, and BO models at $J = 0.464$. OLE ($\Delta \bar{C}_L$). The percentage of OLE attributed to the body ($\Delta \bar{C}_L|_{\text{body}} / \Delta \bar{C}_L$) are shown in (b). (c) Comparison of cycle-averaged coefficient of power output, \bar{C}_{PW} , at various body angles.

Figure 3-11(c) shows the changes in the cycle-averaged coefficient of power output with body angle. The power output is the rate of the output work done by the hummingbird model. It has the form $\oint (\bar{\boldsymbol{\sigma}} \cdot \mathbf{n}) \cdot \mathbf{V} ds$, where \oint denotes the integration over the surface, $\bar{\boldsymbol{\sigma}}$ and \mathbf{V} are the stress tensor and the velocity vector of the fluids adjacent to the model surface, respectively, and \mathbf{n} is the normal vector of surface. The coefficient of power output (C_{PW}) is defined as, $C_{PW} = \oint (\bar{\boldsymbol{\sigma}} \cdot \mathbf{n}) \cdot \mathbf{V} ds / 0.5\rho U_{tip}^3 A$, where U_{tip} is the tip velocity and A is the area of a single wing. It was found all \bar{C}_{PW} increased monotonically with an increasing body angle. Little \bar{C}_{PW} difference

between the WB model and the WO/BO models ($\bar{C}_{PW}|_{WB} - \bar{C}_{PW}|_{WO/BO}$) were found at 10° and 20° body angles. All \bar{C}_{PW} differences then increased with body angle monotonically, resulting in a 14% overall \bar{C}_{PW} difference at body angle 50° . The increasing power output may reflect the increasing energy consumption of the hummingbird flying with an increasing body angle during forward flight.

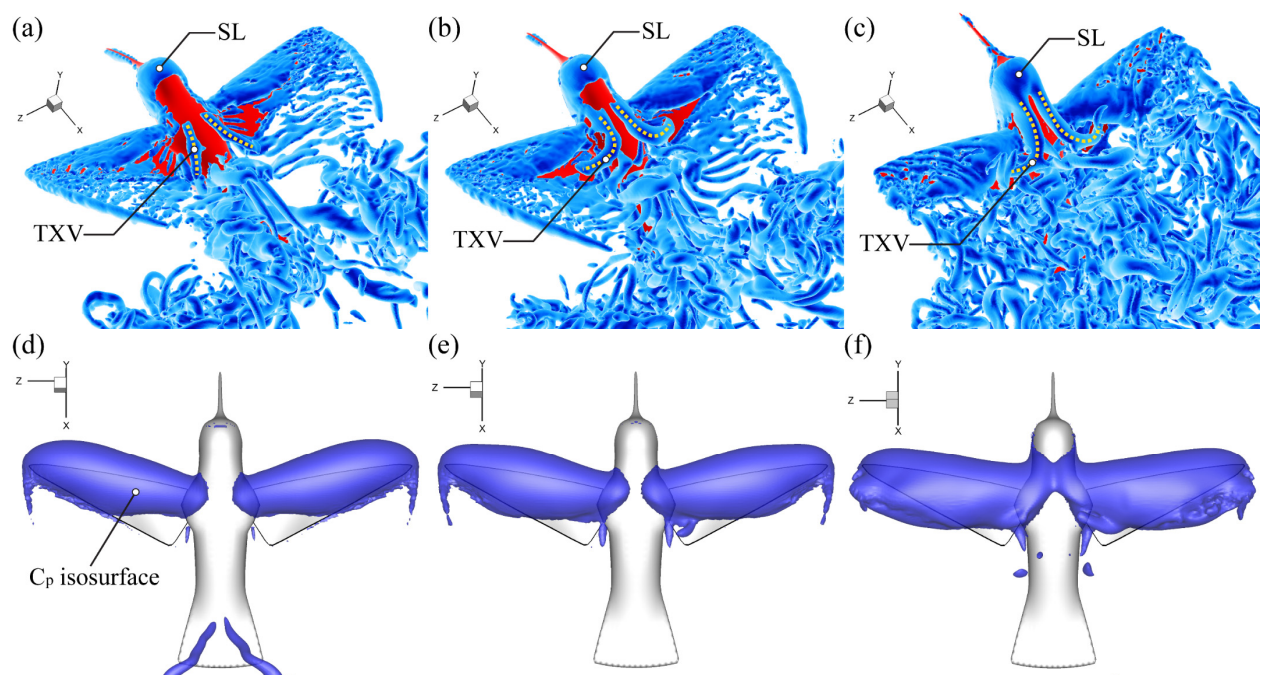


Figure 3-12: Comparisons of three-dimensional wake structure (a)–(c) and pressure coefficient isosurface (d)–(f) of the WB model, respectively, at $t/T = 0.27$ between body angle, $\beta = 20^\circ$ (a) and (d), $\beta = 30^\circ$ (b) and (e), and $\beta = 50^\circ$ (c) and (f). The shear layer (SL) and the thorax vortex (TXV) are identified in (a)–(c).

Figure 3-12(a)–(c) show the Q-isosurface of the WB model at mid-downstroke ($t/T = 0.27$) for $\beta = 20^\circ$, 30° , and 50° , respectively. Clear TXV pair was observed at all three body angles. However, significant differences in the shape and strength of TXV pair were found. The TXV tubes at $\beta = 20^\circ$ were thinner than those at higher body angles and did not exhibit the L-shape shown in Figure 3-12(b) and (c). The TXV pair at $\beta = 50^\circ$ was the strongest by connecting to the head SL and fed by it, which did not happen at $\beta = 20^\circ$ or 30° . Figure 3-12(d)–(f) show the pressure isosurface ($C_p = -0.25$) corresponding to the flow fields in Figure 3-12(a)–(c). It was found the low-pressure regions on two wings expanded towards the body median plane as the body angle increased. They finally merged at $\beta = 50^\circ$. The increasing low-pressure regions on the body reaffirmed the increasing lift enhancement contribution by the body in Figure 3-11(b).

3.4.5 Effect of Advance Ratio on WBI

Figure 3-13(a) illustrates the changes in cycle-averaged lift coefficients with advance ratio. The advance ratio, J ($J = U_f/U_{tip}$), denotes the ratio between the forward flight speed U_f and the average wing tip speed U_{tip} . For a flapping flyer in forward flight, the aerodynamics is not only governed by the unsteady effect of the wing flapping but also affected by the advection effect induced by the forward flight speed. Because the advance ratio reflects the intensity ratio between the advection effect and the unsteady effect, it serves as an important nondimensional parameter of flapping-wing flyers in forward flight from an aerodynamic perspective. In the present parametric study, the advance ratio was varied by changing the flapping frequency. As a result, the Reynolds number based on the incoming flow speed U_f was maintained the same at different advance ratios. In general, it was found the wing pair lift decreased and the body lift increased

with increasing advance ratio. Lift enhancement was found on both the wing pair and the body. In Figure 3-13(b), high OLE ($\Delta\bar{C}_L > 27\%$) was found over the range of advance ratio studied. In addition, a peak OLE value of 32% was found at $J = 0.371$. Note that peak OLE values were also found in the previous fruit fly study [45] when the advance ratio changes and in the previous cicada study [7] when changing reduced frequency. We hypothesize that there may exist an optimal advance ratio when the unsteady flow induced by the flapping-wing system is best exploited by the flow advection introduced by the forward speed so that the OLE can be maximized. The previous studies of fruit fly [45] and cicada [7] partially supported this hypothesis in a way that increasing OLE was observed with increasing advance ratio before the OLE peak was reached, which indicated that the exploit of unsteady flow by the increasing advection could contribute to OLE. However, this hypothesis requires further studies to prove. Besides, the wing pair was found to play a major role in the lift enhancement by contributing more than half of the OLE over the J range studied. The $\Delta\bar{C}_L|_{\text{wing pair}}/\Delta\bar{C}_L$ ratio, in general, increased as the advance ratio increased and reached up to 58% at $J = 0.928$.

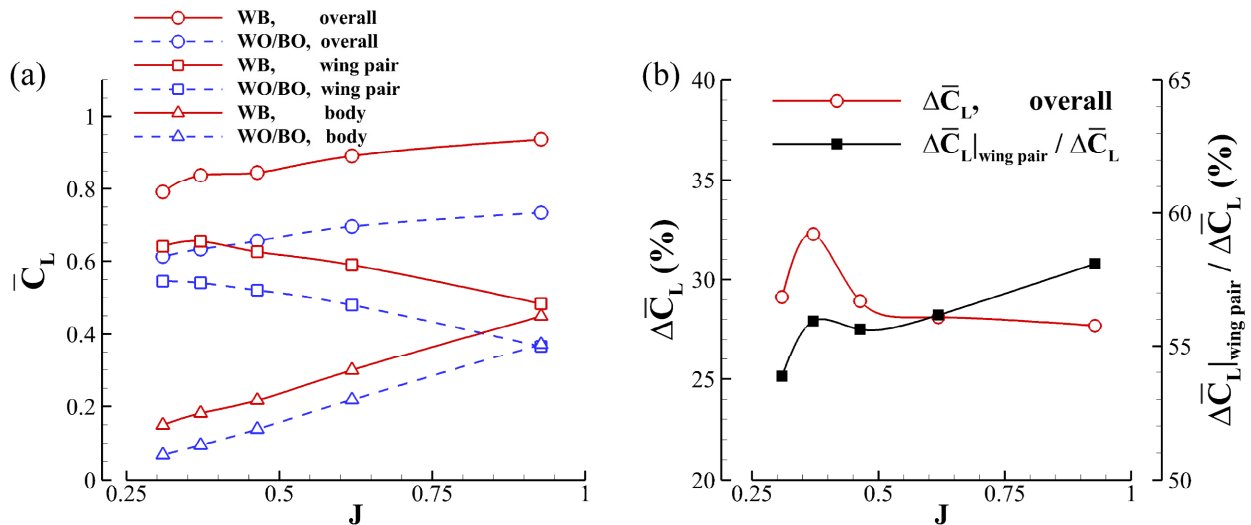


Figure 3-13: (a) Comparison of cycle-averaged lift coefficients, \bar{C}_L , at various advance ratios, J , between the WB, WO, and BO models at $\beta = 30^\circ$. OLE ($\Delta\bar{C}_L$) and the percentage of OLE attributed to the wing pair ($\Delta\bar{C}_L|_{\text{wing pair}}/\Delta\bar{C}_L$) are shown in (b).

Figure 3-14(a) and (b) compare the spanwise vorticity (ω_z) contour at mid-downstroke ($t/T = 0.27$) between $J = 0.317$ and 0.619 associated with Q -isosurfaces. It was found both the LEV and the L-shape TXV had a more elongated shape at a higher advance ratio, likely caused by the stronger advection introduced by the incoming flow. The LEV shape on Slice 2 was compared in Figure 3-14(c) and (d). It was found the LEV core of $J = 0.317$ only covered half of the wing chord from the leading edge, while the LEV core of $J = 0.619$ was obviously stretched, and covered the entire wing chord. In addition, the LEV was more lifted at higher J . The stretched and lifted up LEV was also observed at higher J in the forward flight of an insect-like flapping wing [90]. Likely because of the suppression effect of the stronger advection at higher J , the LEV size at the leading edge was smaller at higher J than at lower J , which was also observed in the previous experimental results [90].

The changes in LEV and TXV further caused the lift enhancement distributions ($\Delta C_P|_{WB} - \Delta C_P|_{WO}$) on the wing to change, as compared in Figure 3-14(e) and (f). The spanwise distributions of lift enhancement were similar between the two advance ratios, in which major enhancement was located within $0.4L$ from the wing root. In contrast, chordwise distributions were significantly different. The high lift enhancement region (in red) shifted downstream when the advance ratio increased. The larger area of the lift enhancement region at higher J was consistent with the higher OLE contribution from the wing pair at higher J , as shown in Figure 3-13(b). A strong correlation

was found between the location of the high enhancement region on the wing and the enhanced LEV location at both advance ratios, reaffirming that the fundamental cause of the wing lift enhancement was the reinforced LEV.

The change in advection effect with advance ratio shown in Figure 3-14 also partially supported our hypothesis on the optimal OLE point because the pattern of WBI has been substantially changed by advection at different advance ratios. A more systematic study on the OLE peak phenomenon will be conducted in the future.

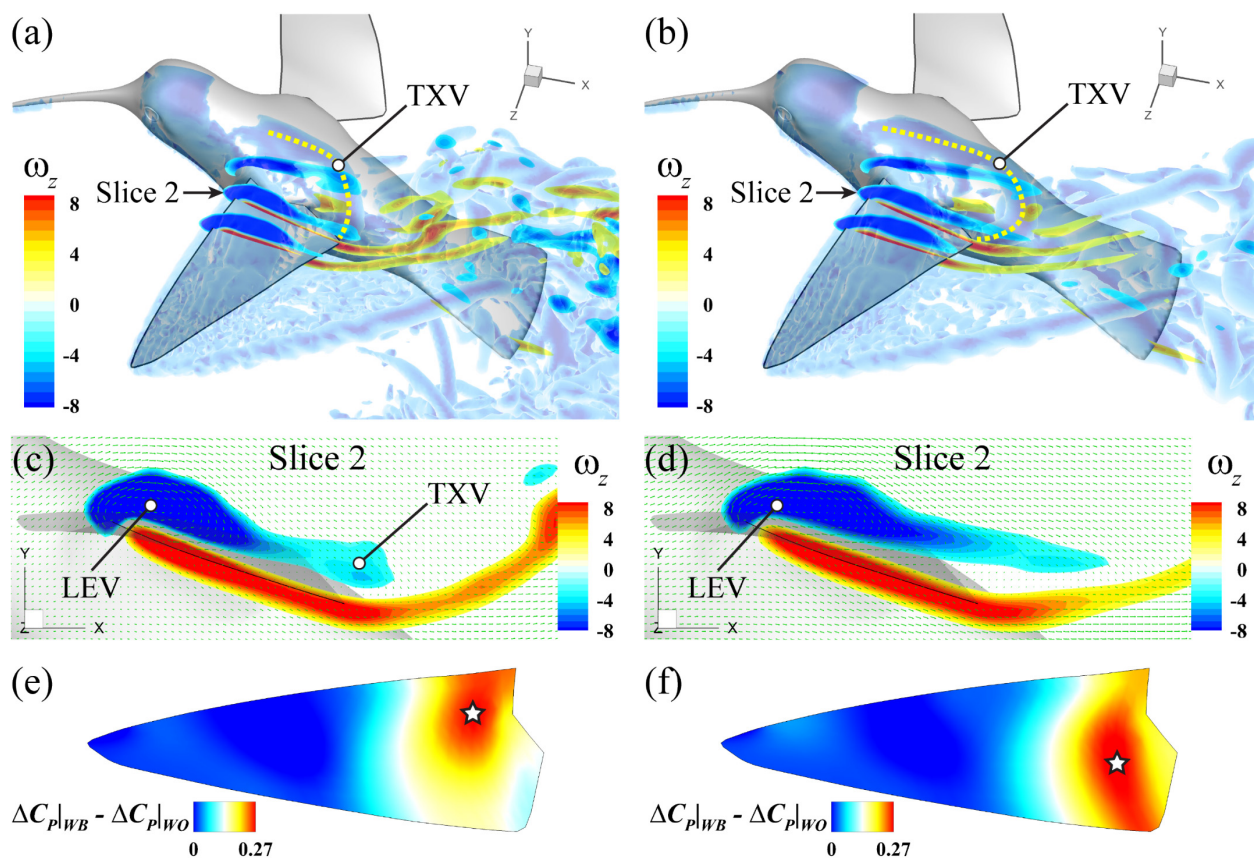


Figure 3-14: Comparisons of vortex structure (a) and (b), 2-D spanwise vorticity on slice-cut (c) and (d), and lift enhancement distribution contour on the left wing (e) and (f) of the WB model at $t/T = 0.27$ between $J = 0.317$ (a), (c), and (e) and $J = 0.619$ (b), (d), and (f), respectively. The Q -

isosurface in (a,b) is visualized by $Q = 60$. The yellow dashed lines indicate the vortex core locations of the thorax vortex. ω_z is normalized by U_f/c . The star shapes in (e) and (f) denote the locations of maximum lift enhancement.

3.4.6 Effect of Tail Shape on WBI

In nature, the tail geometry of a flying bird usually varies with its flight style [92]. For instance, the bird will fully spread its tail during hovering and maneuvering, while decreases its tail span in forward flight with increasing flight speed. It is worth noting that tail vortices caused by the spreading tail geometry were observed in Figure 3-7(c) and Figure 3-9(c). To understand the effect of tail geometry on WBI, we have performed a parametric study by changing the tail span s_T , as shown in Figure 3-15(a)–(c). Here, we introduce a new parameter, tail span ratio R_S , which defines the ratio between the tail span s_T and the body width at tail root s_B as $R_S = s_T/s_B$. The body in Figure 3-15(a) corresponds to the body used in the present hummingbird model which has $R_S = 1.69$. Decreased tail spans were modeled in Figure 3-15(b) and Figure 3-15(c) with tail span ratios of 1.0 and 0.64, respectively.

Figure 3-15 shows the changes in cycle-averaged lift coefficients with tail span ratio. As expected, the body lift of BO and WB models both increased with tail span ratio. But wing pair lift change was not significant (less than 1%), and the overall lift change was also small (around 5%). Most importantly, since the tail is located downstream of the wings and body thorax where WBI mainly happens, the effect of tail span change on WBI in the upstream is minimal under the advection effect induced by the incoming flow velocity U_f . Table 3-5 lists the changes in net lift enhancement ($\bar{C}_L|_{WB} - \bar{C}_L|_{WO/BO}$) on the body, wing pair, and the entire model (overall) when the

tail span ratio increased from 0.64 to 1.69. Small net lift enhancement changes with tail span ratio were found. The change in overall net lift enhancement was less than 0.008, corresponding to an OLE ($\Delta\bar{C}_L$) change less than 1.2%.

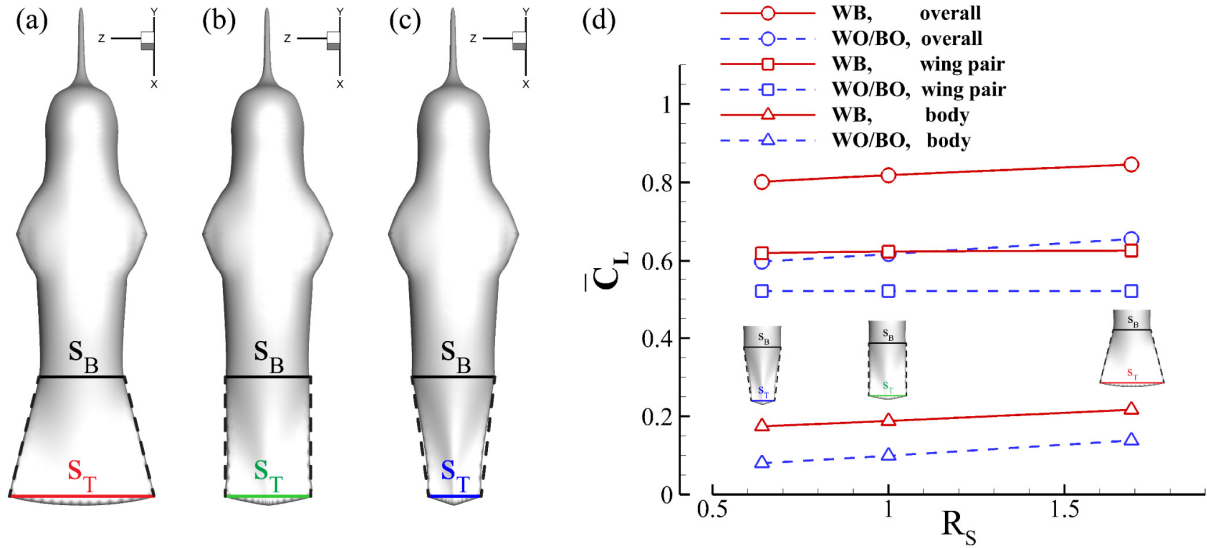


Figure 3-15: (a)–(c) Comparison of hummingbird body at three tail spans. The tail span ratios R_S in (a), (b), and (c) are 1.69, 1.00, and 0.64, respectively. (d) Comparison of cycle-averaged lift coefficients, \bar{C}_L , at various tail span ratios between the WB, WO, and BO models at $\beta = 30^\circ$ and $J = 0.464$.

The small effect of tail span change on WBI was further confirmed by the comparison of pressure iso-surfaces of the WB models at the three tail span ratios in Figure 3-16. The difference in the pressure field was not significant on wings and thorax.

Table 3-5: Net lift enhancement ($\bar{C}_L|_{WB} - \bar{C}_L|_{WO/BO}$) change at various tail span ratios.

Tail span ratio (R_S)	Body	Wing pair	Overall
0.64	0.101	0.097	0.198
1.00	0.095	0.101	0.196
1.69	0.085	0.105	0.190

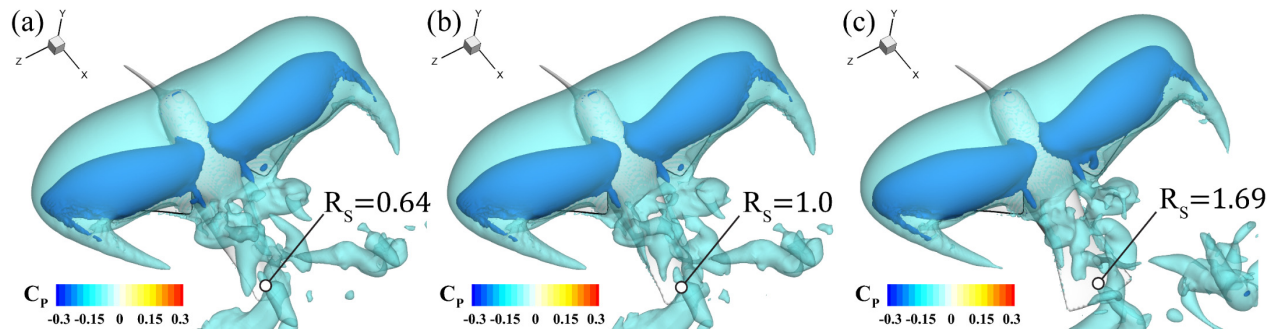


Figure 3-16: Comparisons of pressure isosurface of WB model at $\beta = 30^\circ$, $J = 0.464$, and $t/T = 0.27$ between different tail span ratios at (a) $R_S = 0.64$, (b) $R_S = 1.00$, and (c) $R_S = 1.69$. the transparent outer shell is visualized by $C_p = -0.08$ and the inner core by $C_p = -0.25$. The pressure isosurfaces are flooded by C_p .

3.5 Chapter Summaries

In this section, the lift enhancement mechanism due to WBI has been numerically investigated in hummingbird's forward flight. High-fidelity simulations using an immersed-boundary based flow solver have been conducted on the hummingbird's WB, WO, and BO models to examine unique features in the aerodynamic performance and vortex dynamics of WBI.

Results have shown a 29% overall lift enhancement (OLE) due to WBI, among which the majority 55% of OLE was attributed to the wing pair and 45% to the body. This OLE was higher than those of the insects previously studied in forward flight, as listed in Table 3-6. It is worth noting that the hummingbird also had the highest advance ratio and $A_{0.3L}/A$ ratio of the wing among the studies.

Table 3-6: Summary of lift enhancement due to WBI on insects and birds.

Flapping wing flyers	Flight mode	J	$A_{0.3L}/A$	β	Lift enhancement			Study
					Body	Wing pair	Total	
Hummingbird	Forward flight	0.46	38%	30°	12.8%	16.2%	29.0%	Current
Hummingbird	Forward flight	1.02	N/A	N/A	13.8%	N/A	N/A	Song et al. (2016) [47]
Hummingbird	Forward flight	1.12±0.03	N/A	11°±6°	N/A	N/A	N/A	Tobalske et al. (2007) [49]
Cicada	Forward flight	0.32	35.3%	27°	12.0%	6.7%	18.7%	Liu et al. (2016) [7]
Fruit fly	Forward flight	0.22	21.2%	28.3°	3.0%	4.2%	7.2%	Liang & Sun (2013) [45]
Fruit fly	Forward flight	0.09	21.2%	60°	0.7%	1%	1.7%	Liang & Sun (2011) [93]
Fruit fly	Hover	0	23%±2%	45°	N/A	N/A	2%	Aono et al. (2008) [35]

Parametric studies showed significant lift enhancement at wide ranges of body angle ($10^{\circ}\sim 50^{\circ}$) and advance ratio (0.309~0.982), respectively. In general, the contribution of OLE from the hummingbird body increased with increasing body angle, and the wing pair's contribution increased as the advance ratio increased. Within the tested range of these governing parameters, the OLE presented at least 25% for all cases. The peak OLE value can reach up to 32% when changing the advance ratio. These observations highlight the importance as well as the ubiquity of WBI in hummingbird forward flight.

Vortex dynamics analyses showed the formation and development of major vortex structures associated with the unsteady flapping flight in the WB model, including head SL, body TXVs and nTXVs, and wing LEVs. Significant interactions between the TXVs and LEVs were observed, resulting in strengthened LEVs near the wing root during the downstroke. Further analyses on surface pressure revealed stronger low-pressure regions created by the TXVs and strengthened LEVs, respectively, above the hummingbird body and wings of the WB model than those of WO and BO models, which were the fundamental reason for the enhanced lift production in the WB model. Results from this study supported that lift enhancement due to WBI is potentially a general mechanism adopted by flapping wing flyers, including insects and birds. Further investigations of WBI on different types of flapping wing platforms, such as bats, and different types of flight modes, such as takeoff and landing flight, are expected to extend the understanding of WBI and to inspire the design of flapping wing MAV that pursue higher performance.

4 In-Line Propulsion: A Computational Hydrodynamic Analysis of Finlet Function

Finlets are a series of small non-retractable fins common to scombrid fishes (mackerels, bonitos, and tunas) which are known for their high swimming speed. It is hypothesized these small fins could potentially affect propulsive performance. Here we combine experimental and computational approaches to investigate the hydrodynamics of finlets in yellowfin tuna (*Thunnus albacares*) during steady swimming.

A key general goal of this section is to study the flow past scombrid fish finlets with biologically realistic geometric and kinematic complexity. In this work, we have conducted a combined experimental and numerical study on the hydrodynamics of tuna finlets during forward swimming. High-speed videos of the motion of finlets in freely-swimming yellowfin tuna (*Thunnus albacares*) were obtained to provide kinematic data on the *in vivo* motion of finlets. A biologically realistic model of finlets was reconstructed based on measurements of finlets in yellowfin tuna specimens and kinematics of live fish during free, forward swimming. Simulations of the flow past the model finlets were then conducted using a high-fidelity flow solver. By providing detailed flow field information and hydrodynamic performance data, we aim to extend previous experimental and computational research and fill the gap between numerical studies using simplified finlet models [66-68] and previous experimental work [56, 58]. Moreover, we are able to compute the effect of finlet-finlet interaction and the effect of pitching kinematics on the wake structure and hydrodynamic performance of finlets and compare the function of individual finlets with an assembled collective array of finlets present in tuna.

4.1 Tuna Kinematics and Finlet Morphology

Swimming kinematics of yellowfin tuna (*Thunnus albacares*) were obtained at the Greenfins tuna facility (Narragansett, Rhode Island, USA) where tuna averaging 1 meter in fork-length swim freely at approximately 1 body length per second (~ 1.0 - 1.2 m/s) in a 12.2 m diameter tank containing 473,000 liters of salt water [65]. This tank is approximately 3 m deep and thus tuna are effectively unconstrained in their locomotion and free to change direction and maneuver (Figure 4-1a). Video sequences were obtained with both a Photron Fastcam[®] high-speed camera (250 to 500 fps, at 1024×1024 pixel resolution, Photron USA, Inc.) and a GoPro[®] camera (GoPro, Inc) mounted above the tank, and another GoPro[®] camera against the tank wall. Videos provided both an overview of body and tail kinematics, and a dorsal view of the dorsal finlets located between the second dorsal fin and the tail. Yellowfin tuna have nine dorsal (A to I, Figure 4-1a) and nine ventral finlets in the caudal peduncle region [94] (Figure 4-1b), but detailed kinematics of the first two and last two were difficult to visualize in freely swimming tuna. Thus, we focus here on finlets three to seven which we label C to G (Figure 4-1a). Previous research has documented that finlets can be activated by up to three pairs of specialized muscles on each side which allow scombrid fishes to actively move finlets [56, 57] (Figure 4-1c), and active motion does not always result in symmetrical side-to-side finlet amplitude. We frequently observed finlet oscillatory motion with slight right-left asymmetry, and tuna are able to actively move finlets to one side of the body during maneuvers [65] (not studied here). For the purposes of this computational investigation, we used kinematics from the dorsal finlets only to study their effect on locomotor dynamics.

Anatomical studies of tuna finlets were undertaken to confirm muscular attachments indicated in previous research on mackerel [56] and to quantify the shape of yellowfin tuna finlets. We used photography to document finlet shape and surface area (Figure 4-1d,e), and micro-CT

scans of finlet internal skeletal and muscular anatomy [65]. Figure 4-1f shows the shape of a tuna finlet overlapped by the computational finlet model used in this study. Here, s denotes the span length of the finlet. The chord length c is defined at midspan. c_{max} denotes the longest chord measured at finlet root. c was chosen as the reference length for the hydrodynamic analysis later in this study.

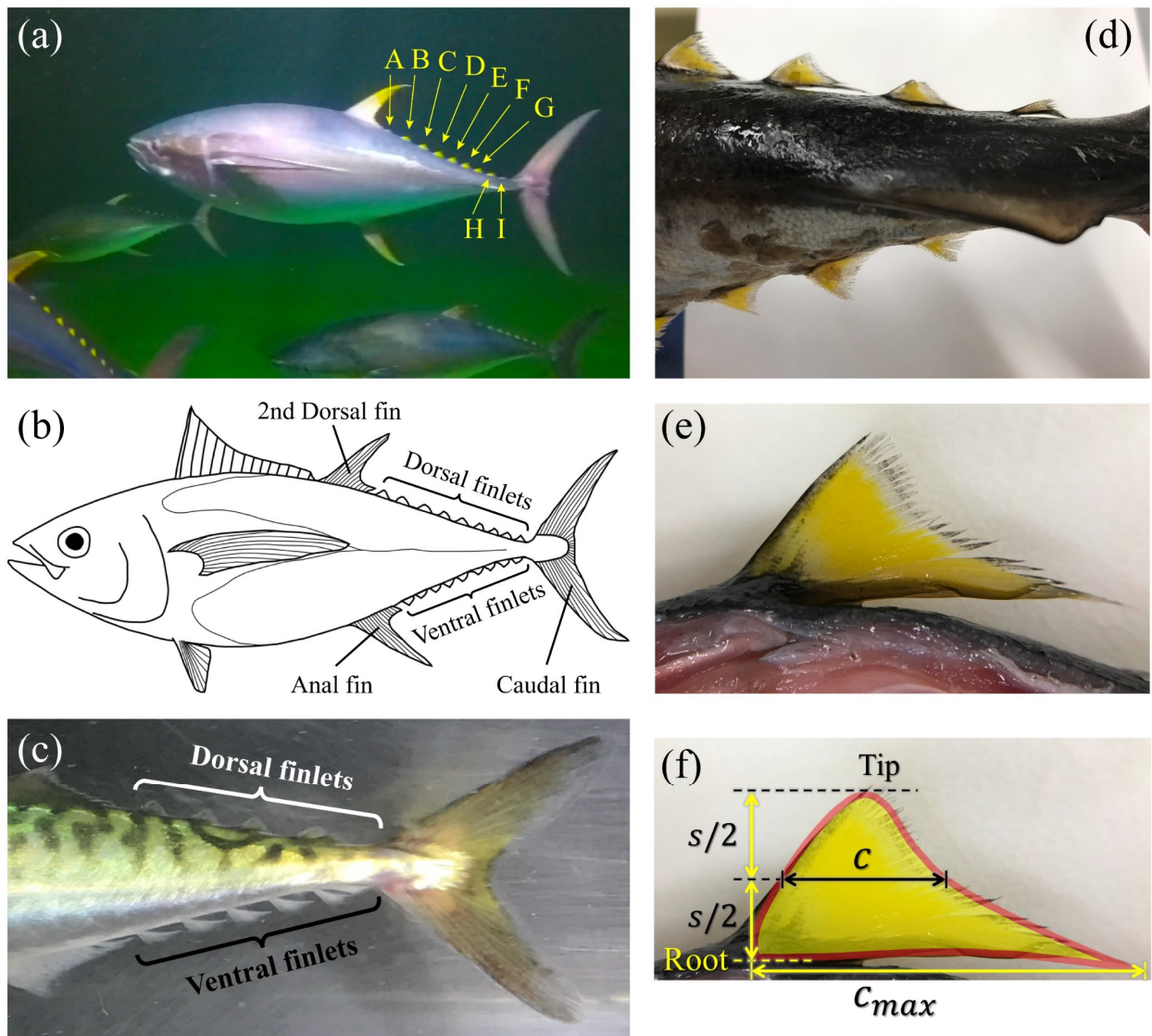


Figure 4-1: (a) Live yellowfin tuna (*Thunnus albacares*) swimming (with nine finlets indicated by letters A to I). (b) Illustration of the dorsal and ventral finlets of a yellowfin tuna. (c) Dorsal and ventral finlets of a mackerel during free swimming. (d) Caudal peduncle region of a yellowfin tuna with finlets. (e) A single tuna finlet to show the attached base and free posterior region. (f) Tuna finlet overlapped by the computational finlet model (red outline).

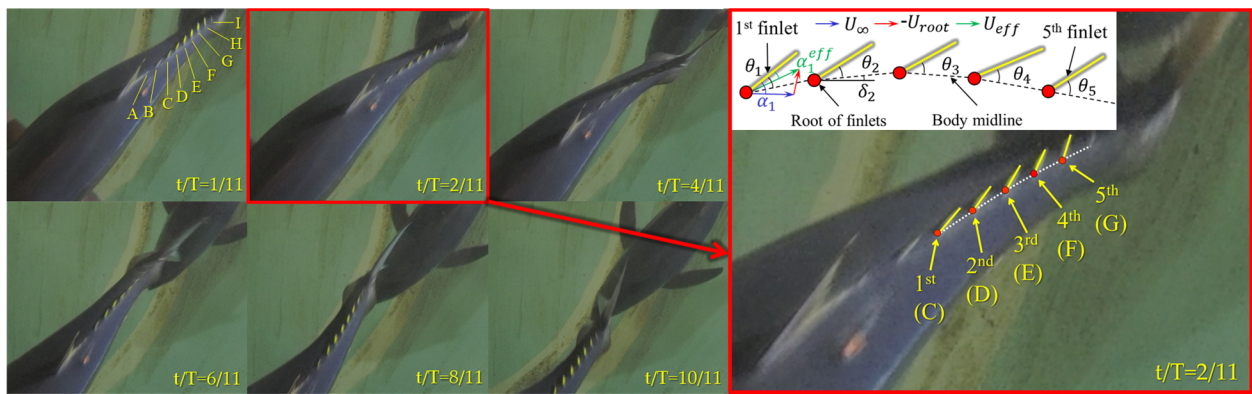


Figure 4-2: Top-view snapshots of a yellowfin tuna (*Thunnus albacares*) in forward swimming during one tail beat cycle. Nine finlets (A to I) are labeled in the upper left panel, but only the function of five (C to G) were analyzed in detail here. Body midline angle (δ) defines the angle between the body midline and the body sagittal plane. The geometric angle of attack (α) is the angle between the finlet and the body sagittal plane. Finlet angle (θ), effective angle of attack (α_{eff}), effective velocity (U_{eff}), swimming velocity (U_{∞}), and the instantaneous root velocity of the finlet (U_{root}) are also shown.

We captured 17 top-view videos of tuna bodies during forward swimming, among which significant finlet kinematics were observed in 12 videos. Figure 4-2 presents sample image

sequences during a complete tail beat cycle (T) of one individual tuna in free forward swimming with an approximately constant speed U_∞ at 28.4 chord length per tail beat cycle (c/T). Nine finlets, from A to I, are labeled. Significant changes in finlet orientations with respect to the body midline were observed during swimming. Among the nine total finlets present, we were able to reconstruct the kinematics of five consecutive finlets beginning with finlet C with the greatest accuracy, and hence focus on these five which we label C to G, as shown in frame $t/T=2/11$. The five finlets are highlighted in yellow and assigned with numeric indices from the first (1st) to the fifth (5th). Finlet roots are highlighted with red dots. Body midline is shown as white dashed line segments that each connect the roots of two consecutive finlets. Finlet angle θ defines the pitching motion of the finlet with respect to the body midline. The effective flow velocity U_{eff} at a finlet root was estimated as the superposition of swimming velocity U_∞ and root velocity U_{root} . The effective angle of attack α_{eff} was defined as the angle between the effective velocity U_{eff} and finlet orientation, which serves as an important indicator of the hydrodynamic performance of finlets.

Table 4-1: Summary of key parameters of tuna steady swimming and finlet kinematics

	Fork-length, L_B (m)	Swimming speed, U_∞ (m/s)	Tail beat frequency, f (Hz)	Normalized speed, U_∞/fL_B	Peak-to-peak pitching amplitude, H_θ (deg.)				
					1 st finlet	2 nd finlet	3 rd finlet	4 th finlet	5 th finlet
Observed range	0.8~ 1.2	1.0~1.2	2.3~3.4	0.25~0.46	20~ 35	40~ 55	45~ 60	70~ 90	80~ 120
Present kinematics	1.0	1.0	2.8	0.36	28	52	54	81	109

From the 17 top-view videos, we obtained the ranges of the key parameters of tuna steady swimming and finlet kinematics, including the tuna fork-length L_B , swimming speed U_∞ , tail beat frequency f , normalized speed U_∞/fL_B , and peak-to-peak pitching amplitude H_θ of five finlets (Table 4-1). We found that the parameter values from the video chosen for reconstructing finlet kinematics fall well within the range of experimental observations.

In this section, an image-guided reconstruction method [79] was adopted to reconstruct the finlet kinematics of the yellowfin tuna in Autodesk Maya[®] (Autodesk, Inc.). This method has been successfully adopted to reconstruct manta ray [80] and fish [9] swimming (see our previous work [9] for more details). The geometric shape shown in Figure 4-1*f* was scaled to match the actual sizes of tuna finlets in video during reconstruction.

The reconstructed finlet model and associated kinematics quantifications are presented in Figure 4-3. Finlets motion during the left-to-right (L-to-R) stroke and right-to-left (R-to-L) stroke, respectively, are shown every $T/24$ (Figure 4-3a) associated with the side view of finlet model and the top view of finlet kinematics in a local coordinate system O-XYZ (Figure 4-3b). The figure-eight shapes denote the root trajectories of finlets. The arrows represent the longest chords of finlets. Noticeable asymmetry in finlet angles was observed between the L-to-R and the R-to-L strokes, and this was commonly observed during finlet motion in swimming tuna. The normalized geometric quantities of the finlet model are marked in Figure 4-3*b* and listed in Table 4-2. Here, A denotes the peak-to-peak amplitude of the finlet root. L denotes the total length of the assembly of finlets when the posterior body is stretched and no finlets kinematics is applied, and L is 10.1*c*. All lengths are normalized by the chord length c of the 1st finlet, and the finlet area S is normalized by c^2 .

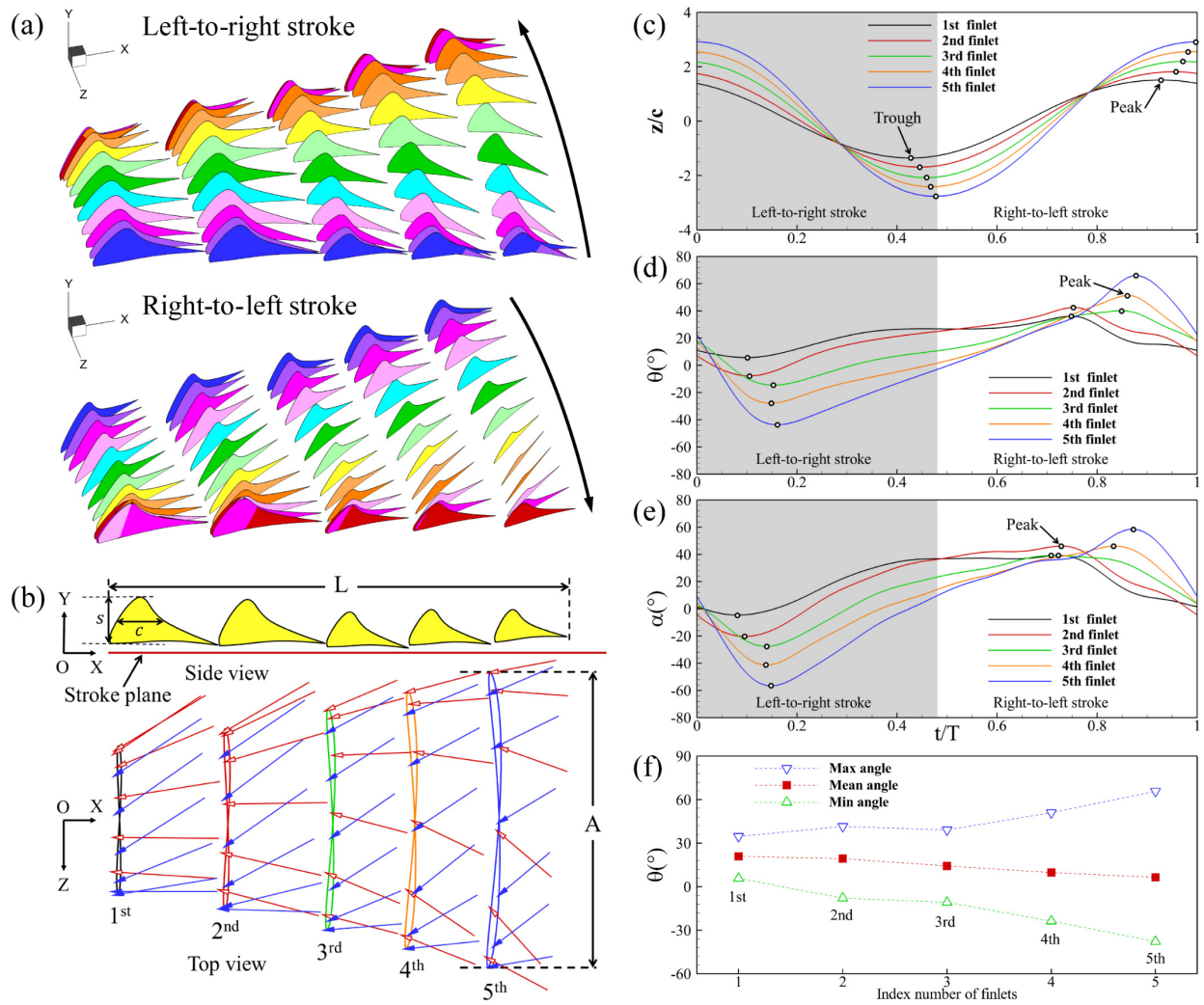


Figure 4-3: Reconstructed finlet motion during the left-to-right stroke and the right-to-left stroke, respectively, from a perspective view (a) and top view (b). In (a), A change in finlets color corresponds to a change in time of $T/24$. The instantaneous lateral root displacement (z/c), finlet angle (θ), and geometric angle of attack (α) of the five finlets during one tail beat cycle are plotted in (c–e), respectively. The maximum, minimum, and mean values of each finlet angle are shown in (f).

It was found the peak-to-peak values of the normalized instantaneous lateral root displacement (z/c), finlet angle (θ), and geometric angle of attack (α) all increased posteriorly from the 1st finlet to the 5th finlet (Figure 4-3c–e). The phase difference in the peaks of z/c , θ , and α , in general, increased posteriorly. Through the maximum, minimum, and mean values of finlet angle in Figure 4-3f, we found the asymmetry in θ alleviated posteriorly with mean angle decreased from 20.9° at the 1st finlet to 6.4° at the 5th finlet. An analytical representation of finlet model kinematics is provided in the supplementary material.

Table 4-2: Normalized geometric quantities of reconstructed finlet model.

Reconstructed model	Chord length, c	Max chord length, c_{max}	Span length, s	Finlet area, S	Root amplitude, A
1 st finlet	1.00	2.31	1.01	1.02	2.86
2 nd finlet	0.98	2.26	0.99	0.97	3.50
3 rd finlet	0.76	1.75	0.77	0.59	4.28
4 th finlet	0.75	1.73	0.76	0.57	4.97
5 th finlet	0.67	1.54	0.67	0.45	5.85

4.2 Computational Setup

A Cartesian computational grid with stretching grid configuration was employed in the simulations (Figure 4-4a). The computational domain size was $40c \times 16c \times 20c$ with total grid points around 9.0 million ($385 \times 81 \times 289$) and a minimum grid spacing at $\Delta_{min} = 0.029c$. The grid was designed to resolve the fluid field in the vicinity of the computational model and its wake with high resolution. The left-hand boundary was set as velocity inlet with constant incoming flow

speed U_∞ . A homogeneous Neumann boundary condition was used for the pressure at all boundaries. A no-slip boundary condition was applied at the model surface. Previous numerical results of tuna [66, 67, 95, 96] and jackfish [9] swimming and recent experimental flow visualization of robotic tuna models [5, 10] both show that the local flow past the posterior bodies of the fishes/model was converging to the posteriorly narrowed bodies. Therefore, the incoming flow U_∞ in this study was set to be parallel to the stroke plane of finlets to mimic the local flow condition of finlets as in tuna swimming. We do not include the effect of the body and caudal fin of tuna in these simulations so that finlet flows can be studied in isolation, although in the supplemental material we provide additional computational results that illustrate the effect of the body on finlet flow, and the effect of finlet flow patterns on the function of the caudal fin. More details on the validation of the uniform incoming flow assumption are provided in the supplementary material.

The size of the computational domain was proven to be sufficiently large to obtain converged results by extensive simulation tests. In addition, a convergence study was performed to demonstrate the grid-independent results. Figure 4-4b shows the comparison of instantaneous drag coefficient of the isolated 1st finlet at four different grid densities. The minimum grid spacings of the coarse, medium, fine, and dense meshes are $0.088c$, $0.044c$, $0.029c$, and $0.016c$, respectively. The drag coefficient converged as the grid spacing decreased. The mean drag difference between the fine and the dense mesh was less than 3.0%.

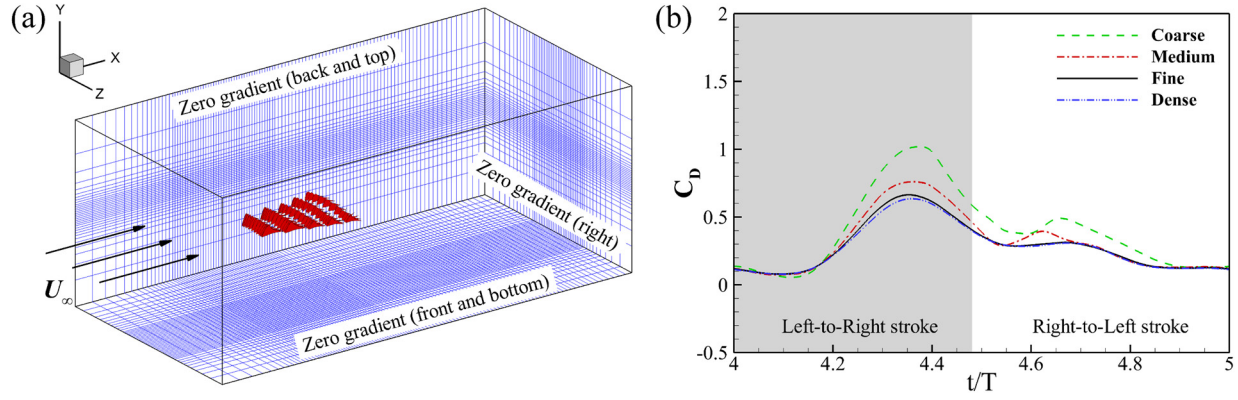


Figure 4-4: (a) Schematic of the computational mesh and boundary conditions used in the present simulation, where U_∞ denotes incoming flow speed. (b) Comparison of instantaneous drag coefficient of the isolated 1st finlet between coarse, medium, fine, and dense mesh. In (a), five finlets are shown at 24 different times throughout the tail beat cycle.

In this study, the key parameters associated with the flow simulation of finlets are the Reynolds number Re and the reduced frequency k defined as follows, respectively,

$$Re = \frac{U_\infty c}{\nu} \qquad k = \frac{fA}{U_\infty} \qquad (4-1)$$

where U_∞ is incoming flow pointing to x-positive, c is the chord length of the 1st finlet, ν denotes the kinematic viscosity, f is the tail beat frequency, and A is the peak-to-peak root amplitude of the 5th finlet.

In this study, the measured k of finlets during living tuna swimming was around 0.206, and the measured Re of the 1st finlet was around 1.0×10^4 . The corresponding Re of the yellowfin tuna was approximately 1.0×10^6 , which is challenging for direct numerical simulations. The purpose of conducting viscous flow simulation is to characterize the fundamental flow features of finlets.

Previous studies have shown that key wake structure features in the propulsion of flapping foils [77] and fish pectoral fin [97] swimming are robust to changing Re . Zhong *et al.* [10] simulated a model fish swimming at $Re=2100$, and the wake patterns obtained from the simulation showed strong similarities with their experimental results using the same model but conducted at Re value 20 to 50 times higher. There are also other precedents in simulating fish swimming [9, 80, 98] that reduce the Re to the order of 10^3 or lower to study the fundamental flow mechanisms at a feasible computational cost. In this study, in order to understand the vortex dynamics, the finlets were simulated at Re in the order of 10^3 to meet both requirements of accuracy and computational cost. Validation study on the Re used for the present simulations is provided in the supplementary material.

In this study, the simulations were conducted at $Re=999.6$ and $k=0.206$. The results presented, including the hydrodynamic performance and wake topology of the reconstructed finlet model, are from the fifth tail beat cycle of the simulations when the flow field has reached a periodic state. The effect of finlet-finlet interaction is investigated by comparing the results of the array of all five finlets with results from a single isolated finlet. In addition, the effect of pitching kinematics of finlets is studied by comparing the results of finlet motion with (w/) and without (w/o) pitching. A list of the computational cases conducted is provided in the supplementary material.

The hydrodynamic force acting on finlets is computed by the direct integration of instantaneous pressure and shear over the finlet surface. The hydrodynamic power output is defined as the rate of instantaneous work done by finlet. The drag (F_x), lateral (F_z) forces, and power output (P_{out}) are nondimensionalized as drag (C_D), lateral (C_Z), and power (C_{PW}) coefficients, respectively, as shown in (4-2).

$$C_D = \frac{F_x}{\frac{1}{2}\rho U_\infty^2 S} \quad C_Z = \frac{F_z}{\frac{1}{2}\rho U_\infty^2 S} \quad C_{PW} = \frac{P_{out}}{\frac{1}{2}\rho U_\infty^3 S} \quad (4-2)$$

where, F_x points to x-positive, F_z points to z-positive, ρ is fluid density, S denotes the area of the 1st finlet, and U_∞ is the incoming flow speed at 28.4 chord length per tail beat cycle.

4.3 Results

We first present the hydrodynamics performance and wake topology of the five reconstructed finlets together in section 3.1. We found all finlets were drag producing. Vortex dynamics analysis revealed a unique vortex matrix consisting of counter-rotating vortex tube pairs. The hydrodynamic effect of finlet-finlet interaction was then studied in section 3.2. It was found the total drag of the finlets array was reduced by 21.5% due to flow interactions between finlets. The effect of pitching kinematics of finlets was studied in section 3.3. Significant mean lateral forces were produced due to finlets pitching, which could help tuna to maneuver by generating yaw torques. Pitching kinematics also helped reduce the total power consumption by 20.8% and generate constructive force to facilitate posterior body flapping. In addition, clear flow channels between pitching finlets were found, which supports several aspects of previous hypotheses on finlet function.

4.3.1 Hydrodynamic Performance and Wake Topology of Finlets

The instantaneous drag and lateral force coefficients of the array of five finlets (Figure 4-5a,b) both show two major peaks associated with the unsteady flapping motions of finlets near

the midstroke of L-to-R and R-to-L strokes, respectively. Forces produced by finlets show a strong correlation with the effective angle of attack α_{eff} (Figure 4-5c). In general, larger α_{eff} corresponds to larger drag and lateral force generations. Due to the asymmetry in finlet angle (θ), both forces show noticeable asymmetric behavior between the two strokes.

We found that all finlets were drag-producing during forward swimming and that no thrust was generated (Figure 4-5a), which is in line with the conclusion of drag-producing mackerel finlets [58]. The 1st finlet (finlet C, Figure 4-2) produced the most drag among all finlets, followed by the 2nd finlet (finlet D). Large positive lateral forces were produced at the 1st and 2nd finlets during L-to-R stroke (Figure 4-5b). More posterior finlets had more symmetric behavior in lateral force between two strokes, which is in line with the behavior of the finlet angle (Figure 4-2d).

The cycle-averaged drag (\bar{C}_D) and lateral force coefficients (\bar{C}_Z) in Table 4-3 shows the 1st finlet produced 39.9% of the total \bar{C}_D and 55.2% of the total \bar{C}_Z . It was found \bar{C}_Z decreased posteriorly, sharing the same trend of mean finlet angle in Figure 4-2f.

Table 4-3: Cycle-averaged drag (\bar{C}_D) and lateral force (\bar{C}_Z) coefficients of finlet.

Index	1 st finlet	2 nd finlet	3 rd finlet	4 th finlet	5 th finlet	Total
\bar{C}_D	0.283	0.164	0.083	0.085	0.095	0.710
\bar{C}_Z	0.535	0.235	0.106	0.080	0.013	0.969

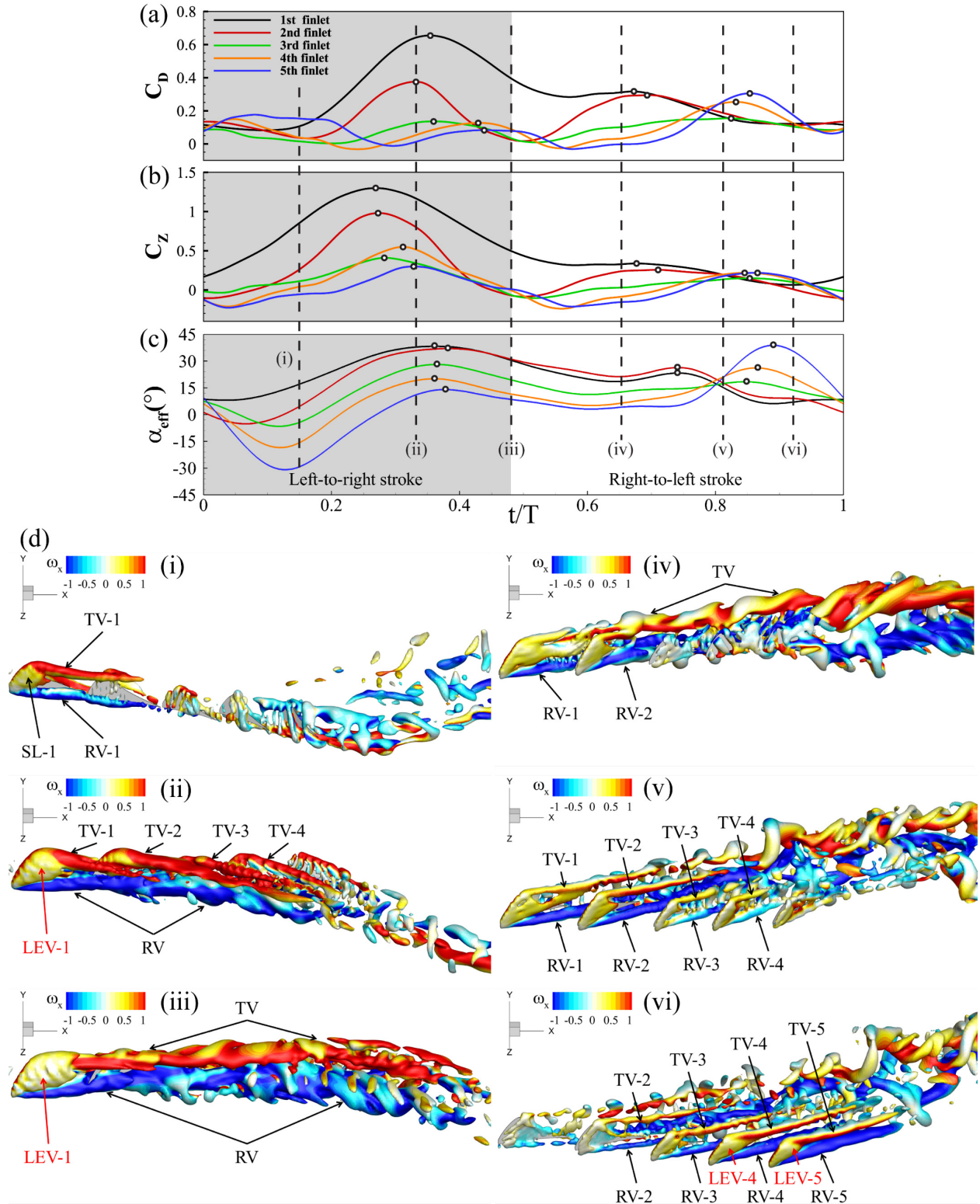


Figure 4-5: Instantaneous drag coefficient (a), lateral force coefficient (b), and effective angle of attack (c) of finlets during one tail beat cycle of tuna forward swimming. (d) Three-dimensional

wake structure of finlets at (i) $t/T=0.15$, (ii) $t/T=0.33$, (iii) $t/T=0.48$, (iv) $t/T=0.65$, (v) $t/T=0.81$, and (vi) $t/T=0.92$, respectively, from a perspective view. The isosurface of the wake structures is visualized by $Q=150$. The Q -isosurface is filled by the contour of vorticity ω_x which is normalized by U_∞/c . The tip vortex (TV), root vortex (RV), shear layer (SL), and leading edge vortex (LEV) are identified for each finlet.

Vortex dynamics of finlet flow are analyzed in detail during a tail beat cycle (Figure 4-5d(i–vi)). The instantaneous 3-D wake structure was visualized using isosurfaces of Q -criterion [99] and flooded by vorticity ω_x . Comparing between the two strokes, the most distinctive difference in vortex topology was that the TVs and RVs merged into one strong counter-rotating vortex pair during the L-to-R stroke (Figure 4-5(i-iii)), while they remained separated as five vortex pairs during the R-to-L stroke to form a parallel-aligned 5×2 vortex tube matrix (Figure 4-5(iv-vi)).

Specifically, at early L-to-R stroke (i), a pair of counter-rotating vortices, including a tip vortex (TV) and a root vortex (RV), emerged at the tip and root of the 1st finlet. A shear layer (SL-1) was also observed. At middle L-to-R stroke (ii), significant TVs were developed at the first four finlets (1st to 4th) as four vortex tubes (TV-1 to TV-4), and the RVs merged to form a coherent vortex tube. Meanwhile, the SL-1 has strengthened into a leading edge vortex (LEV-1) attaching to the leeward of the 1st finlet. At late L-to-R stroke (iii), the individual TVs also merged into one coherent TV tube, resulting in a pair of parallel and strong counter-rotating vortex tubes (TV and RV).

At early R-to-L stroke (iv), the reversal in finlet motion caused the previously formed TV and RV to shed, and new RVs started to form individually at finlet roots. At middle R-to-L stroke

(v), the newly formed TVs and RVs of the first four finlets (1st to 4th) developed into four pairs of counter-rotating vortex tubes that elongated parallelly toward downstream. No obvious merge of TVs or RVs was observed. At late R-to-L stroke (vi), the vortex pairs of the 1st and 2nd finlets shrank, while those of the 4th and 5th finlets intensified. The SL-4 and SL-5 also strengthened and developed into LEVs.

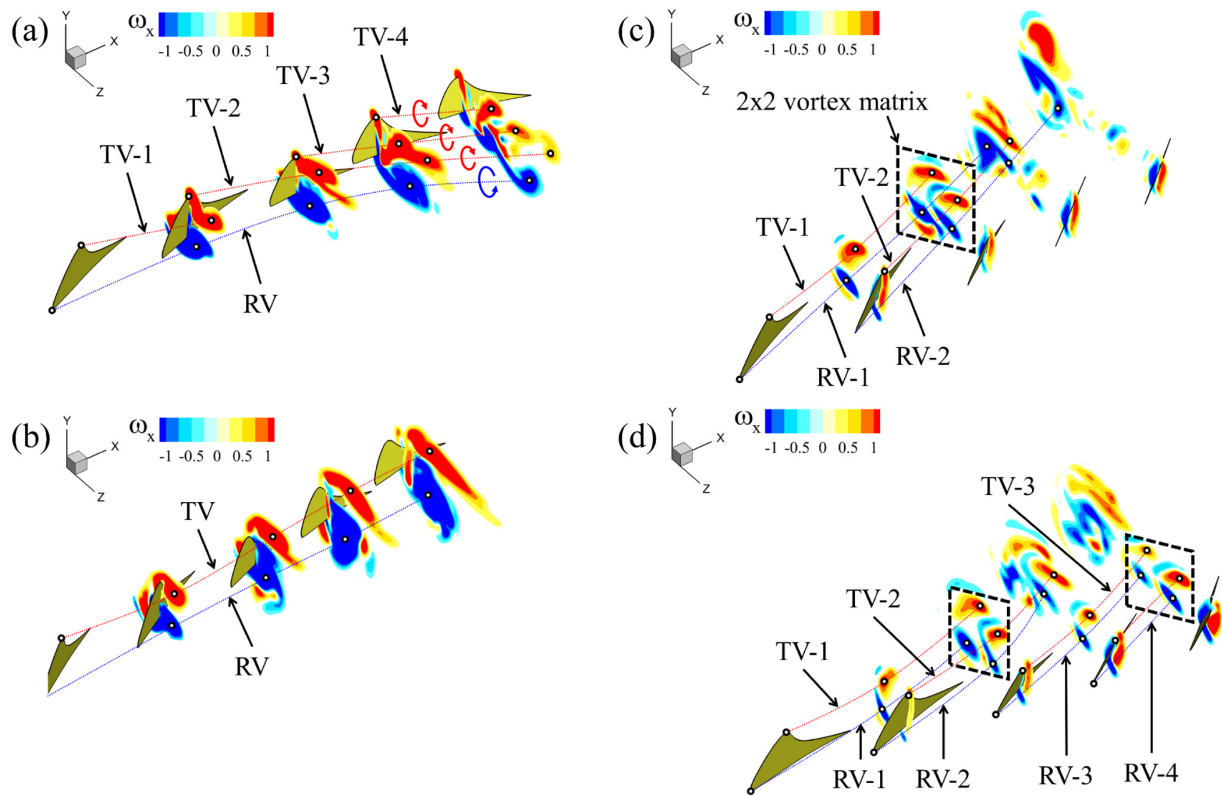


Figure 4-6: Contour of ω_x on four vertical slices cutting the 2nd, 3rd, 4th, and 5th finlet, respectively, at (a) $t/T=0.33$, (b) $t/T=0.48$, (c) $t/T=0.81$, and (d) $t/T=0.92$, from a perspective view. ω_x is normalized by U_∞/c . The centerlines of RV and TVs are illustrated with dotted red and blue lines, respectively, connecting vortex cores (white dots) on each slice. The tip vortex (TV) and root vortex (RV) are identified.

The wake topology of finlets was further clarified with x -vorticity contours (ω_x) (Figure 4-6a–d). In general, the vortex structures revealed by vorticity contours are consistent with the Q-isosurfaces in Figure 4-5d. At middle R-to-L stroke ($t/T=0.81$), the TVs and RVs, corresponding to those shown in Figure 4-5d(v), are clearly identified. Multiple vortices, including TV-1, TV-2, RV-1, and RV-2, were cut simultaneously by the slice on the 3rd finlet. The four vortices formed a unique pattern of counter-rotating 2×2 vortex matrix (dashed black box in Figure 4-6c), with the TV and RV cores clearly separated and parallel aligned. No noticeable interactions were observed among them. At $t/T=0.92$, another 2×2 vortex matrix was formed containing the wake from the 3rd and 4th finlets. It is noteworthy that the strengths of individual TVs and RVs from R-to-L stroke were much weaker than those from L-to-R stroke, indicating weaker disturbances of the incoming flow by finlets, which may explain the smaller lateral force generation during the R-to-L stroke (Figure 4-5b).

Shear layers on finlets are visualized by y -vorticity contour ω_y (Figure 4-7a–d). Due to the asymmetry in pitching kinematics of finlets, the interactions between the shear layer and downstream finlets were more significant during the L-to-R stroke than the R-to-L stroke. At middle L-to-R stroke ($t/T=0.33$), due to the large effective angle of attack of the 1st finlet ($\alpha_{eff}=38.2^\circ$, Figure 4-5c), a leading edge vortex (LEV) was formed, which explained the large drag and lateral force generations of the 1st finlet at this moment (ii, Figure 4-5a,b). At $t/T=0.48$, the LEV core detached from the finlet, resulting in drops in both the drag and lateral forces (iii, Figure 4-5a,b). At middle R-to-L stroke ($t/T=0.81$), no LEV was formed due to the low α_{eff} at all finlets (approximately 17° , Figure 4-5c). All shear layers were found to be attached to the finlets and elongated toward downstream of local flow to form a parallel wake pattern, which was also observed by the corresponding Q-isosurfaces in Figure 4-5d(v). At $t/T=0.92$, the shear layer

wakes were maintained separated with each other. LEVs start to develop on the 4th and 5th finlets due to their high α_{eff} at the moment (vi, Figure 4-5c).

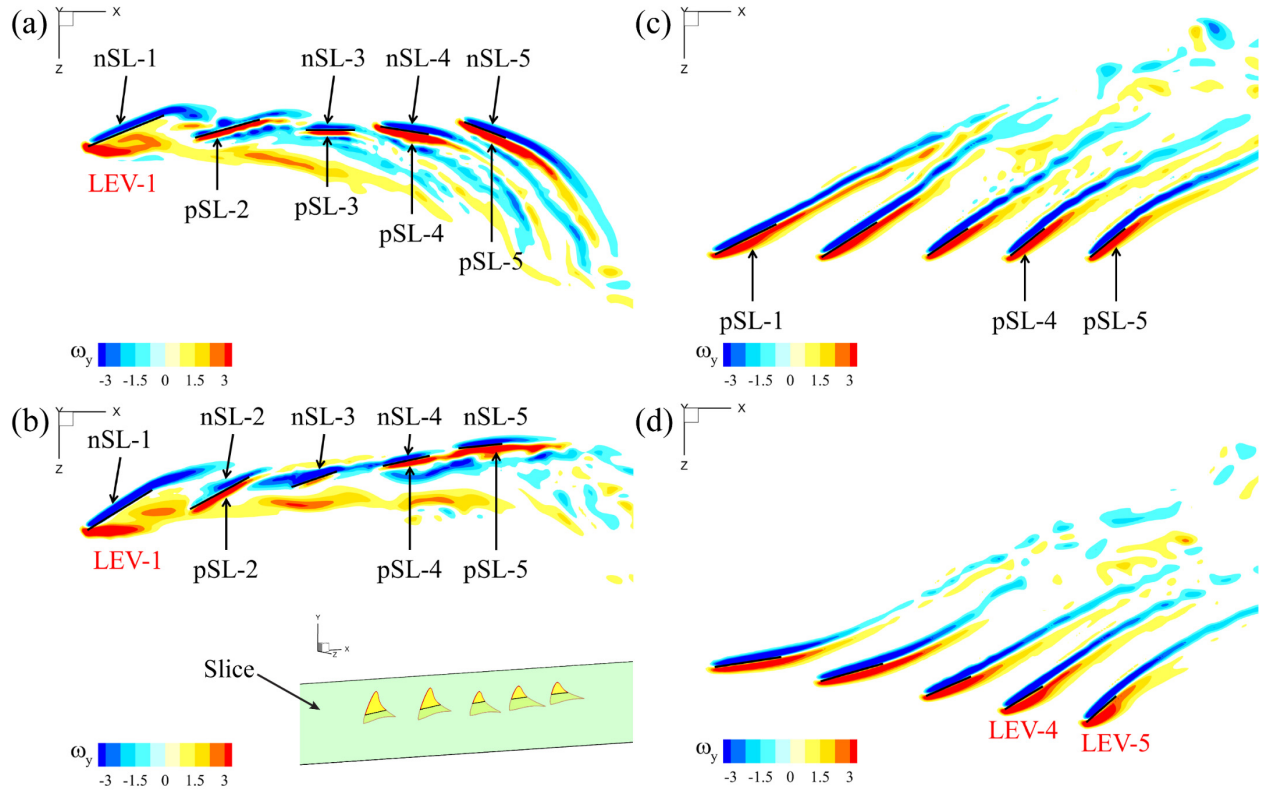


Figure 4-7: Contour of ω_y on a horizontal slice cutting through a horizontal slice 0.3s above the root of the 1st finlet at (a) $t/T=0.33$, (b) $t/T=0.48$, (c) $t/T=0.81$, and (d) $t/T=0.92$, respectively, from top view. ω_y is normalized by U_∞/c . The negative shear layer (nSL), positive shear layer (pSL), and leading edge vortex (LEV) are identified for each finlet.

4.3.2 Effects of Finlet-Finlet Interaction

To study the effect of finlet-finlet interactions, we compare the force and flow results between an isolated finlet and the finlet when located within the five-finlet assembly. For the 2nd finlet, a significant difference in instantaneous drag coefficient (C_D) was found during late L-to-R

and early R-to-L stroke with the largest discrepancy at $t/T=0.48$ (Figure 4-8a). The cycle-averaged drag coefficient (\bar{C}_D) of isolated finlets and finlets in-assembly are plotted in Figure 4-8b. A significant drop in \bar{C}_D was found for the last four finlets (2nd to 5th), which was caused by hydrodynamic interactions between the finlets as shown in Figure 4-7a,b.

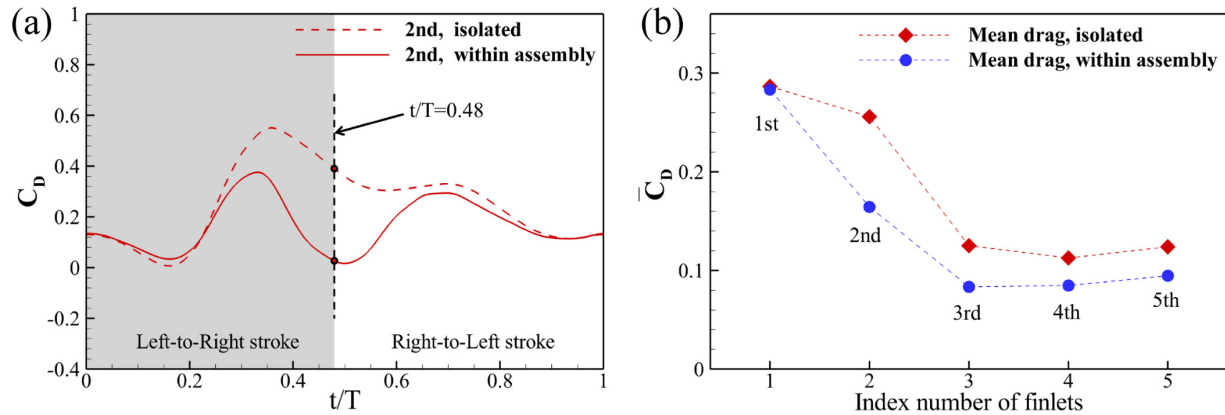


Figure 4-8: (a) Comparison of instantaneous drag coefficient (C_D) between the isolated 2nd finlet and the 2nd finlet when located within the assembly of five. (b) Comparison of cycle-averaged drag coefficient (\bar{C}_D) between the isolated finlets and their within-assembly counterparts.

The individual and total drag reduction of finlets due to finlet-finlet interaction (FFI) are calculated in Table 4-4. The drag reduction ratio ($\Delta\bar{C}_D$) is defined by $\Delta\bar{C}_D = (\bar{C}_{D|isolated} - \bar{C}_{D|within\ assembly})/\bar{C}_{D|isolated}$. The largest drag reduction happened at the 2nd finlet with a 35.9% drop in drag compared with the isolated 2nd finlet. The total drag of the assembly of five was 21.5% less than the summed drag of their isolated counterparts.

Table 4-4: Drag reduction due to finlet-finlet interaction

	1 st finlet	2 nd finlet	3 rd finlet	4 th finlet	5 th finlet	Total
Drag reduction, $\Delta\bar{C}_D$	1.0%	35.9%	33.6%	24.8%	23.4%	21.5%

The fundamental reason for FFI-induced drag reduction is revealed by comparing the wake structure and pressure field between the isolated finlet and the finlet within assembly (Figure 4-9) when instantaneous drag coefficient on the 2nd finlet has the largest difference (Figure 4-8a). Because the 2nd finlet was located at the lee side of the 1st finlet, the 1st finlet was acting as a deflector which prevented the direct impact of the incoming flow on the 2nd finlet. As a result, the strengths of pSL-2 and nSL-2 within the assembly of five (Figure 4-9b) were much weaker than those of their isolated counterparts (Figure 4-9a). Instead, nSL-1 and LEV-1, which are similar to those of the isolated 2nd finlet in shape and strength, were formed at the 1st finlet. In addition, the pSL-2 in Figure 4-9b was attached to the finlet, which is different from the detached LEV-2 in Figure 4-9a.

The FFI-induced drag reduction is confirmed by comparing the pressure contour around finlets between the two models (Figure 4-9c,d). A large pressure difference between the two sides of the isolated 2nd finlet was found, which creates a large pressure force normal to the finlet surface with its x-positive component contributing to drag production. For the 2nd finlet within the assembly, because of the deflection effect created by the 1st finlet, there was no significant pressure difference between the two sides, resulting in a much lower instantaneous drag than that of the isolated 2nd finlet at this moment ($t/T=0.48$, Figure 4-8a).

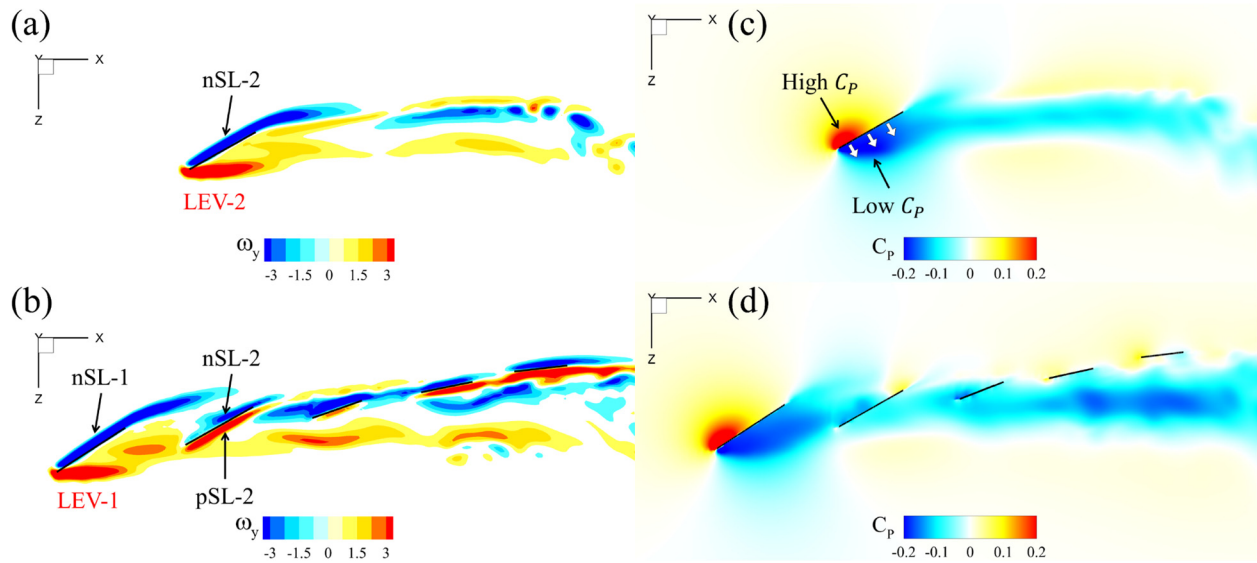


Figure 4-9: Comparisons of the vorticity ω_y (a,b) and pressure coefficient C_p (c,d) contours between the isolated 2nd finlet (a,c) and its in-assembly counterpart (b,d), respectively, at $t/T=0.48$ on a horizontal slice cutting through a chord of the 1st finlet. The negative shear layer (nSL), positive shear layer (pSL), and leading edge vortex (LEV) are identified. In (c), white arrows denote pressure force.

4.3.3 Effect of Pitching Kinematics of Finlets

We investigate the effect of pitching kinematics of finlets by comparing the force and flow between finlets with (w/) and without (w/o) pitching. The finlets w/o pitching were fixed to the body along the local body centerline at all times and thus did not move independently of the body centerline motion pattern. Major differences in instantaneous lateral forces coefficient (C_Z) happens between finlets w/ and w/o pitching during the right-to-left stroke when their α_{eff} were opposite in signs (Figure 4-10a,c). In addition, clear flow channels between neighboring finlets were observed for pitching finlets at $t/T=0.81$. In contrast, the body-fixed finlets were

consecutively placed in a row with small clearances between each other. Therefore, no channel between finlets was formed (Figure 4-10d-g).

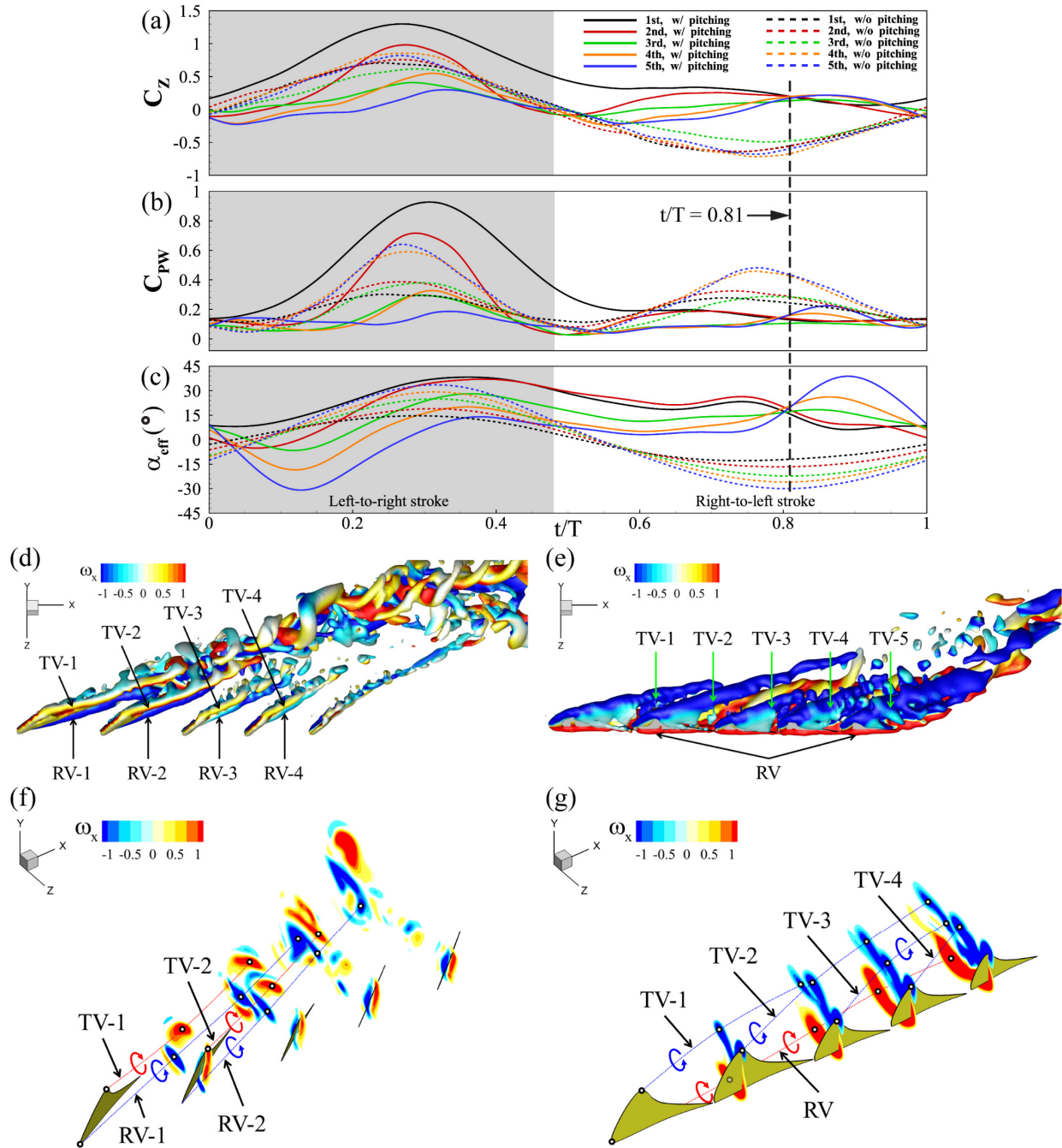


Figure 4-10: Comparisons of the instantaneous lateral force coefficient (a), power coefficient (b), effective angle of attack (c), wake structure (d,e), and x-vorticity contour (f,g), respectively, between finlets with and without pitching kinematics. The wake structures and x-vorticity contours are shown at $t/T=0.81$. The tip vortex (TV) and root vortex (RV) are identified for each finlet.

The α_{eff} of the body-fixed finlets (Figure 4-10c) were more symmetric between the left-to-right and the right-to-left strokes than that of the pitching finlets, resulting in more symmetric C_Z and power consumption (C_{PW}) between the two strokes. For the flow, it was interesting to find the rotation directions of both the TVs and RVs generated by pitching finlets were opposite to those generated by body-fixed finlets (Figure 4-10f,g), resulting from the opposite signs of α_{eff} . In addition, the merged RV of the body-fixed finlets kept in close proximity to the finlets array, while the TVs of pitching finlets were maintained separated and diverged from the finlets (Figure 4-10f,g). Stronger tip and root vortices were generated by the body-fixed finlets caused the higher α_{eff} (Figure 4-10d,e).

The cycle-averaged lateral force coefficient (\bar{C}_Z) show large mean lateral forces produced by the 1st and 2nd finlets due to their asymmetric pitching angles (Figure 4-11a), which accounted for 79% of the total mean lateral force of the five finlets. The lateral force could help fish to maneuver by generating yaw torques, which is a potentially beneficial hydrodynamic effect of the pitching kinematics of the finlets. In support of this idea, low-speed maneuvers in scombrid fishes using only finlets have been observed [58]. Due to the symmetric property of lateral forces for body-fixed finlets, little mean net force was produced (Figure 4-11a).

The cycle-averaged power consumption (Figure 4-11b) in general increased posteriorly for the body-fixed finlets but decreased posteriorly for the pitching finlets. The pitching kinematics of finlets resulted in much smaller mean power at the last three finlets than their body-fixed counterparts.

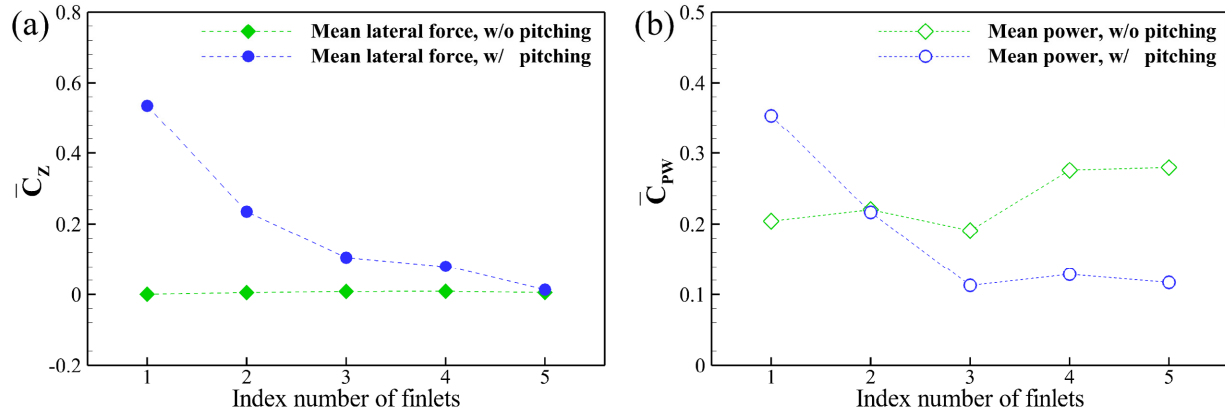


Figure 4-11: Comparisons of the cycle-averaged lateral force (a) and power coefficients (b), respectively, between the finlets with and without pitching kinematics.

The pitching-induced power reductions of finlets are calculated and listed in Table 4-5. The power reduction ($\Delta\bar{C}_{PW}$) is defined by $\Delta\bar{C}_{PW} = (\bar{C}_{PW|(w/o)} - \bar{C}_{PW|(w)})/\bar{C}_{PW|(w/o)}$. Over half of the hydrodynamic power of the last two finlets (4th and 5th) was reduced due to pitching. Even though the power consumption of the 1st finlet increased by a large 73% because of its role in generating mean lateral force, the total power consumption of the pitching finlets was still 20.8% less than that of finlets without pitching, which is a beneficial hydrodynamic effect of finlet pitching motion.

Table 4-5: Power reduction due to pitching kinematics of the finlets

	1 st finlet	2 nd finlet	3 rd finlet	4 th finlet	5 th finlet	Total
Power reduction, $\Delta \bar{C}_{PW}$	-73.0%	1.8%	40.8%	53.6%	58.1%	20.8%

It was found the instantaneous lateral force on pitching finlets could facilitate the posterior body flapping (Figure 4-12a). Specifically, the direction of lateral force generated by the pitching 5th finlet was along negative z-axis during the first half of L-to-R stroke, which was in the same direction of the flapping motion of the posterior body of fish. This could facilitate the oscillation of fish posterior body by providing augmented lateral force from the finlet, which we call the constructive force. This same constructive force from the pitching 5th finlet was found during the second half of R-to-L stroke. However, for the 5th finlet without pitching, the lateral force was always in the opposite direction of posterior body motion for the entire tail beat cycle (Figure 4-12a), which means the 5th finlet was always generating destructive force that add more lateral drag to the posterior body. Moreover, the amplitude of the destructive force of body-fixed finlet was much larger than that of pitching finlet, which caused the increases in both the mean and the instantaneous power consumption (Figure 4-11b & Figure 4-12b). Besides the 5th finlet, significant constructive forces were also generated by the 4th finlet during the first half of L-to-R stroke and the second half of R-to-L stroke, and by the 1st and 2nd finlets at entire R-to-L stroke (Figure 4-10a).

The mechanism of hydrodynamic pressure force production is demonstrated by the instantaneous pressure contour around pitching finlets (Figure 4-13a) at $t/T=0.81$. The α_{eff} for all finlets are positive (Figure 4-10c) at the moment, which is in line with the positive α_{eff} of the

fifth mackerel finlet at a similar tail flapping phase observed by Nauen and Lauder [58] using flow visualization. As a result, high- and low-pressure zones were formed on the right and the left side of finlets, respectively, producing pressure forces normal to the finlet surfaces pointing to the left (white arrows in Figure 4-13a). Due to the positive geometric angle of attack (α) of finlets, the pressure forces had positive x-components, which contributes to the finlets drag. The positive z-components of the pressure forces were in the same direction of the posterior body motion, which are the sources of constructive forces on finlets at the moment (Figure 4-10a). However, for finlets without pitching kinematics (Figure 4-13b), the α_{eff} of finlets were all negative (Figure 4-10c), resulting in pressure force directions being opposite to the flapping direction, therefore destructive for posterior body flapping. Also, the pressure differences between the two sides of body-fixed finlets were much larger than those of the pitching finlets, causing more severe destructive drag on the posterior body during middle R-to-L stroke.

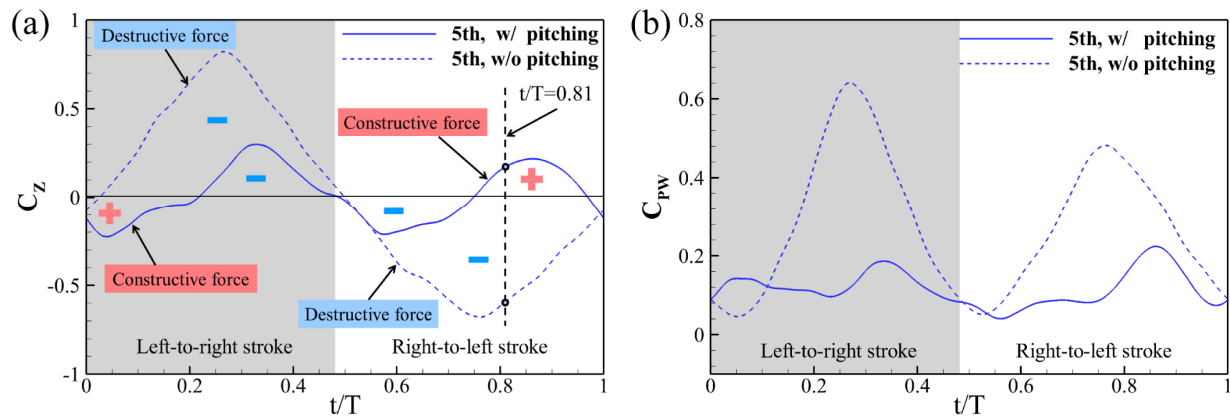


Figure 4-12: Comparisons of instantaneous lateral force coefficients (a) and power coefficients (b), respectively, between the 5th finlet with and without pitching. In (a), the regions between

constructive force and $C_z=0$ are marked with red plus sign (“+”) and those between the destructive force and $C_z=0$ are marked with blue minus sign (“-”).

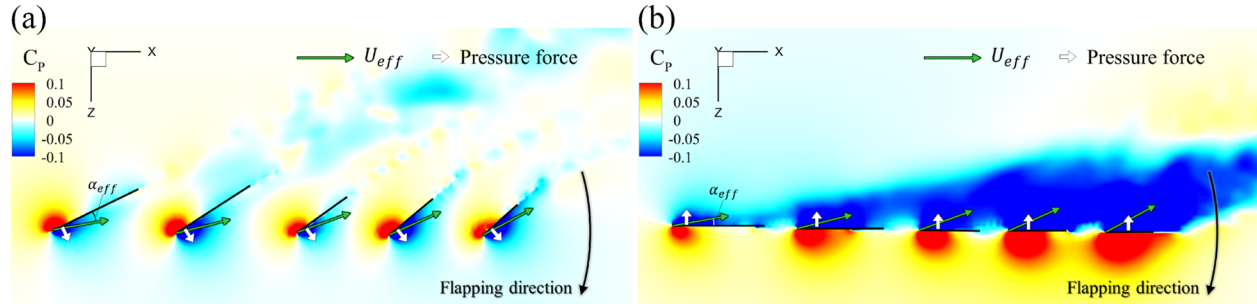


Figure 4-13: Comparisons of the normalized pressure coefficient (C_p) contour of the finlets with (a) and without (b) pitching motions, respectively, at $t/T=0.81$ on a horizontal slice cutting through a chord of the 1st finlet. α_{eff} denotes the effective angle of attack and U_{eff} denotes the effective velocity at finlet root.

Since finlets are located immediately upstream of caudal fin, it is important to investigate the effect pitching kinematics of finlets on the local flow that is incident to the main propulsor of fish. It was found the flow past pitching finlets was redirected into streams parallel to the orientation of finlets at middle R-to-L stroke ($t/T=0.81$) (Figure 4-14a). These streams move across the body midline through channels between finlets towards the opposite direction of tail flapping (Figure 4-14c). For finlets without pitching (Figure 4-14b), however, the local flow was trapped and carried away by finlets toward the same direction of tail flapping. Significant positive lateral flow velocity (in red, Figure 4-14d) induced by body-fixed finlets was found at the region where the water was trapped. The strong positive lateral flow may explain the much higher power consumption of the last three body-fixed finlets in Figure 4-11b because more work from finlets

is required to increase the kinetic energy of trapped water. Additional effects of finlet flows on the caudal fin are presented in the supplemental material.

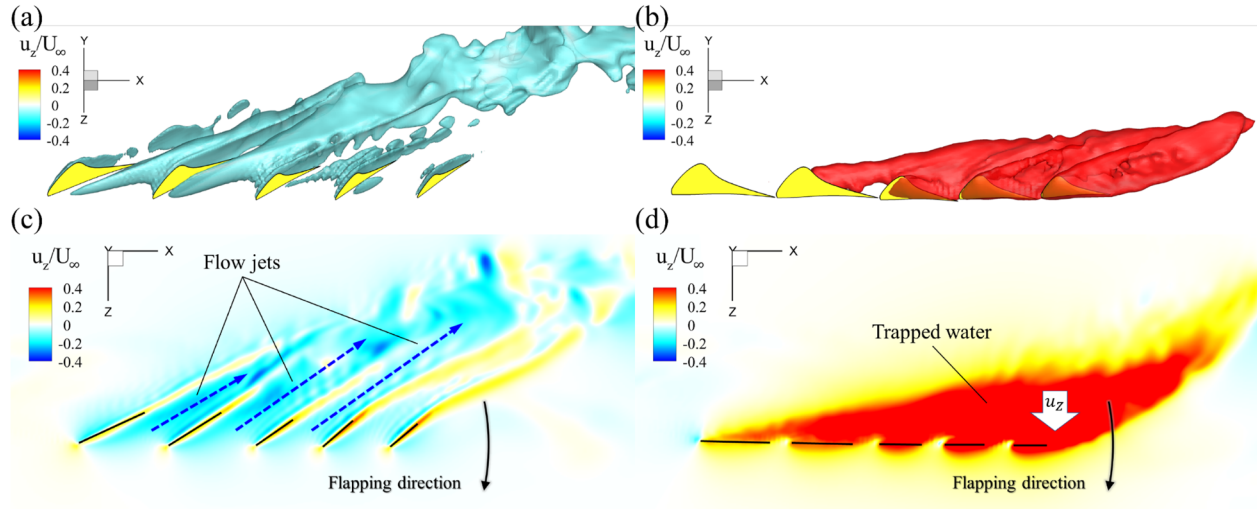


Figure 4-14: Comparisons of the normalized lateral velocity (u_z/U_∞) isosurface (a,b) and contour (c,d) of the finlets with (a,c) and without (b,d) pitching kinematics, respectively, at $t/T=0.81$ on a horizontal slice cutting through a chord of the 1st finlet.

4.4 Discussion

The flow pattern of pitching finlets in Figure 4-14a,c was in line with the finding by Nauen and Lauder [56] that cross-peduncular flow redirected by finlets exists in the horizontal plane. The current results support the hypotheses of Walters [59], Webb [60], and Lindsey [55] that transverse flow was redirected by the finlets and also support the “flow fences” hypothesis by Magnuson [61] that finlets helped direct the water smoothly across the caudal peduncle. Due to the absence of a caudal fin, the results above could not directly support the vorticity enhancement hypothesis by Nauen and Lauder [56] on the mackerel suggesting that finlets can direct flow into the vortex formation at the caudal fin. However, the existence of the redirected flow has provided a

potentially favorable local flow environment upstream of the caudal fin and suggests that such caudal vortex enhancement is a distinct possibility. As an extended effort to demonstrate the finlet-caudal fin interaction, we have provided simulation results of tuna full-body swimming in the supplementary material, in which substantial interactions between the finlets-induced vortex and the caudal fin are observed.

Although beneficial interactions that enhance caudal fin thrust have been found between the median and the caudal fins in thunniform [66] and carangiform swimming [9], the fluid dynamics of finlet-caudal fin interactions may be different than other median fins studied previously. Specifically, the simplified finlets and median fin models adopted by previous computational studies [9, 66-68] were strip-like elongated fins, and not individual distinct and isolated finlets each moving independently. The flow induced by the tip of the simplified strip-like finlets [67] and dorsal/anal fins [9] was generally a cone shape vortex tube along the strip with the apex attached to the upstream end, similar to the vortex wake generated by the body-fixed finlets in Figure 4-10*e,g*. In contrast, the wake topology changed drastically after adding independent pitching kinematics to the individual finlets. Each finlet generated a vortex pair with its orientation deviating from the body midline, creating a matrix of parallel vortex tubes in Figure 4-6*e,f*. This is a new flow pattern found here for finlet flows, and is distinct from previous computational studies of median fin function [9, 66-68]. These data suggest the potential for novel fluid dynamic interactions between finlet flows and the tail fin in swimming fish, a phenomenon that will be explored in future work.

Limitations on the numerical modeling of this work include the use of uniform incoming flow without a tuna body (although see supplemental material for simulations that include the body) at a reduced Reynolds number, which has been proven to be valid for the current conclusions (see

section 4.2 and supplementary material for further details). The present simulation is representative of yellowfin tuna steady swimming at speeds 0.25~0.46 body length per tail beat cycle. The main conclusions may not apply to tuna swimming at speeds greater than this range or other swimming behaviors (maneuver, acceleration/desecration), or for other Scombridae species with finlet morphology distinct from yellowfin tuna.

4.5 Chapter Summaries

In this section, both anatomically and kinematically accurate finlet models have been reconstructed based on video data from freely swimming yellowfin tuna. Direct numerical simulation results show that finlets were drag producing mainly due to the drag component of hydrodynamic pressure force which is determined by both the geometric angle of attack and the effective angle of attack of finlets. The finlet-finlet interaction significantly helped reduce total finlet drag, and the pitching kinematics of finlets helped reduce finlet power consumption during swimming. Significant mean lateral forces were generated by the finlets that may assist in maneuvering by generating yaw torques. Moreover, the pitching finlets created constructive forces to facilitate posterior body flapping when their effective angles of attack and root z-velocities have the same sign. Wake dynamics analysis revealed a unique vortex tube matrix structure and the associated flow jets redirected through the channels between pitching finlets, which supports previous hypotheses that finlets can redirect and modulate the transverse flow. These findings suggest that although pitching finlets do not produce thrust, they have substantially transformed the flow incident to the tail, which may further cause beneficial interactions with the tail fin.

4.6 Supplementary Material

4.6.1 Analytical Representation of Finlet Model Kinematics Using Fourier Series

In order to generate an analytical presentation of the finlet model kinematics, Fourier series were used to interpolate the lateral (z/c) and surge (x/c) displacements of the finlet root as well as the finlet angle (θ) of the five finlets during one tail beat cycle as follows,

$$\begin{cases} \zeta(\tau) = a_0 + \sum_{n=1}^3 [a_n \cos(2\pi n\tau) + b_n \sin(2\pi n\tau)], \\ \xi(\tau) = g_0 + \sum_{n=1}^3 [g_n \cos(2\pi n\tau) + h_n \sin(2\pi n\tau)]; \end{cases} \quad 0 \leq \tau \leq 1 \quad (4-3)$$

$$\theta(\tau) = \gamma_0 + \sum_{n=1}^6 [\gamma_n \cos(2\pi n\tau) + \varepsilon_n \sin(2\pi n\tau)],$$

where ζ and ξ denote the lateral ($\zeta = z/c$) and surge ($\xi = x/c$) displacements, respectively. θ denotes the finlet angle, τ is the normalized time with $\tau=t/T$. a , b , g , h , γ , and ε are the coefficients of the Fourier series which are calculated and listed in Table 4-6–Table 4-8. The R-square values of the Fourier series interpolations are larger than 0.9995.

Table 4-6: Coefficients of Fourier series representing the lateral displacement of finlet root

Finlet No	a_0	a_1	b_1	a_2	b_2	a_3	b_3
1 st	0.116	1.287	-0.672	-0.023	0.029	0.008	0.019
2 nd	0.112	1.665	-0.597	-0.026	0.047	0.001	0.020
3 rd	0.119	2.104	-0.483	-0.035	0.066	-0.015	0.017
4 th	0.131	2.487	-0.387	-0.037	0.080	-0.030	0.016
5 th	0.137	2.873	-0.274	-0.045	0.099	-0.046	0.018

Table 4-7: Coefficients of Fourier series representing the surge displacement of finlet root

Finlet $N_{\underline{0}}$	g_0	g_1	h_1	g_2	h_2	g_3	h_3
1 st	0.150	-0.007	0.002	-0.037	-0.013	0.003	-0.003
2 nd	2.235	-0.007	0.004	-0.051	-0.020	0.004	-0.005
3 rd	4.244	-0.013	0.003	-0.071	-0.032	0.007	-0.005
4 th	5.809	-0.019	-0.001	-0.091	-0.043	0.010	-0.006
5 th	7.420	-0.026	-0.006	-0.107	-0.055	0.014	-0.004

Table 4-8: Coefficients of Fourier series representing finlet angle θ .

Finlet $N_{\underline{0}}$	γ_0	γ_1	ε_1	γ_2	ε_2	γ_3	ε_3	γ_4	ε_4	γ_5	ε_5	γ_6	ε_6
1 st	21.0	-9.11	-7.11	-3.46	-2.54	1.06	1.54	1.73	-0.07	0.54	-0.94	-0.32	-0.45
2 nd	19.4	-10.3	-15.7	-4.23	-5.51	0.93	-0.78	2.02	-0.83	0.50	-1.20	-0.71	-0.43
3 rd	13.8	0.81	-22.6	-0.33	-8.13	1.68	-0.81	0.76	0.17	0.26	0.69	0.45	0.59
4 th	9.09	5.34	-31.1	-0.10	-12.3	0.82	-3.25	0.74	0.13	0.37	0.98	0.44	0.88
5 th	5.86	9.76	-41.6	5.16	-17.2	1.69	-6.53	-0.41	-1.24	-0.36	0.96	0.43	1.05

4.6.2 Validation Study on the Uniform Incoming Flow Assumption

In this section, we do not include the effect of the body and caudal fin of tuna in these simulations so that finlet flows can be studied in isolation. Isolated fins were also used in previous hydrodynamic studies of fish pectoral fin [100] and ribbon-fin [101]. In order to test our assumption and examine the possible change of flow past finlets due to the presence of the body, we have included the body in the simulation of pitching finlets. Figure 4-15 shows the comparison

of finlets flow with (Figure 4-15b&d) and without (Figure 4-15a&c) body at mid-right-to-left (Figure 4-15a&b) and mid-left-to-right (Figure 4-15c&d) stroke, respectively. It is found the vortex structures are highly similar in shape, orientation, and magnitude between finlets flow w/ and w/o body, indicating the flow features are dominated by the steady swimming speed and the lateral motion of finlets and the impact of flow direction change on finlets due to the presence of the body is not significant. Therefore, the uniform incoming flow assumption is valid for the present finlets study.

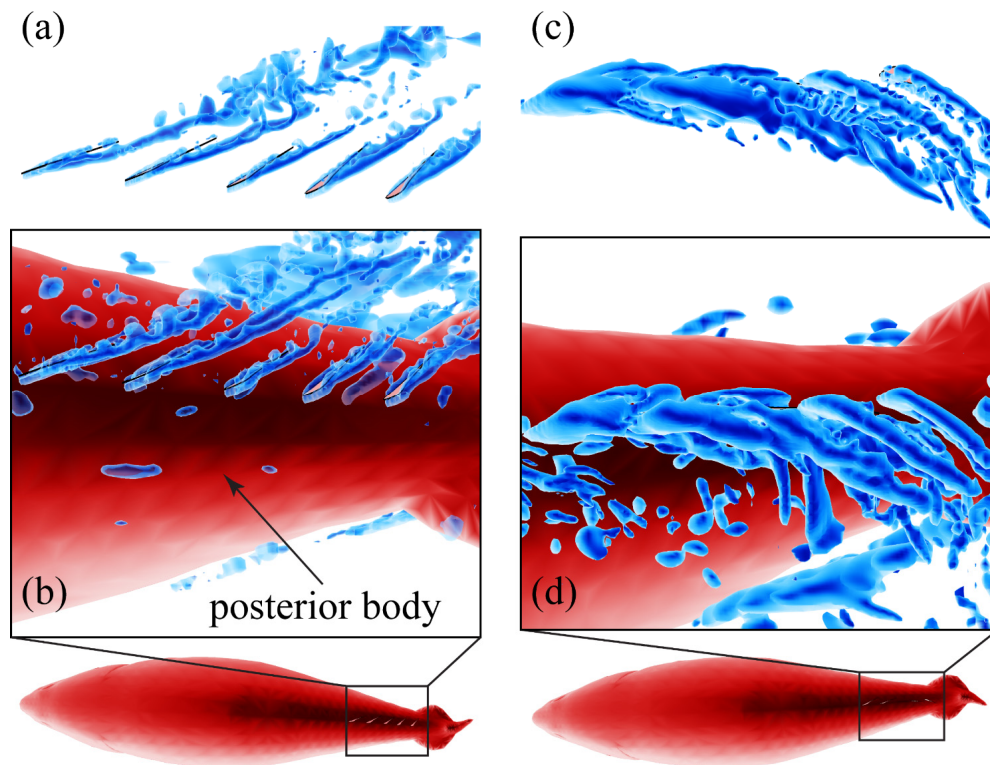


Figure 4-15: Comparison of vortex structure of flow past pitching finlets w/ (b,d) and w/o (a,c) body at mid-right-to-left (a,b) and mid-left-to-right (c,d) stroke, respectively. The blue vortex structure is identified by Q-isosurface with the same value of Q-criterion.

4.6.3 Validation study on the reduced Reynolds number

Simulation of fish swimming at a high Reynolds number is always a challenge. The measured Reynolds number of the present yellowfin tuna swimming is around 1 million and the Re of a single finlet is around 10^4 , at which the flow is dominated by the inertia effect. In our simulations, the flow for the finlet is set at $Re=999.6$ (close to 10^3) due to the current computational capability. Although this flow condition corresponds to a juvenile tuna fish model, it is still in the inertia-dominated flow region. This can be observed from the following Figure 4-16, in which the inertia force ($C_{D,pressure}$) is much higher than that of viscous force ($C_{D,viscous}$).

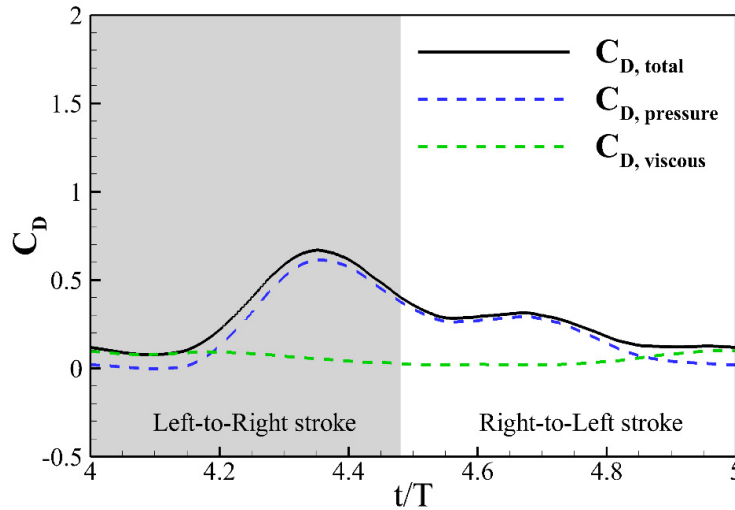


Figure 4-16: Instantaneous drag force coefficient ($C_{D,total}$) of the isolated 1st finlet and its pressure ($C_{D,pressure}$) and viscous ($C_{D,viscous}$) components at $Re=999.6$.

A parametric study on a wide range of Re is conducted to further clarify the change of cycle-averaged finlet drag coefficients with Re , as shown in Figure 4-17. It is noteworthy that by using the high-fidelity DNS flow solver, the parametric study results have already included the effect of possible flow separation behavior due to Re change into the force calculations ($\bar{C}_{D,total}$, $\bar{C}_{D,pressure}$

and $\bar{C}_{D,viscous}$). Results show that pressure drag is not sensitive to change in Re, while viscous drag decreased quickly at Re below 500. The total drag force is not sensitive to Re change at Re=999.7 (use for current simulation) and above (within the tested range), where the pressure force dominates and viscous component is small. The difference in the total drag force between Re=999.7 and Re=2000 is less than 5%. The Re effect we find here is also in line with previous findings of unsteady flapping motions [9, 102-106].

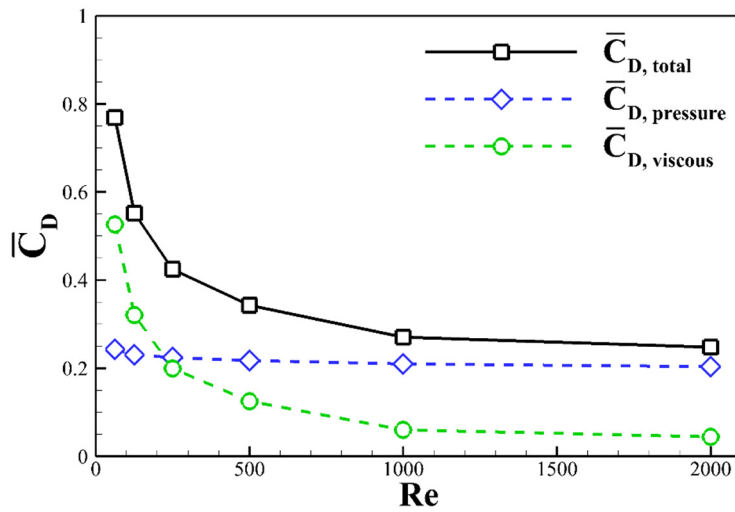


Figure 4-17: Cycle-averaged drag force coefficient ($\bar{C}_{D,total}$) of the isolated 1st finlet and its pressure ($\bar{C}_{D,pressure}$) and viscous ($\bar{C}_{D,viscous}$) components at various Re numbers.

In general, the Reynolds number may affect the separation position of a flow over a blunt body. However, the major flow structures in the current study are mainly dominated by the flapping motion of the finlets, not the fish body. Past similar research has also shown that the higher viscosity (low Re) dissipates the smaller scale vortex structures quickly, but the major features of the flow can still be captured and used for understanding the associated flow physics

([107]; [100]). Most recently, Zhong et al. [10] simulated a model fish swimming at $Re=2100$, and the wake patterns obtained from the simulation showed strong similarities with their experimental results using the same model but conducted at Re value 20 to 50 times higher.

To be confident about the major flow phenomenon discovered in this work, we have compared the flow field of lateral velocity between $Re=500$, 999.7 , and 2000 in Figure 4-18. It is found the finlets-induced flow jets share similar velocity magnitude and orientation over a wide range of Re , indicating the robustness of the flow pattern discovered under changing Re .

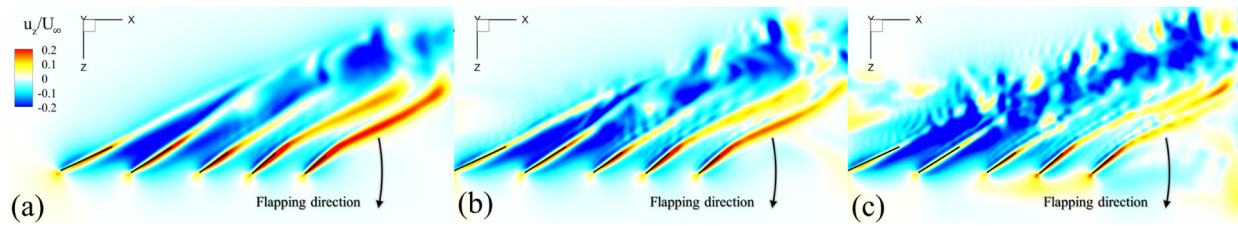


Figure 4-18: Comparisons of the normalized lateral velocity (u_z/U_∞) contour between $Re=500$ (a), $Re=999.7$ (b), and $Re=2000$ (c) at $t/T=0.81$ on a horizontal slice cutting through a chord of the 1st finlet.

4.6.4 Summary of finlet arrangement and kinematics used for computations

Table 4-9: Summary of finlet arrangement and kinematics used for computations.

Case No	1	2	3	4	5	6	7
Geometry	All five finlets	1 st finlet	2 nd finlet	3 rd finlet	4 th finlet	5 th finlet	All five finlets
Pitching motion	w/	w/	w/	w/	w/	w/	w/o

5 In-Line Propulsion: Hydrodynamic Interactions and Enhanced Propulsive Performance Owing to Finlets in Tuna Swimming

Tunas along with many high-performance fishes of the Scombridae family are equipped with finlets—a series of small, triangular, independently mobile fins—that have been hypothesized to enhance hydrodynamic performance. Here we use experimental and computational approaches to investigate the hydrodynamic role of finlets in the propulsive performance of yellowfin tuna (*Thunnus albacares*) during steady swimming.

We have previously studied the hydrodynamics of finlets in yellowfin tuna (*Thunnus albacares*) steady swimming [108] by flow simulations of biologically realistic finlets with finlet morphology and pitching kinematics reconstructed from high-speed videography. A key goal of this section is to examine the hydrodynamic role of finlets in the propulsive performance of tuna locomotion with biologically realistic geometric and kinematic complexity. We have combined experimental and numerical approaches to study the hydrodynamic performance and vortex dynamics of tuna during steady swimming. High-speed videos of freely swimming yellowfin tuna were obtained to provide simultaneous kinematics of the trunk, median fins, and finlets of the fish. A biologically realistic computational model of yellowfin tuna was reconstructed based on live fish kinematics and measurements of finlets in yellowfin tuna specimens. Simulations of tuna swimming were conducted using a high-fidelity flow solver. We aim to fill the gap between simplified finlet studies [10, 66, 73] and previous experimental work [56, 58, 65] by extending our previous work and providing quantitative data on the performance and flow field.

By comparing hydrodynamic performance and vortex dynamics between computational models with and without finlets, we can quantify potential performance enhancement owing to

finlets and reveal the change in flow physics, thereby testing the thrust enhancing hypothesis of finlets. In addition, by comparing models with pitching finlets and fixed finlets, we can study the potentially important effect of pitching kinematics on the performance and vortex dynamics of tuna swimming.

5.1 Tuna Morphology and Kinematics

Live yellowfin tuna averaging 1 meter in fork-length were studied at the Greenfins Aquaculture Tuna Center (Narragansett, Rhode Island, USA), where tunas were kept in a circular tank (12.2 m in diameter, more than 3 m in water level) containing more than 473,000 liters of seawater. Tuna locomotion is effectively unconstrained in this large tank. We use both submerged GoPro cameras (GoPro Inc., USA) at 120 fps and 1920×1080 pixel resolution and submerged Photron high-speed cameras (Photron USA Inc., USA) at 250 to 500 fps and 1024×1024 to 2048×2048 pixel resolutions to film tunas freely swimming at approximately 1 body length per second (~ 1.0 - 1.2 m/s) (Figure 5-1a).

GoPro videos provided a lateral overview of tuna morphology (Figure 5-1a), and high-speed videos provided both a posterior view (Figure 5-1d) and a dorsal view (Figure 5-1e) of tuna morphology and swimming kinematics with detailed information on finlet morphology and pitching motions. Finlet internal anatomy using micro-CT scans has confirmed both skeletal and muscular supports at the base of the leading edge, where finlet attaches to the body, allowing active control of finlet movements [65]. The dorsal and ventral finlets of yellowfin tuna each contain nine individual finlets (A to I, Figure 5-1a) of similar triangular shape (Figure 5-1c). The sizes of the posterior-most (A) finlet and anterior-most (I) finlet are significantly smaller than those in between

(B to H), making them difficult to visualize during swimming. Thus, here we focus on finlets B to H.

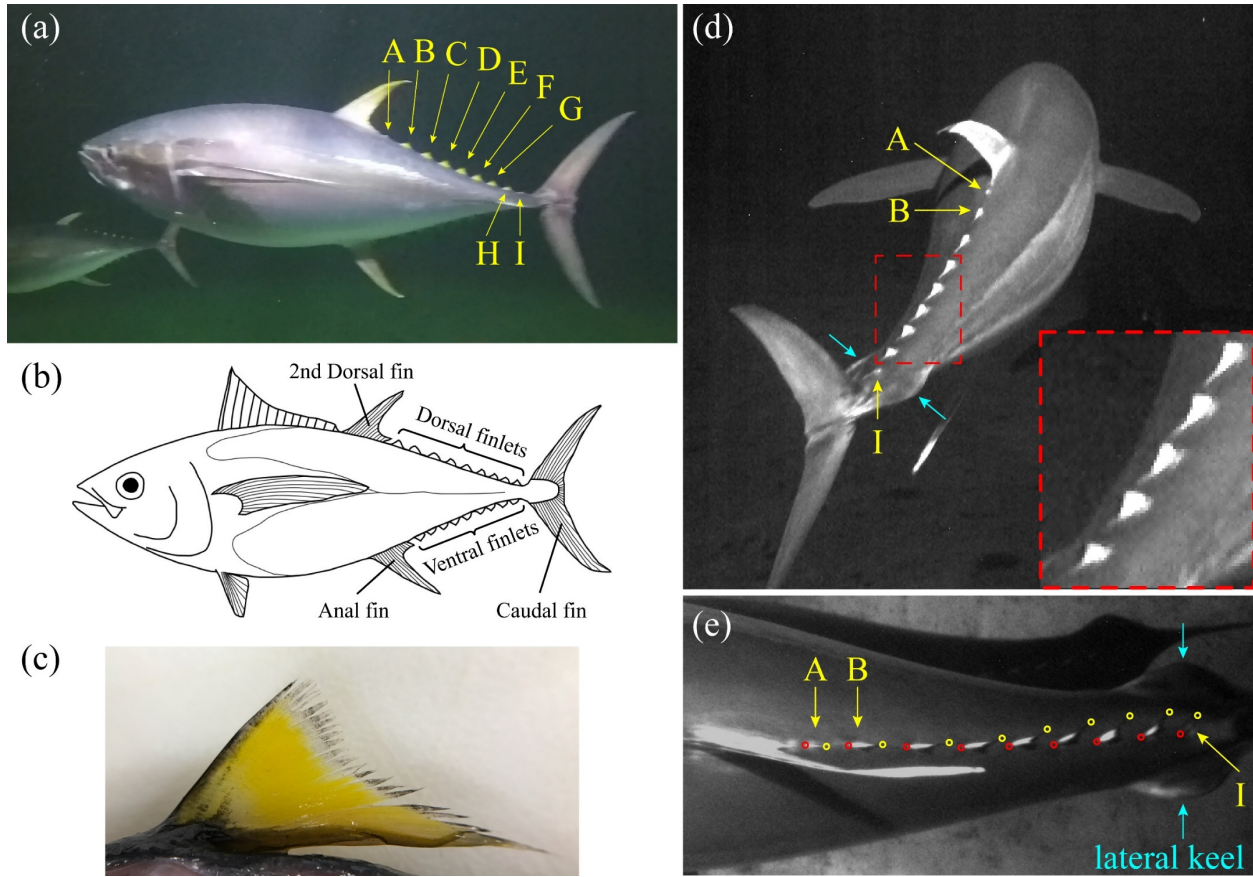


Figure 5-1: (a) Live yellowfin tuna (*Thunnus albacares*) swimming (with nine finlets indicated by letters A to I). (b) Illustration of body parts of a yellowfin tuna with dorsal and ventral finlets. (c) A single tuna finlet to show the attached base and free posterior region. (d) Posterior view of yellowfin tuna swimming showing pitching finlets. (e) Dorsal view of the caudal peduncle of a swimming tuna showing both the dorsal finlets and the lateral keel.

5.2 Reconstruction of Computational Model with Swimming and Finlet Kinematics

The 3-D computational model of yellowfin tuna (Figure 5-2a), including the trunk, caudal fin, dorsal fin, anal fin, and finlets, was reconstructed based on morphological measurements from video images during live fish swimming and the computed tomography (CT) scanned 3-D models and images of the body, tail, peduncle, and finlets obtained from dissections of fresh yellowfin tuna specimens. Specifically, for finlets, the geometric shape of a finlet in the computational model overlaps with that of the yellowfin tuna (Figure 5-2b).

We captured over 40 dorsal-view high-speed videos of tuna steady swimming with significant finlet motions. A representative dorsal-view video sequence with both an inclusion of the entire fish (Figure 5-2b) and a clear view on finlets during a complete tail beat cycle (Figure 5-2c) was chosen to allow for the simultaneous reconstruction of swimming kinematics and finlet kinematics of the computational model using an image-guided reconstruction method [79] in Autodesk Maya® (Autodesk, Inc.). This method has been successfully adopted to reconstruct fish swimming [9] and finlet kinematics (see the previous work [9] for more details).

A comparison between the reconstructed 3-D computational model and the swimming tuna at an instantaneous high-speed video frame (Figure 5-2c) shows good agreement in both the morphological and kinematical features between the two. We were able to reconstruct the kinematics of seven dorsal finlets with the greatest accuracy, and hence included these seven finlets in the computational model. For each reconstructed finlet, the size, pitching kinematics, and its location along the body midline agree with those of the tuna finlet (Figure 5-2c). We were not able to visualize the ventral finlets during tuna swimming, hence we mirrored the dorsal finlets to the ventral side of the body assuming that the ventral finlet shares the size, pitching kinematics, and longitudinal location with its dorsal counterpart.

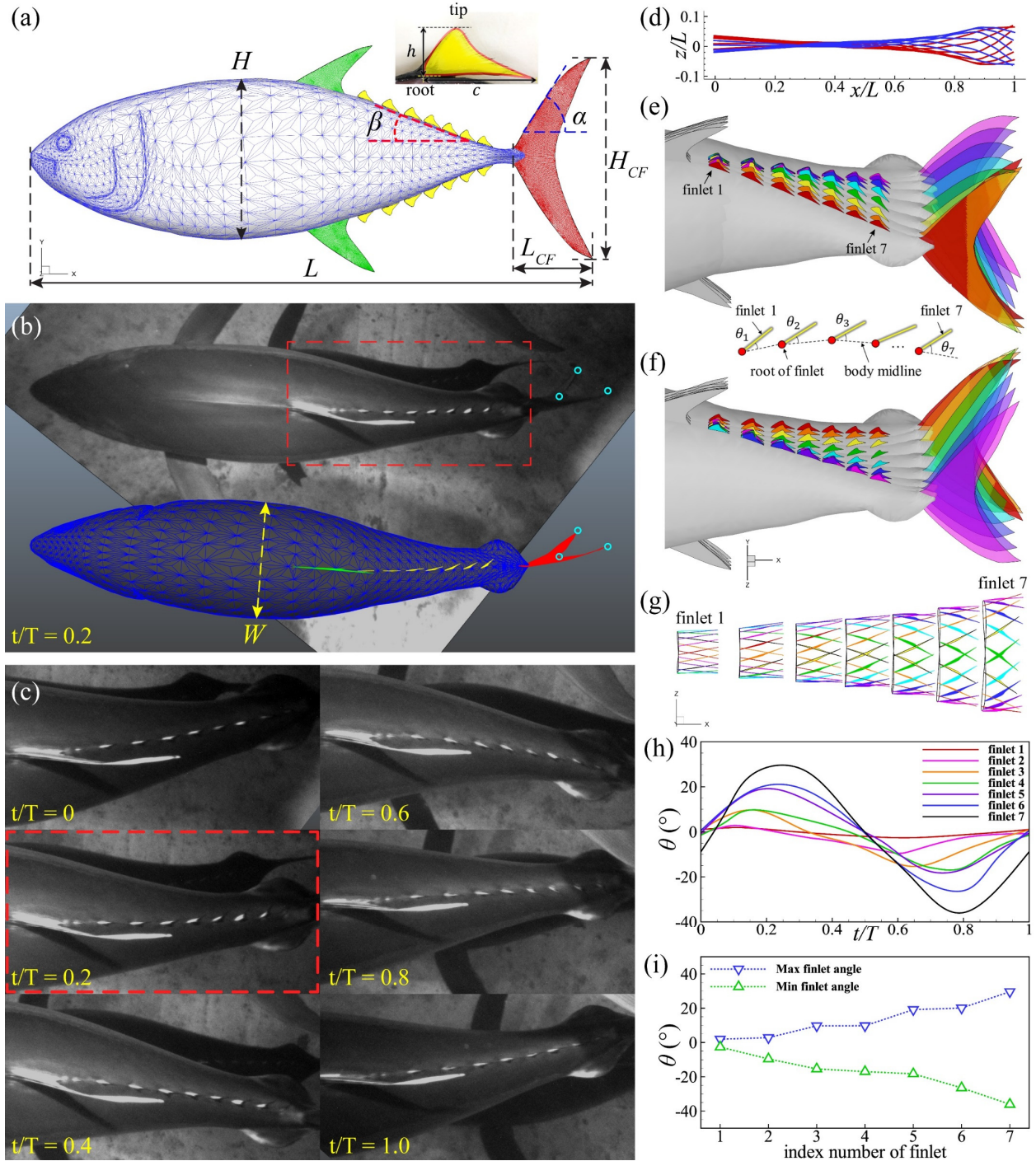


Figure 5-2: (a) A lateral view of the reconstructed computational model of a yellowfin tuna (*Thunnus albacares*) with trunk (in blue), dorsal and anal fins (in green), dorsal and anal finlets (in yellow), and caudal fin (in red). (b) A side-by-side comparison between the live tuna and the computational model from the top view at $t/T=0.2$. (c) Snapshots on the posterior body and dorsal

finlets of a yellowfin tuna swimming steadily during a representative tail beat cycle. (d) Midlines of the reconstructed computational model during the left-to-right stroke (in blue) and right-to-left stroke (in red) of a tail beat cycle. (e) Reconstructed finlet kinematics and swimming kinematics of the posterior trunk and caudal fin during the left-to-right stroke. (f) Reconstructed finlet kinematics and swimming kinematics of the posterior trunk and caudal fin during the right-to-left stroke. (g) A top view of dorsal finlet kinematics during a tail beat cycle. In (e), (f), and (g), a color change corresponds to a time change of $T/16$. (h) Instantaneous finlet angle (θ) of the dorsal finlets during a tail beat cycle. (i) Finlet angle ranges of the dorsal finlets during a tail beat cycle.

The body midline profile (Figure 5-2d) shows the reconstructed swimming kinematics of the computational model, which is similar to those of yellowfin tuna swimming reported [5, 109]. The reconstructed kinematics of the finlets and caudal fin of the computational model is shown every $T/16$ during the left-to-right stroke (Figure 5-2e) and right-to-left stroke (Figure 5-2f), respectively, associated with the top view of finlet kinematics and the root trajectories (Figure 5-2g). The pitching kinematics of a finlet is described by finlet angle θ which defines the angle between the finlet chord and the body midline. It is found that finlets undergo both heaving and pitching motion (Figure 5-2h) and are delayed in phase from finlet 1 to finlet 7 (Figure 5-2i). Both motion amplitudes increase posteriorly, being consistent with our previous findings [108]. The peak-to-peak pitching amplitude at finlet 7 is 64.2° , while this value is only 4.6° at finlet 1. Finlet angles show noticeable asymmetry between the L-to-R and the R-to-L strokes, which is commonly observed in tuna [65, 108] and mackerel swimming [56, 57].

The key geometric quantities of the computational model are marked in Figure 5-2a and measured at stretched body position. Quantities of the trunk, dorsal, anal, and caudal fins are listed in Table 5-1 and those of the finlets in Table 5-2. Here, L denotes the body length, L_{CF} is the length of the caudal fin. H and H_{CF} denote the heights of the trunk and caudal fin, respectively. W denotes the widths of the trunk. A_{CF} , A_{DF} , and A_{AF} denote the areas of the caudal fin, dorsal fin (secondary), and anal fin, respectively. the aspect ratio (AR) of the caudal fin is calculated as $AR = H_{CF}^2/A_{CF}$. α and β are the angles of the dorsal edge of the posterior body and the leading edge of the caudal fin with respect to the horizontal plane, respectively. A_{FL} and L_{FL} denote the area and chord length of each finlet, respectively. All lengths are normalized by the body length L , and areas are normalized by A_{AF} . It is found that the summed area of finlets in yellowfin tuna is 18.8% of the caudal fin area, which is larger than the 15% found in mackerel [56].

Table 5-1: Normalized geometric quantities of trunk and fins

L	L_{CF}	H	H_{CF}	W	A_{CF}	A_{DF}	A_{AF}	AR	α	β
1.000	0.138	0.288	0.359	0.209	1.000	0.225	0.231	7.33	58°	21°

Table 5-2: Normalized geometric quantities of finlets (dorsal only)

	finlet 1	finlet 2	finlet 3	finlet 4	finlet 5	finlet 6	finlet 7	Averaged	Sum
L_{FL}	0.0297	0.0331	0.0339	0.0334	0.0320	0.0303	0.0291	0.0316	--
A_{FL}	0.0118	0.0146	0.0154	0.0149	0.0136	0.0122	0.0113	0.0134	0.0938

5.3 Simulation Setup

A Cartesian computational grid with stretching grid configuration was employed in the simulations (Figure 5-3a). The computational domain size was $12L \times 6L \times 6L$ with total grid points around 14.0 million ($449 \times 193 \times 161$) and a minimum grid spacing at $\Delta_{min} = 0.0021L$. The grid was designed to resolve the fluid field in the vicinity of the computational model and its wake with high resolution. The left-hand boundary was set as velocity inlet with constant incoming flow speed U_∞ . A homogeneous Neumann boundary condition was used for the pressure at all boundaries. A no-slip boundary condition was applied at the model surface. Denser meshes are given around the finlets and caudal fin to better resolve the morphology and the kinematics of finlets and the vortex wake associated with the finlet-caudal fin interaction.

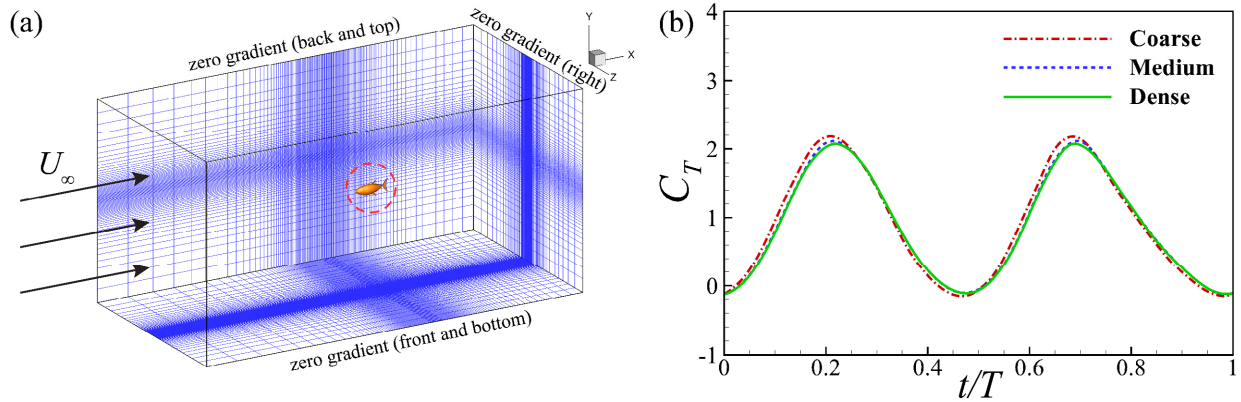


Figure 5-3: (a) Schematic of the computational mesh and boundary conditions used in the present simulation, where U_∞ denotes swimming speed. (b) Comparison of instantaneous thrust coefficient of the caudal fin between coarse, medium, and dense meshes.

The size of the computational domain was proven to be sufficiently large to obtain converged results by extensive simulation tests. In addition, a convergence study was performed to demonstrate the grid-independent results. Figure 5-3*b* shows the comparison of the instantaneous thrust coefficient of the caudal fin at four different grid densities. The minimum grid spacings of the coarse, medium, and dense meshes are $0.0043L$, $0.0030L$, and $0.0021L$, respectively. The drag coefficient converged as the grid spacing decreased. The mean drag difference between the fine and the dense mesh was less than 2.0%.

In this study, the key parameters associated with the flow simulation of tuna swimming are the Reynolds number Re and the Strouhal number St defined as follows, respectively,

$$Re = \frac{U_{\infty}L}{\nu} \qquad St = \frac{fA}{U_{\infty}} \qquad (5-1)$$

where U_{∞} is incoming flow pointing to x-positive, L is the body length, ν denotes the kinematic viscosity, f is the tail beat frequency, and A is the peak-to-peak amplitude of the caudal fin.

The measured Reynolds number of the yellowfin tuna was approximately 1.0×10^6 , which is challenging for direct numerical simulations. The purpose of conducting viscous flow simulation is to characterize the fundamental flow features of tuna swimming. Previous studies have shown that key wake structure features in the propulsion of flapping foils [77] and fish pectoral fin [97] swimming are robust to changing Re . In this study, in order to understand the vortex dynamics, the tuna swimming is simulated at $Re=6000$ to meet both requirements of accuracy and computational cost.

Among the steady swimming videos captured, the measured swimming speed is around 1.0~1.2 m/s, the tail beat frequency is from 2.3~3.4 Hz, the peak-to-peak tail beat amplitude is

from $0.12L$ to $0.17L$, and the Strouhal number ranges from 0.31 to 0.55. The Strouhal number for the present reconstruction is 0.483 and is used for the simulation.

The hydrodynamic force acting on tuna is computed by the direct integration of instantaneous pressure and shear over the trunk, fin, and finlet surfaces. The hydrodynamic power output is defined as the rate of instantaneous work done by the trunk and fins. The thrust (F_T), lateral (F_Z) forces, and power output (P_{out}) are nondimensionalized as thrust (C_T), lateral (C_Z), and power (C_{PW}) coefficients, respectively, as shown in (5-2).

$$C_T = \frac{F_T}{\frac{1}{2}\rho U_\infty^2 A_{CF}} \quad C_Z = \frac{F_Z}{\frac{1}{2}\rho U_\infty^2 A_{CF}} \quad C_{PW} = \frac{P_{out}}{\frac{1}{2}\rho U_\infty^3 A_{CF}} \quad (5-2)$$

where, F_T points to x-negative, F_Z points to z-positive, ρ is fluid density, A_{CF} denotes the area of the caudal fin, and U_∞ is the incoming flow speed at 0.27 body length per tail beat cycle. Note that if $C_T < 0$, $C_D = -C_T$.

5.4 Results

The hydrodynamics performance and vortex dynamics of the reconstructed computational model with original finlet pitching kinematics (M1) are presented in section 5.4.1. It is found that trunk, dorsal fin, anal fin, and finlets all produce net drag during each tail beat cycle, and the drag forces are balanced by the thrust produced by the caudal fin. Dorsal and ventral finlets generate a counter-rotating conical vortex pair during each stroke and interact with the caudal fin at the middle part.

The hydrodynamic effect of finlets on swimming performance is then studied in section 5.4.2, where the performance results between M2 (computational model with finlets removed) and M1 are compared. It is found that finlets help increase caudal fin thrust by 8% and reduce trunk drag by 7%. We also introduce the nominal propulsive efficiency of finlets—a metric on the efficiency of finlets to gain thrust enhancement for the swimming system—and found that the effect of swimming with finlets is equivalent to adding a propulsor with propulsive efficiency of 23.6%. By analyzing the surface pressure, we have located the regions that produce more thrust at the posterior trunk and the middle of the caudal fin owing to the presence of finlets. By analyzing the flow field in detail, we have demonstrated that the presence of finlets at the dorsal and ventral margins is responsible for the trunk drag reduction and the interactions between the finlet-induced vortex pair and the caudal fin is responsible for the caudal thrust enhancement.

The hydrodynamic effect of pitching kinematics of finlets is studied in section 5.4.3, where the finlet forces and the overall performance of tuna swimming between M3 (computational model with finlets fixed to the body along the local body centerline at all times) and M1 are compared. It is found that the pitching kinematics of finlets help reduces the finlet drag, lateral force amplitude, and power consumption. The lower drag and power consumption of the pitching finlets results in a higher nominal propulsive efficiency of 23.6% than the 16.6% of body-fixed finlets.

5.4.1 Hydrodynamic Performance and Vortex Dynamics of Tuna Swimming

The hydrodynamic force/power, surface pressure, thrust distribution, and wake topology of the reconstructed computational model (M1) are presented during the fifth tail beat cycle of the simulation when the results have reached a periodic state (Figure 5-4).

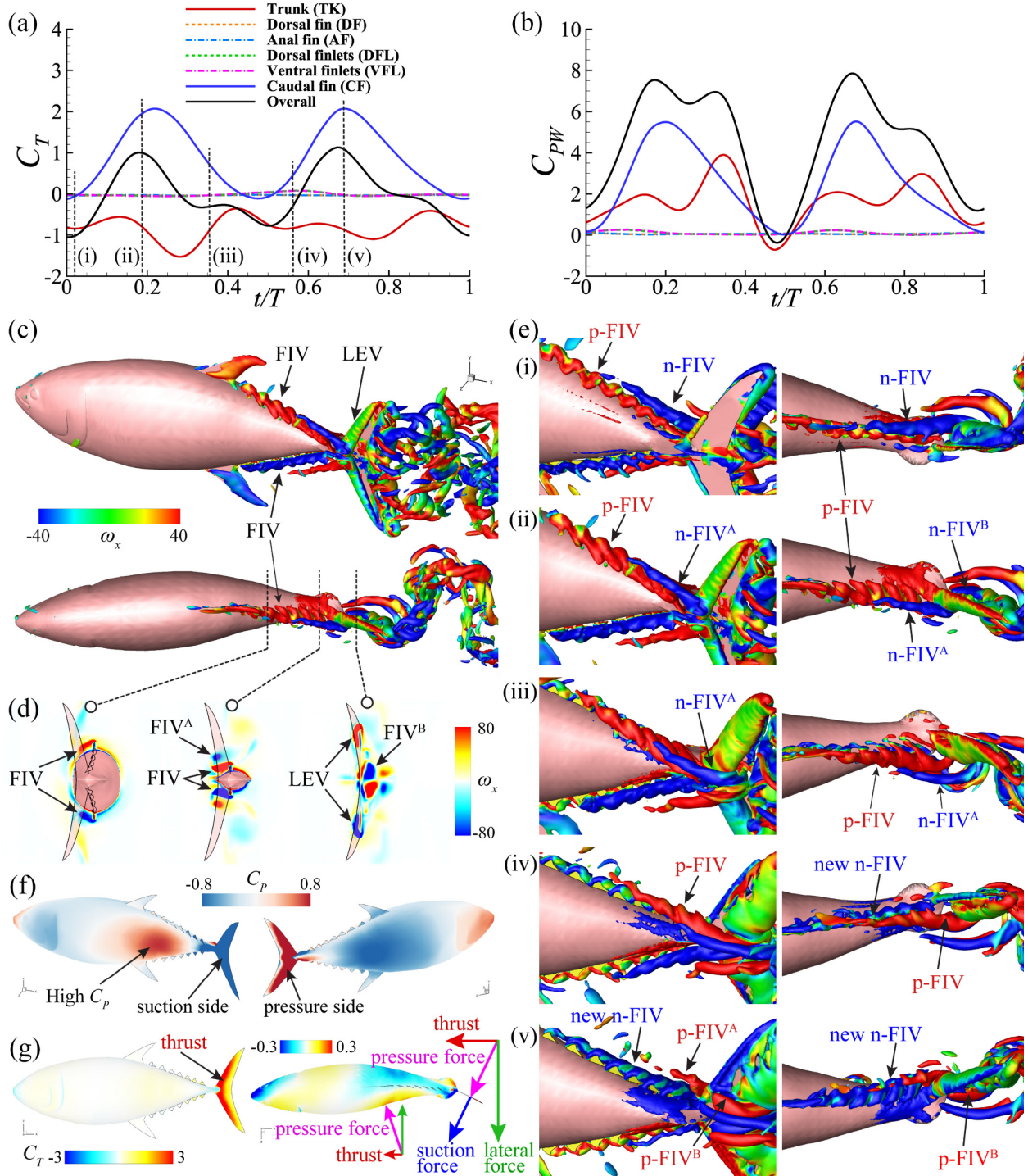


Figure 5-4: (a) Instantaneous thrust coefficient and (b) power coefficient of the trunk, fins, and finlets during one tail beat cycle of tuna forward swimming. (c) Three-dimensional vortex wake structure of tuna swimming at (ii) $t/T=0.19$ from perspective view and top view, respectively. (d)

x-vorticity contours at three transverse planes cutting through the posterior trunk and caudal fin. (e) Vortex structure of the posterior trunk, finlets, and caudal fin at (i) $t/T=0.02$, (ii) $t/T=0.19$, (iii) $t/T=0.35$, (iv) $t/T=0.56$, and (v) $t/T=0.69$, respectively, from both a perspective view and a top view. (f) Instantaneous surface pressure over the trunk, fins, and finlets at (ii) $t/T=0.19$. (g) Instantaneous thrust production over the trunk, fins, and finlets at (ii) $t/T=0.19$. The isosurface of the wake structures is visualized by $|\lambda_i|=5$. The λ_i -isosurface is filled by the contour of vorticity ω_x which is normalized by U_∞/L . The finlet induced vortex (FIV) and leading edge vortex (LEV) are identified.

The instantaneous hydrodynamic force (Figure 5-4a) and power consumption (Figure 5-4b) of all six parts of M1 show that the trunk produces drag at all times, while the caudal fin produces thrust with two major peaks at the mid-strokes of L-to-R and R-to-L strokes, respectively, being consistent with its instantaneous power consumption. From their cycle averaged values listed in Table 5-3 and Table 5-4, it is found that caudal fin consumes 56% of the total power to produce thrust that balance the drag generated by other parts (with a minimal overall net drag of -0.0015). The dorsal fin, anal fin, and finlets (dorsal and ventral) all produce small drag forces at low power consumption. Specifically, dorsal and ventral finlets together generate use 4.8% of the total power and generate 3.1% of the total drag.

The instantaneous 3-D wake structure of M1 during middle L-to-R stroke is visualized using isosurfaces of λ_i -criterion [110] flooded by vorticity ω_x (Figure 5-4c) and vorticity contour of ω_x at three transvers planes cutting through the posterior body and caudal fin (Figure 5-4d). Major vortex structures are identified including the finlet-induced vortices (FIVs) at the dorsal and ventral

margins of the trunk, Leading-edge vortex (LEV) formed on the caudal fin, and interconnected vortex rings generated by the caudal fin in the downstream.

Detailed analysis of vortex dynamics (Figure 5-4e) at the posterior body shows significant interactions between FIVs and the caudal fins. It is found that, during each stroke, dorsal and ventral finlets each induce a conical vortex that converges to the middle of the caudal fin as they convect downstream, forming a counter-rotating vortex pair before cutting by the caudal fin into two parts. This process happens twice during each tail beat cycle with the rotation directions of FIVs altered between each stroke.

Specifically, at early L-to-R stroke (Figure 5-4e(i)), positive FIV (p-FIV) starts to form at individual finlets, while negative FIV (n-FIV) has been fully developed into a coherent conical vortex. Around mid-stroke (Figure 5-4e(ii)), p-FIV continues to develop at each finlet and start to merge, while n-FIV is cut by caudal fin into two parts—n-FIV^A and n-FIV^B on different sides of the caudal fin. At late L-to-R stroke (Figure 5-4e(iii)), p-FIV is stronger and more coherent and begins to detach from finlets, while n-FIV^A becomes more elongated to the left of the caudal fin. At early R-to-L stroke (Figure 5-4e(iv)), the p-FIV is fully developed into a conical vortex and converges to the middle of the tail, forming a counter-rotating vortex pair with its ventral counterpart, while new n-FIV starts to form at the leading edge. At mid-stroke (Figure 5-4e(v)), p-FIV is cut by caudal fin, a mirrored process happened to n-FIV around half tail beat cycle ago (Figure 5-4e(ii)).

Surface pressure contour of C_p at $t/T=0.19$ (Figure 5-4f) shows high-pressure and low-pressure regions on the trunk as well as the pressure side and suction side of the caudal fin. The instantaneous thrust distributions on the body and caudal fin (Figure 5-4g) are then calculated from

the surface pressure distributions. It is found that most of the thrust is produced at the leading-edge region of the caudal fin where LEV is formed. A thrust-producing region is found at the left side of the posterior trunk where high surface pressure presents, despite that the entire trunk is drag-producing.

Table 5-3: Cycle-averaged thrust coefficient \bar{C}_T of different parts of the tuna models and the overall axial thrust force \bar{C}_X . Note that negative values denotes drag producing.

	TK	DF	AF	DFL	VFL	CF	\bar{C}_X
M1	-0.7969	-0.0327	-0.0311	-0.0136	-0.0141	0.8869	-0.0015
M2	-0.8569	-0.0323	-0.0314	--	--	0.8209	-0.0997
M3	-0.7982	-0.0328	-0.0313	-0.0205	-0.0203	0.9074	0.0043

Table 5-4: Cycle-averaged power coefficient \bar{C}_{PW} of different parts of the tuna models and the overall power consumption \bar{C}_{PW} .

	TK	DF	AF	DFL	VFL	CF	\bar{C}_{PW}
M1	1.610	0.059	0.064	0.106	0.110	2.523	4.472
M2	1.530	0.058	0.062	--	--	2.407	4.057
M3	1.660	0.059	0.064	0.166	0.173	2.563	4.685

5.4.2 Caudal Fin Thrust Enhancement and Trunk Drag Reduction Owing to Finlets

To study the hydrodynamic role of finlets in propulsive performance and the underlying flow physics, the hydrodynamic force/power, surface pressure, and flow results are compared between M2 (computational model with finlets removed) and M1.

The comparisons of instantaneous caudal fin thrust and trunk drag (Figure 5-5a) show larger caudal fin thrust production and less trunk drag generation in M1 than those of M2, respectively. The instantaneous caudal fin thrust enhancement ΔC_T and trunk drag reduction ΔC_D are calculated by $\Delta C_T = (C_{T|M1} - C_{T|M2})/\bar{C}_{T|M2}$ and $\Delta C_D = (C_{D|M1} - C_{D|M2})/\bar{C}_{D|M2}$, respectively, and plotted in Figure 5-5b. Significant trunk drag reductions are found at the early stages of L-to-R and R-to-L strokes, respectively, with peak reductions over 15%. It is noteworthy that, the phase of high trunk drag reduction corresponds to the phase when FIVs are generated during each stroke, indicating the correlation between trunk drag reduction and FIV generation. Significant caudal fin thrust enhancement is peaked both at the early and later stages of each stroke with the largest peak value near 20%.

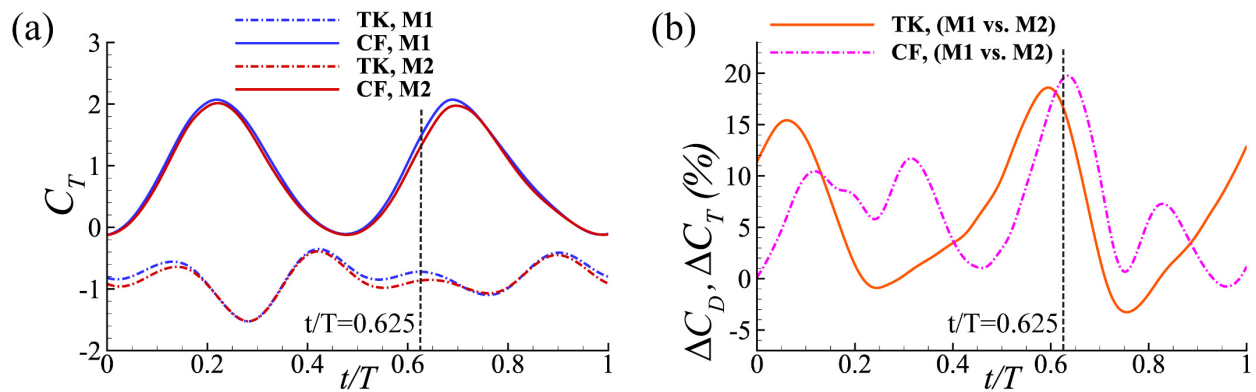


Figure 5-5: (a) Comparison of instantaneous thrust coefficient (C_T) of trunk and caudal fin between the M1 and M2. (b) Instantaneous caudal fin thrust enhancement (ΔC_T) and trunk drag reduction (ΔC_D) of M1 with pitching finlets.

The cycle-averaged thrust enhancement $\Delta \bar{C}_T$ and drag reduction $\Delta \bar{C}_D$ are calculated $\Delta \bar{C}_T = (\bar{C}_{T|M1} - \bar{C}_{T|M2})/\bar{C}_{T|M2}$ and $\Delta \bar{C}_D = (\bar{C}_{D|M1} - \bar{C}_{D|M2})/\bar{C}_{D|M2}$, respectively and listed in Table 5-5. It is found that finlets help increase caudal fin thrust by 8% and reduce trunk drag by 7%.

Table 5-5: Caudal fin thrust enhancement and trunk drag reduction by pitching finlets

	CF, \bar{C}_T	CF, $\Delta \bar{C}_T$	TK, \bar{C}_D	TK, $\Delta \bar{C}_D$
M1	0.8869	8.0%	0.7969	7.0%
M2	0.8209	--	0.8569	--

Although finlets do not generate thrust, their effects on caudal fin thrust enhancement and trunk drag reduction result in more propulsive force production of the system. Therefore, the effect of finlets is similar to a propulsor. To quantify the finlets' effect in increasing propulsive force for the system, we define a nominal propulsive efficiency η_{nominal} as,

$$\eta_{\text{nominal}} = \frac{\Delta \bar{C}_X}{\Delta \bar{C}_{PW}} \quad (5-3)$$

where $\Delta\bar{C}_X$ is the difference in cycle-averaged overall axial force between tuna models with pitching finlets (M1 and M3) and the tuna model with finlet removed (M2). $\Delta\bar{C}_{PW}$ is the difference in cycle-averaged overall power coefficient between M1 and M3 and M2. For example, to calculate the η_{nominal} of pitching finlets in M1, $\eta_{\text{nominal}} = (\bar{C}_{X|M1} - \bar{C}_{X|M2})/(\bar{C}_{PW|M1} - \bar{C}_{PW|M2})$. It is found that the effect of swimming with finlets is equivalent to adding a propulsor with propulsive efficiency of 23.6% (Table 5-6).

Table 5-6: Cycle-averaged overall axial thrust force (\bar{C}_X) and overall power (\bar{C}_{PW}) coefficients, and nominal propulsive efficiency η_{nominal} of pitching finlets in M1.

Cases	\bar{C}_X	$\Delta\bar{C}_X$	\bar{C}_{PW}	$\Delta\bar{C}_{PW}$	η_{nominal}
M2	-0.0997	--	4.057	--	
M1	-0.0015	0.0982	4.472	0.415	23.7%

To reveal the flow phenomenon associated with the performance enhancement, we compare the vortex topology, surface pressure, and flow field information between M1 and M2 at $t/T=0.625$ when both thrust enhancement and drag reduction are pronounced.

Vortex topology of M1 and M2 (Figure 5-6a) show similar LEV and interconnected vortex rings generated by the caudal fin. However, because of the absence of finlets in M2, no n-FIV or p-FIV are generated. Instead, a negative shear layer (n-SL) and a positive peduncle vortex (p-PV) are formed at the dorsal surface of the posterior trunk and left side of the caudal fin, respectively. Hence, the caudal fin in M2 is interacting with a counter-rotating PV pair instead of the much stronger FIV pair in M1.

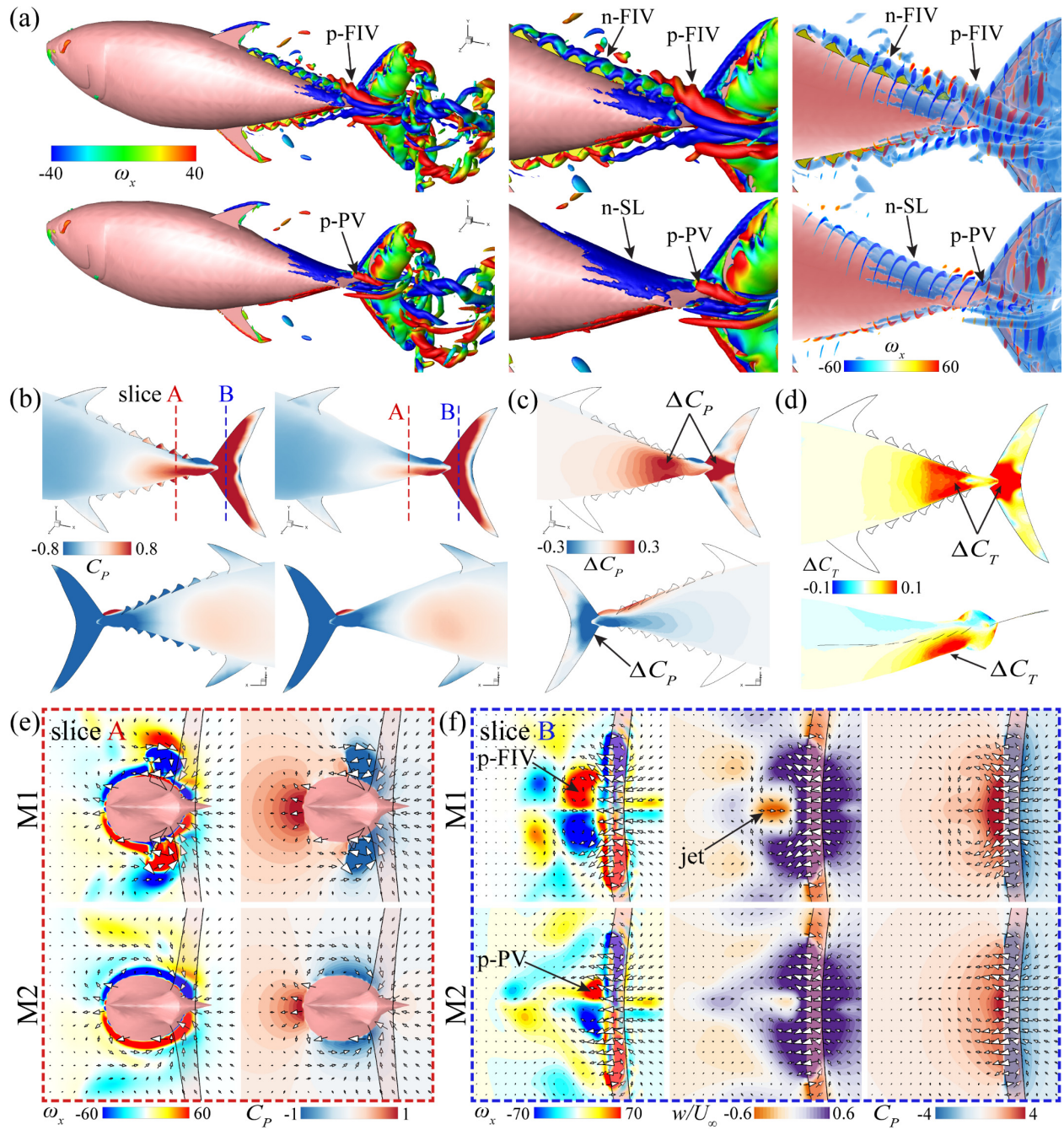


Figure 5-6: Comparison of (a) three-dimensional wake structure and (b) surface pressure C_p between M1 and M2 at $t/T=0.625$. (c) The surface pressure difference ΔC_p between M1 and M2. (d) Thrust enhancement ΔC_T regions in M1 owing to pitching finlets. (e) Comparison of vorticity contour and field pressure on slice A cutting through the posterior trunk between M1 and M2 (f) Comparison of vorticity contour and field pressure on slice B cutting through the posterior trunk between M1 and M2

Comparison of vorticity contour, lateral velocity, and field pressure on slice B cutting through the caudal fin. PV denotes peduncle vortex, SL denotes shear layer.

The comparison of surface pressure between M1 and M2 (Figure 5-6b) shows both higher positive pressure over the left surface and lower negative pressure over the right surface of the posterior trunk of M1 than those of M2. Differences in caudal fin pressure patterns are also shown. To better understand the pressure change, we have calculated the distribution of pressure difference on the trunk and caudal fin (Figure 5-6c) by subtracting the surface pressure of M2 from M1. It is found that major pressure differences happen on the left surface of the posterior body and the middle of the caudal fin on both sides.

The changes in surface pressure at the posterior body and caudal fin have further caused the change in thrust production at the corresponding regions (Figure 5-6d). The higher pressure at the posterior body generates more pressure force that is normal to the local surface, and the longitudinal component of this force contributes to thrust. Similarly, on the caudal fin, the pressure differences cause higher pressure force on the pressure side and lower suction force on the suction side, both contributing to more thrust production.

We have calculated the distribution of thrust difference over the trunk and caudal fin (Figure 5-6d), note that the thrust difference on the caudal fin combines both thrust changes of the pressure side and suction side). It is found that the location and pattern of thrust enhancement distribution exhibit a strong correlation with those of the pressure difference distribution. Specifically, the high thrust enhancement region on the caudal fin shows an outline that includes outline features of both

the increased pressure region on the pressure side and decreased pressure region on the suction side.

To connect the surface pressure distribution and vortex dynamics, we present flow field information including vorticity, velocity, and field pressure on transverse planes cutting through the posterior body (slice A, Figure 5-6e) and caudal fin (Figure 5-6f) where the thrust enhancement is pronounced. On slice A, the transverse flow moves past the posterior body of M2 freely and creates continuous shear layers. A high-pressure zone centered at the left stagnation point of the body and low-pressure regions surrounding the dorsal and ventral edges were found. In M1, however, the dorsal and ventral finlets have prevented the transverse flow from freely passing the posterior body. As a result, stagnation points and FIVs are created at the left side and right side of the finlets, respectively. In addition, the deflection of transverse flow by finlets impedes the relief of field pressure in the fluid domain on the left side of the body, resulting in higher field pressure in this domain. While lower negative pressure is found in the recirculation zone of the finlets on the right side. Slice B shows the hydrodynamics interactions between FIV pair and caudal fin in M1 and between PV pair and caudal fin in M2, respectively. The strong counter-rotating FIVs in M1 induce a water jet amid the FIV cores with the jet direction against the direction of caudal fin flapping. In contrast, the much weaker PVs in M2 do not induce significant water jet. It is found that the interaction of the water jet with the caudal fin in M1 creates higher field pressure in the fluid domain on the left of the caudal fin than that of M2. The increase in field pressure at both the posterior body and caudal fin are consistent with the surface pressure increases and the consequent thrust enhancements in these regions.

To further explore the thrust enhancement and the associated flow physics, the flow analysis of M1 and M2 (Figure 5-7) are compared at $t/T=0.31$ —the thrust enhancement peak during the

late L-to-R stroke. During this time instance (Figure 5-7a), the newly generated FIV pair in M1 and PV pair in M2 have not reached the caudal fin. Instead, the caudal fin in M1 is interacting with the PIV^A pair on the suction side. The distribution of surface pressure difference (Figure 5-7b) between M1 and M2 shows a significant negative pressure difference on the middle suction side of the caudal fin but no substantial pressure difference on the pressure side. The location and pattern of negative pressure difference are consistent with that of the thrust enhancement distribution of the caudal fin (Figure 5-7c), indicating that the lower suction pressure in M1 is the major contribution to the thrust enhancement at the moment.

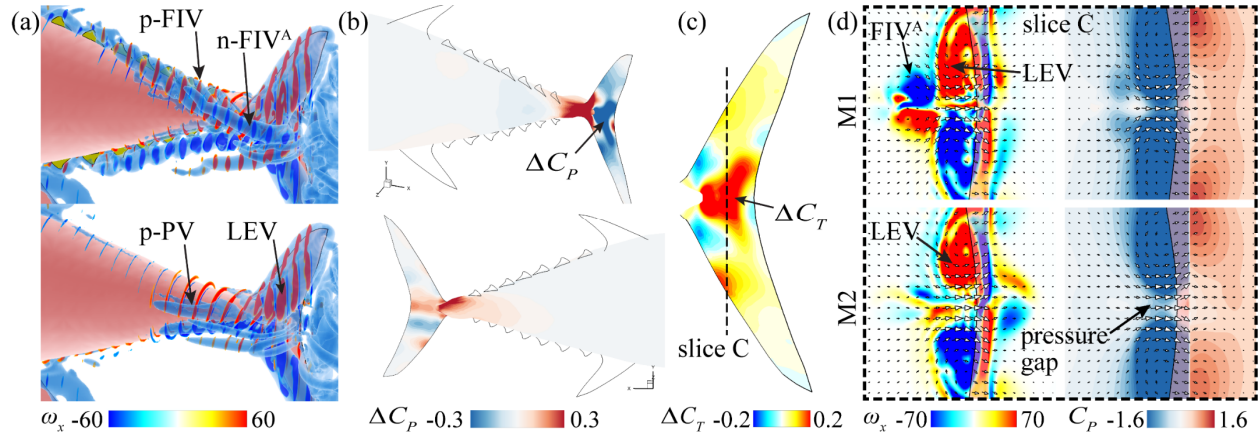


Figure 5-7: (a) Comparison of three-dimensional wake structure between M1 and M2 at $t/T=0.313$. (b) The surface pressure difference ΔC_p between M1 and M2 at $t/T=0.313$. (c) Thrust enhancement ΔC_T regions in M1 owing to pitching finlets. (d) Comparison of vorticity contour and field pressure on slice C cutting through the caudal fin between M1 and M2.

The vorticity and field pressure (Figure 5-7d) contours on slice C show that the dorsal and ventral LEVs in M2 are separated, leaving a clearance amid the two LEV cores at the middle of the caudal fin and consequently a pressure gap between dorsal and ventral low-pressure zones. In

contrast, because of the interaction with the FIV^A pair, the dorsal and ventral LEVs in M1 meet at the middle of the caudal fin and cover the entire span of the caudal fin with negative pressure. Therefore, the middle of the caudal fin in M1 has lower negative field pressure than that of M2, being consistent with the distributing of surface pressure difference and the thrust enhancement.

5.4.3 Hydrodynamic Benefit of Pitching Kinematics of Finlets

To study the effect of finlet kinematics on propulsive performance, we compare both the overall swimming performance and the finlet forces between M3 (computational model with finlets fixed to the body along the local body centerline at all times) and M1.

Comparison of instantaneous caudal fin thrust and trunk drag between M1, M2, and M3 (Figure 5-8a) shows that the caudal fin thrust in models with finlets (M1 and M3) is higher than that without finlets (M2) and that the trunk drag is lower in both the M1 and M3 than that in M2. The cycle-averaged thrust enhancement (Table 5-7) of M3 is 10.5%, which is even higher than the 8% of M1 (Table 5-5), while the cycle-averaged drag reduction of M3 is 6.9%, being similar to the 7% of M1.

Table 5-7: Caudal fin thrust enhancement and trunk drag reduction by fixed finlets.

	CF, \bar{C}_T		TK, \bar{C}_D
M3	0.9074	M3	0.7982
M2	0.8209	M2	0.8569
$\Delta\bar{C}_T$	10.5%	$\Delta\bar{C}_D$	6.9%

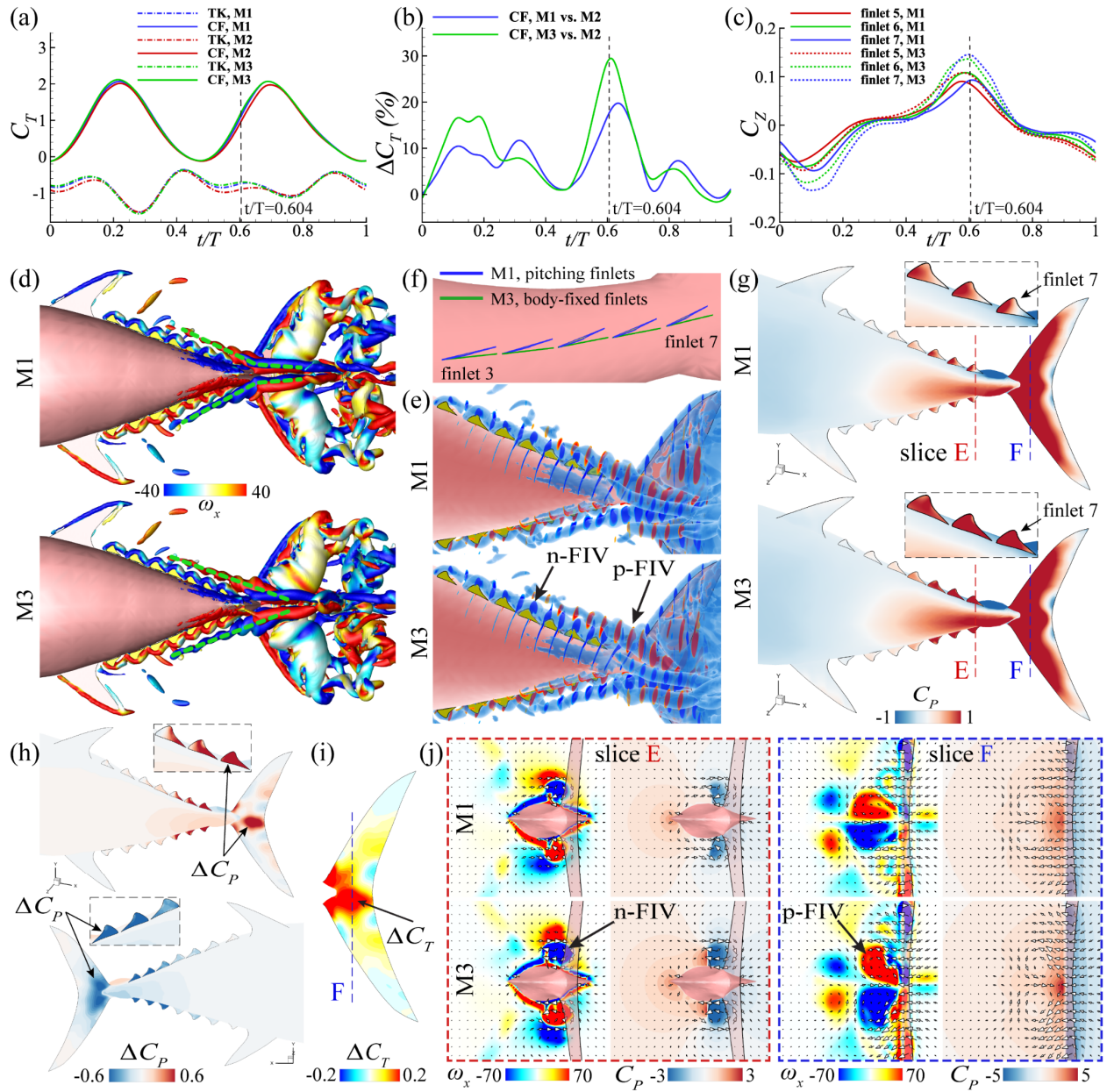


Figure 5-8: (a) Comparison of instantaneous thrust coefficient (C_T) of trunk and caudal fin between the M1, M2, and M3. (b) Comparison of instantaneous caudal fin thrust enhancement (ΔC_T) between M1 and M3. (c) Comparison of lateral force of finlet 5, 6, and 7 between M1 and M3. Comparison of three-dimensional wake structure from (d) a lateral view and (e) a perspective view, (f) pitching kinematics of finlets, (g) and surface pressure C_p over trunk, finlets, and caudal fin between M1 and M3 at $t/T=0.604$. (h) The surface pressure difference ΔC_p between M1 and M3. (i) The surface pressure difference ΔC_T between M1 and M3. (j) Comparison of three-dimensional wake structure from a lateral view and (e) a perspective view.

(i) Thrust enhancement ΔC_T region on caudal fin in M3 owing to fixed finlets. (j) Comparison of vorticity contour and field pressure on slice E cutting through the posterior trunk and slice F cutting through the caudal fin between M1 and M3, respectively.

The comparison of instantaneous thrust enhancement between M1 and M3 (Figure 5-8b) shows a larger enhancement of M3 at both the early stages of L-to-R and R-to-L strokes. We present the comparisons of wake structure, surface pressure, and flow field information on transverse planes between M1 and M3 at $t/T=0.6$ when a significant difference in thrust enhancement happens.

The wake topology (Figure 5-8d&e) shows more coherent FIVs in M3 than in M1. The dorsal and ventral FIVs in M1 converge to the peduncle quickly and meet at the leading edge of the caudal fin, resulting in an obtuse-angled shape in FIVs. While FIVs in M3 are less curved. They converge slower than those in M1 and meet more posteriorly at the middle of the caudal fin.

The difference in FIVs causes the difference in surface pressure on the caudal fin (Figure 5-8g). The distribution of surface pressure difference (Figure 5-8g) shows increased pressure on the pressure side and reduced pressure on the suction side both at the middle of the caudal fin, resulting in the enhanced thrust production (Figure 5-8i) at corresponding regions of pressure change.

The vorticity plots on slice D (Figure 5-8j) confirm that the LEV cores of M3 are more separated and that they are better attached to the left caudal fin surface than M1, indicating stronger interactions between FIVs and the caudal fin in M3. Meanwhile, higher field pressure in M3 around the middle of the caudal fin is found, being consistent with the higher surface pressure and larger thrust production at corresponding regions of the caudal fin.

The instantaneous surface pressure of finlets at $t/T=0.6$ is also compared between the independently pitching finlets in M1 and the body-fixed finlets in M3 (Figure 5-8c). For both the pitching finlets and body-fixed finlets, it is found that the positive pressure increases posteriorly from finlet 1 to finlet 7 with higher pressure found on finlets 5 to 7, and hence we focus on these three.

In M3 (Figure 5-8g), high pressure covers the entire left surface of body-fixed finlets 5 to 7, while in M1, high-pressure regions are much reduced and concentrated at the leading edge of each finlet. The distributions of the pressure difference between M1 and M3 show that pitching finlet 5 to 7 have lower positive pressure on the left side and higher negative pressure on the right side, resulting in the significantly lower lateral force generations of pitching finlet 5 to 7 at $t/T=0.6$ than the body-fixed ones.

Vorticity plots on slice D (Figure 5-8j) show less strength in dorsal and ventral FIVs generated by the pitching finlet 7 compared with that of the fixed finlet 7, alleviating the negative pressure in FIV cores on the right side of pitching finlets. In addition, the lower positive pressure on the left side of pitching finlets indicates that the pitching kinematics facilitate the relief of pressure on the pressure side.

We further compare the cycle-averaged drag and power consumption of finlets between M1 and M3 (Figure 5-9). Note that the force and power values plotted for each index number are the summed results of both the dorsal finlet and the corresponding ventral finlet. It is found that both the mean drag and mean power of pitching finlets are lower than those of the fixed finlets. Because of the pitching motion of finlets, the total finlet drag reduction is 32.1% and the total finlet power

reduction is 36.3% (Table 5-8), which are both beneficial for the propulsive performance of the entire swimming system.

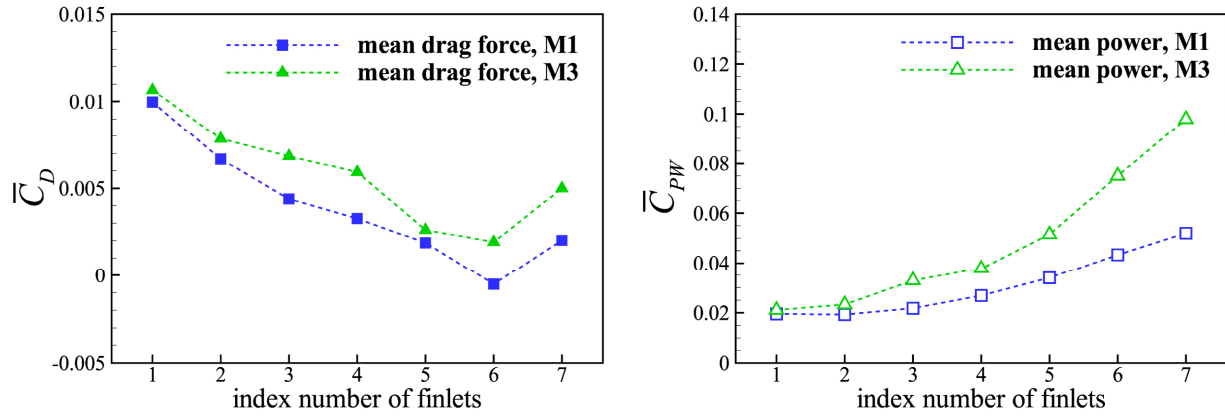


Figure 5-9: Comparison of cycle-averaged (a) drag coefficient (\bar{C}_D) and (b) power coefficient (\bar{C}_{PW}) of finlets between M1 and M3.

Table 5-8: Cycle-averaged overall thrust (\bar{C}_T) and power (\bar{C}_{PW}) coefficients of finlets and their changes.

	FL, \bar{C}_D		FL, \bar{C}_{PW}
M3	0.0408	M3	0.339
M1	0.0277	M1	0.216
$\Delta\bar{C}_D$	32.1%	$\Delta\bar{C}_{PW}$	36.3%

The lower drag and power consumption of the pitching finlets results in a higher nominal propulsive efficiency of 23.6% than the 16.6% of body-fixed finlets. (Table 5-9).

Table 5-9: Cycle-averaged overall axial force (\bar{C}_X) and power (\bar{C}_{PW}) coefficients, and nominal propulsive efficiency η_{nominal} of fixed finlets in M3.

Cases	\bar{C}_X	$\Delta\bar{C}_X$	\bar{C}_{PW}	$\Delta\bar{C}_{PW}$	η_{nominal}
M2	0.0997	--	4.057	--	
M3	-0.0043	0.1040	4.685	0.628	16.6%

5.5 Discussion

Two major performance enhancement mechanisms—lateral flow deflection by finlets at the posterior trunk (Figure 5-10a) and finlet-induced vortex (FIV) capture by caudal fin (Figure 5-10b)—are found to be responsible for the trunk drag reduction and caudal fin thrust increase.

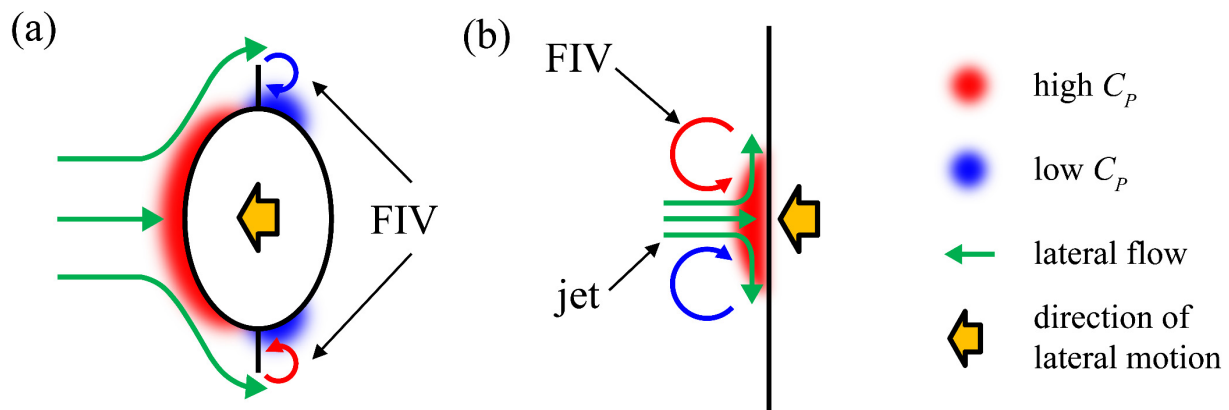


Figure 5-10: Schematics on mechanisms of (a) lateral flow deflection by finlets at the posterior trunk and (b) finlet-induced vortex (FIV) capture by caudal fin.

The lateral flow deflection mechanism (Figure 5-10a) shows that the dorsal and ventral finlets deflect the lateral flow and induces FIVs during the lateral motions of the posterior body. The deflection of lateral flow by finlets impedes the relief of hydrodynamics pressure on the side of the body against the lateral flow, resulting in higher pressure in the fluid domain.

The FIV capture mechanism (Figure 5-10b) shows that the caudal fin captures and interacts with the counter-rotating FIV pair during the flapping motion. The FIV pair induces a water jet that flows against the caudal fin motion. The FIV-induced jet interacts with the caudal fin at the middle part and creates higher hydrodynamic pressure in the fluid domain over the FIV capture site.

5.6 Chapter Summaries

In this section, we have combined experimental and numerical approaches to investigate the hydrodynamic role of finlets in the propulsive performance of tuna during steady swimming. High-speed videos of freely swimming yellowfin tuna were obtained to provide simultaneous kinematics of the trunk, median fins, and finlets of the fish. A biologically realistic computational model of yellowfin tuna was reconstructed based on live fish kinematics and measurements of finlets in yellowfin tuna specimens. High-fidelity flow simulations of tuna swimming were conducted using both the original computational model with pitching finlets (M1) and modified computational models with finlets removed (M2) and finlets fixed to the body (M3), respectively. The effect of finlets and the pitching kinematics of finlets on the hydrodynamic performance and vortex dynamics are examined by comparing the results across computational models, respectively.

It is found that finlets help increase caudal fin thrust by 8% and reduce trunk drag by 7%. The effect of swimming with finlets is equivalent to adding a propulsor with propulsive efficiency of 23.6%. Analyses on surface pressure and thrust distribution show regions that produce more thrust at the posterior trunk and the middle of the caudal fin owing to the presence of finlets. Vortex dynamics analysis shows that dorsal and ventral finlets generate a counter-rotating conical vortex pair during each stroke and interact with the caudal fin at the middle part. Detailed flow analysis reveals that the presence of finlets at the dorsal and ventral margins is responsible for the trunk drag reduction and the interactions between the finlet-induced vortex pair and the caudal fin is responsible for the caudal thrust enhancement.

It is further found that body-fixed finlets help increase caudal fin thrust by 10.5% and reduce trunk drag by 6.9%. Comparing the pitching finlets and body-fixed finlets, it is found that the pitching kinematics of finlets help reduces the finlet drag, lateral force amplitude, and power consumption. The lower drag and power consumption of the pitching finlets results in a higher nominal propulsive efficiency of 23.6% than the 16.6% of body-fixed finlets.

6 In-Line Propulsion: Enhanced Hydrodynamic Performance by Dorsal Fin and Anal Fin in Trout Swimming

Many fishes of the Salmonidae family, such as trout and salmon, are high-performance carangiform swimmers known for their long-distance migrations and high-speed swimming against strong currents. Recent studies have shown that the dorsal fin and anal fin play an important role in the hydrodynamics of trout swimming [25, 69, 70]. A key general goal of this section is to combine experimental and numerical approaches to examine the enhanced hydrodynamic performance by dorsal fin and anal fin in juvenile rainbow trout steady swimming. Four computational models, including the full fish model (M1: trunk (TK) + dorsal fin (DF) + anal fin (AF) + caudal fin (CF) + pelvic fins (PF)), the model with dorsal fin removed (M2: TK+AF+CF+PF), the model with anal fin removed (M3: TK+DF+CF+PF), and the model with pelvic fins removed (M4: TK+DF+AF+CF), were employed to examine the hydrodynamic effects of the dorsal fin, anal fin, and pelvic fins on the propulsive performance, respectively. For example, by comparing the hydrodynamic performance and vortex dynamics between the full fish model (M1) and the model with dorsal fin removed (M2), potential hydrodynamic interactions between dorsal fin, trunk, and caudal fin can be quantified.

6.1 Trout Kinematics and Computational Modes

Live fish experiments of juvenile rainbow trout (*Oncorhynchus mykiss*) steady swimming were conducted in a recirculating water tunnel (Figure 6-1), where we swam three individuals (6.0 to 7.2 cm total length L) at 0.8 to 1.6 body length per second ($L \cdot s^{-1}$) with tail beat frequencies from 2.8 to 3.6 Hz. The swimming kinematics is recorded with three synchronized high-speed

cameras (FASTCAM Mini AX50, Photron USA, Inc.) at 1000 fps and 1024×1024 pixel resolution from lateral, ventral, and posterior views, respectively. We have captured 13 video sequences where the fish perform free, steady swimming for 3 to 5 consecutive tail beat cycles. Since the swimming kinematics is robust with swimming speed, we have chosen one representative swimming kinematics of an individual at medium speed ($1.4 L \cdot s^{-1}$, $L=7.2\text{cm}$) for the kinematics reconstruction of the computational model in the present study.

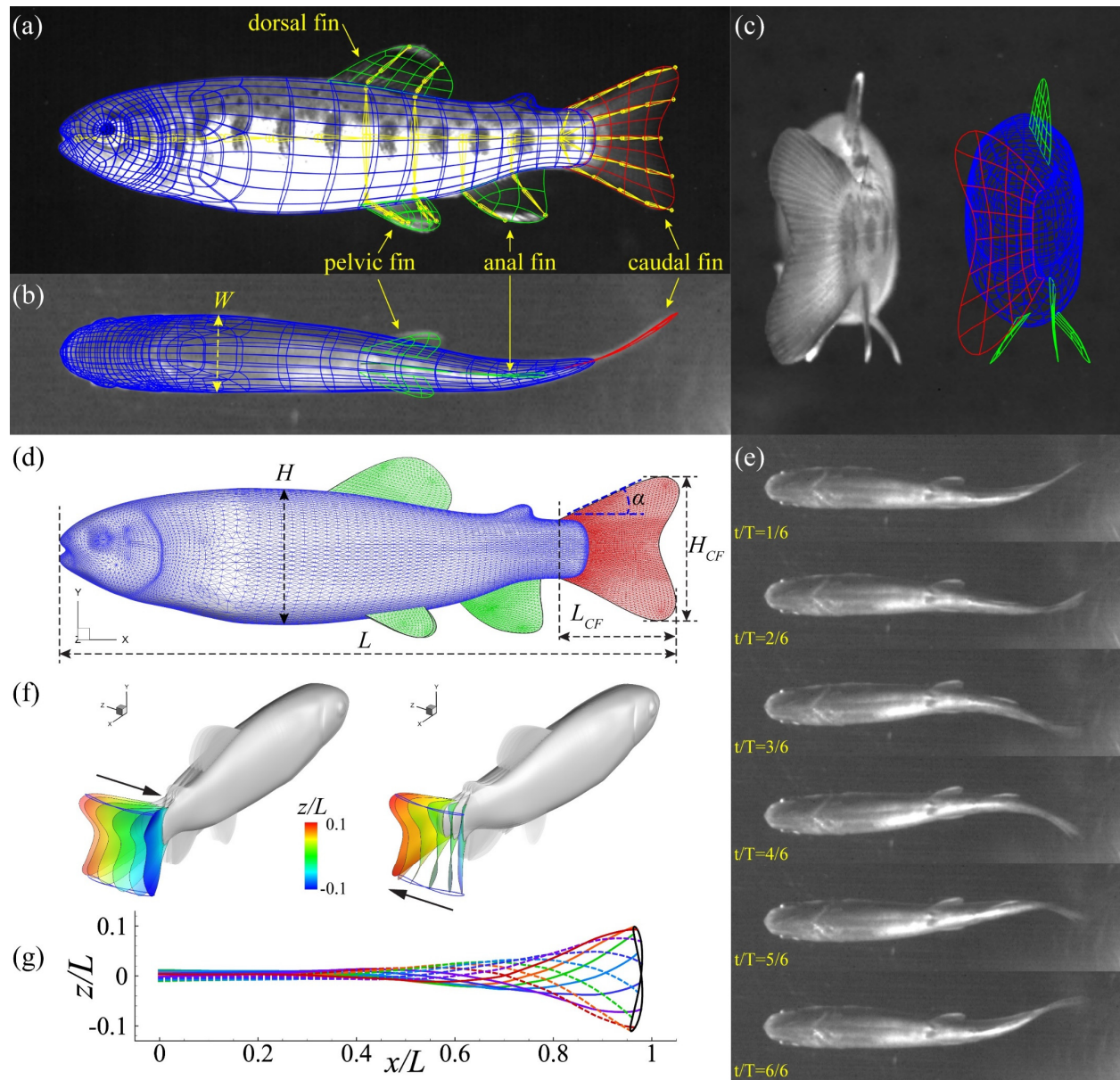


Figure 6-1: Morphological and kinematical modeling of juvenile rainbow trout (*Oncorhynchus mykiss*) during steady swimming. (a–b) High-speed camera images of live rainbow trout swimming overlapped with the reconstructed computational model from lateral and ventral views, respectively, at $t/T=1/6$. (c) Side-by-side comparison of live trout and computational model from posterior view at $t/T=1/6$. (d) The reconstructed computational model of juvenile rainbow trout with fine surface mesh on body and fins. (e) Kinematics of rainbow trout swimming during a tail-beat cycle from a ventral view. (f) Reconstructed swimming kinematics of computational model during left-to-right (L-to-R) and right-to-left (R-to-L) strokes, respectively. (g) A single tuna finlet to show the attached base and free posterior region. (f) Midlines of the computational model during L-to-R (dashed) and R-to-L (solid) strokes, respectively.

The 3-D computational model of juvenile rainbow trout (*O. mykiss*) (Figure 6-1) was reconstructed based on high-speed video images of live fish swimming. Among the videos captured, the pectoral fins of the fish were folded against the body throughout swimming, which is not expected to cause notable changes in hydrodynamics. Therefore, we consider the trunk (TK), dorsal fin (DF), anal fin (AF), caudal fin (CF), and pelvic fins (PF) in the computational model where the trunk is modeled as a solid body and the fins as zero-thickness membranes. A total number of 5.0×10^4 triangular elements were used on the model surface to resolve the morphological features of the trunk and fins of juvenile rainbow trout (TK: 3.7×10^4 , DF: 1.4×10^3 , AF: 2.4×10^3 , CF: 8.1×10^3 , and $2 \times \text{FP}$: 1.2×10^3). The swimming kinematics of the model is reconstructed in Autodesk Maya[®] (Autodesk, Inc.) using an image-guided reconstruction method [79]. This method has been successfully adopted to reconstruct manta ray [80] and fish [9] swimming (see our previous work [9] for more details).

The key geometric quantities of the computational model are marked in (Figure 6-1d) and measured at stretched body position. Quantities of the trunk (TK) and fins (DF, AF, CF, and PF) are listed in Table 6-1. Here, L denotes the body length, L_{CF} is the length of the caudal fin. H , and H_{CF} denote the heights of the trunk, caudal fin, respectively. W denote the width of the trunk. A_{DF} , A_{AF} , A_{CF} , and A_{PF} denote the areas of the dorsal fin, anal fin, caudal fin, and pelvic fin, respectively. the aspect ratio (AR) of the caudal fin is calculated as $AR = H_{CF}^2/A_{CF}$. α is the angle between the leading edge of the caudal fin and the horizontal plane. All lengths are normalized by the body length L , and are areas are normalized by A_{CF} .

Table 6-1: Normalized geometric quantities of the computational model of juvenile rainbow trout

L	L_{CF}	H	H_{CF}	W	A_{DF}	A_{AF}	A_{CF}	A_{PF}	AR	α
1.0	0.194	0.221	0.233	0.126	0.357	0.284	1.000	0.142	1.86	25°

6.2 Computational Setup

A Cartesian computational grid with stretching grid configuration was employed in the simulations (Figure 6-2a). The computational domain size was $10c \times 6c \times 6c$ with total grid points around 13.3 million ($513 \times 161 \times 161$) and a minimum grid spacing at $\Delta_{min} = 0.0024L$. The grid was designed to resolve the fluid field in the vicinity of the computational model and its wake with high resolution. The left-hand boundary was set as velocity inlet with constant incoming flow speed U_∞ . A homogeneous Neumann boundary condition was used for the pressure at all boundaries. A no-slip boundary condition was applied at the model surface.

The size of the computational domain was proven to be sufficiently large to obtain converged results by extensive simulation tests. In addition, a convergence study was performed to demonstrate the grid-independent results. Figure 6-2b shows the comparison of the instantaneous drag coefficient of the caudal fin at four different grid densities. The minimum grid spacings of the coarse, medium, fine, and dense meshes are $0.0048L$, $0.0038L$, $0.0030L$, and $0.0024L$, respectively. The drag coefficient converged as the grid spacing decreased. The mean drag difference between the fine and the dense mesh was less than 2.0%.

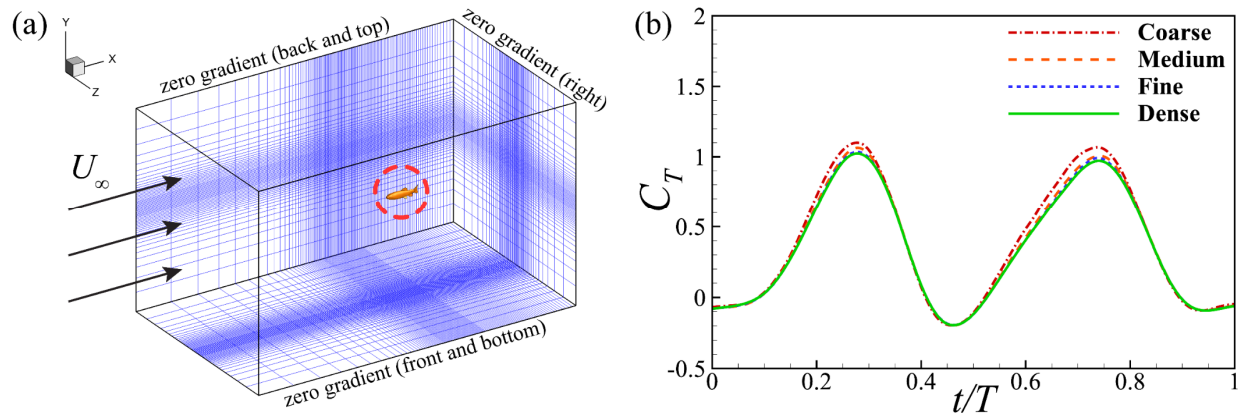


Figure 6-2: (a) Schematic of the computational mesh and boundary conditions used in the present simulation, where U_∞ denotes incoming flow speed. (b) Comparison of instantaneous thrust coefficient C_T of the caudal fin between coarse, medium, fine, and dense mesh.

In this study, the key parameters associated with the flow simulation of trout swimming are the Reynolds number Re and the Strouhal number St defined as follows, respectively,

$$\text{Re} = \frac{U_\infty L}{\nu} \quad \text{St} = \frac{fA}{U_\infty} \quad (6-1)$$

where U_∞ is incoming flow pointing to x-positive, L is the fish body length, ν denotes the kinematic viscosity, f is the tail beat frequency, and A is the peak-to-peak tip amplitude of the caudal fin.

Among the 13 steady swimming videos captured, the observed Re ranges from 3000 to 7800, and the St ranges from 0.46 to 0.73. In the representative video chosen for kinematics reconstruction (Figure 6-1e), the measured Re is 7100 and St is 0.47, which were then used for the numerical simulations.

The simulations were conducted at Re=7100 and St=0.47. The results presented, including the hydrodynamic performance and wake topology of the reconstructed computational model, are from the fifth tail beat cycle of the simulations when the flow field has reached a periodic state.

The hydrodynamic force acting on the computational model is computed by the direct integration of instantaneous pressure and shear over the trunk and fin surfaces. The hydrodynamic power output is defined as the rate of instantaneous work done by the trunk and fins. The thrust (F_T), and power output (P_{out}) are nondimensionalized as thrust (C_T), and power (C_{PW}) coefficients, respectively, as shown in (2.3).

$$C_T = \frac{F_T}{\frac{1}{2} \rho U_\infty^2 A_{CF}} \quad C_{PW} = \frac{P_{out}}{\frac{1}{2} \rho U_\infty^3 A_{CF}} \quad (6-2)$$

where, F_T points to x-negative, ρ is the fluid density, A_{CF} denotes the area of the caudal fin, and U_∞ is the swimming speed.

Four computational models, including the full fish model (M1: TK+DF+AF+CF+PF), the model with dorsal fin removed (M2: TK+AF+CF+PF), the model with anal fin removed (M3: TK+DF+CF+PF), and the model with pelvic fin removed (M4: TK+DF+AF+CF), were employed to examine the hydrodynamic effects of the dorsal fin, anal fin, and pelvic fins on the propulsive performance, respectively. For example, by comparing the hydrodynamic performance and vortex dynamics between the full fish model (M1) and the model with dorsal fin removed (M2), potential hydrodynamic interactions between dorsal fin, trunk, and caudal fin can be quantified.

6.3 Results

The hydrodynamics performance and wake topology of the full fish model (M1) are presented in section 6.3.1. It is found that the trunk, dorsal fin, and pelvic fins all produce net drag under the current swimming speed while the anal fin force is neutral. The drag forces are balanced by the thrust produced by the caudal fin. During each tail beat stroke, the dorsal fin induces lateral flow and generates a vortex that interacts with the caudal fin.

The hydrodynamic effects of the dorsal fin, anal fin, and pelvic fins on propulsive performance are studied in sections 6.3.2, 6.3.3, and 6.3.4, respectively, by comparing the performance and flow results between the full fish model (M1) and its counterpart with the dorsal fin removed (M2), anal fin removed (M3), or pelvic fins removed (M4). It is found that the dorsal fin helps increase caudal fin thrust by 11% but did not reduce trunk drag significantly. The anal fin helps both increase caudal fin thrust by 4.3% and reduce trunk drag by 6.9%. In addition, the pelvic fins significantly reduce the anal fin drag. Further analyses on surface pressure and vortex

dynamics reveal that the beneficial hydrodynamic interactions among the fins and the body are responsible for the thrust enhancements and drag reductions.

6.3.1 Hydrodynamic Performance and Vortex Structure of Trout Swimming

The hydrodynamic force/power, surface pressure, thrust distribution, and wake topology of the full fish model (M1) are presented during the fifth tail beat cycle of the simulation.

The instantaneous hydrodynamic force (Figure 6-3a) and power consumption (Figure 6-3b) of the trunk and fins of M1 show that the caudal fin and trunk dominate the hydrodynamic force productions and power consumptions. The caudal fin produces thrust with two major peaks at the mid-strokes of L-to-R and R-to-L strokes, respectively, being consistent with its instantaneous power consumption while the trunk drag production is relatively stable throughout the tail beat cycle. The cycle-averaged hydrodynamic forces (Table 6-2 and Table 6-3) show that the caudal fin consumes 57.3% of the overall power and produces sufficient thrust ($\bar{C}_T=0.384$) to balance the drag generated by the trunk and other fins, resulting in a minimal overall net thrust of 0.003. The dorsal fin and pelvic fins (left and right) produce small drag forces, while the anal fin net force is neutral. Specifically, dorsal, ventral, and anal fins together produce 14.9% of the total drag consumes 8.8% of the total power.

The instantaneous 3-D wake structure of M1 during middle R-to-L stroke was visualized using isosurfaces of λ_i -criterion [110] and the vorticity contour of ω_x was plotted at four transvers planes cutting through the posterior body and caudal fin (Figure 6-3c). Major vortex structures generated by the trunk and fins are identified, including the vortices induced by the dorsal fin (DFV), anal fin (AFV), and pelvic fins (PFVs), the vortex across the peduncle (PV), the leading

edge vortex (LEV) formed on the caudal fin, and the interconnected vortex rings (R1 to R3) generated by the caudal fin in the downstream. In addition, substantial interaction between DFV and the dorsal edge of the caudal fin is observed, which is analyzed in detail.

Table 6-2: Cycle-averaged thrust (\bar{C}_T) coefficients of the trunk and fins in trout computational models

	TK	DF	AF	PF (left)	PF (right)	CF	Overall
M1	-0.324	-0.025	-0.000	-0.015	-0.016	0.384	0.003
M2	-0.329	--	-0.000	-0.015	-0.016	0.346	-0.013
M3	-0.348	-0.024	--	-0.016	-0.017	0.368	-0.031
M4	-0.326	-0.025	-0.004	--	--	0.378	0.026

Table 6-3: Cycle-averaged power (\bar{C}_{PW}) coefficients of the trunk and fins in trout computational models

	TK	DF	AF	PF(L)	PF(R)	CF	Overall
M1	0.459	0.044	0.031	0.021	0.022	0.774	1.352
M2	0.450	--	0.031	0.021	0.022	0.735	1.258
M3	0.471	0.044	--	0.022	0.022	0.809	1.368
M4	0.455	0.044	0.035	--	--	0.760	1.295

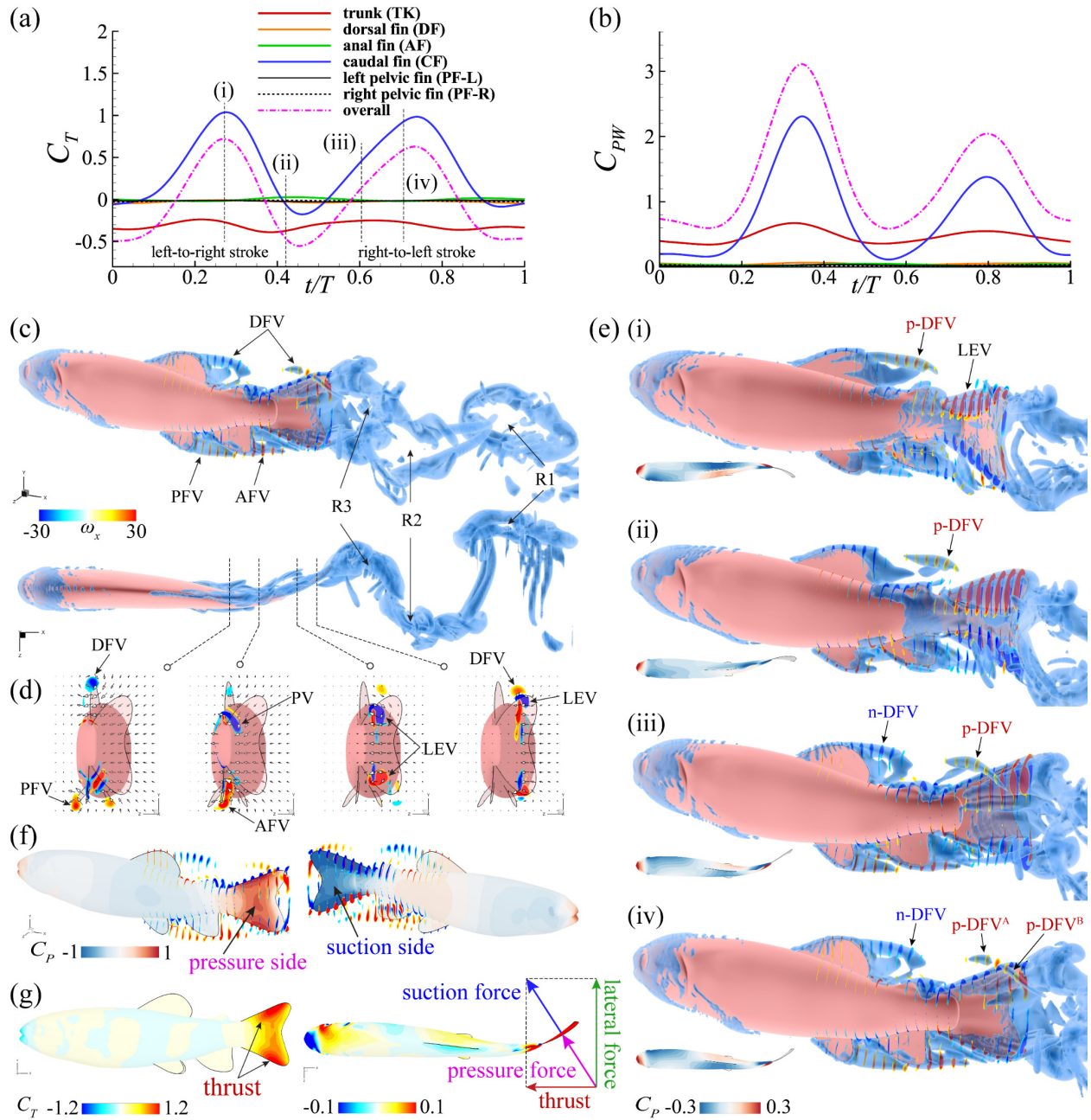


Figure 6-3: (a) Instantaneous thrust coefficient and (b) power coefficient of trunk and fins during one tail beat cycle of trout forward swimming. (c) Three-dimensional vortex wake structure of trout swimming at (iv) $t/T=0.71$ from perspective view and top view, respectively. (d) x-vorticity contours at four transverse planes cutting through the posterior trunk and caudal fin. (e) Vortex structure of the posterior trunk and fins at (i) $t/T=0.27$, (ii) $t/T=0.42$, (iii) $t/T=0.60$, and (iv)

$t/T=0.71$, respectively, from perspective view, associated with trunk surface pressure contour from the top view. (f) Instantaneous surface pressure over the trunk and fins at (iv) $t/T=0.71$. (g) Instantaneous thrust production over the trunk and fins at (iv) $t/T=0.71$. The isosurface of the wake structures is visualized by $|\lambda_i|=3.7$. The λ_i -isosurface is filled by the contour of vorticity ω_x which is normalized by U_∞/L . The dorsal fin vortex (DFV), anal fin vortex (AFV), pelvic fin vortex (PFV), peduncle vortex (PV), and leading edge vortex (LEV) are identified.

Vortex dynamic analysis (Figure 6-3e) shows that, during each stroke, the dorsal fin induces a DFV tube that is parallel to the flow direction. The DFV tube then convects downstream and interact with the caudal fin at the dorsal edge where it was cut into two parts. This process happens twice during each tail beat cycle with the rotation directions of DFV altered between each stroke. Specifically, at the middle L-to-R stroke (Figure 6-3e(i)), a positive DFV tube (p-DFV) starts to shed from the dorsal fin tip. The p-DFV tube shape is maintained while transporting downstream (late L-to-R stroke, Figure 6-3e(ii)) and is stretched and twisted when arrives at the dorsal edge of the caudal fin (early R-to-L stroke, Figure 6-3e(iii)). Meanwhile, a negative DFV tube (n-DFV) is formed at the dorsal fin. At the middle R-to-L stroke (Figure 6-3e(iv)), the p-DFV is elongated and cut into two parts—p-DFV^A on the right side of the fin and p-DFV^B on the right side—while interacting with the caudal fin. The n-DFV is fully developed at this time.

Surface pressure contour of C_p at $t/T=0.71$ (Figure 6-3f) shows pressure regions (positive surface pressure) and suction regions (negative surface pressure) on the trunk as well as the pressure side and suction side of the caudal fin. The instantaneous thrust distributions on the body and caudal fin (Figure 6-3g) are then calculated from the surface pressure distributions. For example, on the caudal fin, the suction force and the pressure force that are normal to the fin

surface both contribute to the thrust production in the longitudinal direction. It is found that most of the thrust is produced at the leading-edge regions of the caudal fin where LEVs are formed. Suction thrust is also produced at the right side of the head where negative surface pressure presents, being consistent with the airfoil-like thrust production mechanism found on the anterior body of adult trout swimming [111].

6.3.2 Caudal Fin Thrust Enhancement by Dorsal Fin

To study the hydrodynamic role of the dorsal fin in propulsive performance and the underlying flow physics, we compare the hydrodynamic force/power, surface pressure, and flow results between M2 (computational model with dorsal fin removed) and M1.

The force comparisons (Figure 6-4a) show significantly larger caudal fin thrust production in M1 than M2, while the difference in trunk drag generation is minimal. The instantaneous caudal fin thrust enhancement and trunk drag reduction are calculated by $\Delta C_T = (C_{T|M1} - C_{T|M2})/\bar{C}_{T|M2}$ and $\Delta C_D = (C_{D|M1} - C_{D|M2})/\bar{C}_{D|M2}$, respectively, and plotted in Figure 6-4b. Significant caudal fin thrust enhancement is found at middle L-to-R and R-to-L strokes, respectively, with peak enhancement over 25%. It is noteworthy that, the phase of high thrust enhancement corresponds to the phase when DFV interacts with the caudal fin, indicating the correlation between hydrodynamic interaction and thrust enhancement. In contrast, the trunk drag reduction owing to the dorsal fin is small.

The cycle-averaged thrust enhancement $\Delta \bar{C}_T$ and drag reduction $\Delta \bar{C}_D$ are calculated by $\Delta \bar{C}_T = (\bar{C}_{T|M1} - \bar{C}_{T|M2})/\bar{C}_{T|M2}$ and $\Delta \bar{C}_D = (\bar{C}_{D|M1} - \bar{C}_{D|M2})/\bar{C}_{D|M2}$, respectively, and are listed in Table 6-4. It is found that the presence of dorsal fin helps increase caudal fin thrust by a significant 11%, while it helps reduce trunk drag by only 1.5%.

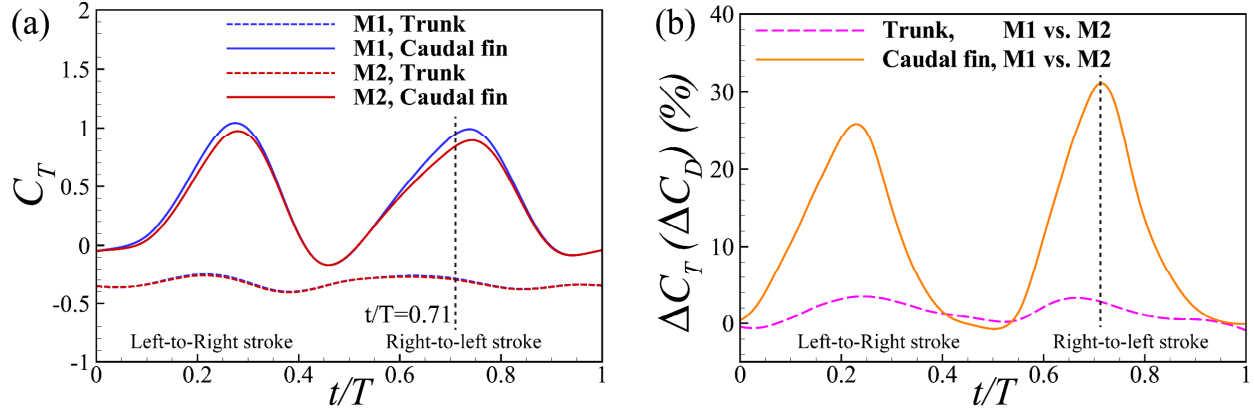


Figure 6-4: (a) Comparisons of instantaneous thrust coefficient (C_T) of trunk and caudal fin between M1 and M2, respectively. (b) Instantaneous caudal fin thrust enhancement (ΔC_T) and trunk drag reduction (ΔC_D) of M1 owing to dorsal fin compared to M2.

Table 6-4: Caudal fin thrust enhancement $\Delta \bar{C}_T$ and trunk drag reduction $\Delta \bar{C}_D$ owing to dorsal fin

	CF, \bar{C}_T	CF, $\Delta \bar{C}_T$	TK, \bar{C}_D	TK, $\Delta \bar{C}_D$
M1	0.384	11.0%	0.324	1.5%
M2	0.346	--	0.329	--

To reveal the flow phenomenon associated with the thrust enhancement, we compare the vortex topology, surface pressure/thrust, and flow field information between M1 and M2 at the instantaneous thrust enhancement peak ($t/T=0.71$) where $\Delta C_T=31\%$.

Vortex topology of M1 and M2 (Figure 6-5a) show similar AFV, PFV, and vortex ring structures between the two models. However, because of the presence of the dorsal fin in M1, significant p-DFV or n-DFV are generated and interacts with the caudal fin.

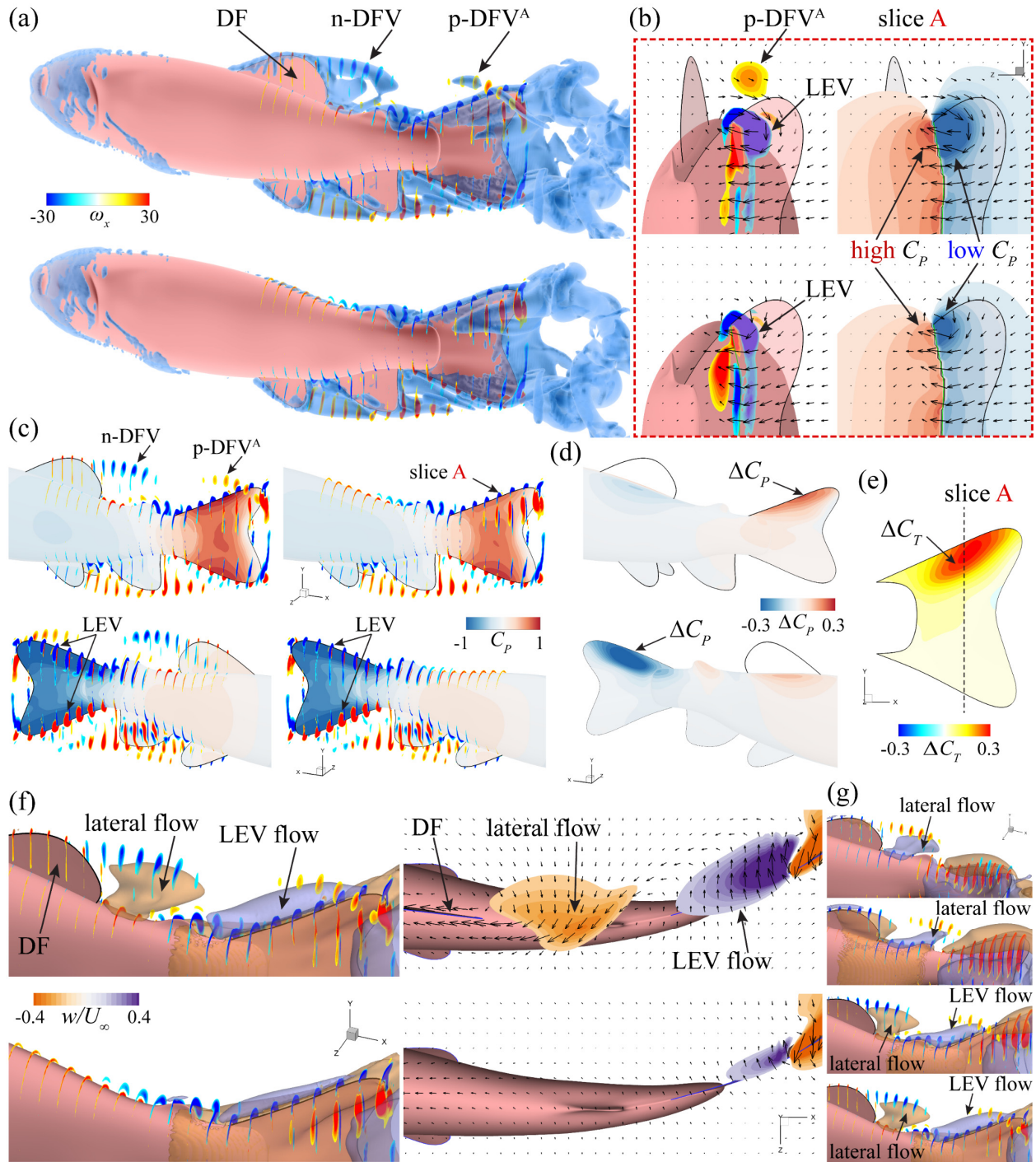


Figure 6-5: Comparison of (a) three-dimensional wake structure, (b) vorticity contour and field pressure on slice A cutting through the caudal fin, and (c) surface pressure C_p between M1 and M2 at $t/T=0.71$. (d) The surface pressure difference ΔC_p on trunk and caudal fin between M1 and M2 at $t/T=0.71$. (e) Thrust enhancement ΔC_T region on caudal fin in M1 owing to the dorsal fin

compared to M3. (f) Comparison of the isosurface of lateral flow (left) and lateral velocity contour on a coronal plane cutting through the dorsal fin and caudal fin (right). (g) The evolution of lateral velocity isosurface in M1 at (i) $t/T=0.27$, (ii) $t/T=0.42$, (iii) $t/T=0.60$, and (iv) $t/T=0.71$.

The comparison of surface pressure (C_p) between M1 and M2 (Figure 6-5c) shows higher positive pressure on the left side and lower negative pressure on the right side of the caudal fin in M1 both near the dorsal leading edge where interaction between P-DFV and caudal fin happens, while no significant pressure difference is found near the ventral leading edge of the caudal fin. It is also found that the dorsal leading edge in M1 is covered with stronger LEV, indicating that the dorsal LEV in M1 is strengthened by the hydrodynamic interaction.

To better understand the pressure change, we have calculated the distribution of pressure difference (ΔC_p) on the trunk and caudal fin (Figure 6-5d) by subtracting the surface pressure of M2 from M1. The ΔC_p contour shows that major pressure differences happen near the dorsal leading edge on both sides of the caudal with more significant ΔC_p found on the suction side.

The changes in surface pressure on the caudal fin have further caused the change in thrust production in the corresponding regions (Figure 6-5e). The pressure differences (ΔC_p) cause both larger pressure force on the pressure side and larger suction force on the suction side that are normal to the caudal fin surface, both contributing to more thrust production in the longitudinal direction. We have calculated the thrust difference distribution (ΔC_T) over the caudal fin (Figure 6-5e, note that the ΔC_T on the caudal fin combines thrust changes of both the pressure side and suction side). It is found that the location and pattern of thrust enhancement distribution (ΔC_T) on caudal fin exhibit a strong correlation with those of the pressure difference distribution (ΔC_p).

To connect the surface pressure distribution and vortex dynamics, we present flow field information including vorticity and field pressure on a transverse plane cutting through the caudal fin (slice A, Figure 6-5b) where thrust enhancement is pronounced. On slice A, a much stronger LEV core is found in M1, creating much lower negative pressure in the region covered by the LEV core in M1 than that in M2, which is responsible for the negative ΔC_p on the left side of the caudal fin that contributes to the consequent thrust enhancement ΔC_T .

In addition, significant lateral velocity is found between the p-DFV^A and the LEV in M1 but not in M2 at the corresponding location, hence we further analyze the lateral flow produced by the dorsal fin. The evolution of lateral velocity isosurface in M1 (Figure 6-5g) shows that, during each stroke, the dorsal fin produces lateral flow between the DFV and the dorsal edge of the peduncle. The lateral flow convects downstream with the DFV and merges with the lateral flow of the LEV. The comparison of lateral velocity between M1 and M2 (Figure 6-5f) shows that the lateral flow of LEV in M1 is much stronger than that in M2 after merging with the lateral flow produced by the dorsal fin, indicating that the lateral flow helps strengthen the LEV in M1 by introducing larger lateral velocity over the dorsal leading edge.

6.3.3 Trunk Drag Reduction and Caudal Fin Thrust Enhancement by Anal Fin.

To study the hydrodynamic role of the anal fin, we compare the hydrodynamic force/power, surface pressure/thrust distributions, and flow results between M3 (computational model with anal fin removed) and M1.

The force comparisons (Figure 6-6a) show smaller trunk drag generation and mostly larger caudal fin thrust production in M1 than those in M3. The instantaneous changes in trunk drag (ΔC_D)

and caudal fin thrust (ΔC_T) (Figure 6-6b) show significant trunk drag reduction at late L-to-R and R-to-L strokes, respectively, with peak reductions around 15%, while the caudal fin thrust enhancement peaks at early strokes with peak values around 20%. The cycle-averaged drag reduction $\Delta \bar{C}_D$ and thrust enhancement $\Delta \bar{C}_T$ (Table 6-5) show that the presence of anal fin helps reduce trunk drag by a considerable 6.9% and increase caudal fin thrust by 4.3% at the same time.

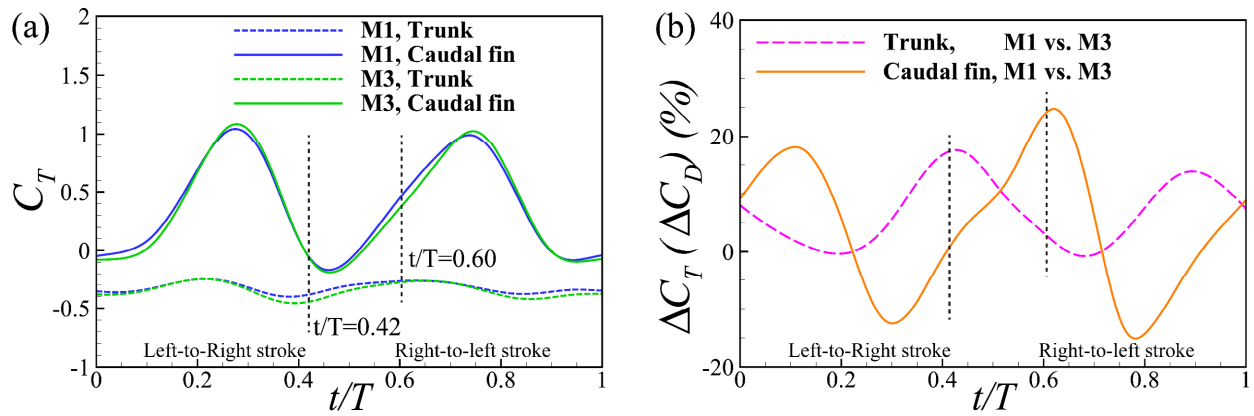


Figure 6-6: (a) Comparisons of instantaneous thrust coefficient (C_T) of trunk and caudal fin between M1 and M3, respectively. (b) Instantaneous caudal fin thrust enhancement (ΔC_T) and trunk drag reduction (ΔC_D) of M1 owing to anal fin compared to M3.

Table 6-5: Caudal fin thrust enhancement $\Delta \bar{C}_T$ and trunk drag reduction $\Delta \bar{C}_D$ owing to anal fin

	CF, \bar{C}_T	CF, $\Delta \bar{C}_T$	TK, \bar{C}_D	TK, $\Delta \bar{C}_D$
M1	0.384	4.3%	0.324	6.9%
M3	0.368	--	0.348	--

The flow physics associated with the trunk drag reduction by anal fin is analyzed in detail (Figure 6-7). The vortex topology, surface pressure/thrust, and flow field information between M1 and M3 at $t/T=0.42$ are presented when drag reduction reaches its maximum value of 17.5%.

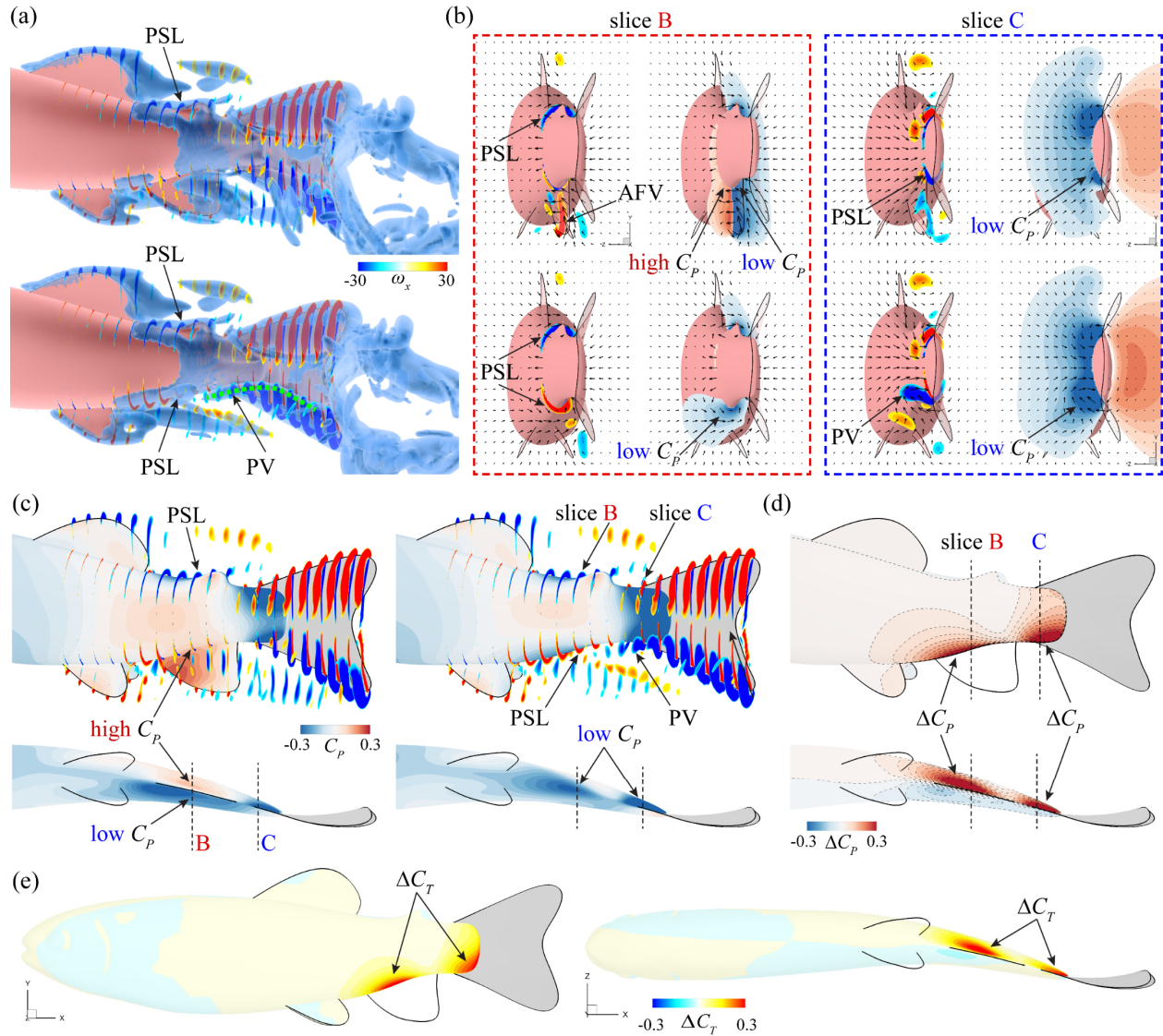


Figure 6-7: Comparison of (a) three-dimensional wake structure, (b) vorticity contour and field pressure on slice B cutting through the trunk and anal fin and slice C cutting through the caudal fin, and (c) surface pressure C_p between M1 and M3 at $t/T=0.42$. (d) The trunk surface pressure ΔC_p , and (e) the trunk surface pressure ΔC_T .

difference ΔC_p between M1 and M3 at $t/T=0.42$. (e) Thrust enhancement ΔC_T region on trunk in M1 owing to the anal fin compared to M3.

Vortex topology of M1 and M3 (Figure 6-7a) shows a similar peduncle shear layer (PSL), DFV, and LEV on the dorsal side of the fish. However, significant differences in vortex structure are found on the ventral side. Specifically, because of the absence of anal fin in M3, PSL and peduncle vortex (PV) are formed on the ventral edge of the peduncle. In contrast, AFV and is formed in M1 and no significant PV is found.

The comparison of surface pressure (C_p) between M1 and M3 (Figure 6-7c) shows higher positive pressure on the left side of the trunk in M1 where the anal fin connects to the body and lower negative pressure on the left side of the posterior peduncle in M3 where the PV is located. Ventral views show a distinct pressure difference between the left side and right side of the trunk at the ventral edge divided by the anal fin in M1, while only negative pressure is found at the corresponding location in M3.

The ΔC_p contour (Figure 6-7d) shows two regions with the major positive pressure difference between M1 and M3 on the left side of the trunk where the anal fin connects to the body (region B) and where PV is located (region C), respectively. The positive pressure differences (ΔC_p) have caused both larger pressure force in region B and less suction force in region C in M1, both contributing to thrust production in the longitudinal direction on these regions in M1. The thrust difference distribution (ΔC_T) over the trunk ((Figure 6-7e) show consistent locations and patterns between the thrust enhancement distribution (ΔC_T) and the pressure difference distribution (ΔC_p).

To illustrate the vortex dynamics associated with the pressure change, we further present flow field information of vorticity and field pressure on two transverse planes cutting through region B (slice B) and region C (slice C) where thrust enhancement is pronounced (Figure 6-7b). On slice B, because of the absence of anal fin in M3, lateral flow can move freely across the ventral edge of the peduncle, creating PSL and negative C_p over the ventral side of the trunk. In contrast, the presence of the anal fin in M1 prevents the lateral flow across the peduncle. Instead, AFV is formed on the right side of the anal fin and a significant pressure difference is built between the two sides of the anal fin and the ventral edge of the trunk where the anal fin is connected to. The positive pressure on the left side is responsible for the thrust enhancement in region B. On slice C, strong PV is formed on the ventral edge of the posterior peduncle in M3, while the presence of anal fin in M1 has prevented the formation of PV and only slight PSL is formed in M1 at the corresponding location. The PV core induces much lower negative pressure on the left side of the peduncle in M3 than that of M1 induced by PSL. The lower negative pressure at region C in M3 produces a larger suction force that contributes to drag production in the longitudinal direction, therefore being destructive for drag reduction. In M1, because of the absence of PV, the destructive suction force in region C is reduced, resulting in less drag force production. Therefore, the anal fin uses two different mechanisms—increased pressure force in region B and reduced suction force in region C—to help reduce the trunk drag.

The flow physics associated with the caudal fin thrust enhancement by the anal fin is analyzed next (Figure 6-8). The vortex topology, surface pressure/thrust, and flow field information between M1 and M3 at $t/T=0.60$ when thrust enhancement is 24.1%, near its peak value.

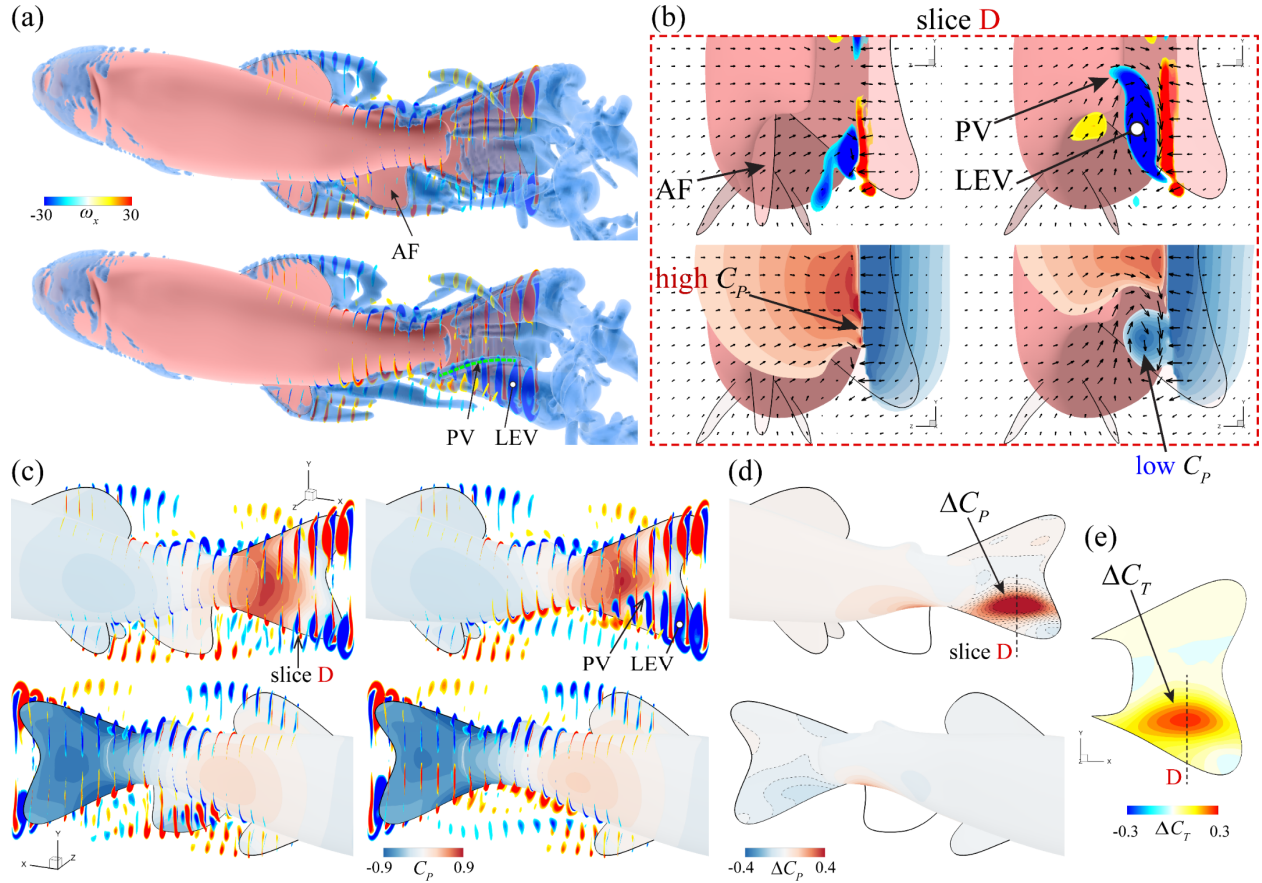


Figure 6-8: Comparison of (a) three-dimensional wake structure, (b) vorticity contour and field pressure on slice D cutting through the caudal fin, and (c) surface pressure C_p between M1 and M3 at $t/T=0.60$. (d) The surface pressure difference ΔC_p on trunk and caudal fin between M1 and M3 at $t/T=0.60$. (e) Thrust enhancement ΔC_T region on caudal fin in M1 owing to the anal fin compared to M3.

Vortex topology of M1 and M3 (Figure 6-8a) shows strong PV and more pronounced LEV covering mostly the ventral half of the caudal fin in M3, while in M1 no PV is found on the caudal fin, and the LEV strength is relatively weaker and only covers the ventral end of the caudal fin.

The comparison of surface pressure (C_p) between M1 and M3 (Figure 6-8c) shows higher positive pressure on the left side of the caudal fin in M1. It is obvious to see the drop in positive pressure on the left side of the caudal fin in M3 where the PV is located. No significant difference in negative pressure is found on the right side of the caudal fin.

The ΔC_p contour (Figure 6-8d) shows a major positive pressure difference between M1 and M3 on the left side of the dorsal fin because of the absence of PV, resulting in a larger pressure force in M1 on the caudal fin, which contributes to more thrust production in the longitudinal direction. The thrust difference distribution (ΔC_T) over the caudal fin (Figure 6-8e) confirms the location and pattern of the pressure difference distribution (ΔC_p).

The vorticity and field pressure information on a transverse plane (slice D) cutting through the ventral half of the caudal fin at the thrust enhancement region (Figure 6-8b) shows that the PV and the strong LEV core in M3 induce negative pressure on the pressure side of the caudal fin, therefore being destructive for thrust production. In M1, because of the absence of PV and the much weaker LEV, positive pressure covers most of the caudal fin on the pressure side, resulting in more thrust production.

6.3.4 Constructive Interactions among Pelvic Fins, Anal Fin, and Caudal Fin.

Here we compare the hydrodynamic force, surface pressure/thrust, and flow results between M4 (computational model with pelvic fins removed) and M1 to study the hydrodynamic role of pelvic fins in propulsive performance and the associated flow physics.

The force comparisons (Figure 6-9a) show significantly smaller anal fin drag in M1 than M4, while the force changes in trunk and dorsal fin are minimal. The cycle-averaged thrust

enhancement $\Delta\bar{C}_T$ and drag reduction $\Delta\bar{C}_D$ (Table 6-6) show that the presence of pelvic fins helps reduce all the anal fin drag and increase caudal fin thrust by 1.6%. The force changes in the dorsal fin and the trunk are less than 1%.

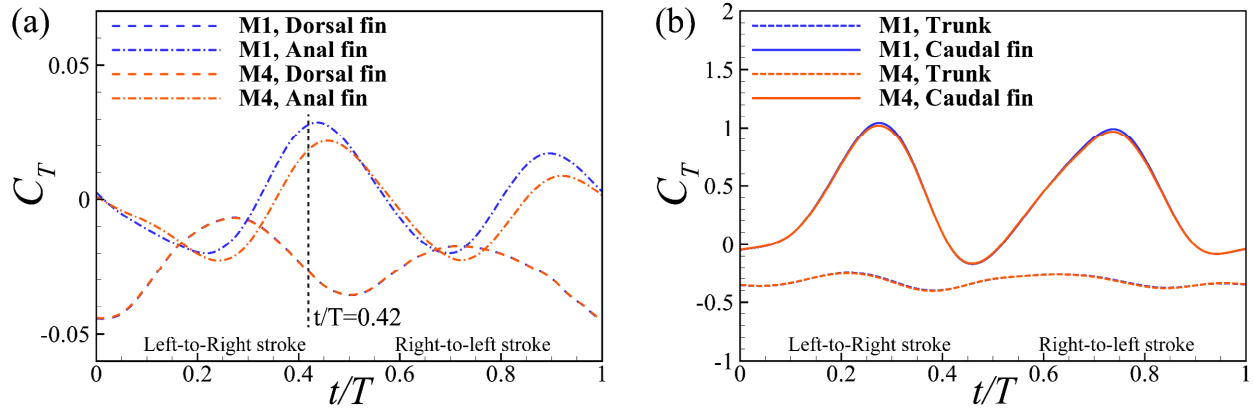


Figure 6-9: (a) Comparisons of instantaneous thrust coefficient (C_T) of dorsal fin and anal fin between M1 and M4, respectively. (b) Comparisons of instantaneous thrust coefficient (C_T) of trunk and caudal fin between M1 and M4, respectively.

Table 6-6: Trunk and fin force changes owing to pelvic fin.

\bar{C}_D	Anal fin drag	\bar{C}_T	Caudal fin thrust	\bar{C}_D	Dorsal fin drag	\bar{C}_D	Trunk drag
M1	0.000	M1	0.384	M1	0.025	M1	0.324
M4	0.004	M4	0.378	M4	0.025	M4	0.326
$\Delta\bar{C}_D$ (%)	100%	$\Delta\bar{C}_T$ (%)	1.6%	$\Delta\bar{C}_D$ (%)	-0.4%	$\Delta\bar{C}_D$ (%)	0.6%

It is found that anal fin drag reduction happens during the late middle L-to-R and R-to-L strokes, respectively, indicating constructive hydrodynamic interactions between pelvic fins and anal fin during this time. We then analyze the flow physics associated with the anal fin drag reduction by pelvic fins. The vortex topology, surface pressure/thrust, and flow field information between M1 and M4 are compared at $t/T=0.42$ when drag reduction is pronounced (Figure 6-10).

Vortex topology of M1 and M4 (Figure 6-10a&b) show significant differences in vortex structure on the ventral side of the fish. Specifically, pronounced hydrodynamic interactions between anal fin and the PFV shed from the pelvic fins in the upstream are found in M1, creating stronger AFV at the leading edge of anal fin in M1, while in M4, no significant interaction between anal fin and the other part of the body is found.

The comparison of surface pressure (C_p) between M1 and M4 (Figure 6-10c) shows lower negative pressure on the right side of the anal fin in M1 near the leading edge where the hydrodynamic interactions happen. The ΔC_p contour (Figure 6-10d) shows a major negative pressure difference between M1 and M4 on the right side of the anal fin, resulting in a larger suction force generation over this region that contributes to thrust production in the longitudinal direction. The thrust difference distribution (ΔC_T) over the anal fin (Figure 6-10e) confirms the location and pattern of the pressure difference distribution (ΔC_p).

The vorticity (Figure 6-10f) and field pressure (Figure 6-10g) information on a frontal plane (slice E) cutting through the anal fin at the thrust enhancement region shows substantial interaction between PFV shed from the pelvic fin and the anal fin at the leading edge in M1. A stronger AFV on the right side of the anal fin is found in M1 than that in M4, causing lower negative field pressure in this region in M1, which is consistent with the surface pressure distribution.

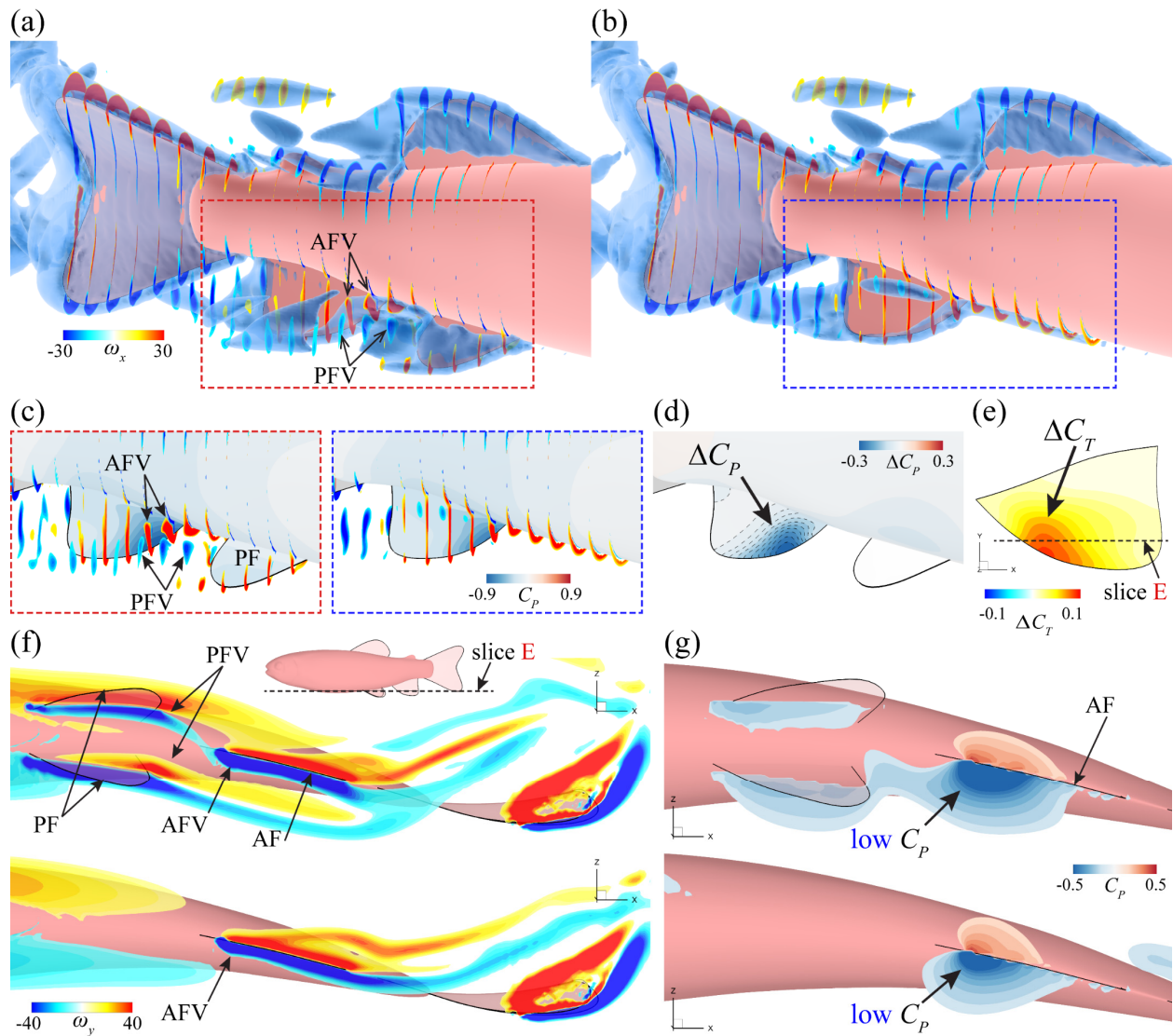


Figure 6-10: Comparison of (a-b) three-dimensional wake structure and (c) surface pressure C_p between M1 and M4 at $t/T=0.42$. (d) The surface pressure difference ΔC_p on anal fin between M1 and M4 at $t/T=0.42$. (e) Thrust enhancement ΔC_T region on anal fin in M1 owing to the pelvic fin compared to M4. Comparison of (f) y-vorticity contour and (g) field pressure on a coronal plane (slice E) cutting through the pelvic fin, anal fin, and caudal fin.

6.4 Discussion

Three major mechanisms are found to enhance the hydrodynamic performance of trout swimming. The dorsal fin vortex (DFV) and lateral flow capture by caudal fin (Figure 6-11a) and the peduncle vortex (PV) prevention by anal fin (Figure 6-11b) are found to be responsible for the caudal fin thrust increase, and the lateral flow prevention by anal fin (Figure 6-11c) is responsible for the trunk drag reduction.

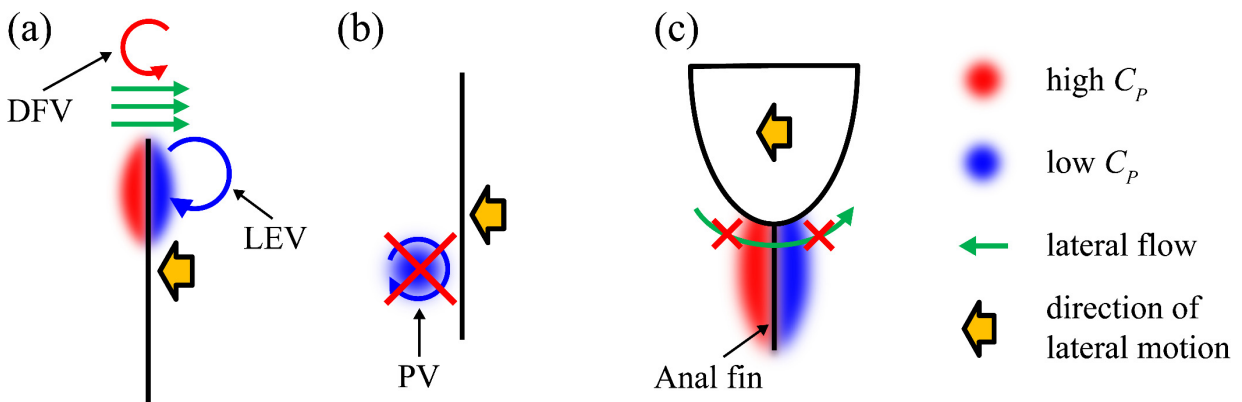


Figure 6-11: Schematics on mechanisms of (a) dorsal fin vortex (DFV) and lateral flow capture by caudal fin, (b) peduncle vortex (PV) prevention by anal fin, and (c) lateral flow prevention by anal fin.

The DFV and lateral flow capture mechanism (Figure 6-11a) show that the caudal fin captures the DFV and lateral flow induced by the dorsal fin at the dorsal edge during the lateral flapping motion. The DFV and lateral flow enhance the strength of the LEV and create a larger pressure difference between the two sides of the caudal fin with higher positive pressure on the pressure side and lower negative pressure on the suction side.

The PV prevention mechanism (Figure 6-11b) shows that the presence of the anal fin prevents the formation of PV and avoids the low-pressure region over the ventral part of the caudal fin.

The lateral flow prevention mechanism (Figure 6-11c) shows that the anal fin prevents the lateral flow that would otherwise flow across the ventral edge of the trunk. Therefore, a larger pressure difference is built up between the two sides of the anal fin and the ventral edge of the trunk.

6.5 Chapter Summaries

In this section, we have combined experimental and numerical approaches to investigate the hydrodynamic roles of the dorsal fin, anal fin, and pelvic fins, respectively, in the propulsive performance of juvenile rainbow trout during steady swimming. High-speed videos of freely swimming juvenile rainbow trout were obtained to provide the undulating kinematics of the trunk and fins of the fish. A biologically realistic computational model of the trout was reconstructed based on live fish kinematics. High-fidelity flow simulations of trout swimming were conducted using both the full fish model (M1) and its counterparts with the dorsal fin removed (M2), anal fin removed (M3), and pelvic fins removed (M4). The effect of the dorsal fin, anal fin, and pelvic fins on the hydrodynamic performance and vortex dynamics are examined by comparing the simulation results between the full fish model (M1) and modified models (M2, M3, and M4), respectively.

It is found that the dorsal fin helps increase caudal fin thrust by 11% but did not reduce trunk drag significantly. During each tail beat stroke, the dorsal fin induces a lateral flow behind its trailing edge and a vortex (DFV) at its dorsal tip that both convect downstream and interact with

the caudal fin at its dorsal leading edge. The lateral flow and DFV induce larger lateral velocity at the caudal fin, which strengthens the leading edge vortex (LEV) and creates lower negative pressure on the suction side and higher positive pressure on the pressure of the caudal fin, resulting in increased thrust production.

The anal fin helps both reduce trunk drag by 6.9% and increase caudal fin thrust by 4.3%. The presence of the anal fin prevents the local lateral flow across the ventral edge of the trunk, which builds up a significant pressure difference between the two sides of the trunk with the positive pressure side producing more local thrust, thereby reducing the overall trunk drag. In addition, the presence of the anal fin prevents the formation of the peduncle vortex that is destructive for caudal fin thrust production, thereby increasing the caudal fin thrust.

The pelvic fins help reduce all the anal fin drag and increase caudal fin thrust by 1.6%. The force changes in the dorsal fin and the trunk are less than 1%. The vortex shed from the pelvic fins interacts with the anal fin at the leading edge, which enhances the anal fin vortex and creates lower negative pressure on the suction side, resulting in more suction thrust production to balance the anal fin drag.

7 In-Line Propulsion: Effect of Body Flattening on Thrust

Production Mechanism and Vortex Dynamics in Leech

Swimming

Leeches are invertebrate anguilliform swimmers that perform dorsoventral undulations during swimming. It is hypothesized that the flattening of body cross section in leech could enhance the thrust production of the body. A key general goal of this section is to combine numerical and experimental approaches to examine the thrust production mechanism and associated vortex dynamics in leech swimming. Effect of trunk cross section aspect ratio (AR), Reynolds number (Re), and Strouhal number (St) on the thrust production mechanism and vortex dynamics of leech during steady swimming are investigated over wide ranges of the parameters. High-fidelity flow simulations of leech swimming were conducted using both the original model (M1) at $AR=2.48$ and modified models (M2 at $AR=1.24$ and M3 at $AR=4.96$). The effect of Reynolds number and Strouhal number on the hydrodynamic performance and vortex dynamics are examined by comparing the simulation results over wide ranges of Re (156~15600) and St (0.355~0.798).

7.1 Leech Kinematics and Computational Modes

Live medicinal leech (*Hirudo medicinalis*) swimming experiments were conducted in a transparent tank with interior dimensions $58 \times 3 \times 15$ cm filled with still water, where leeches were allowed to swimming freely from one end to the other. We swam 8 individuals (8.5 to 9.6 cm total length L) at 1.4 to 1.8 body length per second ($L \cdot s^{-1}$) with tail beat frequencies from 3.4 to 3.9 Hz. The swimming kinematics is recorded with three synchronized high-speed cameras

(FASTCAM SA3, Photron USA, Inc.) at 500 fps and 1024×1024 pixel resolution from lateral and ventral views, respectively (Figure 7-1a&b). Among the 36 leech free-swimming videos we have captured, the leeches in 9 videos perform steady, level, forward swimming for at least 2.5 consecutive tail beat cycles. Since the undulating kinematics does not change much with swimming speed, one representative body kinematics of an average-sized individual ($L=9.4$ cm) at a speed of $1.77 L \cdot s^{-1}$ (Figure 7-1d) was selected for the kinematics reconstruction of the computational model in the present study.

The 3-D computational model of the medicinal leech (*H. medicinalis*) (Figure 7-1c) was reconstructed based on the representative high-speed video sequence chosen for reconstruction. The entire leech was modeled as a solid body with a total number of 1.4×10^4 triangular elements over the model surface to resolve the morphological features of the body and posterior sucker of swimming leech. The swimming kinematics of the model is reconstructed in Autodesk Maya[®] (Autodesk, Inc.) using an image-guided reconstruction method [79]. This method has been successfully adopted to reconstruct manta ray [80] and fish [9] swimming (see our previous work [9] for more details).

Key geometric quantities of the computational model (M1, marked in Figure 7-1c) are measured during swimming and listed in Table 7-1. Here, L denotes the body length, L_{PS} is the length of the posterior sucker. H and W denote the height and width of the trunk at the middle transverse plane, respectively. H_{PS} , W_{PS} , and A_{PS} denote the height, width, and projected area of the posterior sucker, respectively. The aspect ratio (AR) of the cross section of the trunk at the middle transverse plane is calculated as $AR = W/H$. All lengths are normalized by the body length L , and areas are normalized by L^2 .

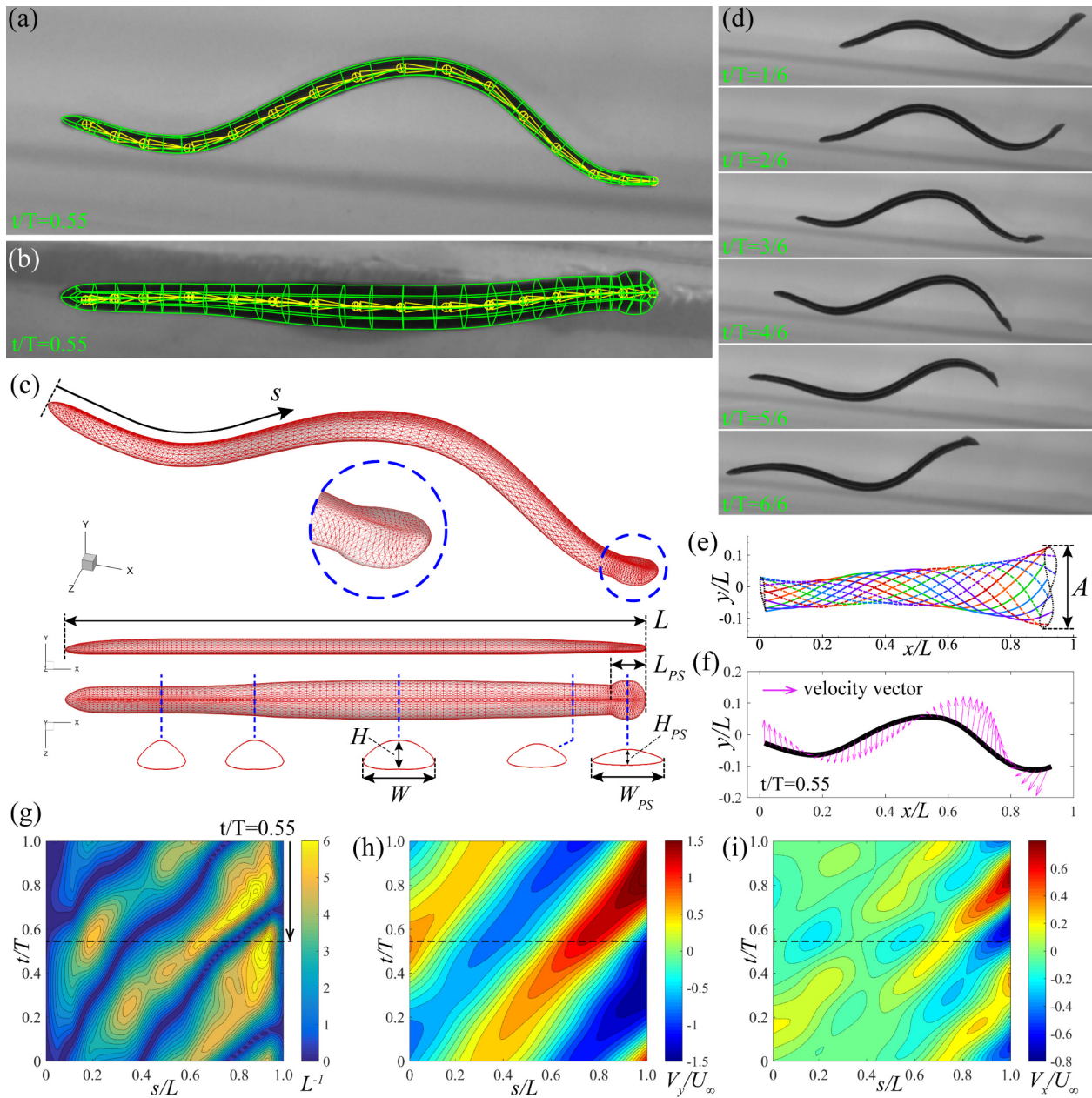


Figure 7-1: Morphological and kinematical modeling of the medicinal leech (*Hirudo medicinalis*) during steady swimming. (a–b) High-speed camera images of live medicinal leech swimming overlapped with the reconstructed computational model from lateral and ventral views, respectively, at $t/T=0.55$. (c) The reconstructed computational model of medicinal leech with fine surface mesh. (d) Kinematics of medicinal leech swimming during a tail-beat cycle from a lateral view. (e) Midlines of the reconstructed computational model with swimming kinematics during a

tail beat cycle. Solid lines and dashed lines correspond to $0\sim 0.5T$ and $0.5T\sim 1.0T$, respectively. A color change corresponds to a change in time of $T/12$. (f) Local velocity vectors along the body at $t/T=0.55$. (g) Spatial-temporal distribution of body midline curvature. (h) Spatial-temporal distribution of dorsal-ventral velocity (y-velocity) along body midline. (i) Spatial-temporal distribution of axial velocity (x-velocity) along body midline.

Table 7-1: Normalized geometric quantities of the computational model

L	L_{PS}	H	H_{CF}	W	W_{PS}	A_{PS}	AR
1.000	0.0608	0.0273	0.0147	0.0678	0.0672	0.00350	2.48

7.2 Simulation Setup

A Cartesian computational grid with stretching grid configuration was employed in the simulations (Figure 7-2a). The computational domain size was $10L\times 3L\times 4L$ with total grid points around 9.6 million ($513\times 193\times 97$) and a minimum grid spacing at $\Delta_{min}=0.0017L$. The grid was designed to resolve the fluid field in the vicinity of the computational model and its wake with high resolution. The left-hand boundary was set as velocity inlet with constant incoming flow speed U_∞ . A homogeneous Neumann boundary condition was used for the pressure at all boundaries. A no-slip boundary condition was applied at the model surface.

The size of the computational domain was proven to be sufficiently large to obtain converged results by extensive simulation tests. In addition, a convergence study was performed to demonstrate the grid-independent results. Figure 7-2b shows the comparison of the instantaneous

drag coefficient of the caudal fin at four different grid densities. The minimum grid spacings of the coarse, medium, fine, and dense meshes are $0.0034L$, $0.0026L$, $0.0021L$, and $0.0017L$, respectively. The drag coefficient converged as the grid spacing decreased. The mean drag difference between the fine and the dense mesh was less than 2.0%.

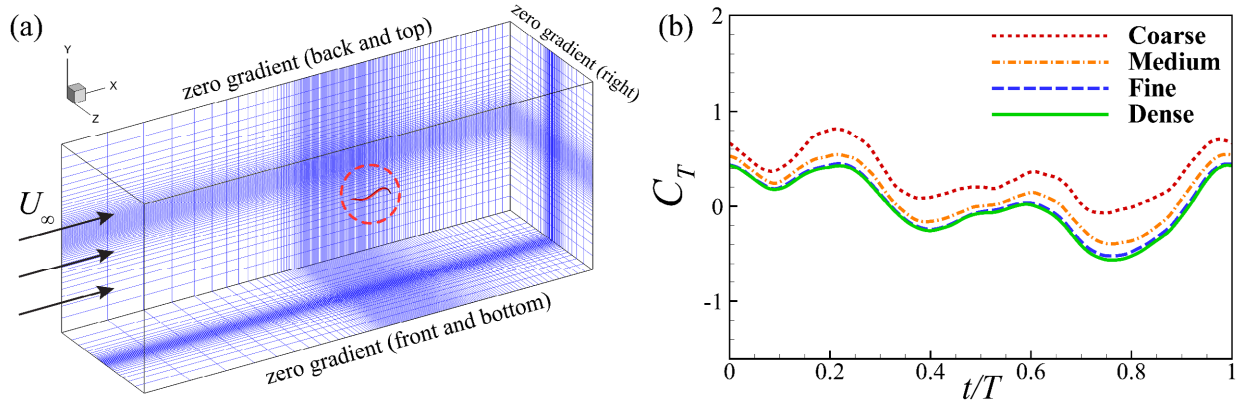


Figure 7-2: (a) Schematic of the computational mesh and boundary conditions used in the present simulation, where U_∞ denotes incoming flow speed. (b) Comparison of instantaneous thrust coefficient C_T of the leech model between coarse, medium, fine, and dense mesh.

In this study, the key parameters associated with the flow simulation of trout swimming are the Reynolds number Re and the Strouhal number St defined as follows, respectively,

$$Re = \frac{U_\infty L}{\nu} \qquad St = \frac{fA}{U_\infty} \qquad (7-1)$$

where U_∞ is the swimming speed, L is the total length of the body, ν denotes the kinematic viscosity, f is the tail beat frequency, and A is the peak-to-peak amplitude of the posterior sucker.

Among the 9 steady swimming videos captured, the observed Re ranges from 1.0×10^4 to 1.7×10^4 , and the St is between 0.5 and 0.7. In the representative video chosen for kinematics reconstruction (Figure 7-1d), the measured Re is 15600 and St is 0.532.

The hydrodynamic force acting on the computational model is computed by the direct integration of instantaneous pressure and shear over the body surfaces. The hydrodynamic power output is defined as the rate of instantaneous work done by the trunk and fins. The thrust (F_T), vertical force (F_Y), and power output (P_{out}) are nondimensionalized as thrust (C_T), vertical force (C_Y), and power (C_{PW}) coefficients, respectively, as shown in (2.3).

$$C_T = \frac{F_T}{\frac{1}{2} \rho U_\infty^2 A_{PS}} \quad C_Y = \frac{F_Y}{\frac{1}{2} \rho U_\infty^2 A_{PS}} \quad C_{PW} = \frac{P_{out}}{\frac{1}{2} \rho U_\infty^3 A_{PS}} \quad (7-2)$$

where, F_T points to x-negative, ρ is the fluid density, A_{PS} denotes the area of the posterior sucker, and U_∞ is the swimming speed.

In order to examine the effect of trunk cross-sectional shape on the hydrodynamic performance and vortex dynamics, two more computational models with altered AR of the cross section—M2 at $AR=1.24$ and M3 at $AR=4.96$, respectively—are employed, so that direct comparisons in simulation results between the original model (M1, $AR=2.48$) and the modified models (M2, and M3) can be performed. The trunk height H and trunk width W of the modified models are inversely proportionally scaled so that the volume of the trunk between models is conserved as in real leeches when their trunk aspect ratio is altered. The morphology of the posterior sucker was kept the same among the models so that the effect of the trunk AR is studied in an isolated manner.

Besides the effect of trunk AR , the effects of Reynolds number and Strohual number on hydrodynamics are also studied over wide ranges. Table 7-2 summarizes the key parameters and their ranges in the simulations performed in this study.

Table 7-2: Key morphological and flow parameters used and their ranges.

AR	Re	St
1.24 ~ 4.96	156 ~ 15600	0.355 ~ 0.798

7.3 Results

We first present the hydrodynamics performance, wake topology, pressure isosurface, surface pressure/thrust, and spatial-temporal thrust production of the reconstructed computational model during steady swimming in section 7.3.1. The simulation results presented are from the fifth tail beat cycle of the simulations when the flow field has reached a periodic state. We found that both the trunk and the posterior sucker produce thrust from pressure forces and suction forces acting on the body surface to balance the viscous drag. During each tail beat stroke, the trunk induces a counter-rotating edge vortex pair that will then interact with the lateral edges of the trunk in the following stroke. The pressure isosurface evolution and spatial-temporal thrust map show traveling waves of the thrust production along the trunk and posterior sucker. The time-averaged thrust distribution shows 19% and 76% of the total thrust produced by the last $0.08L$ of the body (segment 4) and the last $0.4L$ (segment 3 and 4) of the body, respectively.

The effect of trunk aspect ratio on the hydrodynamic performance and vortex dynamics are examined in section 7.3.2 where flow, pressure results, and thrust production patterns are

compared between the original model (M1, $AR=2.48$) and the modified models (M2, $AR=1.24$ and M3, $AR=4.96$). It is found that both the total thrust, power consumption, and propulsive efficiency increase with AR while the total viscous force is maintained at a similar level for various AR s. The trunk thrust increase with AR while the thrust produced by the posterior sucker decrease. The vortex structure shows stronger edge vortices induced by a trunk with larger AR . Pressure isosurface shows larger positive pressure and lower negative pressure regions over the trunk surface with larger AR . The time-averaged thrust distribution shows a significant increase in the percentage of thrust produced by the trunk as AR increase. More significant interactions between the edge vortex pair and the trunk were found at higher AR trunk where the larger suction thrust is produced.

Effects of Reynolds number are examined at the original Re ($Re=15600$) and $1/10$ and $1/100$ of the original Re , respectively. It is found that the total thrust due to pressure, power consumption, and viscous drag all increase as the Re decrease, while propulsive efficiency decrease. The vortex structure shows a less significant edge vortex at lower Re . The pressure isosurface shows larger positive pressure and lower negative pressure regions over the trunk surface at larger Re , which causes more pressure thrust and suction thrust productions. The total thrust production is less fluctuating in time at higher Re as more temporal overlap exists in the thrust-producing regions that travel along the body. The time-averaged thrust distribution along the body shows similar patterns between different Re .

Effects of Strouhal number are examined at the original St ($St=0.532$) and $2/3$ and $3/2$ of the original St , respectively. It is found that the total thrust and propulsive efficiency increase as St increases. While the viscous drag decreases with increasing St . The power consumption is the lowest at the original St . The vortex structure shows severer edge vortex separations associated

with more small-scaled vortex structures at higher St and less strong edge vortex at lower St . The pressure isosurface show larger positive pressure and lower negative pressure regions over both the trunk surface and the posterior sucker at larger St , which corresponds to the larger thrust productions found at both parts of the body. The time-averaged thrust distribution along the body shows significant drag production due to surface pressure of the anterior trunk (segment 1) at lower St . While segment 1 at higher St ($St=0.798$) reaches 6% of the total thrust, which is the highest among all cases studied.

7.3.1 Hydrodynamic Performance and Vortex Structure of Leech Swimming

The hydrodynamic performance, vortex dynamics, and surface pressure/thrust behaviors of the computational model at $AR=2.48$, $Re=15600$, and $St=0.532$ are analyzed to examine the associated thrust production mechanism in leech steady swimming (Figure 7-3).

The instantaneous hydrodynamic forces (Figure 7-3a) in the axial direction $C_X|_{Total}$ comprises the pressure component $C_X|_{Pressure}$ and viscous component $C_X|_{Viscous}$ which are computed by the integration of the surface pressure and surface shear over the leech body at each time instance, respectively. It is found that the pressure component of axial force produces thrust throughout a tail beat cycle to balance the viscous drag, resulting in a combined axial force around zero. The cycle-averaged $C_X|_{Total}$ is 0.017, which is less than 2% of the cycle-averaged $C_X|_{Pressure}$ of 1.07, indicating a thrust-drag balanced condition of the computational model, being consistent with the steady swimming condition of the representative leech locomotion chosen for reconstruction. In the vertical direction (Figure 7-3b), the pressure component dominates the vertical forces. The instantaneous power consumption (Figure 7-3c) shows a relatively steady

power output between $C_{PW}=2$ and 4 during the tail beat cycle. Because the pressure component of hydrodynamic force is the source of thrust production, the analyses in the following sections focus on the surface pressure changes and thrust production owing to surface pressure.

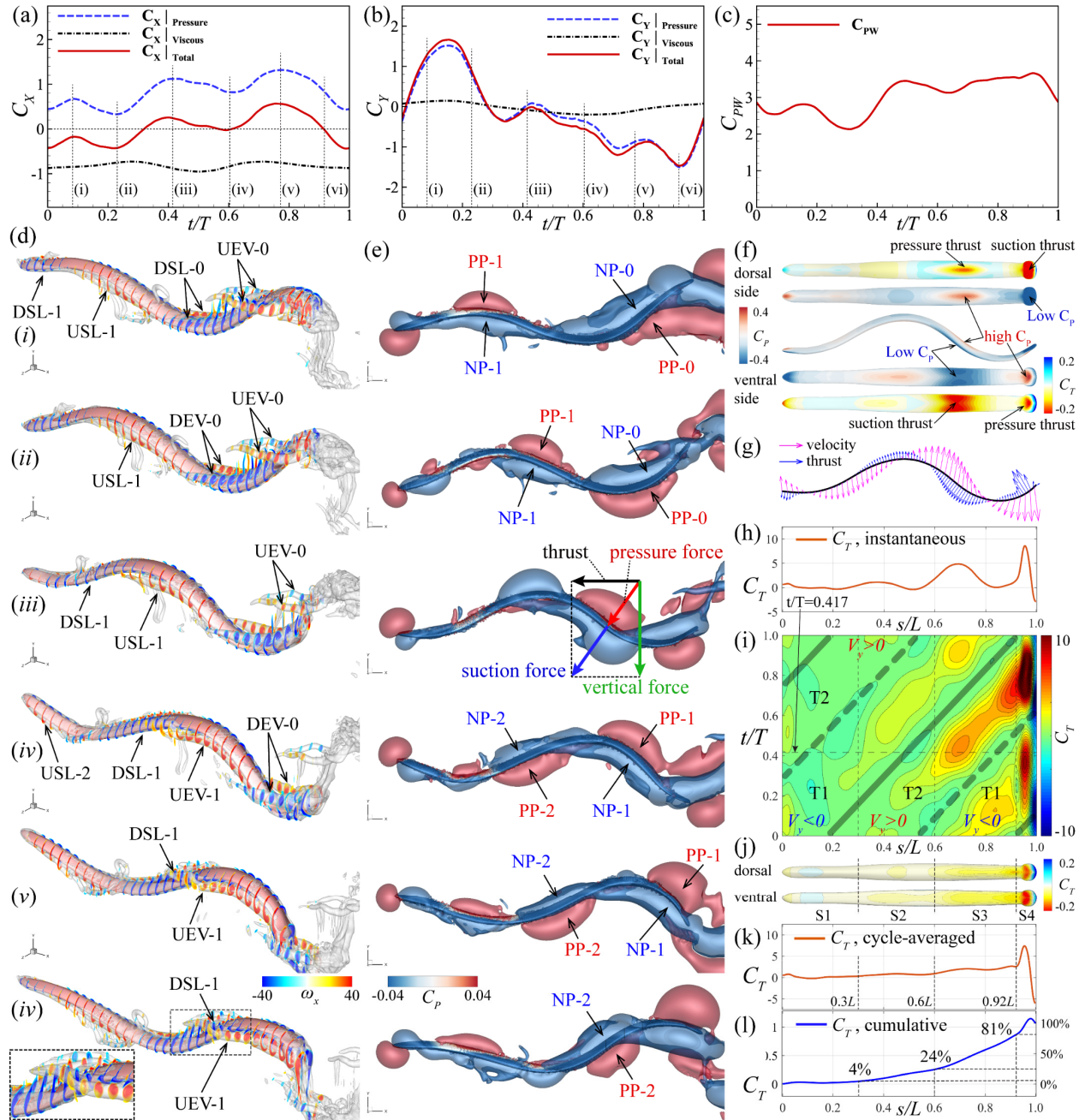


Figure 7-3: (a) Instantaneous axial force coefficients, (b) lateral force coefficients, and (c) power coefficient of leech model during one tail beat cycle of forward swimming. (d) Three-dimensional vortex wake structure of leech swimming at $t/T=0.08$ (i), $t/T=0.23$ (ii), $t/T=0.42$ (iii), $t/T=0.60$ (iv), $t/T=0.77$ (v), and $t/T=0.92$ (vi) from perspective view. (e) Pressure isosurface surrounding the body at six corresponding time instances. (f) Surface pressure contour from dorsal, lateral, and ventral views associated with the distribution of thrust force on the surface from dorsal and ventral views. (g) Local velocity vectors and local hydrodynamic pressure force vectors along the body at $t/T=0.42$. (h) Instantaneous thrust distributions along the body at $t/T=0.417$. (i) Spatial-temporal thrust distributions along the body from the head to the tail tip during a tail beat cycle. (j) Cycle-averaged thrust distribution on dorsal and ventral body surfaces, respectively. (k) Cycle-averaged thrust distribution along the body. (l) Cumulative cycle-averaged thrust productions along the body.

The vortex dynamics are analyzed at six time instances (i to vi) during a tail beat cycle (Figure 7-3d). During each tail undulating cycle, an upstroke shear layer (USL) pair and a downstroke shear layer (DSL) pair are generated at the lateral edges of the anterior trunk. The USL and DSL pairs propagate downstream along the trunk edges during which they are strengthened into an upstroke edge vortex (UEV) pair and a downstroke edge vortex (UEV) pair and interact with the trunk before their shedding into the downstream wake toward the dorsal and ventral directions, respectively. Detailed analysis shows that at $t/T=0.08$ (i) the USL-1 pair is found at the lateral edges of the trunk from $0.2L$ to $0.5L$ during the upstroke motion of this part of the trunk. DSL-0 pair is found from $0.5L$ to $0.8L$ attaching to the trunk, and UEV-0 pair is found detached from the trunk from $0.7L$ to $1.0L$. Meanwhile, a new DSL-1 pair is formed at the head. At $t/T=0.23$ (ii), all vortex structures propagate downstream along the body and continue to develop. The USL-

1 pair is strengthened and the DSL-0 pair has developed into DEV-0. At $t/T=0.42$ (iii), UEV-0 sheds from the tail, and DSL-1 covers the trunk from $0.1L$ to $0.5L$. At $t/T=0.60$ (iv), the USL-1 pair is developed into UEV-1 pair and the DEV-1 pair is detached from the trunk. At the head, a new USL-2 pair is formed. At $t/T=0.77$ (v), the UEV-1 pair starts to interact with the trunk around $0.5L$ when this part of the trunk starts to travel towards the ventral side. The interaction between UEV-1 and the trunk becomes more significant at $t/T=0.92$ (vi). The UEV-1 pair below the trunk is transported above the trunk over the trunk edges and interacts with the DSL-1 as this part of the trunk travels through the UEV-1 pair between the cores during the downstroke motion. More analysis on the hydrodynamic interactions between UEV and the trunk will be presented in section 7.3.2.

The pressure isosurfaces at corresponding time instances (Figure 7-3e) show travelings of positive and negative pressure regions along the body. At $t/T=0.08$ (i), a positive pressure region (PP-1) and a negative pressure region (NP-1) are found at the dorsal and ventral side of the trunk, respectively, from $0.2L$ to $0.4L$, and PP-0 and NP-0 are found at the ventral and dorsal side of the posterior half of the body. Through $t/T=0.23$ (ii) and $t/T=0.42$ (iii), both positive pressure and negative pressure regions propagate downstream along the body. At $t/T=0.60$ (iv), NP-2 and PP-2 are formed and continues to travel down along the body for the rest of the tail beat cycle.

The mechanism of thrust production over the trunk and the posterior sucker are analyzed at $t/T=0.42$ when a thrust peak is found. At $t/T=0.42$, the positive surface pressure region covered by PP-1 and negative surface pressure region covered by NP-1 produce pressure force and suction force that are normal to the body surface, respectively. Thrust is produced from the longitudinal component of both normal forces. Specifically, suction thrust is produced on the ventral side of the trunk from $0.6L$ to $0.8L$ where negative surface pressure presents, and pressure thrust is

produced on the dorsal side of the trunk with positive surface pressure (Figure 7-3f). The same mechanism applies to other parts of the body, on the posterior sucker, suction thrust is produced on the dorsal side due to negative surface pressure by NP-0, and pressure thrust is produced on the ventral side due to positive surface pressure by PP-0 (Figure 7-3f).

The local normal force and local velocity are plotted as vectors along the body at $t/T=0.42$ (Figure 7-3g). Note that the normal force combines both the pressure force and the suction force acting on the dorsal and ventral sides of the trunk locally. Large normal forces are found on the trunk from $0.6L$ to $0.8L$ and on the posterior trunk, being consistent with the surface pressure distributions. Smaller normal forces are found from $0.3L$ to $0.6L$ and at the head. It is also found that the directions of the normal forces are, in general, opposite to the directions of the local velocity, indicating a drag-based propulsion mechanism.

The instantaneous thrust produced by the normal force along the body at $t/T=0.42$ (Figure 7-3h) show larger peaks near $0.7L$ and $0.95L$, corresponding to the locations of larger normal force vectors along the body. A much smaller thrust peak is found near $0.35L$ and a small thrust is found near the head.

A spatial-temporal thrust production map (Figure 7-3i) is obtained based on the instantaneous thrust distribution along the body over a tail beat cycle. The spatial-temporal distributions show two major thrust-producing regions (T1 and T2) that travel along the body posteriorly with time. Strong correlations in the spatial-temporal pattern between thrust production and vertical velocity are found. Specifically, T1 corresponds to the negative vertical velocity region ($V_y < 0$), and T2 corresponds to the positive vertical velocity region ($V_y > 0$). Higher thrust is found at higher vertical velocity regions. In addition, the time phase and wave speed of thrust

productions are highly consistent with those of the vertical velocity, indicating that vertical velocity is the main drive of thrust production. The thrust map also shows two high thrust regions at the posterior sucker associate with the upstroke and downstroke flapping motions.

The cycle-averaged thrust distributions over the dorsal and ventral surface (Figure 7-3j) show thrust production over the majority of the body with more concentrated thrust produced at the posterior trunk and sucker. Note that the negative thrust at the posterior tip of the sucker is due to the negative pressure produced by the flow past the free end. In general, more thrust is produced on the ventral side than the dorsal side.

The cycle-average thrust distribution along the body (Figure 7-3k) shows increasing thrust production along the body peaked at the posterior sucker. Thrust production at the posterior trunk is substantially higher than that of the middle and anterior parts. Therefore, based on the cycle-averaged thrust distribution and the spatial-temporal thrust map, the leech body is divided into four segments including segment 1 (S1, 0~0.3L), segment 2 (S2, 0.3~0.6L), segment 3 (S3, 0.6~0.92L), and segment 4 (S4, 0.92L~1.0L), where the posterior sucker is included in S4. The summed thrust over each segment (Table 7-3, M1) shows that S3 produces 57% of the total thrust. S2 and S4 produce similar thrust at 20% and 19%, respectively. S1 produces the least thrust at 4%. The cumulative thrust along the body (Figure 7-3l) shows that the trunk produces 81% of the total thrust. The posterior 40% of the body produces 76% of the thrust and the anterior 60% only produces 24% of the thrust.

7.3.2 Effect of Trunk Aspect Ratio

Effect of trunk aspect ratio on the hydrodynamic performance, vortex dynamics, surface pressure distributions, and thrust production patterns are examined between the original model (M1, $AR=2.48$) and the modified models (M2, $AR=1.24$ and M3, $AR=4.96$).

The instantaneous axial forces (Figure 7-4a) show that the total thrust production increases with AR , while the viscous drag does not change much as AR increases. The highest thrust peak also shifted from $t/T=0.8$ to $t/T=0.5$ as AR increases from 1.24 to 4.96, which will be further discussed.

The cycle-averaged thrust, power consumption, and propulsive efficiency (Table 7-3) all increase with AR . The thrust produced by M3 (1.58) doubles the thrust produced by M2 (0.75) at a 28% power consumption increase from 2.77 (M1) to 3.55 (M3), resulting in higher propulsive efficiency of 44.6% in M3 than that of the 26.9% in M2.

The vortex structure (Figure 7-4b) shows stronger shear layer pairs and edge vortex pairs induced by the trunk with larger AR . Pressure isosurface (Figure 7-4c) shows larger positive pressure (PP-1) and lower negative pressure (NP-1) regions over the trunk surface with larger AR , being consistent with the surface pressure distribution over the dorsal and ventral surfaces. The instantaneous thrust distributions along the body at $t/T=0.417$ (Figure 7-4d) show that both the S2 and S3 thrust increase as AR increase. Interestingly, however, the S4 thrust decrease with increasing AR . The pressure force vectors along the body (Figure 7-4e) show larger forces acting on the trunk and smaller forces on the posterior sucker with increasing AR , which is consistent with the instantaneous thrust distribution (Figure 7-4f).

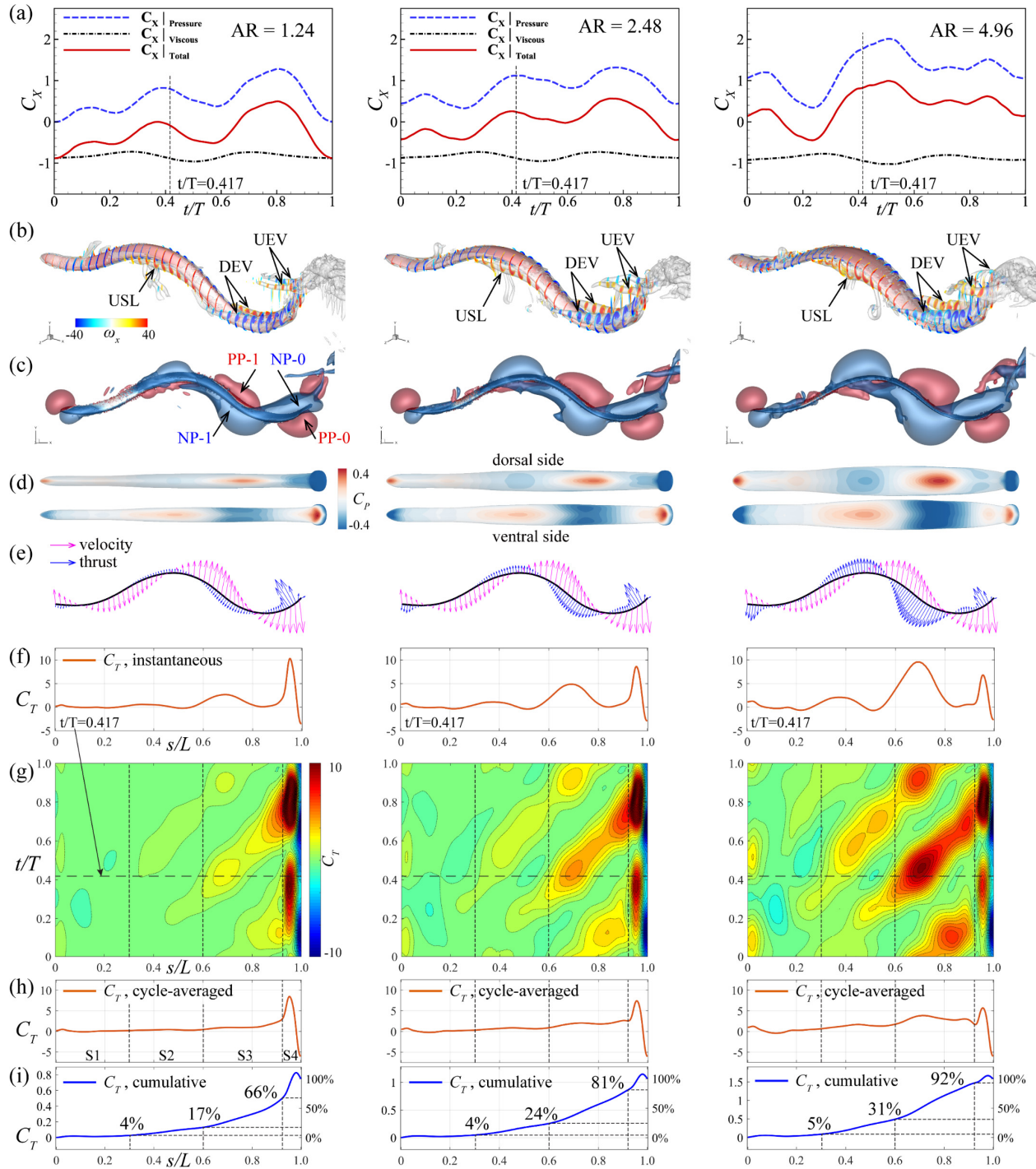


Figure 7-4: Comparisons of (a) instantaneous axial force coefficients, (b) three-dimensional vortex wake structure, (c) pressure isosurface surrounding the body, (d) surface pressure contour from dorsal and ventral views, (e) local velocity and hydrodynamic pressure force vectors along the body, (f) Instantaneous thrust distributions along the body, (g) spatial-temporal thrust distribution

along the body during a tail beat cycle, (j) cycle-averaged thrust distribution on dorsal and ventral surfaces, (h) cycle-averaged thrust distribution along the body, and (i) cumulative cycle-averaged thrust productions along the body at $t/T=0.417$ between M2 (left), M1 (middle), and M3 (right).

The spatial-temporal thrust distributions (Figure 7-4g) show a similar spatial-temporal pattern in thrust production among the three models. However, significant differences in thrust production magnitude are found. The thrust map shows that the trunk (S1+S2+S3) produces more thrust as AR increases while the posterior sucker (S4) produces less thrust. Because of the increased thrust production in M3 between 0.6L and 0.75L from $t/T=0.3$ to $t/T=0.55$, the highest thrust peak is shifted from $t/T=0.8$ to $t/T=0.5$ as AR increase from 1.24 to 4.96

Table 7-3: Cycle-averaged thrust production (from each segment and overall), power consumption, and propulsive efficiency at $AR=1.24, 2.48, \text{ and } 4.96$.

AR	\bar{C}_T					\bar{C}_{PW}	η
	S1	S2	S3	S4	Overall		
1.24 (M2)	0.03 (4%)	0.11 (14%)	0.37 (49%)	0.26 (34%)	0.75	2.77	26.9%
2.48 (M1)	0.04 (4%)	0.21 (20%)	0.61 (57%)	0.20 (19%)	1.07	3.02	35.2%
4.96 (M3)	0.08 (5%)	0.40 (25%)	0.96 (61%)	0.13 (8%)	1.58	3.55	44.6%

The vortex structure is compared between M1, M2, and M3 at $t/T=0.92$ when the interaction between the edge vortex pair and the trunk is pronounced (Figure 7-5). The associated pressure

isosurface contour, surface thrust distribution on the dorsal surface, and the flow field information—vorticity and field pressure contours on transverse planes cutting through the trunk where the dorsal thrust production and hydrodynamic interaction are the most significant—are also compared.

The cycle-averaged thrust distribution along the body (Figure 7-4h) shows a significant thrust increase in S3 and a thrust decrease in S4. The summed thrust over each segment (Table 7-3) shows that the S3 thrust is increased by 159% from 0.37 (M2) to 0.96 (M3), while the S4 thrust is decreased by 20% from 0.26 (M2) to 0.13 (M3). The cumulative thrust distribution along the body shows (Figure 7-4i) a significant increase in the percentage of trust produced by the trunk with increasing AR . As AR increase from 1.24 to 4.96, the trunk thrust percentage increase from 66% to 92%. Among the total trunk thrust, the contribution from S3 alone increases from 49% to 61%.

A significant difference in the morphology of the upstroke edge vortex (UEV) pair is found between the models (Figure 7-5a-c). The UEV strength in M2 is much less than those of the M1 and M3, and the UEV core of M2 ($AR=1.24$) is relatively straight without significant twist, indicating limited interactions between UEV and the trunk in M2. As the AR increases, the UEV pair becomes stronger in strength and the anterior part of the UEV core becomes more twisted towards the median plane of the body while interacting with the stronger DEV core.

The vorticity contours on slices (Figure 7-5d-f) show that as AR increases, the DSL in M2 is strengthened into DEV in M1 and M3, and the UEV interacts more intensely with the DEV. The field pressure contours on slices show lower negative pressure and larger positive pressure over the dorsal and ventral sides of the trunk, respectively, at higher AR .

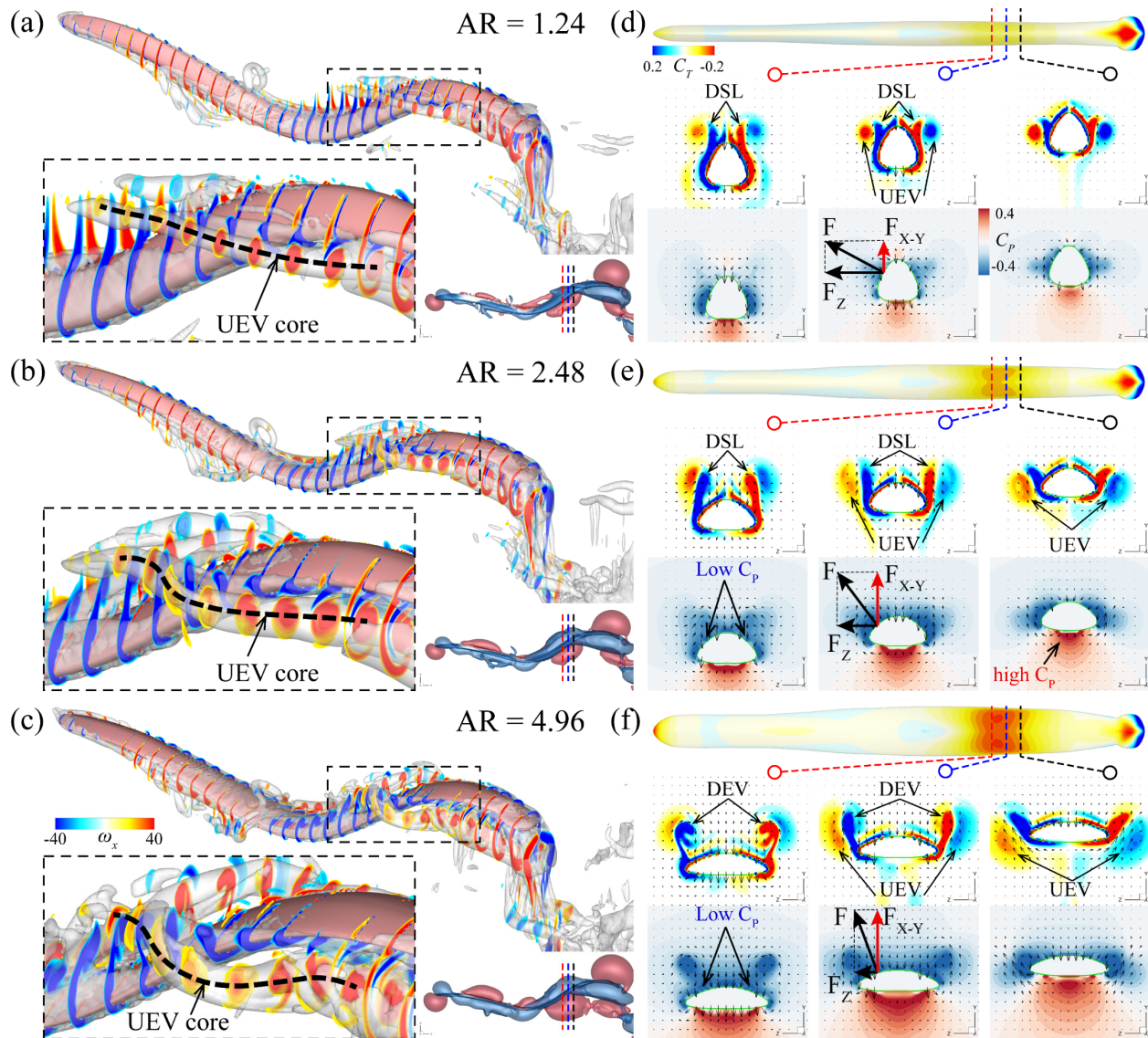


Figure 7-5: Comparison of vortex structure between (a) $AR=1.24$, (b) $AR=2.48$, and (c) $AR=4.96$ at $t/T=0.92$. Comparisons of dorsal surface thrust distribution and the vorticity and field pressure contours at three transverse planes cutting through the high thrust-producing region between (d) $AR=1.24$, (e) $AR=2.48$, and (f) $AR=4.96$ at $t/T=0.92$.

The lower surface pressure over the dorsal surface of higher AR trunks produces higher suction forces that are normal to the local surface (Figure 7-5d-f). In addition, because of the more

dorsal-ventrally orientated normal vectors over the dorsal surfaces of higher *AR* trunks (M1 and M3), more suction force component of M1 and M3 stays within the X-Y plane which helps with thrust production. In contrast, because of the more laterally orientated normal vector in M2, the major suction force component is orientated to the lateral direction (Z-direction), which does not help with thrust production. The larger suction force and more dorsal-ventrally orientated normal vector of the dorsal surface of higher *AR* trunks result in the larger thrust production at this region.

7.3.3 Effect of Reynolds Number

Effects of Reynolds number on the hydrodynamic performance, vortex dynamics, surface pressure distributions, and thrust production patterns are examined at the original Reynolds number ($Re=15600$) and reduced Reynolds numbers ($Re=1560$ and $Re=156$), respectively. The reduced Reynolds numbers cases correspond to smaller leeches swimming at slower speeds.

The instantaneous axial forces (Figure 7-6a) show that the total thrust production increases with *AR*, while the viscous drag increases faster than that of the thrust as *AR* increases. The thrust fluctuation is reduced as Re reduces from 15600 to 156, which will be further discussed.

The cycle-averaged thrust, power consumption, and viscous drag all increase as the Re decrease, while propulsive efficiency decrease (Table 7-4). The thrust produced at $Re=156$ (3.99) is 373% of the thrust produced at $Re=15600$ (1.07). However, the power consumption increases from 3.02 at $Re=15600$ to 24.05 at $Re=156$ by 696%, resulting in a much lower propulsive efficiency of 16.6% at $Re=156$ than that of the 35.2% at $Re=15600$.

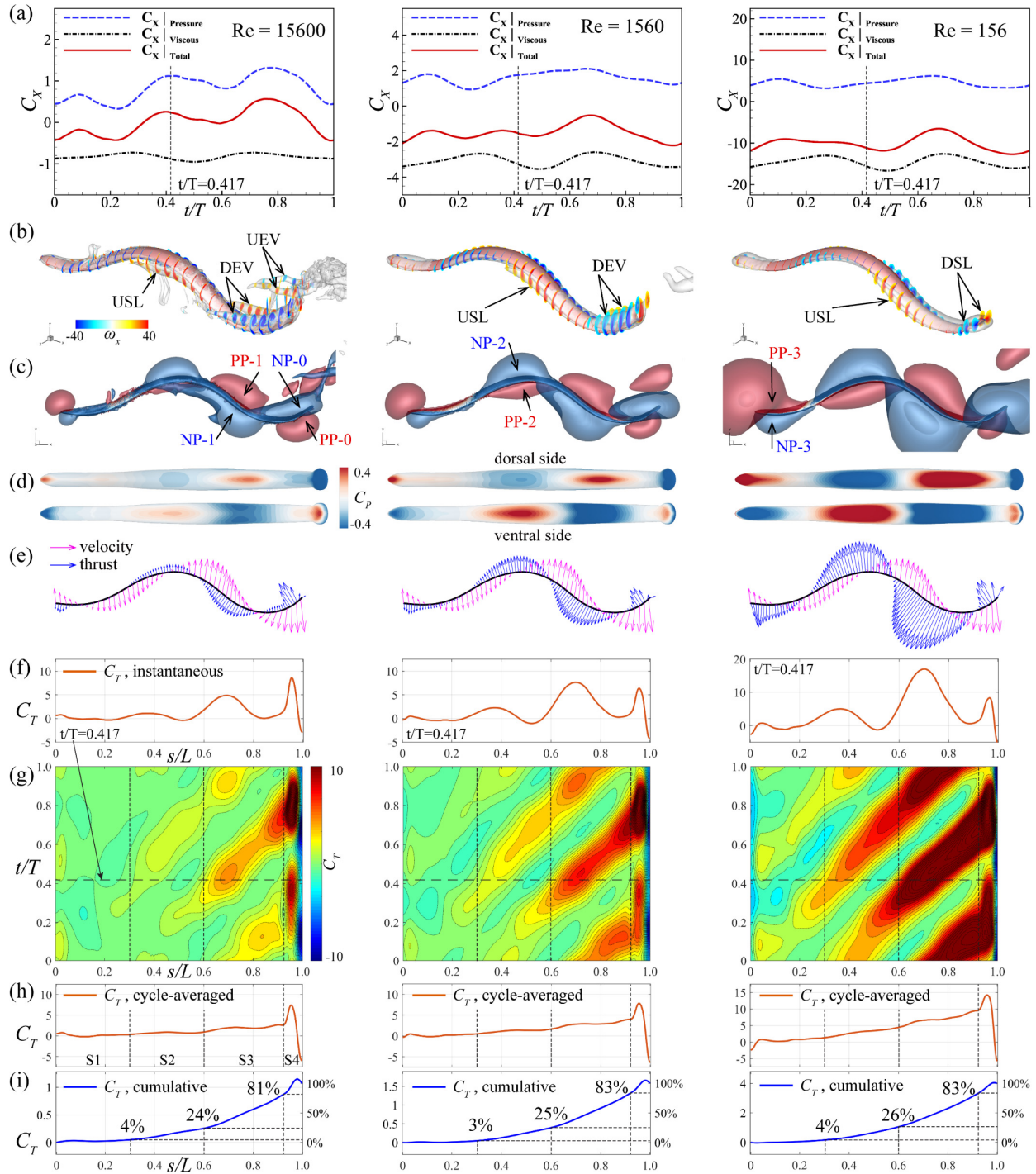


Figure 7-6: Comparisons of (a) instantaneous axial force coefficients, (b) three-dimensional vortex wake structure, (c) pressure isosurface surrounding the body, (d) surface pressure contour from dorsal and ventral views, (e) local velocity and hydrodynamic pressure force vectors along the body, (f) Instantaneous thrust distributions along the body, (g) spatial-temporal thrust distribution

along the body during a tail beat cycle, (j) cycle-averaged thrust distribution on dorsal and ventral surfaces, (h) cycle-averaged thrust distribution along the body, and (i) cumulative cycle-averaged thrust productions along the body at $t/T=0.417$ between $Re=15600$ (left), $Re=1560$ (middle), and $Re=156$ (right).

Table 7-4: Cycle-averaged thrust production (from each segment and overall), power consumption, and propulsive efficiency at $Re=15600$, 1560 , and 156 .

Re	\bar{C}_T					\bar{C}_{PW}	η
	S1	S2	S3	S4	Overall		
15600	0.04 (4%)	0.21 (20%)	0.61 (57%)	0.20 (19%)	1.07	3.02	35.2%
1560	0.05 (3%)	0.35 (22%)	0.92 (58%)	0.27 (17%)	1.58	6.00	26.3%
156	0.16 (4%)	0.88 (22%)	2.27 (57%)	0.68 (17%)	3.99	24.05	16.6%

The vortex structure (Figure 7-6b) shows fewer vortex structures at lower Re . Only shear layer pairs (USL and DSL) are found at lower Re ($Re=1560$ and 156) and no edge vortex pair is found. Pressure isosurface (Figure 7-6c) shows larger positive pressure (PP-1) and lower negative pressure (NP-1) regions over the trunk surface with lower Re , being consistent with the surface pressure distributions over the dorsal and ventral surfaces (Figure 7-6d).

The instantaneous thrust distributions along the body at $t/T=0.417$ (Figure 7-6f) show that both the S2 and S3 thrust increase as Re decreases. The pressure force vectors (Figure 7-6e) along the body show larger forces acting on the trunk with decreasing Re , which is consistent with the instantaneous thrust distribution.

The spatial-temporal thrust distributions (Figure 7-6g) show a more homogeneous spatial-temporal pattern in thrust production at lower Re . Significant differences in thrust production magnitude are found. The thrust map shows that both the trunk (S1+S2+S3) and the posterior sucker (S4) produce more thrust as Re increases. The total thrust production is less fluctuated in time at higher Re as more temporal overlap in the thrust-production regions that travel along the body.

The cycle-averaged thrust distribution along the body (Figure 7-6h) shows a significant thrust increase in all body segments. The summed thrust over each segment (Table 7-4) shows that the S3 thrust is increased by 272% from 0.61 ($Re=15600$) to 2.27 ($Re=156$), while the S4 thrust is increased by 240% from 0.20 to 0.68. The cumulative thrust productions along the body (Figure 7-6i) show a similar percentage of thrust produced by each body segment with increasing Re (3~4% at S1, 20~22% at S2, 57~58% at S3, and 17~19% at S4), indicating that the thrust production pattern due to surface pressure is robust with Reynolds number in leech swimming.

7.3.4 Effect of Strouhal Number

Effects of Strouhal number on the hydrodynamic performance, vortex dynamics, surface pressure distributions, and thrust production patterns are examined at the original Strouhal number ($St=0.532$) and $2/3$ and $3/2$ of the original St ($St=0.355$ and $St=0.798$), respectively. The variations in Strouhal number correspond to changes in undulating frequency during leech swimming.

The instantaneous axial forces (Figure 7-7a) show that the thrust production increases with increasing St , while the viscous drag decreases as St increases, resulting in a large net axial thrust force. The cycle-averaged propulsive efficiency increase as St increases (Table 7-5). The power

consumption is the lowest at the original St. Small thrust (0.1) is produced at $St=0.355$, which is only 9.3% of the thrust produced at $St=0.532$ (1.07) and 4.7% of the thrust produced at $St=0.798$ (2.12). The power consumption at $St=0.355$ is the largest at 3.96, resulting in a very low propulsive efficiency at 2.6%. Among the Strouhal numbers studied, the highest propulsive efficiency of 57.6% is found at $St=0.798$.

The vortex structure shows (Figure 7-7b) severer edge vortex separations associated with more small-scaled vortex structures at higher St. The strengths in both the shear layers and edge vortices increase as St increases. Pressure isosurface (Figure 7-7c) shows no presence of positive pressure region PP-1 and small negative pressure region NP-1 at $St=0.355$. Larger PP-1 and NP-1 are found at higher St, being consistent with the surface pressure distributions over the dorsal and ventral surfaces (Figure 7-7d).

Table 7-5: Cycle-averaged thrust production (from each segment and overall), power consumption, and propulsive efficiency at $St=0.355$, 0.532, and 0.798.

St	\bar{C}_T					\bar{C}_{PW}	η
	S1	S2	S3	S4	Overall		
0.355	-0.04 (-38%)	0.03 (25%)	0.09 (86%)	0.03 (27%)	0.10	3.96	2.6%
0.532	0.04 (4%)	0.21 (20%)	0.61 (57%)	0.20 (19%)	1.07	3.02	35.2
0.798	0.13 (6%)	0.47 (22%)	1.17 (55%)	0.36 (17%)	2.12	3.69	57.6

The instantaneous thrust distributions along the body at $t/T=0.417$ (Figure 7-7f) show thrust increase in both the trunk and the posterior sucker as St increase, being consistent with the larger pressure force vectors acting on the trunk and posterior sucker at higher St (Figure 7-7e).

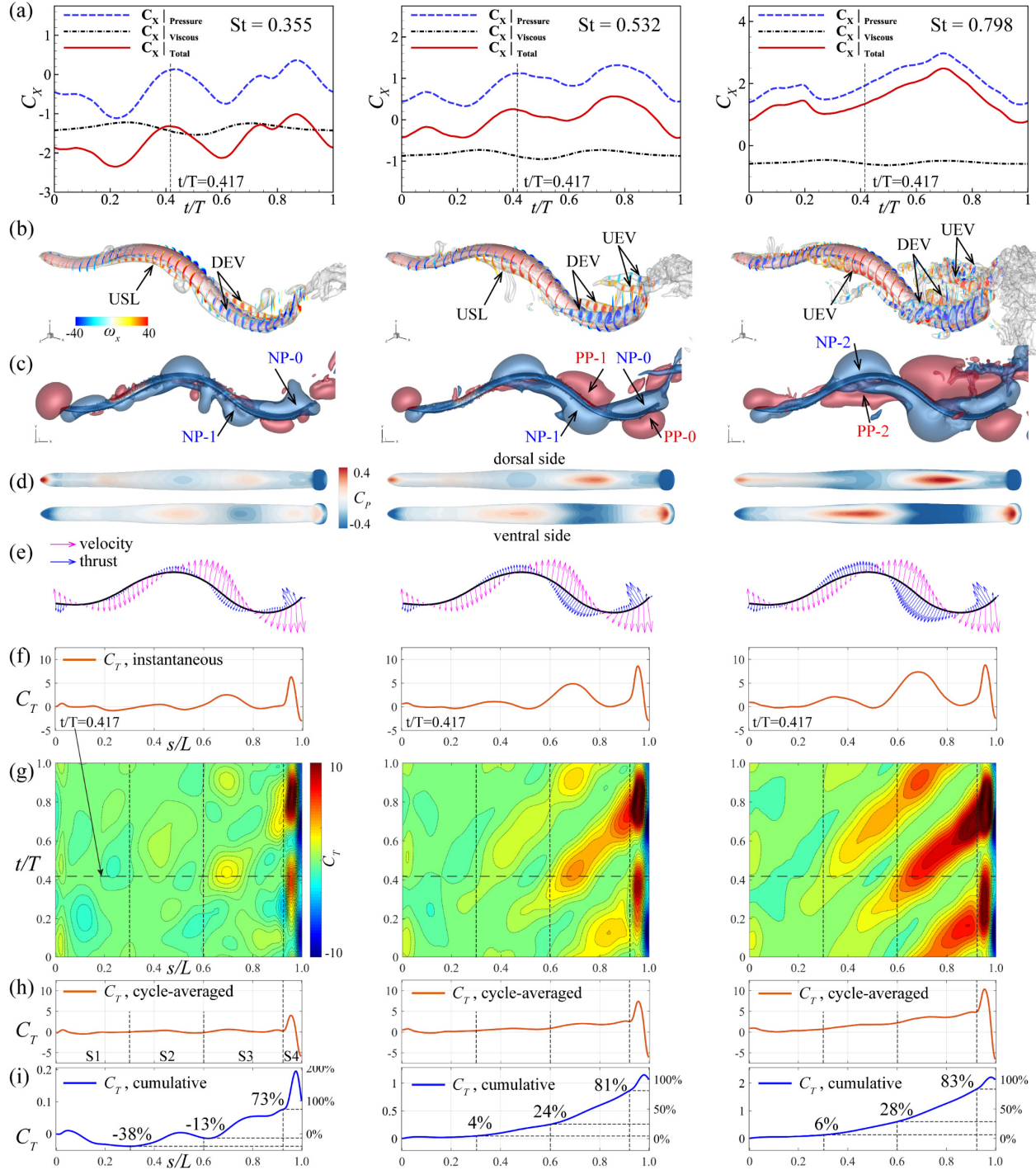


Figure 7-7: Comparisons of (a) instantaneous axial force coefficients, (b) three-dimensional vortex wake structure, (c) pressure isosurface surrounding the body, (d) surface pressure contour from dorsal and ventral views, (e) local velocity and hydrodynamic pressure force vectors along the body, (f) Instantaneous thrust distributions along the body, (g) spatial-temporal thrust distribution

along the body during a tail beat cycle, (j) cycle-averaged thrust distribution on dorsal and ventral surfaces, (h) cycle-averaged thrust distribution along the body, and (i) cumulative cycle-averaged thrust productions along the body at $t/T=0.417$ between $St=0.355$ (left), $St=0.532$ (middle), and $St=0.798$ (right).

The spatial-temporal thrust distributions (Figure 7-7g) show increasing thrust production on both the trunk ($S1+S2+S3$) and the posterior sucker as St increases. No significant thrust production in $S1$ and $S2$ is found at $St=0.355$, while more significant thrust is found in $S1$ and $S2$ at higher St .

The cycle-averaged thrust distribution along the body (Figure 7-7h) shows a significant thrust increase in all body segments as St increase. The summed thrust over each segment (Table 7-5) shows that the $S1$ thrust is negative (-0.04) at $St=0.355$, while the $S1$ thrust increases to 0.13 at $St=0.798$. $S3$ and $S4$ at $St=0.355$ produce 86% and 27% of the total thrust, respectively, while they produce only 55% and 17% of the total thrust at $St=0.798$. The cumulative thrust productions (Figure 7-7i) along the body show an increasing percentage of thrust production by the anterior 60% of the body ($S1+S2$) from -13% at $St=0.355$ to 28% at $St=0.798$. In addition, $S1$ at higher $St=0.798$ reaches 6% of the total thrust, which is the highest among all cases studied.

7.4 Discussion

Two major performance enhancement mechanisms—edge vortex (EV) capture (Figure 7-8) and early vertical flow separation (Figure 7-8) both at the lateral edges of the trunk—are found to be responsible for the trunk thrust increase at a higher trunk cross section aspect ratio (AR).

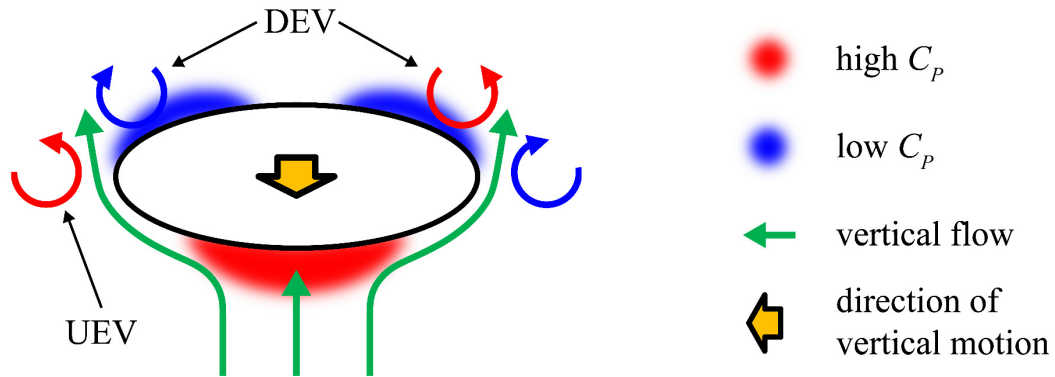


Figure 7-8: Schematics on mechanisms of edge vortex (EV) capture and early vertical flow separation.

The edge vortex (EV) capture mechanism shows that the trunk captures the counter-rotating upstroke edge vortex (UEV) pair at the lateral edges during vertical undulations. The UEV tends to strengthen the vertical flow across the lateral edges. The early flow separation mechanism shows that the separation of vertical flow with the lateral edges of the trunk happens earlier at the trunk with higher AR . The early flow separation creates a counter-rotating downstroke edge vortex (DEV) pair and causes a lower negative pressure in the recirculation zones over the dorsal side of the trunk, contributing to more suction thrust.

7.5 Chapter Summaries

In this section, we have combined experimental and numerical approaches to investigate the effect of trunk cross section shape (AR), Reynolds number (Re), and Strouhal number (St) on the thrust production mechanism and vortex dynamics of leech during steady swimming. High-speed videos of freely swimming medicinal leeches were obtained to provide the undulating kinematics

of the body. A biologically realistic computational model of the leech was reconstructed based on live leech kinematics. High-fidelity flow simulations of leech swimming were conducted using both the original model (M1) at $AR=2.48$ and modified models (M2 at $AR=1.24$ and M3 at $AR=4.96$). The effect of Reynolds number and Strouhal number on the hydrodynamic performance and vortex dynamics are examined by comparing the simulation results over wide ranges of Re (156~15600) and St (0.355~0.798).

It is found that both the trunk and the posterior sucker produce thrust from pressure forces and suction forces acting on the body surface to balance the viscous drag. During each tail beat stroke, the trunk induces a counter-rotating edge vortex pair that then interacts with the lateral edges of the trunk in the following stroke. The pressure isosurface evolution and spatial-temporal thrust map show traveling waves of the thrust production along the trunk and posterior sucker. The time-averaged thrust distribution shows 19% and 76% of the total thrust produced by the last 0.08L of the body (segment 4) and the last 0.4L (segment 3 and 4) of the body, respectively.

It is found that both the total thrust, power consumption, and propulsive efficiency increase with AR . The trunk thrust increase with AR while the thrust produced by the posterior sucker decrease. Pressure isosurface shows larger positive pressure and lower negative pressure regions over the trunk surface with larger AR . The time-averaged thrust distribution shows a significant increase in the percentage of thrust produced by the trunk as AR increase. The comparison in vortex dynamics shows stronger edge vortices and more significant interactions between the edge vortex pair and the trunk at higher AR trunk. A strong correlation between the vortex-trunk interaction and larger suction thrust production at the dorsal trunk surface is found. Analysis shows that the larger suction force and pressure force and more dorsal-ventrally orientated normal vector of the trunk surface result in the larger thrust production at the trunk with higher AR .

The parametric study in Re shows that the total thrust due to pressure, power consumption, and viscous drag all increase as the Re decrease, while propulsive efficiency decrease. The vortex structure shows a less significant edge vortex at lower Re . The pressure isosurface shows larger positive pressure and lower negative pressure regions over the trunk surface at larger Re , which causes more pressure thrust and suction thrust productions. The total thrust production is less fluctuating in time at higher Re as more temporal overlap exists in the thrust-producing regions that travel along the body. The time-averaged thrust distribution along the body shows similar patterns between different Re .

The parametric study in St shows that the total thrust and propulsive efficiency increase as St increases. The power consumption is the lowest at the original St . The vortex structure shows severer edge vortex separations associated with more small-scaled vortex structures at higher St and less strong edge vortex at lower St . The pressure isosurface show larger positive pressure and lower negative pressure regions over both the trunk surface and the posterior sucker at larger St , which corresponds to the larger thrust productions found at both parts of the body. The time-averaged thrust distribution along the body shows significant drag production due to surface pressure of the anterior trunk (segment 1) at lower St . While segment 1 at higher St ($St=0.798$) reaches 6% of the total thrust, which is the highest among all cases studied.

8 Concluding Remarks

The works presented in the current dissertation have investigated body-involved fluid dynamic interactions (BI-FDI) across wide ranges of morphological configuration and locomotion modes using combined experimental and numerical approaches. Results from the current studies aim to advance the understanding of body-involved performance enhancement mechanisms in biological propulsion and to provide novel physical insights into the design of aerial/underwater unmanned vehicles from a fluid dynamics perspective.

8.1 Summary of Contributions

In Chapter 3, a numerical investigation of wing-body interaction (WBI) was performed on the forward flight of a hummingbird. Results have shown significant overall lift enhancement (OLE) due to WBI. The total lift force of the WB model increased by 29% compared with its WO/BO counterparts. Vortex dynamics results showed formations of unique body vortex pairs on the dorsal thorax of the hummingbird where low-pressure zones were created to generate more body lift. Significant interactions between body vortex and leading-edge vortex (LEV) were observed, resulting in strengthened LEVs near the wing root and enhanced wing lift generation during the downstroke. Parametric studies showed strong OLEs over wide ranges of body angle and advance ratio, respectively. The contribution of OLE from the hummingbird body increased with increasing body angle, and the wing pair's contribution increased as the advance ratio increased. Results from this chapter supported that lift enhancement due to WBI is potentially a general mechanism adopted by flyers of various wing-body configurations, and demonstrated the

potential of WBI in the design of flapping-wing micro aerial vehicles (MAV) that pursue higher performance.

In Chapter 4, combined experimental and computational approaches were used to investigate the hydrodynamics of finlets in yellowfin tuna (*Thunnus albacares*) during steady swimming. It was found that finlets undergo both heaving and pitching motion and are delayed in phase from anterior to posterior along the body. Simulation results show that finlets were drag producing and did not produce thrust. The interactions among finlets helped reduce total finlet drag by 21.5%. The pitching motions of finlets helped reduce the power consumed by finlets during swimming by 20.8% compared with non-pitching finlets. Moreover, the pitching finlets created constructive forces to facilitate posterior body flapping. Wake dynamics analysis revealed a unique vortex tube matrix structure and cross-flow streams redirected by the pitching finlets, which supports their hydrodynamic function in scombrid fishes.

Chapter 5 used combined experimental and numerical approaches to examine the hydrodynamic role of finlets in the propulsive performance of tuna locomotion with biologically realistic geometric and kinematic complexity. It is found that finlets help increase caudal fin thrust by 8% and reduce trunk drag by 7%. The effect of swimming with finlets is equivalent to adding a propulsor with propulsive efficiency of 23.6%. Analyses on surface pressure and thrust distribution show regions that produce more thrust at the posterior trunk and the middle of the caudal fin owing to the presence of finlets. Vortex dynamics analysis shows that dorsal and ventral finlets generate a counter-rotating conical vortex pair during each stroke and interact with the caudal fin at the middle part. Detailed flow analysis reveals that the presence of finlets at the dorsal and ventral margins is responsible for the trunk drag reduction and the interactions between the finlet-induced vortex pair and the caudal fin is responsible for the caudal thrust enhancement. It is

further found that body-fixed finlets help increase caudal fin thrust by 10.5% and reduce trunk drag by 6.9%. Comparing the pitching finlets and body-fixed finlets, it is found that the pitching kinematics of finlets help reduce the finlet drag, lateral force amplitude, and power consumption. The lower drag and power consumption of the pitching finlets results in a higher nominal propulsive efficiency of 23.6% than the 16.6% of body-fixed finlets.

Chapter 6 combines experimental and numerical approaches to examine the enhanced hydrodynamic performance by dorsal fin and anal fin in juvenile rainbow trout steady swimming. It is found that the dorsal fin helps increase caudal fin thrust by 11% but did not reduce trunk drag significantly. During each tail beat stroke, the dorsal fin induces a lateral flow behind its trailing edge and a vortex (DFV) at its dorsal tip that both convect downstream and interact with the caudal fin at its dorsal leading edge. The lateral flow and DFV induce larger lateral velocity at the caudal fin, which strengthens the leading edge vortex (LEV) and creates lower negative pressure on the suction side and higher positive pressure on the pressure of the caudal fin, resulting in increased thrust production. The anal fin helps both reduce trunk drag by 6.9% and increase caudal fin thrust by 4.3%. The presence of the anal fin prevents the local lateral flow across the ventral edge of the trunk, which builds up a significant pressure difference between the two sides of the trunk with the positive pressure side producing more local thrust, thereby reducing the overall trunk drag. In addition, the presence of the anal fin prevents the formation of the peduncle vortex that is destructive for caudal fin thrust production, thereby increasing the caudal fin thrust. The pelvic fins help reduce all the anal fin drag and increase caudal fin thrust by 1.6%. The force changes in the dorsal fin and the trunk are less than 1%. The vortex shed from the pelvic fins interacts with the anal fin at the leading edge, which enhances the anal fin vortex and creates lower negative

pressure on the suction side, resulting in more suction thrust production to balance the anal fin drag.

Chapter 7 combined numerical and experimental approaches to examine the thrust production mechanism and associated vortex dynamics in leech swimming over wide ranges of trunk cross section shape (AR), Reynolds number (Re), and Strouhal number (St). It is found that both the trunk and the posterior sucker produce thrust from pressure forces and suction forces acting on the body surface to balance the viscous drag. During each tail beat stroke, the trunk induces a counter-rotating edge vortex pair that then interacts with the lateral edges of the trunk in the following stroke. The pressure isosurface evolution and spatial-temporal thrust map show traveling waves of the thrust production along the trunk and posterior sucker. The time-averaged thrust distribution shows 19% and 76% of the total thrust produced by the last $0.08L$ of the body (segment 4) and the last $0.4L$ (segment 3 and 4) of the body, respectively. It is found that both the total thrust, power consumption, and propulsive efficiency increase with AR . The trunk thrust increase with AR while the thrust produced by the posterior sucker decrease. Stronger edge vortices and more significant interactions between the edge vortex pair and the trunk at higher AR trunk. A strong correlation between the more intense vortex-trunk interaction and larger suction thrust production at the dorsal trunk surface is found. The larger suction force and pressure force and more dorsal-ventrally orientated normal vector of the trunk surface result in the larger thrust production at the trunk with higher AR . The parametric study of Re shows that the total thrust, power consumption, and viscous drag all increase as the Re decrease, while propulsive efficiency decrease. The vortex structure shows a less significant edge vortex at lower Re . A similar pattern in thrust distribution along the body is found at different Re . The parametric study in St shows that the total thrust and propulsive efficiency increase as St increases. The vortex structure shows

severer edge vortex separations associated with more small-scaled vortex structures at higher St and less strong edge vortex at lower St . Thrust production of the anterior trunk (segment 1) is most sensitive to St change, with drag production at lower St ($St=0.355$) and the highest thrust production (6% of the total thrust) among all cases at higher St ($St=0.798$).

8.2 Summary of Body-Involved Performance Enhancement Mechanisms

Two major categories of the performance enhancement mechanisms—the deflection or prevention of transverse flow across body edges and wake capture or wake prevention at the propulsor—found in the BI-FDIs examined in this dissertation work are listed in Table 8-1 and Table 8-2, respectively.

Although the transverse flow deflection/prevention mechanisms are found across different body configurations and locomotion modes, they share common features—(1) the mechanisms all involve deflection/prevention of lateral or vertical flows across the body edge, (2) the mechanisms usually happen at the posterior body where the undulation/oscillation amplitudes are relatively large, (3) significant pressure difference is created between the two sides of the body and fin/wing, (4) the enhancements happen instantaneously with the transverse motion of the body.

The common features of the wake capture/prevention mechanisms include (1) capture of the vortex wake convected from upstream by the propulsor, (2) the location of wake capture is dependent on the location of incoming vortex wake, (3) the wake capture/prevention mechanisms are delayed in phase than the transverse flow deflection/preventions mechanisms.

Table 8-1: Performance enhancement mechanisms on the deflection or prevention of transverse flow across body edges

Major category	Specific mechanism	Illustration	Enhancement type and value
Deflection or prevention of transverse flow across body edges	Lateral flow deflection at the posterior trunk		<ul style="list-style-type: none"> 7% trunk drag reduction. (Chapter 5 of the present dissertation)
			<ul style="list-style-type: none"> 15% and 50% increases in speed economy, respectively. (Zhong et al., 2019 [10])
			<ul style="list-style-type: none"> 20% body drag reduction. (Liu et al., 2017 [9])
	Lateral flow prevention at the posterior trunk		<ul style="list-style-type: none"> 6.9% trunk drag reduction. (Chapter 6 of the present dissertation)
			<ul style="list-style-type: none"> 22.2% trunk drag reduction. (Han et al., 2020 [17])
	Vertical flow early separation at lateral edges of trunk		<ul style="list-style-type: none"> Trunk thrust increases with increasing <i>AR</i>. (Chapter 7 of the present dissertation)
	Vertical flow prevention by body		<ul style="list-style-type: none"> 29% overall lift enhancement. (Wang et al., 2019 [23])

Table 8-2: Performance enhancement mechanisms on the wake capture or prevention

Major category	Specific mechanism	Illustration	Enhancement type and value
Wake capture or prevention at propulsor	Finlet induced vortex capture by caudal fin		<ul style="list-style-type: none"> 8% caudal fin thrust increase. (Chapter 5 of the present dissertation) 15% and 50% increases in speed economy, respectively. (Zhong et al., 2019 [10])
	Dorsal fin vortex and lateral flow capture by caudal fin		<ul style="list-style-type: none"> 11.3% caudal fin thrust increase. (Chapter 6 of the present dissertation)
			<ul style="list-style-type: none"> 25.6% caudal fin thrust increase. (Han et al., 2020 [17])
			<ul style="list-style-type: none"> 13.4% caudal fin thrust increase. (Liu et al., 2017 [9])
	Peduncle vortex prevention by anal fin		<ul style="list-style-type: none"> 4.3% caudal fin thrust increase. (Chapter 6 of the present dissertation)
Edge vortex capture by trunk		<ul style="list-style-type: none"> Trunk thrust increases with increasing AR. (Chapter 7 of the present dissertation) 	

8.3 Future Work

The works presented in this dissertation advance the knowledge of body-involved fluid dynamics interaction (BI-FDI) in biological propulsion over wide ranges of body-propulsor configuration and locomotion modes. However, the current works did not cover all categories of BI-FDI. For example, the BI-FDI in four-winged flyers such as dragonflies, and other locomotion modes such as maneuver, gliding/coasting, and intermittent swimming or flying. Explorations in these directions would gain a more comprehensive understanding of BI-FDI and inspire aerial/underwater unmanned vehicle designs.

Another attractive direction is to develop bio-inspired models as platforms to systematically explore BI-FDI under changes of certain parameters. For example, to develop an in-line propulsion model that is capable of testing the effect of body wavelength or effect of sizes and longitudinal locations of anterior median fins on the hydrodynamic performance of the propulsor. And, to develop a bilateral propulsion model that is capable of testing changes in the aspect ratio of the body and the wings and changes in the number and location of the wings. Explorations in these directions would use the inspirations gained from the current works for more systematically BI-FDI study.

Bibliography

- [1] F.E. Fish, G.V. Lauder, PASSIVE AND ACTIVE FLOW CONTROL BY SWIMMING FISHES AND MAMMALS, *Annual Review of Fluid Mechanics*, 38 (2005) 193-224.
- [2] D.D. Chin, D. Lentink, Flapping wing aerodynamics: from insects to vertebrates, *The Journal of Experimental Biology*, 219 (2016) 920.
- [3] R. Wood, R. Nagpal, G.-Y. Wei, flight of the robobees, *Scientific American*, 308 (2013) 60-65.
- [4] M. Keennon, K. Klingebiel, H. Won, Development of the Nano Hummingbird: A Tailless Flapping Wing Micro Air Vehicle, 50th AIAA Aerospace Sciences Meeting including the New Horizons Forum and Aerospace Exposition, American Institute of Aeronautics and Astronautics 2012.
- [5] J. Zhu, C. White, D.K. Wainwright, V. Di Santo, G.V. Lauder, H. Bart-Smith, Tuna robotics: A high-frequency experimental platform exploring the performance space of swimming fishes, *Science Robotics*, 4 (2019) eaax4615.
- [6] E.F. Fish, M.C. Schreiber, W.K. Moored, G. Liu, H. Dong, H. Bart-Smith, Hydrodynamic Performance of Aquatic Flapping: Efficiency of Underwater Flight in the Manta, *Aerospace*, 3 (2016).
- [7] G. Liu, H. Dong, C. Li, Vortex dynamics and new lift enhancement mechanism of wing-body interaction in insect forward flight, *Journal of Fluid Mechanics*, 795 (2016) 634-651.
- [8] A.T. Bode-Oke, H. Dong, The reverse flight of a monarch butterfly (*Danaus plexippus*) is characterized by a weight-supporting upstroke and postural changes, *Journal of The Royal Society Interface*, 17 (2020) 20200268.
- [9] G. Liu, Y. Ren, H. Dong, O. Akanyeti, J.C. Liao, G.V. Lauder, Computational analysis of vortex dynamics and performance enhancement due to body-fin and fin-fin interactions in fish-like locomotion, *Journal of Fluid Mechanics*, 829 (2017) 65-88.
- [10] Q. Zhong, H. Dong, D.B. Quinn, How dorsal fin sharpness affects swimming speed and economy, *Journal of Fluid Mechanics*, 878 (2019) 370-385.
- [11] S.P. Sane, The aerodynamics of insect flight, *The Journal of Experimental Biology*, 206 (2003) 4191-4208.

- [12] C.P. Ellington, C. van den Berg, A.P. Willmott, A.L.R. Thomas, Leading-edge vortices in insect flight, *Nature*, 384 (1996) 626-630.
- [13] J.M. Birch, M.H. Dickinson, Spanwise flow and the attachment of the leading-edge vortex on insect wings, *Nature*, 412 (2001) 729-733.
- [14] D. Lentink, M.H. Dickinson, Rotational accelerations stabilize leading edge vortices on revolving fly wings, *Journal of Experimental Biology*, 212 (2009) 2705.
- [15] R. Godoy-Diana, B. Thiria, On the diverse roles of fluid dynamic drag in animal swimming and flying, *Journal of The Royal Society Interface*, 15 (2018) 20170715.
- [16] I. Borazjani, M. Daghooghi, The fish tail motion forms an attached leading edge vortex, *Proceedings of the Royal Society B: Biological Sciences*, 280 (2013) 20122071.
- [17] P. Han, G.V. Lauder, H. Dong, Hydrodynamics of median-fin interactions in fish-like locomotion: Effects of fin shape and movement, *Physics of Fluids*, 32 (2020) 011902.
- [18] R.B. Srygley, A.L.R. Thomas, Unconventional lift-generating mechanisms in free-flying butterflies, *Nature*, 420 (2002) 660-664.
- [19] A.L.R. Thomas, G.K. Taylor, R.B. Srygley, R.L. Nudds, R.J. Bomphrey, Dragonfly flight: free-flight and tethered flow visualizations reveal a diverse array of unsteady lift-generating mechanisms, controlled primarily via angle of attack, *Journal of Experimental Biology*, 207 (2004) 4299.
- [20] M.W. Luttges, Accomplished insect fliers, *Frontiers in experimental fluid mechanics*, Springer1989, pp. 429-456.
- [21] R.J. Bomphrey, N.J. Lawson, N.J. Harding, G.K. Taylor, A.L.R. Thomas, The aerodynamics of *Manduca sexta*: digital particle image velocimetry analysis of the leading-edge vortex, *Journal of Experimental Biology*, 208 (2005) 1079.
- [22] H. Wan, H. Dong, K. Gai, Computational investigation of cicada aerodynamics in forward flight, *Journal of The Royal Society Interface*, 12 (2015) 20141116.
- [23] J. Wang, Y. Ren, C. Li, H. Dong, Computational investigation of wing-body interaction and its lift enhancement effect in hummingbird forward flight, *Bioinspiration & Biomimetics*, 14 (2019) 046010.
- [24] E.G. Drucker, G.V. Lauder, Locomotor function of the dorsal fin in teleost fishes: experimental analysis of wake forces in sunfish, *Journal of Experimental Biology*, 204 (2001) 2943.

- [25] E.G. Drucker, G.V. Lauder, Locomotor function of the dorsal fin in rainbow trout: kinematic patterns and hydrodynamic forces, *Journal of Experimental Biology*, 208 (2005) 4479.
- [26] E.D. Tytell, Median fin function in bluegill sunfish Lepomis macrochirus: streamwise vortex structure during steady swimming, *The Journal of Experimental Biology*, 209 (2006) 1516.
- [27] M. Sfakiotakis, D.M. Lane, J.B.C. Davies, Review of fish swimming modes for aquatic locomotion, *IEEE Journal of Oceanic Engineering*, 24 (1999) 237-252.
- [28] R. Dudley, Unsteady Aerodynamics, *Science*, 284 (1999) 1937.
- [29] L. Bennett, Insect Aerodynamics: Vertical Sustaining Force in Near-Hovering Flight, *Science*, 152 (1966) 1263-1266.
- [30] C.P. Ellington, The Aerodynamics of Hovering Insect Flight. III. Kinematics, *Philosophical Transactions of the Royal Society of London. B, Biological Sciences*, 305 (1984) 41-78.
- [31] M.H. Dickinson, K.G. Gotz, UNSTEADY AERODYNAMIC PERFORMANCE OF MODEL WINGS AT LOW REYNOLDS NUMBERS, *The Journal of Experimental Biology*, 174 (1993) 45-64.
- [32] H. Liu, K. Kawachi, A Numerical Study of Insect Flight, *Journal of Computational Physics*, 146 (1998) 124-156.
- [33] M. Sun, J. Tang, Unsteady aerodynamic force generation by a model fruit fly wing in flapping motion, *Journal of Experimental Biology*, 205 (2002) 55-70.
- [34] Z.J. Wang, The role of drag in insect hovering, *Journal of Experimental Biology*, 207 (2004) 4147-4155.
- [35] H. Aono, F. Liang, H. Liu, Near- and far-field aerodynamics in insect hovering flight: an integrated computational study, *Journal of Experimental Biology*, 211 (2008) 239-257.
- [36] R.J. Bomphrey, T. Nakata, N. Phillips, S.M. Walker, Smart wing rotation and trailing-edge vortices enable high frequency mosquito flight, *Nature*, 544 (2017) 92.
- [37] M.H. Dickinson, F.-O. Lehmann, S.P. Sane, Wing Rotation and the Aerodynamic Basis of Insect Flight, *Science*, 284 (1999) 1954-1960.
- [38] S.P. Sane, M.H. Dickinson, The control of flight force by a flapping wing: lift and drag production, *Journal of Experimental Biology*, 204 (2001) 2607.
- [39] F.-O. Lehmann, The mechanisms of lift enhancement in insect flight, *Naturwissenschaften*, 91 (2004) 101-122.

- [40] T. WEIS-FOGH, Quick Estimates of Flight Fitness in Hovering Animals, Including Novel Mechanisms for Lift Production, *Journal of Experimental Biology*, 59 (1973) 169-230.
- [41] M.J. Lighthill, On the Weis-Fogh mechanism of lift generation, *Journal of Fluid Mechanics*, 60 (1973) 1-17.
- [42] W.J. Maybury, F.-O. Lehmann, The fluid dynamics of flight control by kinematic phase lag variation between two robotic insect wings, *Journal of Experimental Biology*, 207 (2004) 4707-4726.
- [43] M. Sun, X. Yu, Aerodynamic Force Generation in Hovering Flight in a Tiny Insect, *AIAA Journal*, 44 (2006) 1532-1540.
- [44] Z.J. Wang, D. Russell, Effect of Forewing and Hindwing Interactions on Aerodynamic Forces and Power in Hovering Dragonfly Flight, *Physical Review Letters*, 99 (2007) 148101.
- [45] B. Liang, M. Sun, Aerodynamic Interactions Between Wing and Body of a Model Insect in Forward Flight and Maneuvers, *Journal of Bionic Engineering*, 10 (2013) 19-27.
- [46] L. Hedrick Tyson, W. Tobalske Bret, G. Ros Ivo, R. Warrick Douglas, A. Biewener Andrew, Morphological and kinematic basis of the hummingbird flight stroke: scaling of flight muscle transmission ratio, *Proceedings of the Royal Society B: Biological Sciences*, 279 (2012) 1986-1992.
- [47] J. Song, B.W. Tobalske, D.R. Powers, T.L. Hedrick, H. Luo, Three-dimensional simulation for fast forward flight of a calliope hummingbird, *Royal Society Open Science*, 3 (2016) 160230.
- [48] Y. Ren, H. Dong, X. Deng, B. Tobalske, Turning on a dime: Asymmetric vortex formation in hummingbird maneuvering flight, *Physical Review Fluids*, 1 (2016) 050511.
- [49] B.W. Tobalske, D.R. Warrick, C.J. Clark, D.R. Powers, T.L. Hedrick, G.A. Hyder, A.A. Biewener, Three-dimensional kinematics of hummingbird flight, *Journal of Experimental Biology*, 210 (2007) 2368.
- [50] R. Dudley, *The biomechanics of insect flight: form, function, evolution*, Princeton University Press 2002.
- [51] H.C. Corben, Wing-beat frequencies, wing-areas and masses of flying insects and hummingbirds, *Journal of Theoretical Biology*, 102 (1983) 611-623.
- [52] R.R. Harbig, J. Sheridan, M.C. Thompson, The role of advance ratio and aspect ratio in determining leading-edge vortex stability for flapping flight, *Journal of Fluid Mechanics*, 751 (2014) 71-105.

- [53] H.S.H. Yuen, Behavior of Skipjack Tuna, *Katsuwonus pelamis*, as Determined by Tracking with Ultrasonic Devices, *Journal of the Fisheries Research Board of Canada*, 27 (1970) 2071-2079.
- [54] F.W.H. Beamish, Swimming Capacity, *Fish Physiology*, 7 (1978) 101-187.
- [55] C.C. Lindsey, Form, Function and Locomotory Habits in Fish, *Locomotion*, (1978).
- [56] J.C. Nauen, G.V. Lauder, Locomotion in scombrid fishes: morphology and kinematics of the finlets of the chub mackerel *Scomber japonicus*, *Journal of Experimental Biology*, 203 (2000) 2247.
- [57] J.C. Nauen, G.V. Lauder, Three-Dimensional Analysis of Finlet Kinematics in the Chub Mackerel (*Scomber japonicus*), *The Biological Bulletin*, 200 (2001) 9-19.
- [58] J.C. Nauen, G.V. Lauder, Locomotion in scombrid fishes: visualization of flow around the caudal peduncle and finlets of the chub mackerel *Scomber japonicus*, *Journal of Experimental Biology*, 204 (2001) 2251.
- [59] V. Walters, Body Form and Swimming Performance in the Scombroid Fishes, *American Zoologist*, 2 (1962) 143-149.
- [60] P.W. Webb, Hydrodynamics and energetics of fish propulsion, *Bulletin of the Fisheries Research Board of Canada*, 190 (1975) 1-159.
- [61] J.J. Magnuson, Hydrostatic Equilibrium of *Euthynnus affinis*, a Pelagic Teleost without a Gas Bladder, *Copeia*, 1970 (1970) 56-85.
- [62] C.S. Wardle, Effects of size on the swimming speeds of fish, *Scale effects in animal locomotion*, (1977) 299.
- [63] I.U. Aleev, Function and gross morphology in fish, *Function and gross morphology in fish*, (1969).
- [64] G. Helfman, B. Collette, D. Facey, *The diversity of fishes*. Malden, Massachusetts: Blackwell Scientific Publications, (1997).
- [65] D.K. Wainwright, G.V. Lauder, Tunas as a high-performance fish platform for inspiring the next generation of autonomous underwater vehicles, *Bioinspiration & Biomimetics*, 15 (2020) 035007.
- [66] Q. Zhu, M.J. Wolfgang, D.K.P. Yue, M.S. Triantafyllou, Three-dimensional flow structures and vorticity control in fish-like swimming, *Journal of Fluid Mechanics*, 468 (2002) 1-28.
- [67] S. Wang, X. Zhang, G. He, Numerical Simulation of a Three-Dimensional Fish-like Body Swimming with Finlets, *Communications in Computational Physics*, 11 (2015) 1323-1333.

- [68] S. Najafi, M. Abbaspour, Numerical study of propulsion performance in swimming fish using boundary element method, *Journal of the Brazilian Society of Mechanical Sciences and Engineering*, 39 (2017) 443-455.
- [69] E.M. Standen, G.V. Lauder, Hydrodynamic function of dorsal and anal fins in brook trout (*Salvelinus fontinalis*), *Journal of Experimental Biology*, 210 (2007) 325-339.
- [70] E.D. Tytell, E.M. Standen, G.V. Lauder, Escaping Flatland: three-dimensional kinematics and hydrodynamics of median fins in fishes, *Journal of Experimental Biology*, 211 (2008) 187-195.
- [71] W.B. Kristan, R.L. Calabrese, W.O. Friesen, Neuronal control of leech behavior, *Progress in Neurobiology*, 76 (2005) 279-327.
- [72] J. Chen, W.O. Friesen, T. Iwasaki, Mechanisms underlying rhythmic locomotion: body–fluid interaction in undulatory swimming, *Journal of Experimental Biology*, 214 (2011) 561-574.
- [73] S. Wang, X. Zhang, G. He, Numerical Simulation of a Three-Dimensional Fish-like Body Swimming with Finlets, *Communications in Computational Physics*, 11 (2012) 1323-1333.
- [74] R. Mittal, H. Dong, M. Bozkurttas, F.M. Najjar, A. Vargas, A. von Loebbecke, A versatile sharp interface immersed boundary method for incompressible flows with complex boundaries, *Journal of Computational Physics*, 227 (2008) 4825-4852.
- [75] A.T. Bode-Oke, S. Zeyghami, H. Dong, Flying in reverse: kinematics and aerodynamics of a dragonfly in backward free flight, *Journal of The Royal Society Interface*, 15 (2018) 20180102.
- [76] C. Li, H. Dong, Wing kinematics measurement and aerodynamics of a dragonfly in turning flight, *Bioinspiration & Biomimetics*, 12 (2017) 026001.
- [77] H. Dong, R. Mittal, F.M. Najjar, Wake topology and hydrodynamic performance of low-aspect-ratio flapping foils, *Journal of Fluid Mechanics*, 566 (2006) 309-343.
- [78] C. Li, H. Dong, G. Liu, Effects of a dynamic trailing-edge flap on the aerodynamic performance and flow structures in hovering flight, *Journal of Fluids and Structures*, 58 (2015) 49-65.
- [79] C. Koehler, Z. Liang, Z. Gaston, H. Wan, H. Dong, 3D reconstruction and analysis of wing deformation in free-flying dragonflies, *The Journal of Experimental Biology*, 215 (2012) 3018.
- [80] G. Liu, Y. Ren, J. Zhu, H. Bart-Smith, H. Dong, Thrust producing mechanisms in ray-inspired underwater vehicle propulsion, *Theoretical and Applied Mechanics Letters*, 5 (2015) 54-57.
- [81] H. Zhao, A fast sweeping method for eikonal equations, *Mathematics of computation*, 74 (2005) 603-627.

- [82] X. Deng, P. Han, J. Wang, H. Dong, A level set based boundary reconstruction method for 3-D bio-inspired flow simulations with sharp-interface immersed boundary method, 2018 Fluid Dynamics Conference, AIAA paper, 2018, pp. 2018-4163.
- [83] J. Wang, H. Tran, M. Christino, C. White, J. Zhu, G. Lauder, H. Bart-Smith, H. Dong, Hydrodynamics and Flow Characterization of Tuna-Inspired Propulsion in Forward Swimming, ASME-JSME-KSME 2019 8th Joint Fluids Engineering Conference, 2019, pp. V001T001A025.
- [84] S. Yang, W. Zhang, Numerical analysis of the three-dimensional aerodynamics of a hovering rufous hummingbird (*Selasphorus rufus*), *Acta Mechanica Sinica*, 31 (2015) 931-943.
- [85] Y. Ren, Low Dimensional Morphology Analysis and Computational Optimization of Flapping Propulsors in Nature, Department of Mechanical and Aerospace Engineering, University of Virginia, 2016.
- [86] J. Song, H. Luo, T.L. Hedrick, Three-dimensional flow and lift characteristics of a hovering ruby-throated hummingbird, *Journal of The Royal Society Interface*, 11 (2014).
- [87] R. Ingersoll, D. Lentink, How the hummingbird wingbeat is tuned for efficient hovering, *The Journal of Experimental Biology*, 221 (2018) jeb178228.
- [88] J. Hunt, A. Wray, P. Moin, Eddies, streams, and convergence zones in turbulent flows, *Studying Turbulence Using Numerical Simulation Databases*, 2, (1988).
- [89] X. Yu, M. Sun, A computational study of the wing–wing and wing–body interactions of a model insect, *Acta Mechanica Sinica*, 25 (2009) 421-431.
- [90] J.-S. Han, J.W. Chang, J.-H. Han, The advance ratio effect on the lift augmentations of an insect-like flapping wing in forward flight, *Journal of Fluid Mechanics*, 808 (2016) 485-510.
- [91] J.-S. Han, J.W. Chang, H.-K. Cho, Vortices behavior depending on the aspect ratio of an insect-like flapping wing in hover, *Experiments in Fluids*, 56 (2015) 181.
- [92] L.R. Thomas Adrian, On the aerodynamics of birds' tails, *Philosophical Transactions of the Royal Society of London. Series B: Biological Sciences*, 340 (1993) 361-380.
- [93] B. Liang, M. Sun, Aerodynamic Interactions Between Contralateral Wings and Between Wings and Body of a Model Insect at Hovering and Small Speed Motions, *Chinese Journal of Aeronautics*, 24 (2011) 396-409.
- [94] B.B. Collette, C.E. Nauen, FAO species catalogue. Volume 2. Scombrids of the world. An annotated and illustrated catalogue of tunas, mackerels, bonitos and related species known to date, 1983, pp. vii + 137pp.

- [95] V. Pavlov, B. Rosental, N.F. Hansen, J.M. Beers, G. Parish, I. Rowbotham, B.A. Block, Hydraulic control of tuna fins: A role for the lymphatic system in vertebrate locomotion, *Science*, 357 (2017) 310.
- [96] N. Li, H. Liu, Y. Su, Numerical study on the hydrodynamics of thunniform bio-inspired swimming under self-propulsion, *PLOS ONE*, 12 (2017) e0174740.
- [97] M. Bozkurtas, R. Mittal, H. Dong, G.V. Lauder, P. Madden, Low-dimensional models and performance scaling of a highly deformable fish pectoral fin, *Journal of Fluid Mechanics*, 631 (2009) 311-342.
- [98] I. Borazjani, F. Sotiropoulos, Numerical investigation of the hydrodynamics of carangiform swimming in the transitional and inertial flow regimes, *Journal of Experimental Biology*, 211 (2008) 1541-1558.
- [99] J.C. Hunt, A.A. Wray, P. Moin, Eddies, streams, and convergence zones in turbulent flows, (1988).
- [100] M. Bozkurtas, R. Mittal, H. Dong, G. Lauder, P. Madden, Low-dimensional models and performance scaling of a highly deformable fish pectoral fin, *Journal of Fluid Mechanics*, 631 (2009) 311-342.
- [101] A.A. Shirgaonkar, O.M. Curet, N.A. Patankar, M.A. MacIver, The hydrodynamics of ribbon-fin propulsion during impulsive motion, *Journal of Experimental Biology*, 211 (2008) 3490.
- [102] K.B. Lua, K.C. Lai, T.T. Lim, K.S. Yeo, On the aerodynamic characteristics of hovering rigid and flexible hawkmoth-like wings, *Experiments in Fluids*, 49 (2010) 1263-1291.
- [103] Y.S. Baik, L.P. Bernal, Experimental study of pitching and plunging airfoils at low Reynolds numbers, *Experiments in Fluids*, 53 (2012) 1979-1992.
- [104] Y.S. Baik, L.P. Bernal, K. Granlund, M.V. Ol, Unsteady force generation and vortex dynamics of pitching and plunging aerofoils, *Journal of Fluid Mechanics*, 709 (2012) 37-68.
- [105] S. Heathcote, Z. Wang, I. Gursul, Effect of spanwise flexibility on flapping wing propulsion, *Journal of Fluids and Structures*, 24 (2008) 183-199.
- [106] W. Medjroubi, B. Stoevesandt, B. Carmo, J. Peinke, High-order numerical simulations of the flow around a heaving airfoil, *Computers & Fluids*, 51 (2011) 68-84.
- [107] J.H. Buchholz, A.J. Smits, The wake structure and thrust performance of a rigid low-aspect-ratio pitching panel, *Journal of fluid mechanics*, 603 (2008) 331-365.

- [108] J. Wang, D.K. Wainwright, R.E. Lindengren, G.V. Lauder, H. Dong, Tuna locomotion: a computational hydrodynamic analysis of finlet function, *Journal of The Royal Society Interface*, 17 (2020) 20190590.
- [109] C.H. White, G.V. Lauder, H. Bart-Smith, Tunabot Flex: a tuna-inspired robot with body flexibility improves high-performance swimming, *Bioinspiration & Biomimetics*, 16 (2021) 026019.
- [110] R. Mittal, S. Balachandar, Generation of Streamwise Vortical Structures in Bluff Body Wakes, *Physical Review Letters*, 75 (1995) 1300-1303.
- [111] K.N. Lucas, G.V. Lauder, E.D. Tytell, Airfoil-like mechanics generate thrust on the anterior body of swimming fishes, *Proceedings of the National Academy of Sciences*, 117 (2020) 10585.